The Redox Chemistry of Sulfur in Cathode Materials for Rechargeable Li-ion Batteries

Rui Qi

Exeter College

University of Oxford

A thesis submitted for the degree of

Doctor of Philosophy

Trinity 2025

Abstract

There is an urgent need for rechargeable batteries with higher energy density. Lithium-rich cathodes represent one of the few routes available to increase the energy density of Li-ion batteries by invoking redox chemistry of both the transition metal (TM) and anionic redox in the lattice.

However, in Li-rich oxide cathodes, the oxidation of O^{2-} is accompanied by the formation of O_2 trapped in nano-sized pores within the cathode and irreversible O_2 loss from the particle surfaces, leading to voltage hysteresis, voltage fade and low first-cycle coulombic efficiency. Moving from Li-rich oxides to Li-rich sulfides using S-redox offers a potential way to mitigate most of these limitations. In this thesis, model Li-rich sulfides have been studied to understand the fundamental process of S-redox.

Firstly, $Li_{1.2}Ti_{0.8}S_2$, with S-redox, is investigated as a direct analogue of layered Li-rich oxides. The formation of persulfide S_2^{2-} species during charge is identified. Dimerization of oxidized S is accompanied by rearrangement of the TM layer to form nanovoids, as in Li-rich oxides, accounting for the presence of voltage hysteresis. In Li-rich sulfides, the S_2^{2-} dimers remain coordinated to TM atoms, offering insights into the differing electrochemical properties of O-redox and S-redox cathodes.

Secondly, the electrochemical performance of $Li_{1.2}Ti_{0.8}S_2$ was examined in all-solid-state batteries (ASSBs). At room temperature, ASSBs using $Li_{1.2}Ti_{0.8}S_2$ deliver an areal capacity of ~ 2.8 mAh cm^{-2} with > 99% capacity retention over 200 cycles under a low stack pressure of 2 MPa. This excellent performance highlights the promise of Li-rich sulfides as cathodes for ASSBs, beyond conventional high-voltage oxides.

Finally, S-redox materials $Li_{1.2}Mn_{0.2}Ti_{0.6}S_2$ and $Li_{1.2}Ti_{0.8}S_2$ are studied in parallel, and the critical role of the TM-S covalency is revealed. Stronger Mn 3*d*-S 3*p* hybridization significantly enhances electronic conductivity during S oxidation in $Li_{1.2}Mn_{0.2}Ti_{0.6}S_2$, while it does not suppress S_2^{2-} dimer formation.

The Redox Chemistry of Sulfur in Cathode Materials for Rechargeable Li-ion Batteries

Rui Qi
Exeter College
University of Oxford

A thesis submitted for the degree of
Doctor of Philosophy
Trinity 2025

Acknowledgements

First and foremost, I would like to thank my supervisor, Professor Sir Peter Bruce. I am very grateful for the opportunity you have given me to study under your supervision as a member of your world-leading group. Thank you also for the outstanding lab resources you have established in Oxford, and for enabling access to world-class synchrotron facilities, without which this work would not have been possible. I have thoroughly enjoyed the challenge of tackling fundamental problems in battery science with academic rigour, and this journey has been both inspiring and rewarding.

Dr Sofia De Sousa Coutinho, it has been an absolute pleasure to work with you over the last three years. I greatly enjoyed working with you in our mutual struggle to unravel the fundamental process of S-redox, as well as the many beam times we experienced together. Dr Mikkel Juelsholt, thank you for your support and guidance on the crystallography work, which has been an indispensable part of this thesis. Dr John-Joseph Maire, thank you for helping me settle into the lab during my early days. Dr Longlong Wang, thank you for introducing me to the all-solid-state battery field and for patiently answering my numerous questions. Thank you also to Dr Jun Chen and Dr Bingkun Hu for your kind advice and support, Dr Mingzhi Cai and Dr Xueyan Hou for proofreading my thesis and others with whom I have worked closely, including Dr Gregory Rees, Dr Javier Castells-Gil, Dr Felix Mocanu, Dr Paul Adamson, Dr Hlynur Gretarsson, and Dr Svemir Rudic. It has been a real privilege to work alongside such dynamic, intelligent and creative scientists as you all.

Professor Robert House, thank you for your continued guidance and support during my degree. Your critical thinking, sharp insights and endless experience have taught and inspired me so much. It has been deeply enriching and joyful to work with you. To Patrick Rees, Lechen Yang, Bartholomew Payne, Nicole Mitchell, Dr Liquan Pi, Dr Miguel Perez-Osario, Yuanhui Zhu, Arun Ramanathan, Jiapeng Liu and the other lab members, thank you for helping me in various ways and contributing to such a cheerful and supportive group atmosphere. I would also like to acknowledge the friendship and camaraderie of Dr Karin Kapadia, Hewen Chen, Shenghuan Ding, and Chen Shen, which I have greatly appreciated over the years.

To my family, thank you for your unconditional support throughout this journey. I owe my greatest gratitude to my parents, whose encouragement and support always gave me the strength to move forward with confidence. I would not be where I am today without your selfless love. My heartfelt thanks also go to my grandparents and brother for their constant care, support, and understanding. Finally, I wish to express my sincere gratitude to my partner, Zixuan Li. I am grateful for the destiny that brought us together in Oxford and allowed us to complete our PhD degrees side by side. Your unwavering love, steadfast support and endless humour have made this journey far more meaningful and colourful.

Abstract

There is an urgent need for rechargeable batteries with higher energy density. Lithium-rich cathodes represent one of the few routes available to increase the energy density of Li-ion batteries by invoking redox chemistry of both the transition metal (TM) and anionic redox in the lattice.

However, in Li-rich oxide cathodes, the oxidation of O^{2-} is accompanied by the formation of O_2 trapped in nano-sized pores within the cathode and irreversible O_2 loss from the particle surfaces, leading to voltage hysteresis, voltage fade and low first-cycle coulombic efficiency. Moving from Li-rich oxides to Li-rich sulfides using S-redox offers a potential way to mitigate most of these limitations. In this thesis, model Li-rich sulfides have been studied to understand the fundamental process of S-redox.

Firstly, $Li_{1.2}Ti_{0.8}S_2$, with S-redox, is investigated as a direct analogue of layered Li-rich oxides. The formation of persulfide S_2^{2-} species during charge is identified. Dimerization of oxidized S is accompanied by rearrangement of the TM layer to form nanovoids, as in Li-rich oxides, accounting for the presence of voltage hysteresis. In Li-rich sulfides, the S_2^{2-} dimers remain coordinated to TM atoms, offering insights into the differing electrochemical properties of O-redox and S-redox cathodes.

Secondly, the electrochemical performance of $Li_{1.2}Ti_{0.8}S_2$ was examined in all-solid-state batteries (ASSBs). At room temperature, ASSBs using $Li_{1.2}Ti_{0.8}S_2$ deliver an areal capacity of ~ 2.8 mAh cm^{-2} with > 99% capacity retention over 200 cycles under a low stack pressure of 2 MPa. This excellent performance highlights the promise of Li-rich sulfides as cathodes for ASSBs, beyond conventional high-voltage oxides.

Finally, S-redox materials $Li_{1.2}Mn_{0.2}Ti_{0.6}S_2$ and $Li_{1.2}Ti_{0.8}S_2$ are studied in parallel, and the critical role of the TM-S covalency is revealed. Stronger Mn 3*d*-S 3*p* hybridization significantly enhances electronic conductivity during S oxidation in $Li_{1.2}Mn_{0.2}Ti_{0.6}S_2$, while it does not suppress S_2^{2-} dimer formation.

Contents

Table of Contents

List of Figures

List of Tables

List of Publications

1. Rui, Q. *et al*. Oxidized S^{2-} forms persulfide S_2^{2-} dimers in Li-rich sulfide cathodes (Manuscript completed)
2. Zixuan, Li., Rui, Q. *et al.* Cation-disordered rocksalt cathode for anode-free Zn-ion batteries. *Energy Environmental Science*. 18, 10135-10146 (2025).
3. Yuan, Q., Dingqiao, J., Yi, Y., Hang, X., Rui, Q. *et al*. Mg-rich disordered rocksalt oxide cathodes for Mg-ion batteries. *Journal of Materials Chemistry A* 12, 27303–27310 (2024).
4. Zixuan, L., Yi, Y., Shengda, P., Rui, Q. *et al.* Achieving planar Zn electroplating in aqueous Zn batteries with cathode-compatible current densities by cycling under pressure. *Advanced Materials.* 36, 2401576 (2024).

List of Abbreviations

TM	Transition metal
ASSBs	All-solid-state batteries
LIB	Lithium-ion battery
TMOs	Transition metal oxides
SEs	Solid-state electrolytes
DFT	Density Functional Theory
XANES	X-ray absorption near-edge structure
EELS	Electron energy loss spectroscopy
sXAS	Soft X-ray absorption spectroscopy
XPS	X-ray photoelectron spectroscopy
RIXS	X-ray inelastic scattering
NMR	Nuclear magnetic resonance
SQUID	Superconducting quantum interference device
XRD	X-ray diffraction
STEM	Scanning transmission electron microscopy
HAXPES	Hard X-ray photoelectron spectroscopy
CAMs	Cathode active materials
ADF	Annular dark field
SEM	Scanning electron microscopy
PFIB-SEM	Plasma focused ion beam – SEM
EDX	Energy dispersive X-ray spectroscopy
X-ray CT	X-ray computed tomography
3D	Three-dimensional
2D	Two-dimensional
PXRD	Powder X-ray diffraction
ND	Neutron diffraction
TOF	Time-of-Flight
PDF	Pair distribution function
PTFE	Polytetrafluorethylene
PVDF	Polyvinylidene fluoride

PTFE	Polytetrafluorethylene PTFE
NMP	N-Methyl-2-pyrrolidone
EC	Ethylene carbonate
DMC	Dimethyl carbonate
PEEK	Polyether Ether Ketone
CC-CV	Constant current-constant voltage
DC	Direct current
UHV	Ultra-high vacuum
TFY	Total fluorescence yield
PFY	Partial fluorescence yield
TEY	Total electron yield
INS	Inelastic neutron scattering
OCV	Open-circuit voltage
FOV	Field of view
KBC	Ketjenblack carbon
PCC	Pristine composite cathode
PPC	Pristine pure cathode
STXM	Scanning transmission X-ray microscopy

1

Introduction

Contents

1.1 Wider Context

Rechargeable batteries have become indispensable in modern life. By providing compact and portable electrical power on demand, they have enabled the widespread use of smartphones, laptops, tablets and countless other devices. Beyond consumer electronics, the global transition to clean energy is driving the development of electric transportation and large-scale renewable energy storage, further motivating research into rechargeable batteries with higher energy density, longer lifetime, improved sustainability and lower cost.

Lithium-ion battery (LIB) technology has dominated in all of these applications.[1, 2] They operate through a controlled, reversible chemical reaction in which Li ions and electrons shuttle back and forth between two host materials to store and release electrical energy. Early research identified graphite as the anode and $LiCoO_2$ as the cathode [3, 4] Subsequent compositional substitutions (e.g., with Mn and Ni) and advances in engineering have significantly improved battery performance.[1] However, much of the available capacity within traditional LIBs has now been exploited, creating pressure to identify genuinely new materials and chemistries for next-generation batteries.

Two major strategies are being pursued. The first is to develop cathode materials with substantially higher capacity, as the present state-of-the-art layered transition metal oxides (TMOs), such as $LiCoO_2$ and $LiNi_{0.8}Co_{0.1}Mn_{0.1}O_2$, fall far behind commercial graphite anodes in capacity.[5, 6] The second is the transition from conventional LIBs with liquid electrolytes to all-solid-state batteries (ASSBs), which employ solid-state electrolytes (SEs). ASSBs, in principle, can apply Li metal anodes and enable bipolar stacking, thereby reducing inactive mass and improving cell-level energy density.[7] Ultimately, success in both approaches requires the development of high-performance cathodes.

In this context, Li-rich oxide cathodes have been developed to overcome the capacity limitations of conventional TMOs.[8-10] By increasing the Li/TM ratio above 1, for example, $Li_{1.2}Ni_{0.13}Mn_{0.54}Co_{0.13}O_2$, these materials access additional capacity through the oxidation and reduction of the oxygen ions (O-redox) in addition to TM redox, nearly doubling the capacity of conventional TMO cathodes.[11, 12] Despite their promise, persistent challenges, including severe voltage hysteresis, rapid voltage decay, and sluggish kinetics related to their bulk structural change, have so far significantly prevented commercialization, even after decades of effort from academia and industry.[13, 14]

Replacing oxide anions with sulfide anions to make Li-rich sulfides has recently emerged as a promising alternative. Li-rich sulfides that exploit S-redox exhibit significant mitigation of the unfavored features with O-redox, while opening a whole new chemical space for high-energy cathodes.[15, 16] They also expand compositional design and often avoid reliance on Co and Ni, elements associated with high cost, limited supply, and ethical concerns, providing further benefits in sustainability.[2] All the materials studied in this thesis are Co- and Ni-free.

A detailed understanding of S-redox chemistry is therefore critical not only for completing the broader picture of anionic redox activity but also for guiding the design of next-generation cathodes. The distinct electrochemical behavior of S-redox compared to O-redox within analogues of Li-rich structures makes it an intriguing scientific phenomenon in its own right. At the same time, Li-rich sulfides are particularly relevant for ASSBs, where their chemical compatibility with sulfide SEs may offer unique advantages.[17, 18] Together, these motivations establish S-redox in Li-rich sulfides as both a compelling scientific question and a promising pathway toward future high-energy-density batteries.

1.2 Fundamentals of Li-ion Batteries

1.2.1 The Layout of a Li-ion Battery

A LIB is made up of three primary functional components: a positive electrode (cathode), an electrolyte and a negative electrode (anode).[19, 20] As shown in Figure 1.1, the electrodes are arranged face-to-face and separated by an electronically insulating separator that is saturated with liquid electrolyte. The electrolyte conducts Li^+ ions but blocks electrons. During charging, Li^+ ions are extracted from the cathode and then migrate through the electrolyte and separator, and finally are inserted into the anode. Simultaneously, electrons travel from the cathode side to the current collector and through the external circuit to the anode electrode, producing the current. During discharge, these processes are reversed, liberating the stored electrical energy.

In commercial LIBs, the active materials are commonly $LiCoO_2$ at the cathode and graphite at the anode. As these materials are powders, polymer binders are used to immobilize them and maintain good contact with the metal current collectors. Due to the intrinsically poor electronic conductivity of most cathodes, a small amount of finely dispersed conductive carbon is typically added to provide an electronic percolation network.[21] The liquid electrolyte, which is typically a Li salt, like $LiPF_6$, dissolved in a non-aqueous solvent, permeates the porous electrodes, ensuring thorough wetting and efficient Li^+ transport between the electrolyte and active particles.

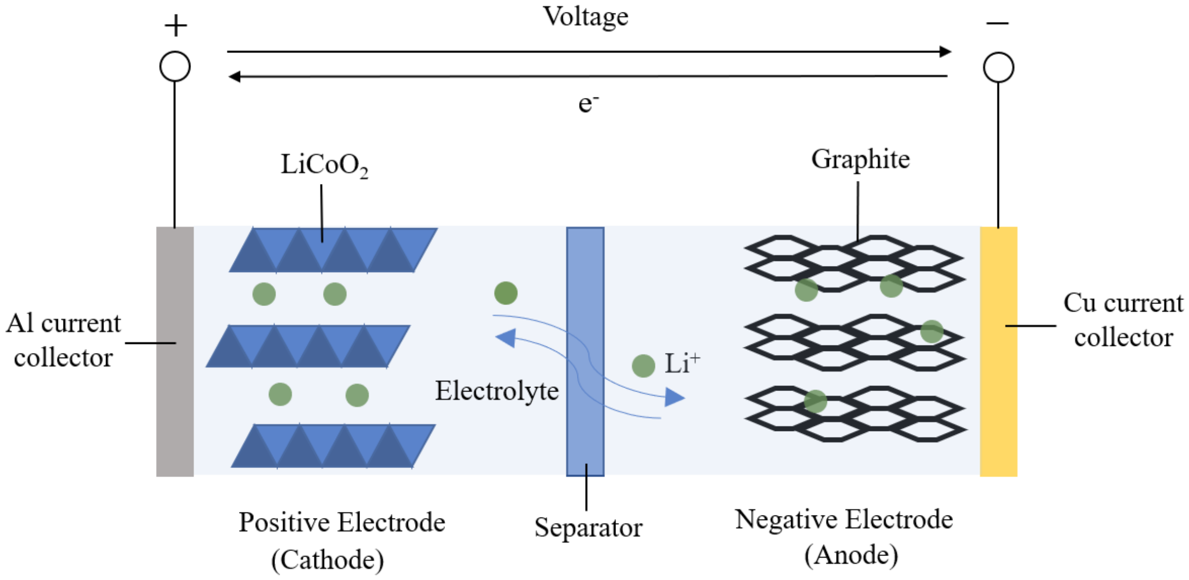

Figure 1.1: Schematic showing the key components of a Li-ion battery.

1.2.2 Energy Storage Mechanism

In an electrochemical cell, the two electrodes are the main reactive components and are where energy is stored in the form of chemical potential energy. Each electrode has a chemical potential associated with it, which depends on the chemical composition of the electrode material.[22-24] The equilibrium voltage of the cell is set by the difference in chemical potential between the cathode and anode electrodes. The Nernst equation can describe this,

$$E = -\frac{\Delta G}{zF} = -\frac{\mu^{(+)} - \mu^{(-)}}{zF} \tag{1.1}$$

Where E is the equilibrium cell voltage, z is the charge of the carrier ion (1 for Li^+), F is the Faraday constant, ΔG is the Gibbs free energy of the system, and $\mu^{(+)}$ and $\mu^{(-)}$ are the chemical potentials of the cathode and anode electrodes, respectively. During operation, as Li^+ and electrons are inserted into or extracted from an electrode, its chemical potential changes to reflect it becoming more reduced or oxidized. Taking a $LiCoO_2$ | graphite battery as an example, as shown in Figure 1.2, during charge, Li^+ ions de-intercalate from the $LiCoO_2$ host structure, oxidizing Co^{3+} toward Co^{4+} and removing electrons in the process, while Li^+ ions intercalate into graphite, reducing the carbon host. At the end of the charge, the chemical potential difference between electrodes is large, providing a strong driving force for the reaction between them to proceed. When an external circuit is closed, the reduction of the cathode and oxidation of the anode will occur spontaneously, until the circuit is opened or the electrode potentials reach equilibrium.

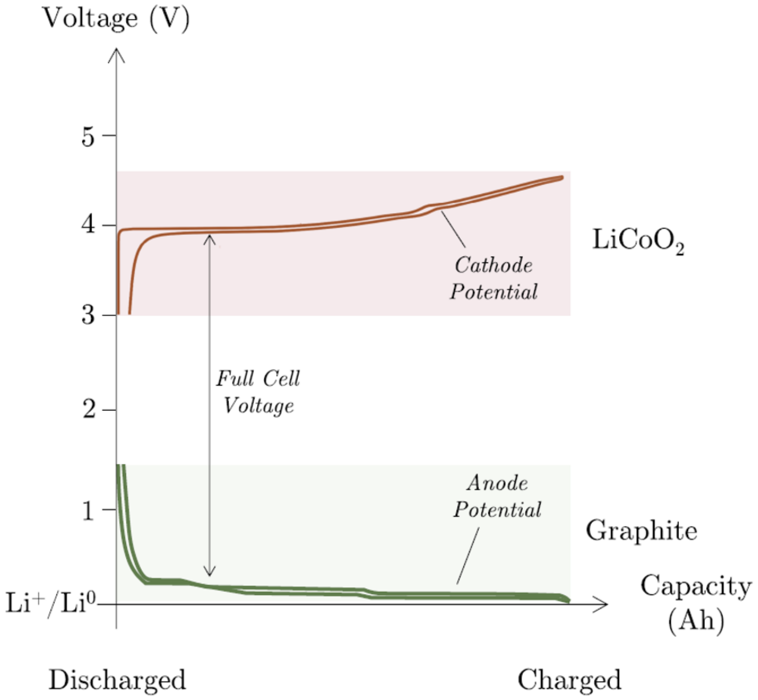

Figure 1.2: Schematic showing the potential variation of each electrode as a function of capacity. The difference between the potential curves at a given capacity is the measured cell voltage. Electrodes are balanced by capacity.

Beyond the voltage of a cell, capacity is the other primary performance metric. Capacity quantifies the total amount of charge the cell can deliver, and for commercial cell, is often reported in Ah. Together, the product of capacity and average operating voltage yields the energy in Wh, determining how much energy can be stored in a battery.[25, 26] Normalizing the total energy by mass or volume gives the gravimetric and volumetric energy densities, Wh kg^{-1} and Wh L^{-1}, respectively.

For battery research, when studying the properties of a specific electrode material, capacity is typically expressed as the specific capacity in mAh g^{-1}. The total theoretical capacity of a given material can be derived from the following equation,

$$Specific\ capacity = \frac{zF}{3.6\ M_w} \tag{1.2}$$

where z is the number of Li^+ or electrons transferred per formula unit, F is the Faraday constant, M_w is the molar mass of the active material in g mol^{-1}, and the factor 3.6 converts coulombs to mAh. In practice, the achievable capacity is constrained by the material composition, accessible redox states within the stability voltage window of the electrolyte, and the need to avoid irreversible structural change of the electrode materials.

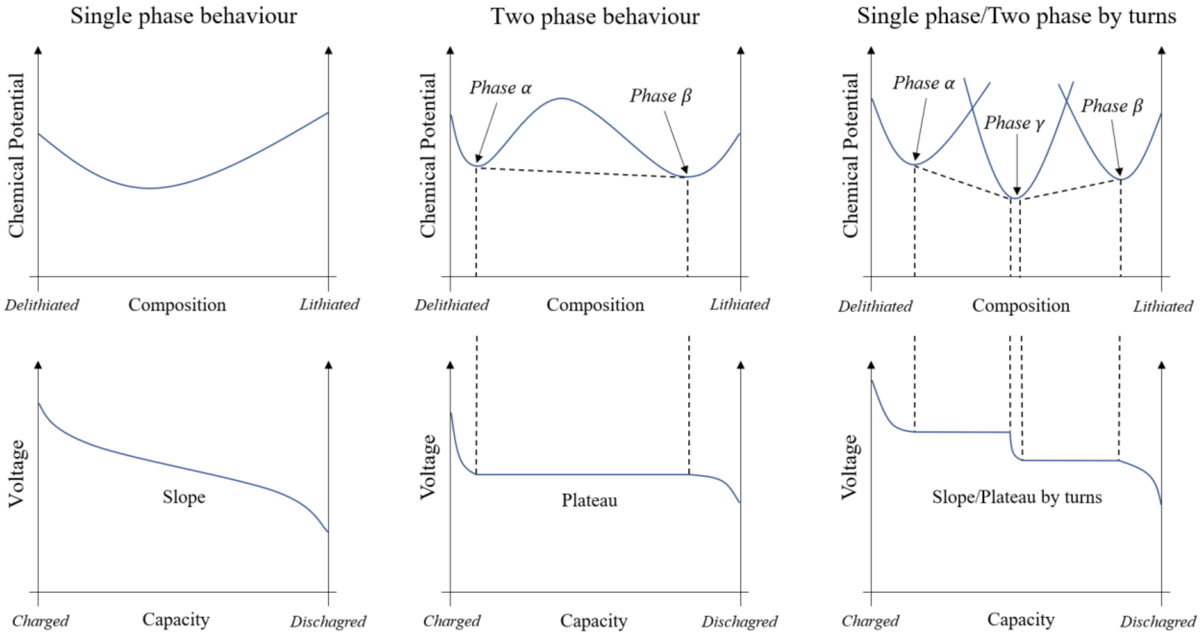

Figure 1.3: Schematic showing the dependence of voltage profile on chemical potential.

Plotting the voltage versus capacity yields the characteristic charge and discharge curves, as shown in Figure 1.2, where the area under each curve corresponds to the charge or discharge energy in Wh. In addition, the shape of these load curves is determined by how their chemical potential changes with composition during cycling, as shown in Figure 1.3. When Li^+ insertion/extraction proceeds as a homogeneous solid solution, the chemical potential varies continuously with composition, producing a sloping voltage load curve. By contrast, if two-phase coexistence is energetically favored over a single-phase solution, the electrode material undergoes a phase segregation into two compositionally distinct phases. In this case, the relative phase fractions evolve at nearly constant chemical potential, giving rise to a flat voltage plateau until the transformation is complete.[27]

1.2.3 The Cathode Development and Challenge

In commercial Li-ion batteries, the electrodes are balanced by capacity such that the potential curves of both electrodes can be fully utilized, as illustrated in Figure 1.2. In practice, anode materials commonly provide higher capacities (~ 300 – 500 mAh g^{-1}) than state-of-the-art commercial cathodes (typically 170–220 mAh g^{-1}).[6] This capacity gap requires a greater cathode mass to match the higher charge storage density of the anode side, thus penalizing overall cell-level energy density. Moreover, the potential of the graphitic anodes (~ 0.1 – 0.25 V vs. Li^+/Li) is already pretty close to 0 V vs. Li^+/Li, leaving little scope for further voltage reduction. Thus, cathode performance is the primary bottleneck to improving energy density, and a vast chemical design space remains to be explored for cathodes.

As mentioned previously, voltage and reversible capacity are the key determinants of the battery energy density, both of which are directly related to the chemical composition of the cathode.[25, 28] Consequently, since the advent of LIB technology, cathode development has focused on increasing operating voltage or accessible capacity.

Early transition metal sulfide

Looking back, TiS_2 was first reported as a Li-insertion cathode by Whittingham in 1975, utilizing the Ti^{3+}/Ti^{4+} redox,[29, 30] as shown in Figure 1.4 (a). Shortly thereafter, other TM chalcogenides, such as MoS_2, VSe_2, were also identified as reversible Li-intercalation hosts.[31]

Conventional layered oxide

The next breakthrough came in 1980, when Goodenough introduced the layered oxide $LiCoO_2$, based on the Co^{3+}/Co^{4+} redox.[3, 32] Since then, $LiCoO_2$ and its derivatives, such as $LiNi_{0.33}Mn_{0.33}Co_{0.33}O_2$ and $LiNi_{0.8}Co_{0.1}Mn_{0.1}O_2$, have dominated commercial cathodes.[33, 34] As illustrated in Figure 1.4 (a) and (b), although TiS_2 and $LiCoO_2$ share similar layered frameworks, their electronic structures lead to markedly distinct electrochemical performance. The Co^{3+}/Co^{4+} redox bands in oxides lie at a lower energy relative to the Ti^{3+}/Ti^{4+} states in sulfides, resulting in significantly higher operating voltages

(~ 2.2 V for TiS_2 and ~ 3.8 V for $LiCoO_2$) and energy densities (~ 450 Wh kg^{-1} for TiS_2 and ~550 Wh kg^{-1} for $LiCoO_2$). The electronic structure of a compound is determined by its composition, chemical bonding and crystal structure, collectively, which can be probed using Density Functional Theory (DFT) through analysis of the band states and Fermi level positions.[25]

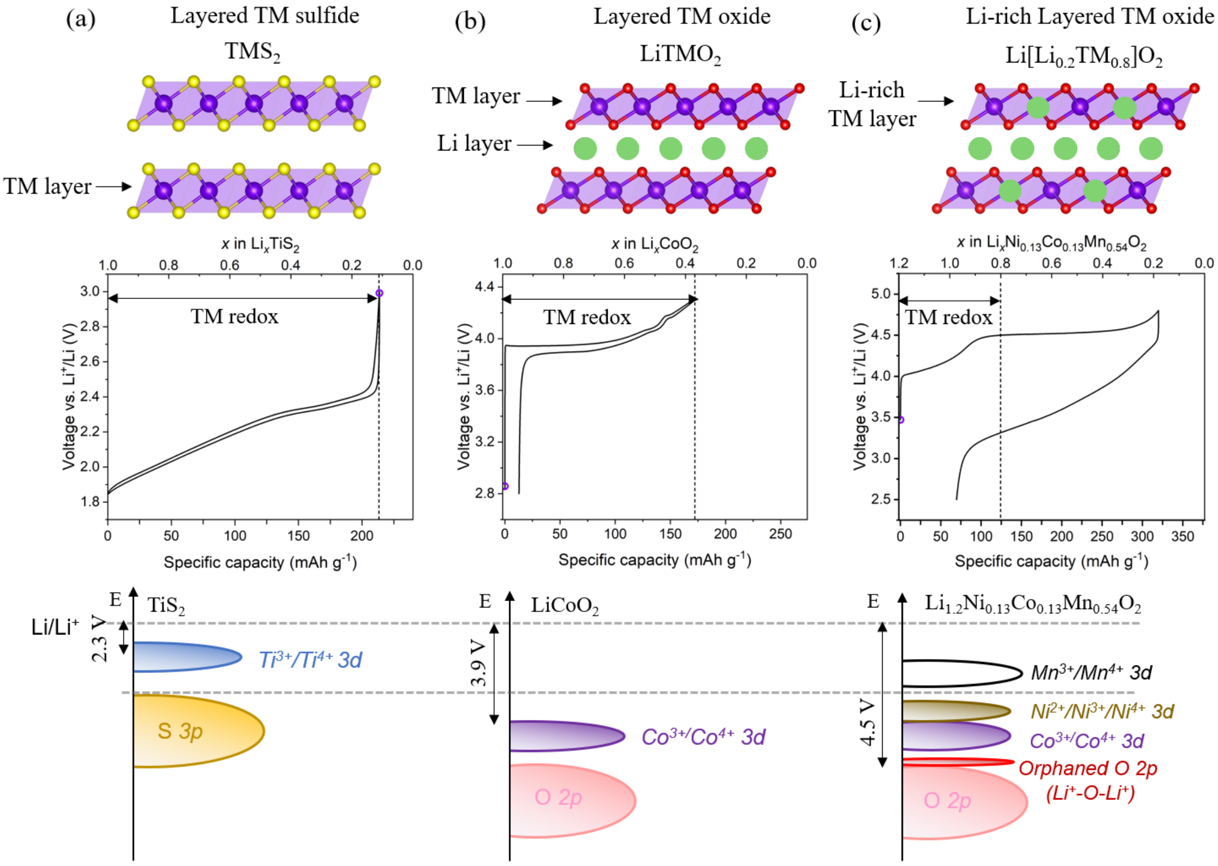

Figure 1.4: Schematic showing a conventional stoichiometric layered sulfide (a), layered oxide (b) and Li-rich layered oxide (c), together with their representative voltage versus capacity plots, as well as corresponding band structures. Purple circles in the first cycle load curves indicate the starting points. Relative band positions are estimated based on references.[25, 35]

Li-rich oxides

For many years, cathode materials have operated solely relying on the reduction and oxidation of the TM redox (cationic redox). To further improve the specific capacity, more Li^+ must be exchanged per unit mass, which in turn demands that the host structure must accommodate more electron transfer. Since 2002, Li-rich layered oxides such as $Li_{1.2}Ni_{0.13}Mn_{0.54}Co_{0.12}O_2$, $Li_{1.2}Ni_{0.2}Mn_{0.6}O_2$, have emerged, which can deliver a high capacity exceeding 270 mAh g^{-1}.[8, 36-38] These compounds are composed of a greater fraction of Li than TM, with Li occupying sites in both the Li and TM layers, as shown in Figure 1.4 (c).

In such materials, the capacity attributable to TM redox (e.g. $Ni^{2+/3+/4+}$ and $Co^{3+/4+}$) accounts only for the initial sloping region of the voltage profile, as shown in Figure 1.4 (c). The additional capacity arises from the redox of O^{2-} ions (anionic redox), namely O-redox, which manifests as a flat plateau near 4.5 V vs. Li^+/Li during the first charge. This mechanism has been regarded as a promising paradigm for developing higher-energy cathodes and remains the subject of intense scrutiny.[39-42]

From the perspective of electronic structure, O-redox arises from the orphaned O 2*p* orbitals associated with the Li^+ (Li^+ in Li layer)-O-Li^+ (Li^+ in TM layer) configurations in Li-rich oxides (Figure 1.4 (c)).[43, 44] These states do not hybridize with any TM 3*d* orbitals and do not align energetically with Li 2*s* states, lying higher in energy than the other hybridized O bonding states and comparable to the non-bonding TM states. Accessing these deeper non-bonding O 2*p* states requires deep delithiation at high voltage (> 4.5 vs. Li^+/Li), which increases the risk of structural instability. Commonly observed consequences include irreversible O_2 loss from the particle surface, out-of-plane migration of the TM ions and surface structure reconstruction, all of which are detrimental to cycling stability.[45-49] Moreover, operation at such high voltages exceeds the electrochemical stability window of traditional liquid electrolytes (typically < 4.5 V), triggering electrolyte decomposition and consequent degradation of performance.[50]

Beyond these issues, Li-rich oxides face two additional electrochemical drawbacks. First, compared to conventional cathodes, they exhibit a much larger gap between charge and discharge load curves, which wastes the stored energy and reduces the round-trip efficiency. This is generally what is referred to by the term voltage hysteresis.[51, 52] Second, they exhibit a gradually evolving discharge curve with a continuous drop in average discharge voltage over cycling, known as voltage decay, resulting in continual energy density loss.[51, 53]

Overall, Li-rich oxides with O-redox behavior have opened a new chemical space, anionic redox, for cathode design and remain a central focus of fundamental research. However, challenges such as large voltage hysteresis, fast voltage decay, irreversible O_2 evolution, and sluggish kinetics continue to hinder commercialisation, raising the question of whether they can offer real competitiveness with conventional layered oxides.[13, 50]

Following both the history and the latest developments in cathodes with O-redox chemistry, several key questions now arise. Are there any other more sustainable and practical forms of anionic redox? Which alternative redox chemistries or compounds can deliver energy density exceeding or comparable to that of conventional layered oxide cathodes? Beyond performance, factors such as cost, sustainability, and resource availability are equally critical. Current major systems, such as $LiCoO_2$, $LiNi_{0.8}Co_{0.1}Mn_{0.1}O_2$, and layered Li-rich oxides, still depend heavily on expensive and geopolitically constrained Ni and Co. Can high-energy-density cathodes be developed without using these elements? Identifying new cathode materials that simultaneously meet these stringent requirements is a formidable challenge, but the potential rewards are transformative. These questions continue to drive intense research across the battery field.

1.3 Sulfur-Redox

1.3.1 Li-rich Sulfides

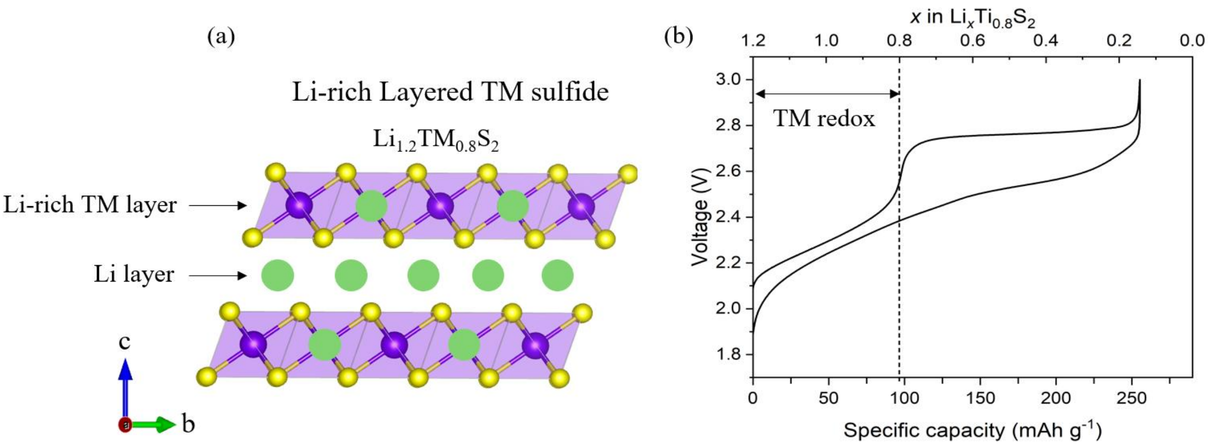

Figure 1.5: Schematic showing a stoichiometric Li-rich layered sulfide (a) and its representative voltage versus capacity plot (b). The plot (b) is obtained from Figure 3.5 in Chapter 3.

Li-rich sulfides that exhibit S-redox behavior have emerged as promising candidates to potentially meet the above requirements. Similar to Li-rich oxides, compositions of Li-rich sulfides contain excess Li relative to the TM. Within this space, the most studied materials are those based on the solid solution between Li_2TiS_3 and $LiTMS_2$ (where TM = Fe, Mn, Ti, also Co and Ni), also written as $x\mathrm{LiTMS_2}\cdot(1-x)$ $\mathrm{Li[Li_{1/3}Ti_{2/3}]S_2}$, where the brackets contain the elements in the TM layer.[16, 54] These layered Li-rich sulfides are direct analogues of layered Li-rich oxides but possess larger unit cells to accommodate the bulkier S anions. They exhibit an O3-type layered structure consisting of TM slabs containing edge-sharing TMS_6 and LiS_6 octahedra, with interslab octahedral sites exclusively occupied by Li ions, as shown in Figure 1.5 (a). Importantly, many undesired features of anionic redox seen in Li-rich oxides are largely suppressed in these sulfides.[16, 55, 56]

An archetypal example is layered $Li_{1.2}Ti_{0.8}S_2$.[57] On the first charge, the voltage profile exhibits an initial slope associated with Ti^{3+}/T^{4+} redox, followed by an extended S-redox voltage plateau at near 2.7 V vs. Li^+/Li, as shown in Figure 1.5 (b). The plateau is not reversed on discharge nor in the following cycles. Instead, discharge proceeds through a sloped S-shaped profile at a lower average voltage, resembling the analogous Li-rich oxides. However, in sharp contrast to the oxide analogues, Li-rich sulfides show negligible irreversible capacity loss in the first cycle and a markedly reduced voltage hysteresis (~ 90% less).

After the first cycle, hysteresis decreases further. Besides, voltage decay is mitigated over long cycling, and kinetics are comparatively fast relative to Li-rich oxides.[16] Although replacing the O ions with S ions lowers the redox potential, owing to the intrinsically higher-lying S 3*p* band compared with O 2*p* states, these Li-rich sulfides can still deliver energy densities of ~ 600 Wh kg^{-1}, comparable to commercialized $LiCoO_2$. This is enabled by their high capacity (> 250 mAh g^{-1}) arising from the S-redox process.

Beyond the above layered frameworks, some other Li-rich sulfides exhibiting S-redox can achieve even higher capacities (> 350 mAh g^{-1}) and energy densities (> 800 Wh kg^{-1}),[58-60] rivalling state-of-the-art Ni-rich oxides ($LiNi_xCo_yMn_{1-x-y}O_2$, typically with x > 0.8). Examples include Li_2FeS_2, which crystallizes into alternating layers of edge-sharing LiS_6 octahedra and mixed Fe/Li tetrahedra (50% Li and 50% Fe) (Figure 1.6 (a)),[61] and disordered rocksalt Li-rich sulfides, in which cations are randomly distributed over the S-sublattice octahedra (Figure 1.6 (b)).[62, 63] Despite their structural diversity, all of these Li-rich sulfide cathodes consistently alleviate the unwanted O-redox behavior, underscoring fundamental differences between O-redox and S-redox chemistry. To enable a direct comparison and contrast with the O-redox process in the same layered Li-rich framework, Li_2FeS_2 and disordered rocksalt Li-rich sulfides are not the focus of this thesis.

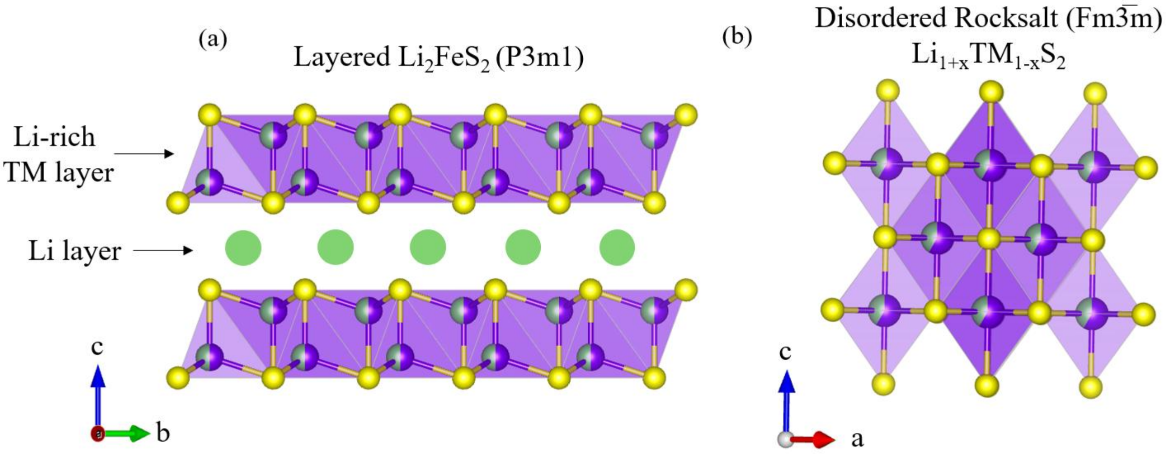

Figure 1.6: Schematic showing the structure of Li_2FeS_2 (a) and disordered rocksalt Li-rich sulfides (b).

1.3.2 A Brief History

Since 1996, ligand hole chemistry in TM sulfides such as FeS_2 ($Fe^{2+}S_2^{2-}$), TiS_3 ($Ti^{4+}S^{2-}S_2^{2-}$), and VS_4 ($V^{4+}(S_2^{2-})_2$) has been well-known, thanks to the pioneering work by Jean Rouxel and others.[64-66] In these materials, sulfur can exist in the form of S_2^{2-} dimers. During electrochemical cycling, the S_2^{2-} dimers are first cleaved to regain the standard S^{2-} state with the insertion of Li^+. However, early studies found that this S-redox activity is only partially reversible and accompanied by rapid capacity fading.[67-70] In 2009, Goodenough and co-workers revisited layered $LiTMS_2$ (TM = Ti, V, Cr, Fe, Ni) and demonstrated that several compounds of this family could undergo both reversible Li removal and insertion.[71, 72] However, it remains unclear whether the capacity involved the S-redox process.[73] Subsequent studies in 2011 and 2014 reported the detailed electrochemical behavior of layered Li_2FeS_2 and disordered rocksalt Li_3NbS_4, respectively, both exhibiting capacities higher than 350 mAh g^{-1}, well beyond what is expected from TM redox alone.[74, 75] Despite these promising results, interest at the time was dominated by layered oxides and the discovery of O-redox, leaving sulfides relatively overlooked.

A turning point came in 2018, when Biao *et al.* introduced Co^{2+} into the electrochemically inert layered $Li_{1.33}Ti_{0.67}S_2$, where Ti^{4+} adopts a d^0 electronic configuration.[76] The resulting compound,

$Li_{1.2}Co_{0.2}Ti_{0.6}S_2$, showed an O3-type layered framework analogous to Li-rich oxides and the reversible S-redox was first directly confirmed by S K-edge X-ray absorption near edge structure (XANES) and DFT calculations.

In 2019, Tarascon and co-workers further demonstrated the feasibility of activating S-redox behavior in O3-type Li-rich sulfides, $Li_{1.33-2y/3}Ti_{0.67-y/3}Fe_yS_2$ ($0<y<0.5$) via Fe^{2+} substitution.[16] The active S-redox was confirmed collectively by S K-edge XANES, S L-edge electron energy loss spectroscopy (EELS), S L-edge soft X-ray absorption spectroscopy (sXAS), and X-ray photoelectron spectroscopy (XPS). Importantly, side-by-side comparisons with Li-rich layered oxides revealed that the fundamental limitations of O-redox, including voltage fade, voltage hysteresis, and sluggish kinetics, can be substantially alleviated in the Li-rich sulfides, highlighting the practical promise of S-redox chemistry.

Since then, Li-rich sulfides have gradually gained attention to explore and harness anionic redox beyond oxygen. A variety of structures and compositions have been investigated, and the scope of S-redox chemistry has begun to extend to Na-ion battery cathodes as well.[77-79]

1.3.3 The Latest Understanding in Anionic Redox

Over the past decades, elucidating anionic redox processes and their relationship to structural evolution and electrochemical performance has proven challenging. A comprehensive understanding of both O-redox and S-redox is essential to harness anionic redox in next-generation high-energy batteries.

Nature of oxidized O

Since the initial discovery of the O-redox in Li-rich oxides, the nature of oxidized O species in the bulk of Li-rich oxides and the process of oxygen oxidation have been intensively studied and fiercely debated. Various models have been proposed, such as hole states on O_2^{-},[43, 44] peroxo-like O_2^{n-} species with long O-O bonds[37, 39] or peroxides O_2^{2-}.[80, 81] Despite these pioneering efforts, direct experimental evidence of oxygen dimer formation remained elusive for many years.

Recent advances, by Bruce and co-workers, have provided compelling evidence for the stabilization of oxidized oxygen in the form of molecular O_2.[82] Using high-resolution X-ray inelastic scattering

(RIXS), they examined a model layered Li-rich oxide, $Li_{1.2}Ni_{0.13}Mn_{0.54}Co_{0.12}O_2$.[83] As presented in Figure 1.7, RIXS spectra collected at different states of charge revealed the formation of O_2 during charging and its disappearance upon discharge. The low energy-loss features in the spectra specifically correspond to the vibrational progressions of molecular O_2, rather than O_2^-, O_2^{2-} or longer peroxo-like O-O bonds.[84]

Additional evidence supporting molecular O_2 formation in the bulk has been obtained through multiple techniques, including O^{17} nuclear magnetic resonance (NMR),[83] superconducting quantum interference device (SQUID) magnetometry,[85] neutron pair distribution function (PDF),[86] and DFT calculations.[87] Subsequent studies have identified similar molecular O_2 signatures across a broader range of O-redox systems, including layered Li-rich oxides containing 4*d*/5*d* TM (e.g. Ru, Ir),[84] Li-rich disordered rocksalt cathodes,[88-90] and even Na-ion cathodes with O-redox chemistry,[91-93] revealing the model unifies a diverse range of O-redox materials.

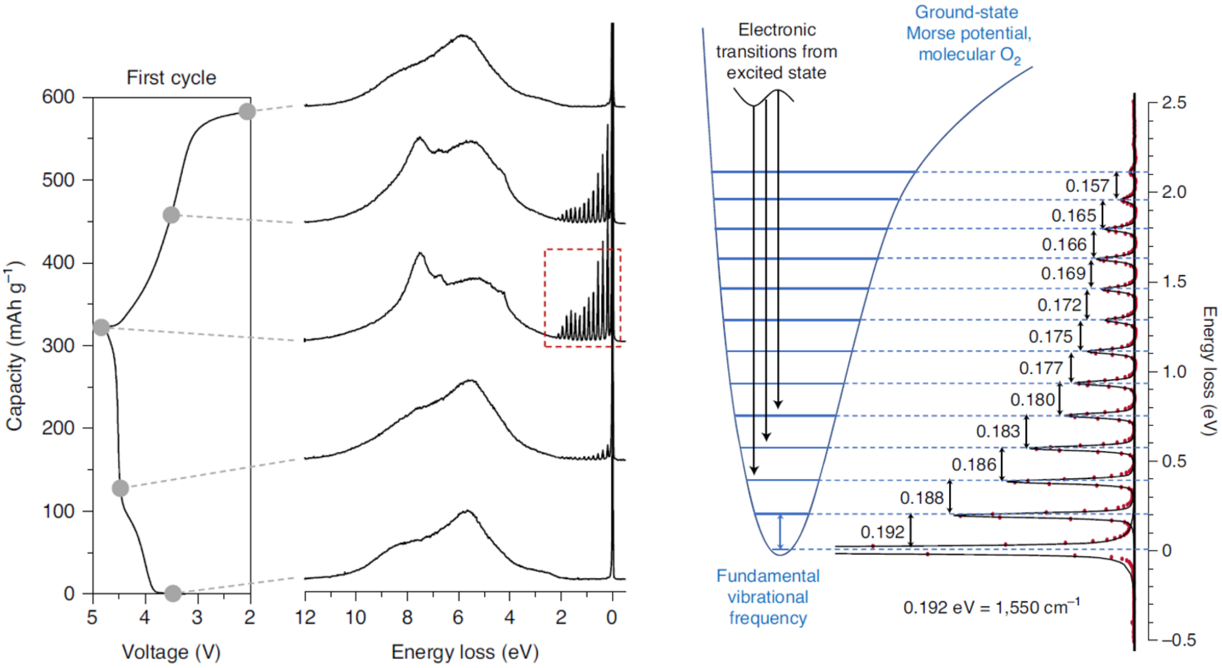

Figure 1.7: High-resolution RIXS data showing molecular O_2 formation in layered Li-rich oxides. The peak progression at the low energy loss corresponds to transitions between different vibrational energy levels of O_2 diatom.[94]

Voltage hysteresis and voltage fade in Li-rich oxides

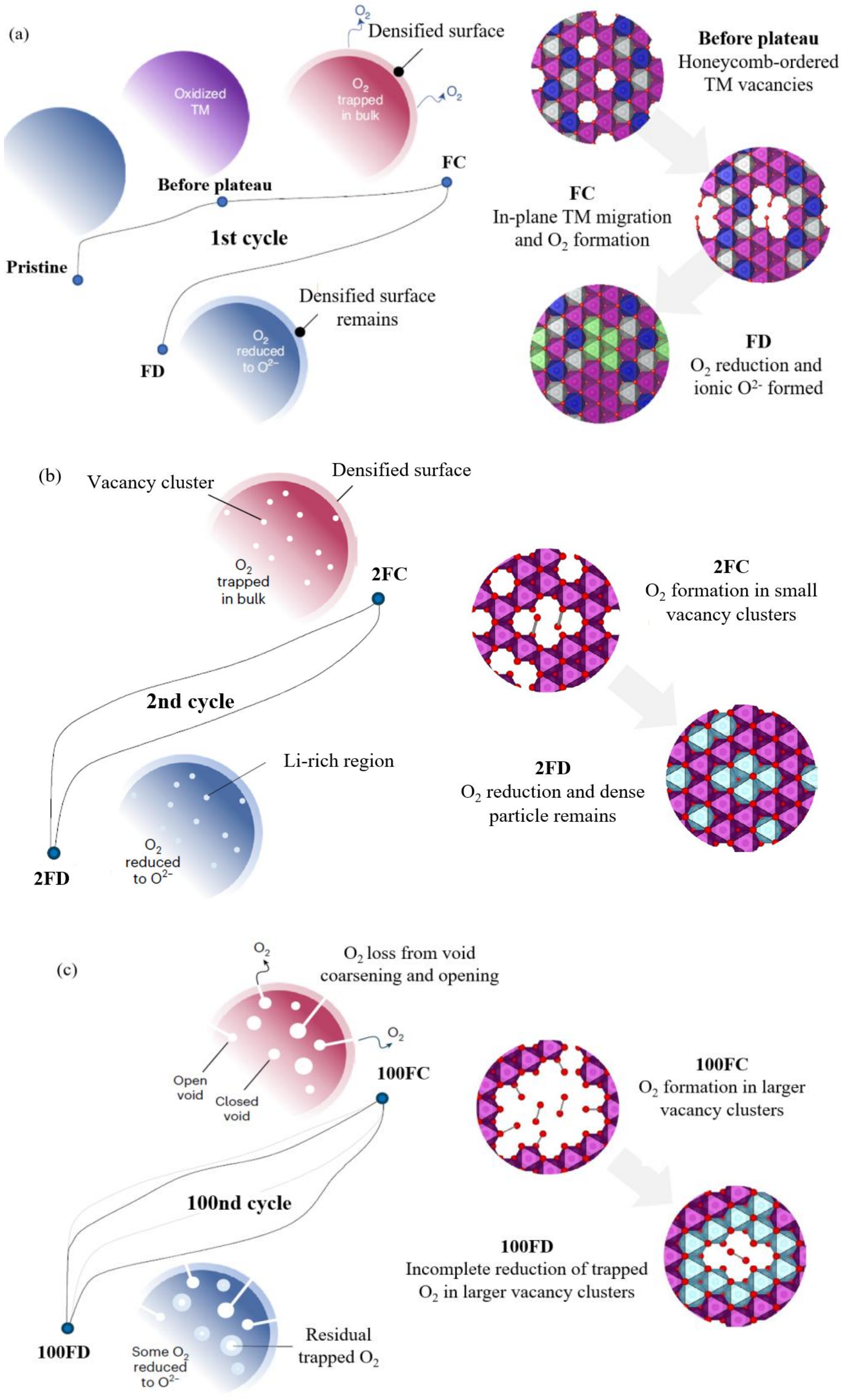

Figure 1.8: Schematic showing the mechanism of first-cycle voltage hysteresis and long-term voltage fade in layered Li-rich oxides.[83, 95] The representative load curves and atomic-scale changes in the transition metal layer are shown for the 1st cycle (a), 2nd cycle (b) and 100th cycle (c).

1.3 Sulfur-Redox

Early studies attributed voltage hysteresis and voltage fade primarily to structural changes, such as the out-of-plane migration of TM ions, surface structure reconstruction, and the formation of nanopores within particles.[35, 48, 96, 97] Voltage decay was also reported to be linked with the progressive changes in the active TM redox couple over cycling, for example the shift from high-voltage couples (Co^{3+}/Co^{4+} and Mn^{4+}) to lower-voltage redox (Co^{2+}/Co^{3+} and Mn^{3+}/Mn^{4+}). However, the specific role of the oxidized oxygen in these phenomena remains unclear.[35]

Recently, a more unified picture has emerged from the bulk molecular O_2 model proposed by Bruce and colleagues.[83] In layered Li-rich oxides (e.g., $Li_{1.2}Ni_{0.13}Mn_{0.54}Co_{0.12}O_2$), the TM layers generally display honeycomb ordering of the TM and Li^+ ions. During the first charge, extraction of Li^+ from the TM layer induces substantial disordering within the TM plane, as evidenced by X-ray diffraction (XRD), Li NMR, and scanning transmission electron microscopy (STEM). DFT calculations based on the experimental results further show that the formation of vacancy clusters is energetically favored at the highly delithiated state. Together with direct evidence of molecular O_2 formation, these observations suggest that in-plane TM migration creates small vacancy clusters, corresponding to a few vacant cation sites (approximately 1 nm in diameter), which accommodate O_2 molecules on the first charge, as shown in Figure 1.8 (a). During the first discharge, O_2 is reversibly reduced with Li^+ re-intercalation. By the end of discharge, the coordination environment around O^{2-} at the center of these vacancy clusters in the TM layer becomes more Li-coordinated. The greater degree of ionicity of the Li^+- O^{2-} interactions raises the energy of these O 2*p* states and thereby lowers the first discharge voltage, resulting in a large first-cycle voltage hysteresis.[83]

In the second cycle, molecular O_2 formation and cleavage occur at lower voltages with minimal further TM migration (Figure 1.8 (b)). This accounts for the markedly reduced hysteresis and the disappearance of the prominent charging plateau in the following cycles.

Notably, over extended cycling, the O-redox mechanism continues to evolve, although more gradually.[95] In $Li_{1.2}Ni_{0.13}Mn_{0.54}Co_{0.12}O_2$, high-resolution RIXS and O^{17} NMR reveal an increasing accumulation of O_2 at the end of discharge on cycling. STEM images reveal that voids within particles increase to 4 – 12 nm after 100 cycles. As these closed voids grow, the trapped O_2 becomes increasingly electrochemically inactive because electron transfer between the O_2 and the void walls becomes more difficult (Figure 1.8 (c)). Near-surface voids can promote particle cracking and open more voids at the surface, releasing O_2 gas. The progressive loss of active O-redox at the expense of a higher proportion of TM-redox at lower voltages on cycling. Overall, the loss of O-redox capacity arises from a combination of a reduction in the reversibility of O^{2-}/O_2 redox process and O_2 loss, offering an explanation for the voltage fade. This model brings together earlier observations of structural reorganization, void formation and opening, and TM reduction within a single mechanism. Taken together, these results point to the thermodynamic driving force to form O_2 as the root cause of the voltage hysteresis and voltage fade in Li-rich oxide cathodes.[94, 95]

Moving to Li-rich sulfides

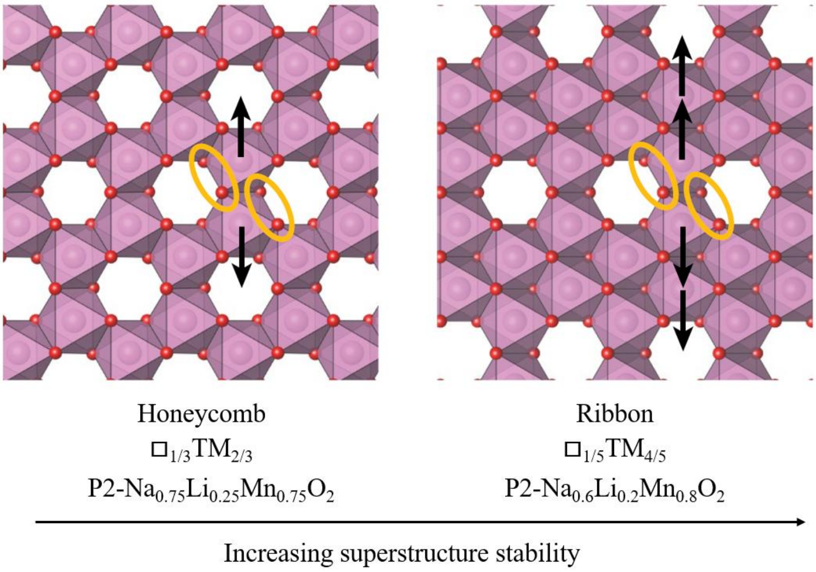

Figure 1.9: Schematic showing the dependence of O-redox stability on superstructure. More Mn ions migrations are required to form O_2 after moving from honeycomb to ribbon ordering.[82]

Based on the understanding above, suppressing voltage hysteresis and voltage fade in Li-rich oxides requires bulk-focused strategies that mitigate the formation of molecular O_2 and the appearance of voids in favor of stabilized hole states on O. This explains why widely used surface coating can effectively improve first-cycle coulombic efficiency and capacity retention in Li-rich oxide cathodes by avoiding irreversible O_2 evolution, yet have only a limited effect on voltage hysteresis and voltage fade.[13, 45, 46]

Bruce *et al.* have demonstrated that regulating the superstructure in the TM layer of layered Na oxides can significantly reduce hysteresis.[82] By moving from a honeycomb ordering in

$Na_{0.75}Li_{0.25}Mn_{0.75}O_2$ to a ribbon superstructure in $Na_{0.6}Li_{0.2}Mn_{0.8}O_2$ (Figure 1.9), the flat charge plateau is largely recovered.

This improvement arises because more dispersed Li ions disfavor vacancy clustering and hence O_2 formation, while promoting the stabilization of electron holes on O^{2-}, as revealed by O K-edge XAS. However, these superstructures are not fully stable during cycling. In $Na_{0.6}Li_{0.2}Mn_{0.8}O_2$, for instance, the discharge plateau is nearly depleted after only ten cycles.[82, 98]

Implementing similar ribbon-like superstructures in Li-rich oxides is intrinsically more challenging. Na layered oxides can tolerate Na deficiency in the Na layer, as in P2 and P3 phases.[99-101] In contrast, introducing ribbon ordering in layered Li-rich oxides requires increasing the Mn^{4+}/Li^{+} ratio in the TM layer, which necessitates Li deficiency to maintain charge neutrality. However, compositions with a smaller Li/TM ratio (< 1) are more thermodynamically compatible with a spinel structure than a layered framework,[28] which makes superstructure engineering far less feasible in lithium systems.

Despite extensive optimization efforts in Li-rich oxides, including surface modification, particle size control, multivalent cation doping, and structural pillaring, neither voltage hysteresis nor voltage fade has been effectively eliminated.[13, 14, 47, 50] By contrast, replacing oxygen with sulfur to form Li-rich sulfides that operate through S-redox can substantially reduce both hysteresis and voltage decay compared with O-redox cathodes, as mentioned earlier. Therefore, advancing the understanding of the S-redox process and the fundamental differences from O-redox is a compelling direction and a key motivation for the growing interest in Li-rich sulfide cathodes.

Designing rules for Li-rich sulfides

The layered Li-rich sulfides are the direct analogue of the layered Li-rich oxides. The family of layered Li-rich oxides ($x LiTMO_2 \cdot (1-x)Li[Li_{1/3}Mn_{2/3}]O_2$, TM are typically Ni, Co, Mn) is initially derived from the parent oxide $Li[Li_{1/3}Mn_{2/3}]O_2$ (commonly written as Li_2MnO_3).[8, 102] However, preparing an analogous thermodynamically stable Mn-based sulfide is not possible. This is because the S 3*p* band lies much closer to the Li/Li^{+} reference than the O 2*p* band, leaving the Mn^{3+}/Mn^{4+} redox band too low-lying.[16]

Among 3*d* TM ions, Ti^{4+} is well-suited to stabilize layered sulfides, since the Ti^{3+}/Ti^{4+} redox couple is located above the S 3*p* band (Figure 1.10). However, in a purely Ti-based Li_2TiS_3, the empty Ti^{3+}/Ti^{4+} band makes this compound electrochemically inactive. This situation is reminiscent of Li_2MnO_3, which also shows poor electrochemistry (without nanosizing) until partial substitution with Ni^{2+} is introduced to activate reversible O-redox (Figure 1.10).[8, 103]

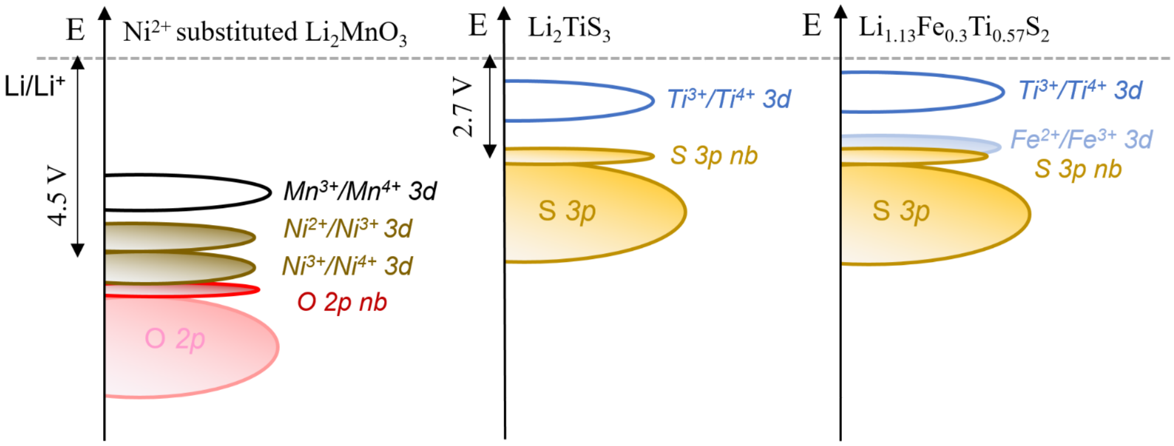

Figure 1.10: Schematic band structures of Ni^{2+} substituted Li_2MnO_3, Li_2TiS_3, and Fe^{2+} substituted Li_2TiS_3. The label *nb* denotes non-bonding states.[16]

Inspired by this analogy, redox-active cations with energy levels positioned just above the S 3*p* band, such as Fe^{2+}/Fe^{3+}, Co^{2+}/Co^{3+}, Mn^{2+}/Mn^{3+} and Ti^{3+}/Ti^{4+}, have been introduced into Li_2TiS_3 to unlock S-redox (Figure 1.10). This redox couple pinning strategy has led to the development of a series of novel Li-rich sulfides with S-redox, including $Li_{1.13}Fe_{0.3}Ti_{0.57}S_2$, $Li_{1.2}Co_{0.2}Ti_{0.6}S_2$, $Li_{1.13}Mn_{0.3}Ti_{0.57}S_2$ and $Li_{1.25}Ti_{0.75}S_2$.[16, 57, 76, 104] These redox couples offer available 3*d* electrons, enabling hybridization between TM 3*d* and S 3*p* states and thereby facilitating charge transfer from the anion band.

This strategy has also been extended to other electrochemically inactive Li-rich sulfides containing d^0/d^{10} TM ions. For example, Fe substitution successfully activates S-redox in Li_2SnS_3 with Sn^{4+} and Li_3NbS_4 with Nb^{5+}, yielding compositions such as $Li_{1.2}Fe_{0.2}Sn_{0.6}S_2$ and $Li_{1.2}Fe_{0.4}Nb_{0.4}S_2$.[77, 105]

Beyond cation substitution, anion substitution offers another design lever. Substituting S with Se can generally increase metal-anion covalency and raise the anion band edge, as Se is less electronegative and its Se 4*p* band lies higher in energy than S 3*p* states.[106] As a result, the Se-substituted sulfides show reduced polarization and improved kinetics, as demonstrated by $Li_{1.13}Fe_{0.3}Ti_{0.57}S_{1.67}Se_{0.33}$.[54] Remarkably, even in redox-inactive layered Li_2TiS_3, Se substitution alone can trigger S-redox, as revealed in $Li_2TiS_xSe_{3-x}$.[107, 108] These results suggest that not only band position but also band symmetry and dispersion affect the S-redox process.

These design rules offer a fertile playground for understanding the S-redox chemistry in Li-rich sulfides. Despite the rapid progress in discovering new compounds, little research has focused on understanding how different cation doping influences S-redox in detail. Why do some closely related compositions display different electrochemical profiles? Are the oxidized sulfur species formed during charging the same across all these materials? The results and understanding presented in Chapter 5 go some way to tackling these issues.

S-redox mechanism

S ions are intrinsically softer and more polarizable than O ions. This difference is widely considered to underlie the lower reactivity and greater stability of S-redox behavior compared with O-redox activity. Despite this, the fundamental mechanism of S-redox in Li-rich sulfides remains poorly understood.

One view holds that S oxidation proceeds with the formation of delocalized electron holes across the S sublattice through TM-S interactions. Support for this model primarily comes from DFT, which shows a progressive band gap closure in highly delithiated states.[16] However, this model fails to explain the disappearance of the first-charge plateau in subsequent cycles, especially given that most of the Li-rich sulfides exhibit highly reversible long-range structural evolution and charge compensation processes.

An alternative model proposes that S^{2-} oxidation is accompanied by a reductive process, enabled by the stronger covalency of S ions compared to O ions.[57] In O3-type $Li_{1.2}Ti_{0.8}S_2$, each Ti is coordinated by six S^{2-}. Upon Li^+ extraction, the local environment is proposed to evolve first from $Ti^{4+}(S^{2-})_6$ to $Ti^{4+}(S^{2-})_5S^-$, and then the reductive coupling occurs, leading to $Ti^{3+}(S^{2-})_4(S_2^{2-})$. S_2^{2-} formation is argued to arise from nearby vacancies left by Li removal, while regions far from vacancies retain Ti^{4+} coordinated only by S^{2-}. This mechanism has also been used to rationalize the disappearance of the charge plateau after the first cycle, attributed to unreduced S_2^{2-} and increased Ti^{3+} content after the first discharge. Yet TM over-reduction has not been experimentally observed in Li-rich sulfides after the initial cycle, and robust evidence for the reductive coupling mechanism is lacking.

More recently, another effort to develop the understanding of S-redox in Li-rich sulfides was published.[109] This work emphasizes that cation vacancies in the TM layer are the prerequisite for activating S-redox. By introducing cation vacancies into the electrochemically inert Li_2TiS_3 while maintaining the Ti^{4+}, S-redox can be triggered in $LiTi_{0.75}\square_{0.25}S_2$ ($\square$ refers to cation vacancies within the TM layer). The argument is that S_2^{2-} dimer formation requires large local distortions that are unfavorable in the absence of vacancies. They also proposed that this model can be extended to O-redox systems, where O-O dimers formed. However, this interpretation is inconsistent with compounds such as Na_2TiS_3 or $NaLi_{1/3}Mn_{2/3}O_2$, which exhibit anionic redox activity without pre-existing vacancies.[110, 111]

Overall, while these proposed mechanisms might account for some structure evolution during the S-redox process, they do not explain why residual first-cycle hysteresis persists in these Li-rich sulfides, albeit diminished compared to O-redox cathodes. And why does the second charge profile deviate so substantially from the first? Clearly, the evolved load curves suggest there is some irreversible process occurring during the first charge, which is not captured by the above models. The results and discussion in Chapter 3 of this thesis will present a new theory to explain how the S-redox process governs the evolution of cycling profiles.

1.3.4 Debate on the Nature of Oxidized Sulfur

The identity of the oxidized anion in charged Li-rich cathodes remains a highly contentious and fiercely debated issue. While it is increasingly accepted that O_2 molecule is the oxidized O species in Li-rich oxides, the nature of oxidized S in Li-rich sulfides is far less certain. From an application perspective, clarifying this question is important for understanding the distinct electrochemical behaviors of O-redox and S-redox cathodes and for unlocking their potential to deliver high-energy cathodes. From a fundamental standpoint, it is also of broad interest to the solid-state chemistry community.

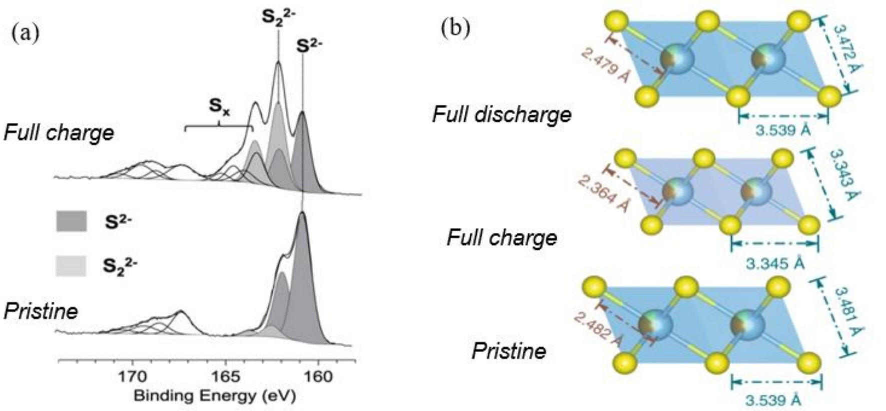

XPS
$Li_{1.25}Ti_{0.75}S_2$

Rietveld refinement of SXRD
$Li_{1.13}Fe_{0.3}Ti_{0.57}S_2$

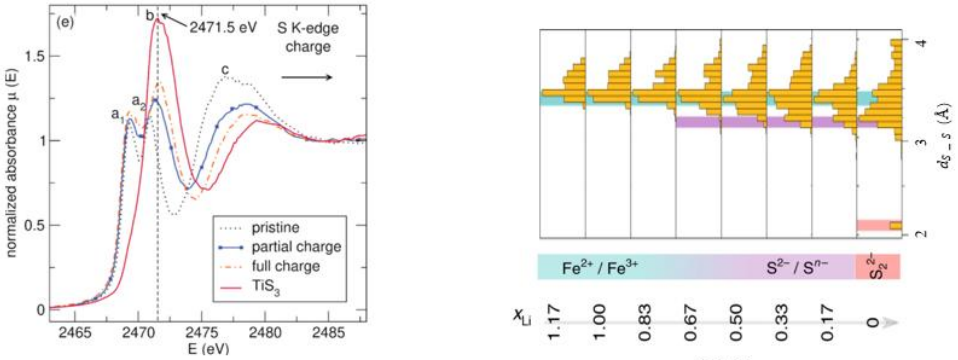

S K-edge XANES
$Li_{1.13}Mn_{0.3}Ti_{0.57}S_2$

DFT
$Li_{1.17}Fe_{0.25}Ti_{0.58}S_2$

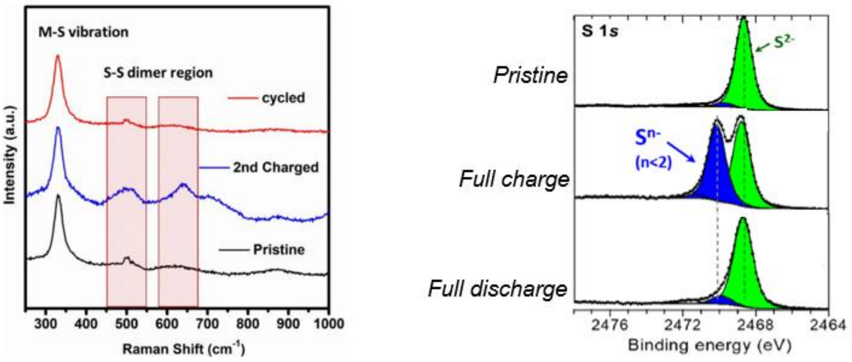

Raman
$Li_{1.2}Fe_{0.2}Sn_{0.6}S_2$

HAXPES
$Li_{1.33}Ti_{0.67}S_{1.6}Se_{0.4}$

Figure 1.11: (a) Key evidence for the formation of persulfide dimers (S_2^{2-}): XPS shows a new peak assigned to S_2^{2-} species, from Reference 57; S K-edge pre-edge for fully charged sample shows similar features as TiS_3 from Reference 104; Raman spectroscopy shows new peaks appearing after charge in the supposedly S-S dimer region range from Reference 105. (b) Key evidence for the formation of localized holes on S ions (S^{n-}, $n < 2$): Rietveld refinement of PXRD shows no short S-S bond length presented in the long-range bulk structure, figure adapted form Reference 16; DFT results show no S_2^{2-} formed until full Li^+ extraction, from Reference 16; HAXPES shows S^{n-} ($n < 2$) formation during charging, from Reference 107.

Given that persulfides S_2^{2-} occur abundantly in natural minerals such as pyrite and marcasite,[67] one might easily assume that oxidized sulfur in battery cathodes would also take the form of persulfides. However, intercalation chemistry often produces metastable species or defect states, making alternative oxidation pathways possible.[112] Conflicting interpretations, therefore, persist regarding how oxidized S are stabilized. The key data on both sides is summarized in Figure 1.11.

On one side of the argument, formation of S_2^{2-} dimers is proposed with short bond lengths at ~ 2 Å. Proponents of this theory point to three main pieces of experimental evidence:

1. A new XPS peak emerges upon charging near 162 eV, slightly higher in energy than the S^{2-} peak at 161 eV, consistent with the presence of a partially oxidized S species.[57]
2. S K-edge XANES of the charged sample exhibits a pre-edge feature similar to that observed in TiS_3, a reference compound known to contain well-oriented S_2^{2-}.[104]
3. *Ex situ* Raman spectroscopy of charged $Li_{1.2}Fe_{0.2}Sn_{0.6}S_2$ show new features appear at ~ 500 cm^{-1} and ~ 650 cm^{-1}, which are assigned to characteristic vibration signals contributed by S_2^{2-} dimers.[105]

Opponents of this theory, however, argue that sulfur oxidation leads to the formation of delocalized hole states (S^{n-}, $n < 2$) and that there is insufficient direct evidence for S–S bonding. In particular, they cite the following evidence:

1. No short bond lengths around 2 Å, indicative of S_2^{2-} dimer formation, have been observed in Rietveld refinements of the synchrotron XRD data.[16]
2. Computational studies capture a progressive closing of the band gap and suggest that complete Li^+ extraction could trigger a structural reorganization involving S_2^{2-} dimer formation. However, full delithiation is not achieved experimentally after charging.[16]
3. Hard X-ray Photoelectron Spectroscopy (HAXPES), which probes deeper into the bulk (~ 50 nm), captures an additional S 1*s* component at approximately 2470 eV, which is assigned to S^{n-} ($n < 2$) species.[107]

The evidence outlined above may be seemingly unequivocal on either side of the debate, but there are nonetheless a number of prominent discrepancies that remain to be addressed. Firstly, similar spectral features associated with oxidized S are often assigned differently in XPS and HAXPES, indicating that these surface-biased probes may not be sufficiently sensitive to capture S-S bonding. Furthermore, in some Li-rich sulfides with a disordered rocksalt framework, a short S-S distance at around 2 Å has been revealed by X-ray PDF analysis.[63] Yet detection of a short interatomic distance alone does not necessarily prove the presence of a true chemical bond. Finally, most layered Li-rich sulfides retain well-ordered layered structures with relatively long S-S distances (> 3.3 Å) after charging. If S_2^{2-} dimers (~ 2 Å) are indeed formed, but how can this occur without causing significant disruption to the long-range structure?

A more detailed examination of oxidized sulfur speciation is therefore necessary. The results in Chapter 3 of this thesis provide a set of new evidence for the identity of the oxidized sulfur species and propose a new theory for how these species are accommodated within layered Li-rich sulfides.

1.4 From Liquid to All-solid-state Batteries

1.4.1 Why All-solid-state Batteries

Beyond exploiting anionic redox in cathode materials, moving from conventional liquid-electrolyte cells to ASSBs represents one of the most promising routes to achieve higher energy density batteries. It is primarily due to the potential usage of Li metal or silicon anodes, as well as the possibility of bipolar stacking.[7, 113]

Replacing the liquid electrolyte and a porous separator with a dense SE layer offers a potential pathway to suppress Li dendrite growth due to the higher stiffness of many SEs. Compared to commercialized graphite, the Li metal anode has a lower redox potential, a lower mass, and a higher theoretical capacity (~ 3860 mAh g^{-1}), thereby improving both gravimetric and volumetric energy density.[114] For example, cell-level calculations that include all internal components indicate that a Li-ion battery using the liquid electrolyte based on $LiNi_{0.8}Co_{0.15}Al_{0.05}O_2$ cathode versus graphite achieves an energy density of 265 Wh kg^{-1} and 635 Wh L^{-1}. By contrast, an ASSB using the same cathode paired with a Li metal anode could, in principle, reach 393 Wh kg^{-1} and 635 Wh L^{-1}, respectively.[115]

Higher device safety is another critical advantage of ASSBs. Liquid electrolytes have inferior thermal stability, as many of them contain organic solvents with a low-boiling point (< 120 °C), and the Li salt, for example, $LiPF_6$, decomposes at a temperature below 100 °C.[116] Over the last decade, despite significant advances in commercialized LIBs and battery management systems, incidents involving flammable liquid electrolytes have continued to be reported.[117] In stark contrast, inorganic SEs are non-volatile and far more thermally stable (generally greater than 300 °C), which is particularly important for electric vehicles and large-scale grid storage.[118] In addition, SEs can inherently mitigate the dissolution of active TM ions in cathodes and their subsequent deposition on the anode, a phenomenon known as cross-talk in batteries, which is a degradation pathway that otherwise severely compromises cyclability.[119, 120]

Given these benefits, ASSB technology has attracted intense interest in both academia and industry. Substantial progress has been reported by companies such as Samsung, Solid Power, Toyota, and QuantumScape.[7]

1.4.2 Composite Cathodes

ASSBs operate on the same fundamental principles as conventional lithium-ion batteries but replace the liquid electrolyte with SEs. Similar to liquid cells, the cathode in ASSBs contributes a significant proportion to the overall battery cost and commonly delivers a lower specific capacity than the anode, thus attracting extensive research interest. Unlike the liquid cells, where liquid electrolytes readily wet the porous cathode and supply ionic transport (Figure 1.12), in ASSBs, the SEs cannot conformally wet cathode active materials (CAMs), so all ionic and electronic transport must occur across rigid particle-particle contacts.[121] Consequently, the cathode in ASSBs is typically referred to as a composite cathode, consisting of a mixture of CAM, SE particles that provide Li^+ conduction, and a carbon conductive additive that ensures electronic percolation within the composite cathode. The applied SE in the composite cathode is typically identical to the material of the SE layer.

The inclusion of various phases introduces interfaces that critically influence electrochemical performance. As a result, ASSB cathodes require design considerations beyond a direct translation from liquid cells, such as chemical and electrochemical compatibility at CAM/SE interfaces, and appropriate particle-size ratios between CAM and SE to achieve simultaneous ionic and electronic percolation with low tortuosity.[119, 122] These aspects are discussed further in Section 1.4.3.

An ideal composite cathode adopts a brick-and-mortar architecture, with CAM particles as the bricks and the SE, together with conductive carbon, as the mortar. Such a microstructure enables continuous pathways for both ionic and electronic transport. To maximize energy density, a high CAM fraction is always desirable, provided that ionic and electronic networks remain sufficiently connected. Within the composite cathode, a broad range of materials can be employed for each composition.

1. CAM: conventional layered oxide cathodes (e.g., $LiCoO_2$, Ni-rich oxides),[123, 124] Li-rich oxides (e.g., $Li_{1.2}Mn_{0.54}Co_{0.13}Ni_{0.13}O_2$),[125, 126] elemental S (Li-S batteries),[127] TM sulfides (e.g., CuS, FeS_2)[128-130] and others.
2. SEs: oxides (e.g., $Li_7La_3Zr_2O_{12}$),[131] sulfides (e.g., $Li_{10}GeP_2S_{12}$, Li_6PS_5Cl, β-Li_3PS_4),[132-134] halides (e.g., Li_3YCl_6, Li_3InCl_6),[135, 136] polymers such as polyethylene oxide (PEO)[137]and others.
3. Electronic conductors: carbon black, Super P, carbon nanotubes, carbon nanofibers (CNFs) and others.[138, 139]

The choice and balance of these components greatly affect the microstructure, electrochemical stability window, mechanical integrity, interfacial compatibility of the composite cathode, and thus the overall performance of ASSBs.

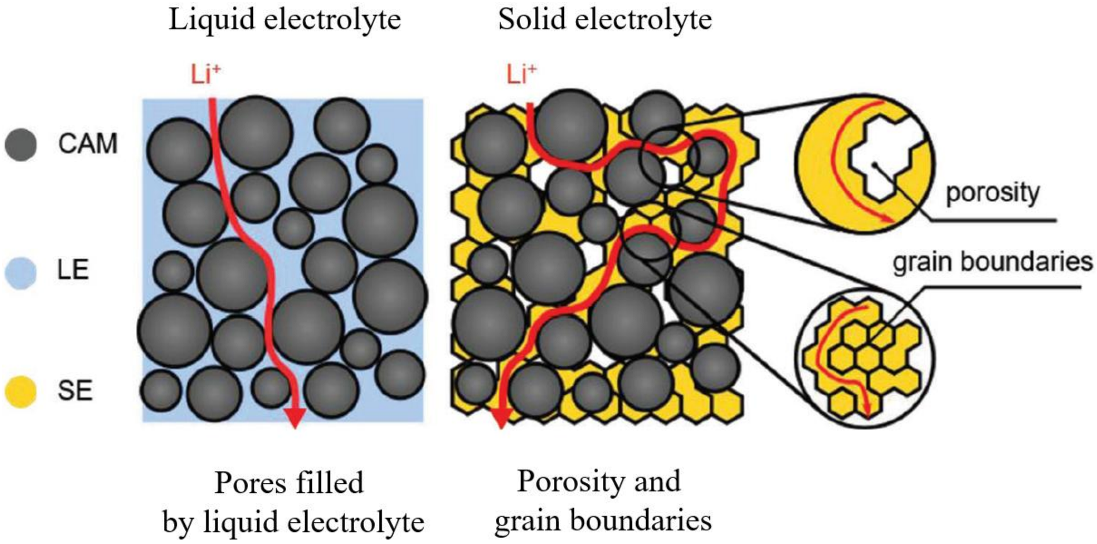

Figure 1.12: Schematic showing the cathode particles in liquid-electrolyte and solid-electrolyte batteries. In ASSBs, charge transport is more tortuous due to residual porosity and grain boundary resistances.[119]

1.4.3 Oxide Cathodes in All-solid-state Batteries

Among all the different CAMs, layered oxides are the most extensively studied in ASSBs. In particular, $LiCoO_2$ and Ni-rich layered oxides have attracted considerable attention owing to their high energy density and commercial success in conventional liquid cells.[32, 140] In ASSBs, these oxides are most often paired with the sulfide SE, Li_6PS_5Cl, because of their high ionic conductivity at room temperature (1–25 mS cm^{-1}), lower cost compared to halide electrolytes, and high mechanical ductility.[141]

When appropriately optimized, oxide cathode | Li_6PS_5Cl systems can deliver capacities comparable to those achieved in liquid cells, demonstrating their promise for high-energy-density ASSBs. However, these systems commonly suffer from rapid capacity fading.[142] More recently, layered Li-rich oxides have also been employed in ASSBs to pursue higher energy density.[126] Yet, the issues with voltage hysteresis and voltage fade discussed in Section 1.3.3 are intrinsic to the bulk structural evolution of Li-rich oxides and are still present in ASSBs. Moreover, Li-rich oxides typically evolve O_2 gas and require higher charging voltages,[11] which exacerbate interfacial reactivity with SEs and compromise safety.

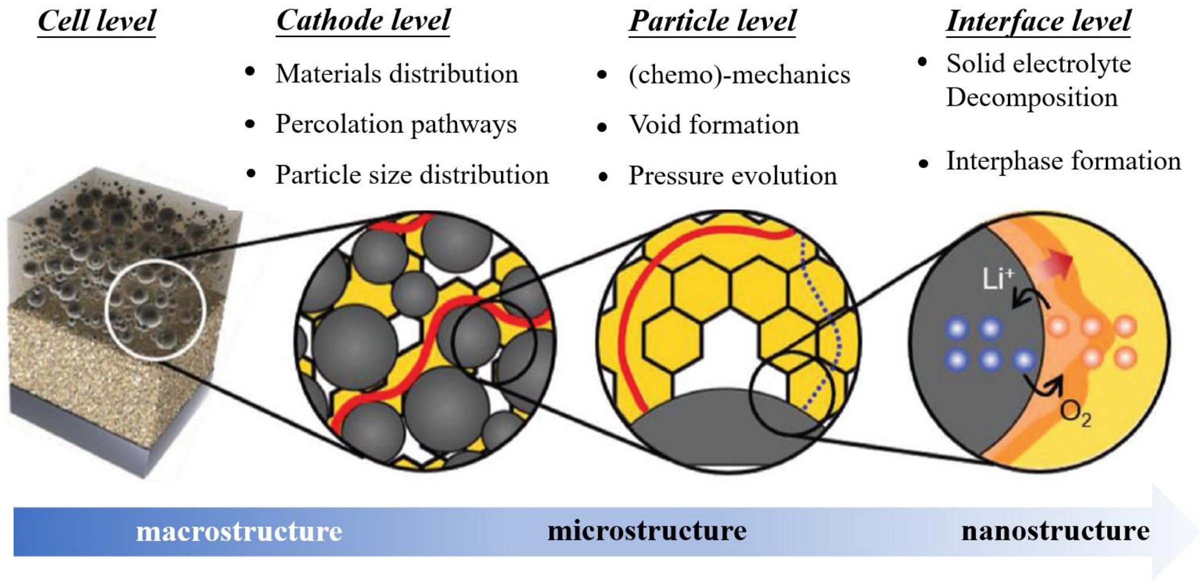

Figure 1.13: Schematic overview of challenges across different length scales in conventional layered oxide cathodes for ASSBs.[119]

Despite progress over the past decade, oxide CAMs in ASSBs continue to face persistent challenges across multiple length scales, ranging from the electrode microstructure to the cathode particle level and nanoscale CAM/SE interfaces (Figure 1.13), as summarized in below:

1. Composite microstructure (electrode-scale): To achieve continuous ionic and electronic percolation in composite cathodes, oxide cathodes typically require a sufficient fraction of Li_6PS_5Cl (generally > 20 wt%) and conductive carbon (generally > 3 wt%), but excessive inactive contents dilute energy density and increase charge transport tortuosity.[142-144] These requirements stem from the intrinsically low ionic conductivity ($< 10^{-8}$ S cm^{-1}) and electronic conductivity ($< 10^{-4}$ S cm^{-1}) of most layered oxides.[34, 145-147] Moreover, porosity in the composite cathode further degrades performance since pores are neither electronically nor ionically conductive.[148] Achieving sufficient densification is particularly difficult because oxide CAMs are mechanically harder than the soft Li_6PS_5Cl, often leaving contact gaps and voids that disrupt Li^+ transport.[142]
2. Mechanical degradation (particle-scale): Ni-rich oxides typically undergo ~ 6–8% volume change when charged to 4.3 V vs. Li^+/Li,[149] while the long-range structure of electrochemically inert Li_6PS_5Cl remains unchanged. This mismatch promotes loss of contact between the CAM and SE particles, leading to disrupted Li^+ conduction.[142, 150, 151] In polycrystalline Ni-rich oxides, anisotropic lattice changes can further drive cracking and disintegration of secondary particles, leaving isolated primary particles electrochemically inactive.[152] Additionally, with the volume change of the CAM, the external stack pressure applied on the ASSBs during operation may fluctuate, further accelerating particle delamination.[142]
3. Interfacial reaction (nano-scale): The electrochemical stability window of sulfide electrolytes such as Li_6PS_5Cl typically lies between ~ 1.7 V and 2.1 V vs. Li^+/Li, far below the operating voltage of oxide cathodes (> 4 V vs. Li^+/Li).[153] This large potential mismatch leads to parasitic reactions at the oxide CAM/sulfide SE interface, causing reconstruction of the layered oxide surface into a rock-salt structure and concomitant decomposition of the Li_6PS_5Cl electrolyte into resistive products such as phosphates, sulfites, sulfates and polysulfides.[154-156] These processes

result in the formation of poorly conductive interfaces that increase the impedance and accelerate capacity fade.[157] Additionally, oxide/Li_6PS_5Cl interfacial degradation can occur even at open circuit voltage, as evidenced by the increased interfacial impedance after cell resting.[158] Protective coatings can partially mitigate these side reactions. but they increase cost and processing complexity and also introduce additional interfaces (CAM/coating and coating/SE), which may have detrimental effects on the charge transport in the composite cathode before careful optimization.[119, 159, 160]

Given these limitations, an ideal CAM for sulfide-based ASSBs should combine the following features:

1. High Li^+ diffusivity and electronic conductivity throughout cycling, reducing the need for a large amount of SE and carbon in the composite cathode.
2. An operating voltage compatible with the electrochemical stability window of sulfides, while still delivering high specific capacity to ensure competitive energy density.
3. Minimal volume change upon cycling to suppress particle crack, contact loss and delamination.
4. Mechanical compliance sufficient to maintain intimate particle contact and accommodate strain.

Meeting all these requirements simultaneously is highly challenging, motivating exploration of redox chemistries and alternative cathodes beyond conventional layered oxides for ASSBs.

1.4.4 Li-rich Sulfides in All-solid-state Batteries

The recently emerging Li-rich sulfides with S-redox chemistry could be promising candidates to meet the requirements outlined above. As sulfide-based materials, they possess several inherent advantages: a lower electrochemical window (< 3 V vs Li^+/Li), mechanical softness that facilitates intimate contact with SEs, and typically higher electronic conductivity compared with oxides.[161, 162] In contrast to traditional TM sulfides (e.g. TiS_2, FeS_2) solely relying on TM redox,[29, 163] the S-redox in Li-rich sulfides significantly enhances both capacity and average voltage, yielding energy densities above 600 Wh kg^{-1}, comparable to $LiCoO_2$. Compared with other S-redox systems, such as Li-S batteries, the intercalation chemistry in Li-rich sulfides confines S-redox within a crystalline host lattice, largely avoiding the involvement of insulating polysulfide intermediates and the extra solid-solid interphase boundaries that hinder electrochemical performance.[112, 164] Nonetheless, studies on the application of layered Li-rich sulfides in ASSBs remain scarce.

A first demonstration was reported in 2020 by Tarascon *et al.*, who paired $Li_{1.13}Fe_{0.3}Ti_{0.57}S_2$ with the sulfide SE, β-Li_3PS_4. The $Li_{1.13}Fe_{0.3}Ti_{0.57}S_2$/$\beta$-$Li_3PS_4$ interface exhibited excellent stability, with low interfacial resistance ($< 70\ \Omega\ cm^{-2}$) maintained throughout cycling.[162] Superior chemical compatibility was further confirmed by the negligible evolution in electronic conductivity and nearly unchanged XRD patterns observed after sintering the composite cathode pellet at 200 °C for five days. When cycled against Li metal, this system delivered a reversible capacity of ~ 215 mAh g^{-1} at room temperature without the need for coatings or conductive additives. In 2025, Martinez et al. investigated the interface between $Li_{1.2}Ti_{0.8}S_2$ and sulfide SE, $Li_{5.7}PS_{4.7}Cl_{1.3}$, using both *in situ* and *ex situ* XPS, confirming that no degradation of electrolyte was detected over 20 cycles.[165] The cells also exhibited negligible capacity fade after 20 cycles, indicating the promise of this system. However, in both studies, the achievable capacity was much lower than that obtained in liquid cells. The long-term cycling stability was not examined and many key variables such as CAM particle size, electrode composition and component ratios were not optimized.

Notably, disordered rocksalt Li-rich sulfides have also been explored in ASSBs.[17, 161] For example, Li_2TiS_3 and Li_3NbS_4 both demonstrate excellent cycling stability (negligible capacity fade after 50 cycles), with reversible capacities of ~ 270 and 370 mAh g^{-1}, respectively, at 0.5 mA cm^{-2} at 50 °C, further highlighting the potential of Li-rich sulfides as ASSB cathodes.[75]

Despite this progress, these studies remain focused on reporting electrochemical performance rather than understanding the underlying electro-chemo-mechanical relationships that govern the behavior of Li-rich sulfides in ASSBs. Furthermore, cell performance is strongly influenced by factors such as external stack pressure, operating temperature, composite cathode design (like loading and component ratio), and material selection (type of carbon, SE, and counter anode). A more systematic investigation and optimization across these parameters is crucial to fully assess the practical potential of Li-rich sulfides in ASSB systems. The results and understanding presented in Chapter 4 aim to address some of these outstanding challenges.

1.5 Thesis Objectives

While battery research is generally driven by strong performance targets—incremental gains in cycle life, energy density and cost, the work in this thesis rather focuses on the fundamental processes of S-redox and its deployment across different cell architectures. As such, most materials studied here are model systems chosen to understand key aspects of S-redox rather than immediate drop-in replacements for state-of-the-art battery cathodes.

It is now well established that lattice sulfur in Li-rich TM sulfides can undergo reversible oxidation and reduction, and that S-redox cathodes show markedly reduced voltage hysteresis, voltage fade, and first-cycle irreversibility compared with their Li-rich oxide analogues. Nevertheless, several important questions remain, which this thesis seeks to address:

1. What is the chemical nature of the oxidized S species in layered Li-rich sulfide cathodes?
2. Why is most of the undesired anionic redox behavior observed in O-redox cathodes significantly suppressed in S-redox cathodes within the same layered Li-rich structure framework?
3. What causes the residual first-cycle voltage hysteresis observed in layered Li-rich sulfides?
4. How does TM–S covalency affect the S-redox process and the speciation of the oxidized sulfur in Li-rich sulfides?
5. Are Li-rich sulfides with S-redox viable cathode candidates for ASSBs?

The answers to these questions will have important implications for the design of high-energy-density cathodes and inform the discovery of new materials that more effectively harness S-redox.

1.6 References

1. Tarascon, J. M.; Armand, M., Issues and challenges facing rechargeable lithium batteries. *Nature* **2001,** *414* (6861), 359-367.

2. Larcher, D.; Tarascon, J. M., Towards greener and more sustainable batteries for electrical energy storage. *Nat. Chem.* **2015,** *7* (1), 19-29.

3. Mizushima, K.; Jones, P. C.; Wiseman, P. J.; Goodenough, J. B., Li_xCoO_2 (0<x<1): A new cathode material for batteries of high energy density. *Mater. Res. Bull.* **1980,** *15* (6), 783-789.

4. Dahn, J. R. *et al.* Mechanisms for Lithium Insertion in Carbonaceous Materials. *Science* **1995,** *270* (5236), 590-593.

5. Thackeray, M. M. *et al.* Electrical energy storage for transportation—approaching the limits of, and going beyond, lithium-ion batteries. *Energy Environ. Sci.* **2012,** *5* (7), 7854-7863.

6. Blomgren, G. E., The Development and Future of Lithium Ion Batteries. *J. Electrochem. Soc.* **2017,** *164* (1), A5019.

7. Janek, J.; Zeier, W. G., Challenges in speeding up solid-state battery development. *Nat. Energy* **2023,** *8* (3), 230-240.

8. Lu, Z.; Beaulieu, L. Y.; Donaberger, R. A.; Thomas, C. L.; Dahn, J. R., Synthesis, Structure, and Electrochemical Behavior of $Li[Ni_xLi_{1/3-2x/3}Mn_{2/3-x/3}]O_2$. *J. Electrochem. Soc.* **2002,** *149* (6), A778.

9. Thackeray, M. M. *et al.* Li_2MnO_3-stabilized $LiMO_2$ (M = Mn, Ni, Co) electrodes for lithium-ion batteries. *J. Mater. Chem.* **2007,** *17* (30), 3112-3125.

10. Thackeray, M. M. *et al.* Advances in manganese-oxide ‘composite’ electrodes for lithium-ion batteries. *J. Mater. Chem.* **2005,** *15* (23), 2257-2267.

11. Nayak, P. K. *et al.* Review on challenges and recent advances in the electrochemical performance of high capacity Li- and Mn-rich cathode materials for Li-ion batteries. *Adv. Energy Mater.* **2018,** *8* (8), 1702397.

12. Assat, G.; Tarascon, J.-M., Fundamental understanding and practical challenges of anionic redox activity in Li-ion batteries. *Nat. Energy* **2018,** *3* (5), 373-386.

13. Zuo, W. *et al.* Li-rich cathodes for rechargeable Li-based batteries: reaction mechanisms and advanced characterization techniques. *Energy Environm. Sci.* **2020,** *13* (12), 4450-4497.

14. Zhao, S. *et al.* Reaction Mechanisms of Layered Lithium-Rich Cathode Materials for High-Energy Lithium-Ion Batteries. *Angew. Chem. Int. Ed.* **2021,** *60* (5), 2208-2220.

15. Chen, M.; Liu, Y.; Zhang, Y.; Xing, G.; Tang, Y., Lithium-rich sulfide/selenide cathodes for next-generation lithium-ion batteries: challenges and perspectives. *Chem. Commun.* **2022,** *58* (22), 3591-3600.

16. Saha, S. *et al.* Exploring the bottlenecks of anionic redox in Li-rich layered sulfides. *Nat. Energy* **2019,** *4* (11), 977-987.

17. Hu, Y. *et al.* Lithium-Rich Li_2TiS_3 Cathode Enables High-Energy Sulfide All-Solid-State Lithium Batteries. *Adv. Energy Mater.* **2023**, *13* (5), 2202756.

18. Hennequart, B. *et al.* Solid-Electrolyte-Free O3-Li_xTiS_2 Cathode for High-Energy-Density All-Solid-State Lithium-Metal Batteries. *ACS Appl. Energy Mater.* **2023,** *6* (16), 8521-8531.

19. Winter, M.; Brodd, R. J., What Are Batteries, Fuel Cells, and Supercapacitors? *Chem. Rev.* **2004,** *104* (10), 4245-4270.

20. Holze, R., Huggins A. Robert, Advanced batteries—materials science aspects. *J. Solid State Electrochem.* **2013,** *17* (8), 2371-2372.

21. Nitta, N.; Wu, F.; Lee, J. T.; Yushin, G., Li-ion battery materials: present and future. *Mater. Today* **2015,** *18* (5), 252-264.

22. *Solid State Electrochemistry*. Cambridge University Press: Cambridge, 1994.

23. Aydinol, M. K.; Kohan, A. F.; Ceder, G., Ab initio calculation of the intercalation voltage of lithium-transition-metal oxide electrodes for rechargeable batteries. *J. Power Sources* **1997,** *68* (2), 664-668.

24. Aydinol, M. K.; Kohan, A. F.; Ceder, G.; Cho, K.; Joannopoulos, J., Ab initio study of lithium intercalation in metal oxides and metal dichalcogenides. *Phys. Rev. B* **1997,** *56* (3), 1354-1365.

25. Goodenough, J. B.; Kim, Y., Challenges for Rechargeable Li Batteries. *Chem. Mater.* **2010,** *22* (3), 587-603.

26. Ceder, G. *et al.* Identification of cathode materials for lithium batteries guided by first-principles calculations. *Nature* **1998,** *392* (6677), 694-696.

27. Van der Ven, A.; Bhattacharya, J.; Belak, A. A., Understanding Li Diffusion in Li-Intercalation Compounds. *Acc. Chem. Res.* **2013,** *46* (5), 1216-1225.

28. Whittingham, M. S., Lithium Batteries and Cathode Materials. *Chem. Rev.* **2004,** *104* (10), 4271-4302.

29. Whittingham, M. S.; Gamble, F. R., The lithium intercalates of the transition metal dichalcogenides. *Mater. Res. Bull.* **1975,** *10* (5), 363-371.

30. Whittingham, M. S., Electrical Energy Storage and Intercalation Chemistry. *Science* **1976,** *192* (4244), 1126-1127.

31. Whittingham, M. S., Chemistry of intercalation compounds: Metal guests in chalcogenide hosts. *Prog. Solid State Chem.* **1978,** *12* (1), 41-99.

32. Wang, L.; Chen, B.; Ma, J.; Cui, G.; Chen, L., Reviving lithium cobalt oxide-based lithium secondary batteries-toward a higher energy density. *Chem. Soc. Rev.* **2018,** *47* (17), 6505-6602.

33. Belharouak, I.; Sun, Y. K.; Liu, J.; Amine, K., $Li(Ni_{1/3}Co_{1/3}Mn_{1/3})O_2$ as a suitable cathode for high power applications. *J. Power Sources* **2003,** *123* (2), 247-252.

34. Noh, H.-J.; Youn, S.; Yoon, C. S.; Sun, Y.-K., Comparison of the structural and electrochemical properties of layered $Li[Ni_xCo_yMn_z]O_2$ (x = 1/3, 0.5, 0.6, 0.7, 0.8 and 0.85) cathode material for lithium-ion batteries. *J. Power Sources* **2013,** *233*, 121-130.

35. Hu, E. *et al.* Evolution of redox couples in Li- and Mn-rich cathode materials and mitigation of voltage fade by reducing oxygen release. *Nat. Energy* **2018,** *3* (8), 690-698.

36. Hy, S. *et al.* Performance and design considerations for lithium excess layered oxide positive electrode materials for lithium ion batteries. *Energy Environ. Sci.* **2016,** *9* (6), 1931-1954.

37. Saubanère, M.; McCalla, E.; Tarascon, J. M.; Doublet, M. L., The intriguing question of anionic redox in high-energy density cathodes for Li-ion batteries. *Energy Environ. Sci.* **2016,** *9* (3), 984-991.

38. Armstrong, A. R. *et al.* Demonstrating oxygen loss and associated Structural reorganization in the lithium battery cathode $Li[Ni_{0.2}Li_{0.2}Mn_{0.6}]O_2$. *J. Am. Chem. Soc.* **2006,** *128* (26), 8694-8698.

39. McCalla, E. *et al.* Visualization of O-O peroxo-like dimers in high-capacity layered oxides for Li-ion batteries. *Science* **2015,** *350* (6267), 1516-1521.

40. Yang, W., Oxygen release and oxygen redox. *Nat. Energy* **2018,** *3* (8), 619-620.

41. Li, B. *et al.* Decoupling the roles of Ni and Co in anionic redox activity of Li-rich NMC cathodes. *Nat. Mater.* **2023,** *22* (11), 1370-1379.

42. Gao, X. *et al.* Clarifying the origin of molecular O_2 in cathode oxides. *Nat. Mater.* **2025,** *24*, 743–752.

43. Seo, D.-H. *et al.* The structural and chemical origin of the oxygen redox activity in layered and cation-disordered Li-excess cathode materials. *Nat. Chem.* **2016,** *8* (7), 692-697.

44. Luo, K. *et al.* Charge-compensation in 3d-transition-metal-oxide intercalation cathodes through the generation of localized electron holes on oxygen. *Nat. Chem.* **2016,** *8* (7), 684-691.

45. Qiu, B. *et al.* Gas–solid interfacial modification of oxygen activity in layered oxide cathodes for lithium-ion batteries. *Nat. Commun.* **2016,** *7* (1), 12108.

46. Zhu, Z. *et al.* Gradient Li-rich oxide cathode particles immunized against oxygen release by a molten salt treatment. *Nat. Energy* **2019,** *4* (12), 1049-1058.

47. Zhang, M. *et al.* Pushing the limit of 3d transition metal-based layered oxides that use both cation and anion redox for energy storage. *Nat. Rev. Mater.* **2022,** *7* (7), 522-540.

48. Yan, P. *et al.* Injection of oxygen vacancies in the bulk lattice of layered cathodes. *Nat. Nanotechnol.* **2019,** *14* (6), 602-608.

49. Boivin, E. *et al.* The Role of Ni and Co in Suppressing O-Loss in Li-Rich Layered Cathodes. *Adv. Funct. Mater.* **2021,** *31* (2), 2003660.

50. Zheng, M. *et al.* Deployment strategies for Li-rich cathode materials in batteries. *Nat. Energy* **2025,** *10* (7), 789-792.

51. Gallagher, K. G. *et al.* Correlating hysteresis and voltage fade in lithium- and manganese-rich layered transition-metal oxide electrodes. *Electrochem. Commun.* **2013,** *33*, 96-98.

52. Croy, J. R. *et al.* Examining hysteresis in composite x Li_2MnO_3·(1–x) $LiMO_2$ cathode structures. *J. Phys. Chem. C* **2013,** *117* (13), 6525-6536.

53. Liu, T. *et al.* Origin of structural degradation in Li-rich layered oxide cathode. *Nature* **2022,** *606* (7913), 305-312.

54. Louis, J. *et al.* Effect of the nature of both cation and anion substitution on the structural symmetry of Li-rich 3d-metal chalcogenide electrodes. *Adv. Energy Mater.* **2023**, *13* (45), 2302158.

55. Li, J.-C. *et al.* From oxygen redox to sulfur redox: a paradigm for Li-rich layered cathodes. *J. Am. Chem. Soc.* **2024,** *146* (11), 7274-7287.

56. Jiang, Z.; *et al.* Metal–Ligand Spin-Lock Strategy for Inhibiting Anion Dimerization in Li-Rich Cathode Materials. *J. Am. Chem. Soc.* **2025,** *147* (4), 3062-3071.

57. Flamary-Mespoulie, F. *et al.* Lithium-rich layered titanium sulfides: Cobalt- and Nickel-free high capacity cathode materials for lithium-ion batteries. *Energy Storage Mater.* **2020,** *26*, 213-222.

58. Patheria, E. S. *et al.* High-Energy Density Li-Ion Battery Cathode Using Only Industrial Elements. *J. Am. Chem. Soc.* **2025,** 147(4), 3062-3071.

59. Sakuda, A. *et al.* Development of Li_2TiS_3–Li_3NbS_4 by a mechanochemical process. *J. Ceram. Soc. Jpn.* **2017,** *125*, 268-271.

60. Sakuda, A. *et al.* A Reversible Rocksalt to Amorphous Phase Transition Involving Anion Redox. *Sci. Rep.* **2018,** *8* (1), 15086.

61. Hansen, C. J. *et al.* Multielectron, Cation and Anion Redox in Lithium-Rich Iron Sulfide Cathodes. *J. Am. Chem. Soc.* **2020,** *142* (14), 6737-6749.

62. Celasun, Y. *et al.* Lithium-Rich Rock Salt Type Sulfides-Selenides ($Li_2TiSe_xS_{3-x}$): High Energy Cathode Materials for Lithium-Ion Batteries. *Materials* **2022,** *15* (9), 3037.

63. Shinoda, M. *et al.* Activation of Anionic Redox for Stoichiometric and Li-Excess Metal Sulfides through Structural Disordering: Joint Experimental and Theoretical Study. *J. Am. Chem. Soc.* **2025,** *147* (30), 26238-26253.

64. Rouxel, J., Anion–Cation Redox Competition and the Formation of New Compounds in Highly Covalent Systems. *Chem. Eur. J.* **1996,** *2* (9), 1053-1059.

65. Rouxel, J., Some solid state chemistry with holes: Anion–cation redox competition in solids. *Curr. Sci.* **1997,** *73* (1), 31-39.

66. Britto, S. *et al.* Multiple Redox Modes in the Reversible Lithiation of High-Capacity, Peierls-Distorted Vanadium Sulfide. *J. Am. Chem. Soc.* **2015,** *137* (26), 8499-8508.

67. Fong, R. *et al.* Electrochemistry of Pyrite-Based Cathodes for Ambient Temperature Lithium Batteries. *J. Electrochem. Soc.* **1989,** *136* (11), 3206-3210.

68. Ōnuki, Y. *et al.* Electrochemical characteristics of transition-metal trichalcogenides in the secondary lithium battery. *Solid State Ionics* **1983,** *11* (3), 195-201.

69. Murphy, D. W.; Trumbore, F. A., The Chemistry of TiS_3 and $NbSe_3$ Cathodes. *J. Electrochem. Soc.* **1976,** *123* (7), 960.

70. Murphy, D. W.; Trumbore, F. A., Metal chalcogenides as reversible electrodes in nonaqueous lithium batteries. *J. Cryst. Growth* **1977,** *39* (1), 185-199.

71. Kim, Y. *et al.* Access to M^{3+}/M^{2+} Redox Couples in Layered $LiMS_2$ Sulfides (M = Ti, V, Cr) as Anodes for Li-Ion Battery. *J. Electrochem. Soc.* **2009,** *156* (8), A703.

72. Kim, Y.; Goodenough, J. B., Reinvestigation of $Li_{1-x}Ti_yV_{1-y}S_2$ Electrodes in Suitable Electrolyte: Highly Improved Electrochemical Properties. *Electrochem. Solid-State Lett.* **2009,** *12* (4), A73.

73. Tarascon, J. M. *et al.* Preparation and chemical and physical properties of the new layered phases $Li_xTi_{1-y}M_yS_2$ with M = V, Cr, or Fe. *Phys. Rev. B* **1983,** *28* (11), 6397-6406.

74. Barker, J.; Kendrick, E., The electrochemical insertion and safety properties of the low-cost Li-ion active material, Li_2FeS_2. *J. Power Sources* **2011,** *196* (16), 6960-6963.

75. Sakuda, A. *et al.* Rock-salt-type lithium metal sulphides as novel positive-electrode materials. *Sci. Rep.* **2014,** *4* (1), 4883.

76. Li, B. *et al.* Thermodynamic Activation of Charge Transfer in Anionic Redox Process for Li-Ion Batteries. *Adv. Funct. Mater.* **2018,** *28* (4), 1704864.

77. Marchandier, T. *et al.* Triggering Anionic Redox Activity in Li_3NbS_4 Through Cationic Disordering or Substitution. *Adv. Energy Mater.* **2022,** *12* (41), 2201417.

78. Sun, Y.; Adelhelm, P., Lifting the redox potential of layered sulfide cathodes for sodium-ion batteries. *Matter* **2022,** *5* (8), 2500-2501.

79. Nasu, A. *et al.* Iron Sulfide Na_2FeS_2 as Positive Electrode Material with High Capacity and Reversibility Derived from Anion–Cation Redox in All-Solid-State Sodium Batteries. *Small* **2022,** *18* (42), 2203383.

80. Hong, J. *et al.* Metal–oxygen decoordination stabilizes anion redox in Li-rich oxides. *Nat. Mater.* **2019,** *18* (3), 256-265.

81. Ben Yahia, M.; Vergnet, J.; Saubanère, M.; Doublet, M.-L., Unified picture of anionic redox in Li/Na-ion batteries. *Nat. Mater.* **2019,** *18* (5), 496-502.

82. House, R. A. *et al.* Superstructure control of first-cycle voltage hysteresis in oxygen-redox cathodes. *Nature* **2020,** *577* (7791), 502-508.

83. House, R. A. *et al.* First-cycle voltage hysteresis in Li-rich 3d cathodes associated with molecular O_2 trapped in the bulk. *Nat. Energy* **2020,** *5* (10), 777-785.

84. House, R. A. *et al.* Covalency does not suppress O_2 formation in 4d and 5d Li-rich O-redox cathodes. *Nat. Commun.* **2021,** *12* (1), 2975.

85. House, R. A. *et al.* Delocalized electron holes on oxygen in a battery cathode. *Nat. Energy* **2023,** *8* (4), 351-360.

86. House, R. A. *et al.* Detection of trapped molecular O_2 in a charged Li-rich cathode by Neutron PDF. *Energy Environ. Sci.* **2022,** *15* (1), 376-383.

87. McColl, K. *et al.* Phase segregation and nanoconfined fluid O_2 in a lithium-rich oxide cathode. *Nat. Materials* **2024,** *23* (6), 826-833.

88. Sharpe, R. *et al.* Redox Chemistry and the Role of Trapped Molecular O_2 in Li-Rich Disordered Rocksalt Oxyfluoride Cathodes. *J. Am. Chem. Soc.* **2020,** *142* (52), 21799-21809.

89. McColl, K. *et al.* Transition metal migration and O_2 formation underpin voltage hysteresis in oxygen-redox disordered rocksalt cathodes. *Nat. Commun.* **2022,** *13* (1), 5275.

90. Pi, L. *et al.* Factors affecting capacity and voltage fading in disordered rocksalt cathodes for lithium-ion batteries. *Matter* **2025,** *8* (3), 101938.

91. Boivin, E. *et al.* Bulk O_2 formation and Mg displacement explain O-redox in $Na_{0.67}Mn_{0.72}Mg_{0.28}O_2$. *Joule* **2021,** *5* (5), 1267-1280.

92. Hu, C. *et al.* Accumulation of Unreduced Molecular O_2 Explains Abnormal Voltage Decay in P2-Type Layered Oxide Cathode. *Adv. Energy Mater.* **2025,** e03491.

93. Mitchell, N. C. *et al.* Influence of Ion Size on Structure and Redox Chemistry in Na-Rich and Li-Rich Disordered Rocksalt Battery Cathodes. *Adv. Mater.* **2025,** *37* (32), 2419878.

94. House, R. A. *et al.* The role of O_2 in O-redox cathodes for Li-ion batteries. *Nat. Energy* **2021,** *6* (8), 781-789.

95. Marie, J.-J. *et al.* Trapped O_2 and the origin of voltage fade in layered Li-rich cathodes. *Nat. Mater.* **2024,** *23* (6), 818-825.

96. Mohanty, D. *et al.* Unraveling the Voltage-Fade Mechanism in High-Energy-Density Lithium-Ion Batteries: Origin of the Tetrahedral Cations for Spinel Conversion. *Chem. Mater.* **2014,** *26* (21), 6272-6280.

97. Hua, W. *et al.* Structural insights into the formation and voltage degradation of lithium- and manganese-rich layered oxides. *Nat. Commun.* **2019,** *10* (1), 5365.

98. Gao, A. *et al.* Topologically protected oxygen redox in a layered manganese oxide cathode for sustainable batteries. *Nat. Sustain.* **2021,** *5* (3), 214-224.

99. Rong, X. *et al.* Structure-Induced Reversible Anionic Redox Activity in Na Layered Oxide Cathode. *Joule* **2018,** *2* (1), 125-140.

100. Zhao, C. *et al.* Rational design of layered oxide materials for sodium-ion batteries. *Science* **2020,** *370* (6517), 708-711.

101. Han, M. H. *et al.* A comprehensive review of sodium layered oxides: powerful cathodes for Na-ion batteries. *Energy Environ. Sci.* **2015,** *8* (1), 81-102.

102. Koga, H. *et al.* Reversible Oxygen Participation to the Redox Processes Revealed for $Li_{1.20}Mn_{0.54}Co_{0.13}Ni_{0.13}O_2$. *J. Electrochem. Soc.* **2013,** *160* (6), A786.

103. Lu, Z. *et al.* Understanding the Anomalous Capacity of Li / $Li[Ni_x Li_{(1/3-2x/3)} Mn_{(2/3-x/3)}] O_2$ Cells Using In Situ X-Ray Diffraction and Electrochemical Studies. *J. Electrochem. Soc.* **2002,** *149* (7), A815.

104. Li, X. *et al.* Reducing Voltage Hysteresis in Li-Rich Sulfide Cathodes by Incorporation of Mn. *Chem. Mater.* **2024,** *36* (11), 5687-5697.

105. Nagarajan, S. *et al.* Mixed Cationic and Anionic Redox in Ni and Co Free Chalcogen-Based Cathode Chemistry for Li-Ion Batteries. *J. Am. Chem. Soc.* **2021,** *143* (38), 15732-15744.

106. Martinolich, A. J. *et al.* Controlling Covalency and Anion Redox Potentials through Anion Substitution in Li-Rich Chalcogenides. *Chem. Mater.* **2021,** *33* (1), 378-391.

107. Leube, B. T. *et al.* Activation of anionic redox in d^0 transition metal chalcogenides by anion doping. *Nat. Commun.* **2021,** *12* (1), 5485.

108. Kumar, K. *et al.* Investigation of Key Electronic States in Layered Mixed Chalcogenides With a d0 Transition Metal as Li-Ion Cathodes. *Adv. Funct. Mater.* **2024,** *34* (46), 2408060.

109. Kim, S. S. *et al.* Cation Vacancies Enable Anion Redox in Li Cathodes. *J. Am. Chem. Soc.* **2024,** *146* (30), 20951-20962.

110. Leube, B. T. *et al.* Layered Sodium Titanium Trichalcogenide Na_2TiCh_3 Framework (Ch = S, Se): A Rich Crystal and Electrochemical Chemistry. *Chem. Mater.* **2022,** *34* (5), 2382-2392.

111. Wang, Q. *et al.* Unlocking anionic redox activity in O3-type sodium 3d layered oxides via Li substitution. *Nat. Mater.* **2021,** *20* (3), 353-361.

112. Zak, J. J. *et al.* An Exploration of Sulfur Redox in Lithium Battery Cathodes. *J. Am. Chem. Soc.* **2022,** *144* (23), 10119-10132.

113. Janek, J.; Zeier, W. G., A solid future for battery development. *Nat. Energy* **2016,** *1* (9), 16141.

114. Krauskopf, T. *et al.* Physicochemical Concepts of the Lithium Metal Anode in Solid-State Batteries. *Chem. Rev.* **2020,** *120* (15), 7745-7794.

115. Betz, J. *et al.* Theoretical versus Practical Energy: A Plea for More Transparency in the Energy Calculation of Different Rechargeable Battery Systems. *Adv. Energy Mater.* **2019,** *9* (6), 1803170.

116. Arbizzani, C.; Gabrielli, G.; Mastragostino, M., Thermal stability and flammability of electrolytes for lithium-ion batteries. *J. Power Sources* **2011,** *196* (10), 4801-4805.

117. Saha, S. Exploration of ionic conductors and Li-rich sulfides for all-solid-state batteries. Sorbonne Université, 2020.

118. Wang, M. J.; Kazyak, E.; Dasgupta, N. P.; Sakamoto, J., Transitioning solid-state batteries from lab to market: Linking electro-chemo-mechanics with practical considerations. *Joule* **2021,** *5* (6), 1371-1390.

119. Minnmann, P. *et al.* Designing Cathodes and Cathode Active Materials for Solid-State Batteries. *Adv. Energy Mater.* **2022,** *12* (35), 2201425.

120. Alsaç, E. P. *et al.* Characterizing Electrode Materials and Interfaces in Solid-State Batteries. *Chem. Rev.* **2025,** *125* (4), 2009-2119.

121. Banerjee, A. *et al.* Interfaces and Interphases in All-Solid-State Batteries with Inorganic Solid Electrolytes. *Chem. Rev.* **2020,** *120* (14), 6878-6933.

122. Shi, T. *et al.* High Active Material Loading in All-Solid-State Battery Electrode via Particle Size Optimization. *Adv. Energy Mater.* **2020,** *10* (1), 1902881.

123. Park, N. *et al.* High-energy, long-life Ni-rich cathode materials with columnar structures for all-solid-state batteries. *Nat. Energy* **2025,** *10* (4), 479-489.

124. Wang, L. *et al.* In-situ visualization of the space-charge-layer effect on interfacial lithium-ion transport in all-solid-state batteries. *Nat. Commun.* **2020,** *11* (1), 5889.

125. Sun, S. *et al.* Eliminating interfacial O-involving degradation in Li-rich Mn-based cathodes for all-solid-state lithium batteries. *Sci. Adv.* **2022,** *8* (47), eadd5189.

126. Xu, L. *et al.* Building Better Batteries: Solid-State Batteries with Li-Rich Oxide Cathodes. *Energy Mater. Adv.* **2023,** *4*, 0045.

127. Liu, Y. *et al.* Surface-localized phase mediation accelerates quasi-solid-state reaction kinetics in sulfur batteries. *Nat. Chem.* **2025,** *17* (4), 614-623.

128. Froboese, L. *et al.* Effect of Microstructure on the Ionic Conductivity of an All Solid-State Battery Electrode. *J. Electrochem. Soc.* **2019,** *166* (2), A318.

129. Santhosha, A. L. *et al.* Macroscopic Displacement Reaction of Copper Sulfide in Lithium Solid-State Batteries. *Adv. Energy Mater.* **2020,** *10* (41), 2002394.

130. Dewald, G. F. *et al.* Influence of Iron Sulfide Nanoparticle Sizes in Solid-State Batteries. *Angew. Chem. Int. Ed.* **2021,** *60* (33), 17952-17956.

131. Murugan, R. *et al.* Fast Lithium Ion Conduction in Garnet-Type $Li_7La_3Zr_2O_{12}$. *Angew. Chem. Int. Ed.* **2007,** *46* (41), 7778-7781.

132. Li, Y. *et al.* A lithium superionic conductor for millimeter-thick battery electrode. *Science* **2023,** *381* (6653), 50-53.

133. Kraft, M. *et al.* Influence of Lattice Polarizability on the Ionic Conductivity in the Lithium Superionic Argyrodites Li_6PS_5X (X = Cl, Br, I). *J. Am. Chem. Soc.* **2017,** *139* (31), 10909-10918.

134. Liu, Z. *et al.* Anomalous High Ionic Conductivity of Nanoporous β-Li_3PS_4. *J. Am. Chem. Soc.* **2013,** *135* (3), 975-978.

135. Asano, T. *et al.* Solid Halide Electrolytes with High Lithium-Ion Conductivity for Application in 4 V Class Bulk-Type All-Solid-State Batteries. *Adv. Mater.* **2018,** *30* (44), 1803075.

136. Li, X. *et al.* Air-stable Li_3InCl_6 electrolyte with high voltage compatibility for all-solid-state batteries. *Energy Environ. Sci.* **2019,** *12* (9), 2665-2671.

137. Chen, R. *et al.* Approaching Practically Accessible Solid-State Batteries: Stability Issues Related to Solid Electrolytes and Interfaces. *Chem. Rev.* **2020,** *120* (14), 6820-6877.

138. Strauss, F. *et al.* Influence of electronically conductive additives on the cycling performance of argyrodite-based all-solid-state batteries. *RSC Adv.* **2020,** *10* (2), 1114-1119.

139. Randau, S. *et al.* On the Additive Microstructure in Composite Cathodes and Alumina-Coated Carbon Microwires for Improved All-Solid-State Batteries. *Chem. Mater.* **2021,** *33* (4), 1380-1393.

140. de Biasi, L. *et al.* Between Scylla and Charybdis: Balancing Among Structural Stability and Energy Density of Layered NCM Cathode Materials for Advanced Lithium-Ion Batteries. *J. Phys. Chem. C* **2017,** *121* (47), 26163-26171.

141. Wang, L. *et al.* High-energy all-solid-state lithium batteries enabled by Co-free $LiNiO_2$ cathodes with robust outside-in structures. *Nat. Nanotechnol.* **2024,** *19* (2), 208-218.

142. Koerver, R. *et al.* Chemo-mechanical expansion of lithium electrode materials – on the route to mechanically optimized all-solid-state batteries. *Energy Environ. Sci.* **2018,** *11* (8), 2142-2158.

143. Bielefeld, A.; Weber, D. A.; Janek, J., Microstructural Modeling of Composite Cathodes for All-Solid-State Batteries. *J. Phys. Chem. C* **2019,** *123* (3), 1626-1634.

144. Kaiser, N. *et al.* Ion transport limitations in all-solid-state lithium battery electrodes containing a sulfide-based electrolyte. *J. Power Sources* **2018,** *396*, 175-181.

145. Dokko, K. *et al.* Kinetic Characterization of Single Particles of $LiCoO_2$ by AC Impedance and Potential Step Methods. *J. Electrochem. Soc.* **2001,** *148* (5), A422.

146. Levasseur, S.; Ménétrier, M.; Delmas, C., On the Dual Effect of Mg Doping in $LiCoO_2$ and $Li_{1+\delta}CoO_2$: Structural, Electronic Properties, and ^{7}Li MAS NMR Studies. *Chem. Mater.* **2002,** *14* (8), 3584-3590.

147. Park, M. *et al.* A review of conduction phenomena in Li-ion batteries. *J. Power Sources* **2010,** *195* (24), 7904-7929.

148. Hlushkou, D. *et al.* The influence of void space on ion transport in a composite cathode for all-solid-state batteries. *J. Power Sources* **2018,** *396*, 363-370.

149. Kondrakov, A. O. *et al.* Anisotropic Lattice Strain and Mechanical Degradation of High- and Low-Nickel NCM Cathode Materials for Li-Ion Batteries. *J. Phys. Chem. C* **2017,** *121* (6), 3286-3294.

150. Gao, X. *et al.* Solid-state lithium battery cathodes operating at low pressures. *Joule* **2022,** *6* (3), 636-646.

151. Ruess, R. *et al.* Influence of NCM Particle Cracking on Kinetics of Lithium-Ion Batteries with Liquid or Solid Electrolyte. *J. Electrochem. Soc.* **2020,** *167* (10), 100532.

152. Ryu, H.-H. *et al.* Capacity Fading of Ni-Rich $Li[Ni_xCo_yMn_{1-x-y}]O_2$ ($0.6 \leq x \leq 0.95$) Cathodes for High-Energy-Density Lithium-Ion Batteries: Bulk or Surface Degradation? *Chem. Mater.* **2018,** *30* (3), 1155-1163.

153. Zhu, Y.; He, X.; Mo, Y., Origin of Outstanding Stability in the Lithium Solid Electrolyte Materials: Insights from Thermodynamic Analyses Based on First-Principles Calculations. *ACS Appl. Mater. Interfaces* **2015,** *7* (42), 23685-23693.

154. Yu, T.-Y. *et al.* Limitation of Ni-rich layered cathodes in all-solid-state lithium batteries. *Journal of Materials Chemistry A* **2023,** *11* (45), 24629-24636.

155. Culver, S. P. *et al.* On the Functionality of Coatings for Cathode Active Materials in Thiophosphate-Based All-Solid-State Batteries. *Adv. Energy Mater.* **2019,** *9* (24), 1900626.

156. Tan, D. H. S. *et al.* Elucidating Reversible Electrochemical Redox of Li_6PS_5Cl Solid Electrolyte. *ACS Energy Lett.* **2019,** *4* (10), 2418-2427.

157. Koerver, R. *et al.* Redox-active cathode interphases in solid-state batteries. *J. Mater. Chem. A* **2017,** *5* (43), 22750-22760.

158. Jung, S.-K. *et al.* Understanding the effects of chemical reactions at the cathode–electrolyte interface in sulfide based all-solid-state batteries. *J. Mater. Chem. A* **2019,** *7* (40), 22967-22976.

159. Kitsche, D. *et al.* Atomic Layer Deposition Derived Zirconia Coatings on Ni-Rich Cathodes in Solid-State Batteries: Correlation Between Surface Constitution and Cycling Performance. *Small Sci.* **2023,** *3* (2), 2200073.

160. Kim, A. Y. *et al.* Effect of surface carbonates on the cyclability of $LiNbO_3$-coated NCM622 in all-solid-state batteries with lithium thiophosphate electrolytes. *Sci. Rep.* **2021,** *11* (1), 5367.

161. Sakuda, A. *et al.* High Reversibility of “Soft” Electrode Materials in All-Solid-State Batteries. *Front. Energy Res.* **2016,** *4*, 19.

162. Marchini, F. *et al.* Li-Rich Layered Sulfide as Cathode Active Materials in All-Solid-State Li–Metal Batteries. *ACS Appl. Mater. Interfaces* **2020,** *12* (13), 15145-15154.

163. Gard, P.; Sourisseau, C.; Ouvrard, G.; Brec, R., Infrared study of lithium intercalated phases in the Li_xFeS_2 system ($0 \leq x \leq 2$). Characterization of a new iron disulfide. *Solid State Ionics* **1986,** *20* (3), 231-238.

164. Ohno, S. *et al.* Linking Solid Electrolyte Degradation to Charge Carrier Transport in the Thiophosphate-Based Composite Cathode toward Solid-State Lithium-Sulfur Batteries. *Adv. Funct. Mater.* **2021,** *31* (18), 2010620.

165. Caspar, M. *et al.* Study of the Cathode/Electrolyte Interface in an All-Sulfide-Solid-State Battery Using Lithium-Rich Transition Metal Sulfide. *ACS Appl. Mater. Interfaces* **2025,** *17* (4), 7142-7150.

2

Experimental Techniques

Contents

This chapter presents the synthesis methods and characterization techniques employed in this thesis. Detailed descriptions of the instruments and facilities used are provided in the experimental sections of the subsequent chapters.

2.1 Materials Synthesis

2.1.1 Solid-state Synthesis

By far, solid-state synthesis is the predominant route for making mixed metal sulfides. This approach involves thoroughly mixing different solid precursor compounds, such as transition metal sulfides, metal powders, and elemental sulfur, followed by heating the mixture at high temperatures.[1] As most sulfide compounds are highly sensitive to moisture and air, performing the reaction in evacuated sealed tubes is essential to eliminate O_2 and prevent the formation of oxide impurities. Additionally, to avoid any side reactions between Li-containing compounds and quartz tubes, all precursors are first placed into a carbon crucible before being transferred into quartz tubes, as shown in Figure 2.1.

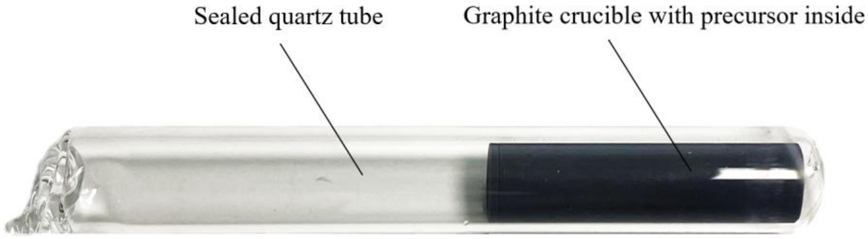

Figure 2.1: Sealed quartz tube with sulfide pellets loaded into a graphite crucible.

Initially, the reagents with appropriate stoichiometric ratios are finely ground using an agate mortar and pestle inside an Ar-filled glove box ($O_2 < 0.1$ ppm, $H_2O < 0.1$ ppm). The resulting mixture is then pressed into dense pellets using a hydraulic press and die set, ensuring intimate contact between particles. Subsequently, the pellets are loaded into the carbon crucible, and the tube is evacuated to a pressure of ~ 5×10^{-5} mbar before being flame-sealed with an oxygen-methane blowtorch, ensuring no exposure to air. The sealed tubes are then subjected to high-temperature treatment (600 – 1000 °C) for prolonged reaction durations (3 – 10 days), allowing sufficient time for diffusion and complete reaction between particles. Notably, different heating temperatures may preferentially stabilize certain crystalline phases over others.

At a given temperature, the reaction equilibrium can be further tuned by the partial pressure of sulfur vapor inside the sealed tube. This is controlled by adjusting either the quantity of reactants or the length of the quartz tube, as sulfur readily sublimes at ~ 100 ℃ under low-pressure conditions. In particular, the formation of sulfur-rich compounds is often favored only at elevated sulfur partial pressures.[2] For example, adding excess sulfur (10 – 15 wt% excess) can push the equilibrium to the right-hand side of the reaction below:

$$\mathrm{TM^{4+}S_2\ (s) + S\ (g) \rightleftharpoons TM^{4+}S_3\ (s)\ (TM = Ti, Nb, etc.)} \tag{2.1}$$

The ramping speed during heating is another important variable in sulfide-based cathode syntheses. Due to the formation of gaseous sulfur during sintering, a slow heating rate (0.3 – 2 ℃/min) is commonly used to avoid a rapid buildup of internal pressure that could rupture the sealed quartz tube. Lastly, the cooling rate also plays a crucial role in determining the final product. Slow cooling (< 2 ℃/min) is generally beneficial for promoting some ordered atomic arrangements that might be randomly distributed at high temperatures.[3, 4] In contrast, quenching samples to room temperature, or even lower temperature (by iced water or liquid N_2), can effectively preserve structures only thermodynamically stable at high temperatures.[5]

2.1.2 Ball-milling Synthesis

Ball-milling is a mechanochemical synthesis method commonly used to thoroughly mix precursors, reduce particle sizes and introduce structural defects into materials. The process begins by loading the precursors into a milling jar along with grinding balls, both made from high-hardness and abrasion-resistant materials, like zirconia, stainless steel and tungsten carbide. For sulfide materials, to prevent air and moisture exposure, the jar must be tightly sealed inside the glove box before being transferred to the milling machine. During milling, the grinding balls collide with each other, the precursor powder and the jar, producing a large amount of localized heating and high pressure, which supplies the energy required to trigger chemical reactions.[6, 7] This energy input and collisions between the powder particles collectively induce repeated deformation, shearing, fracturing and homogenous mixing of the particles. Under these localized high-temperature and high-pressure conditions, some metastable phases can be formed, which may otherwise require high-temperature annealing or a high-pressure environment to synthesize.[8]

2.1.3 Chemical Delithiation

The chemical delithiation method has been widely used to investigate the structure and properties of cathode materials. It allows the removal of Li^+ from cathodes without relying on electrochemical cycling. As a result, no carbon additives are introduced, effectively avoiding the interference or signal contribution from carbon in various characterization techniques. Chemically delithiation also allows the large-scale preparation of delithiated materials, which is greatly helpful for techniques that require substantial quantities (> 10g) of charged/discharged cathode powder. Otherwise, such an amount is impractical to achieve using coin cells alone. In general, Li^+ ions are extracted by reacting the cathode material with chemical oxidants such as NO_2BF_4 and I_2 in an appropriate solvent medium.[9, 10] In this thesis, the sulfide cathodes are chemically delithiated using I_2, following the reaction:

$$LiTM^{3+}S_2 + 0.5\ I_2 \rightarrow LiI + TM^{4+}S_2 \qquad (2.2)$$

The pristine sulfide and iodine are mixed in anhydrous acetonitrile at a molar ratio of 2:1 and stirred at room temperature for 24 hours. After the reaction, the mixture is washed at least three times with anhydrous acetonitrile and dried under vacuum overnight at 50 ℃ to remove any residual reagents and solvent. It is worth noting that the choice of oxidant depends on the main redox couple within the cathodes. Stronger oxidants are required to simulate higher states of charge, equivalent to charging the material to a higher equilibrium potential. Additionally, increasing the concentration of the oxidant and the reaction temperature typically facilitates the lithium extraction process.

2.2 Materials Imaging Characterization

2.2.1 Annular Dark Field Scanning Transmission Electron Microscopy

Scanning Transmission Electron Microscopy (STEM) is a sophisticated imaging technique capable of characterizing materials at the atomic scale. In operation, a highly focused electron beam is rastered over a sample, with transmitted electrons collected beneath the sample.[11] In Annular Dark Field (ADF) mode, an annular (ring-shaped) detector is used to detect electrons scattered at high angles, excluding low-angle or unscattered electrons. This results in images where heavier atoms or denser regions appear as brighter contrast, known as 'Z-contrast', where Z refers to the atomic number. In ADF-STEM, the intensity of the scattered electrons is approximately proportional to Z^2, enhancing contrast between different atoms. In cathode research, ADF-STEM offers indispensable insights into interpreting features such as superstructure, anti-site mixing and stacking faults, as well as directly visualizing defects like grain boundaries, nanovoids, and surface structure changes.[12]

To obtain high-quality images, the sample must be sufficiently thin (< 100 nm) to allow adequate electron transmission, as the electron beam could be heavily attenuated by the material. Therefore, samples are first ground, sonicated in a solvent, drop-cast onto a conductive carbon grid, and finally dried under vacuum. In this way, the number of smaller particles with thin edges can be increased, and particle agglomeration is reduced. During measurement, to obtain atomic-resolution images, the grid is examined to identify particles with a specific zone axis parallel to the direction of the electron beam.

2.2.2 Scanning Electron Microscopy

Scanning Electron Microscopy (SEM) is a powerful imaging method used to visualize particle and surface morphology, particle size distribution and microstructure of materials. In cathode research, these features are closely related to the length of Li^+ diffusion within the bulk material and potential side reactions at the surface during cycling. SEM images allowed spatial resolution down to the nanoscale. This is made possible by using a focused beam of electrons, which have significantly shorter wavelengths than visible light, thus providing much higher resolution than conventional optical microscopes.[13] In the SEM setup, electrons are produced from an electron source, then accelerated and focused before being scanned across the sample. The interaction between the sample and the electron beam results in various scattering and absorption events. Among these, low-energy secondary electrons produced by inelastic scattering constitute the majority of emitted electrons and are most commonly used for imaging. These secondary electrons can escape only from the top few nanometers of the sample surface, and their intensity is determined by the angle of the surface from which they are emitted, providing detailed topological information with a resolution of about 1 nm.[14]

Energy Dispersive X-ray Spectrometry

Combined with SEM, energy dispersive X-ray Spectroscopy (EDX) is commonly used to perform elemental analysis of samples. EDX relies on the interaction between the electron beam and the atoms within the sample. When the incident electron beam excites an inner-shell electron and ejects it from the atom, the resulting vacancy is filled by an electron from a higher-energy outer shell. The energy released during this transition is emitted as a characteristic X-ray of each element, enabling both qualitative and quantitative analysis.[15] In cathode research, EDX provides valuable information on the compositions and spatial distribution of elements for the sample.

Plasma Focused Ion Beam-SEM

SEM can also be coupled with a plasma-focused ion beam, commonly referred to as PFIB-SEM. In this configuration, a plasma source generates a high flux of noble-gas ions (e.g., Xe^+, Ar^+), which are accelerated and focused onto the specimen.[16] The ion beam sputters material surfaces with high precision (spot sizes ~ 10-30 nm), thereby exposing subsurface features. The SEM then images the freshly milled cross-section. In battery research, PFIB-SEM is widely used to visualize internal particle morphologies, such as pores and cracks.

2.2.3 X-ray Computed Tomography

X-ray computed tomography (XCT) is employed to visualize the internal architecture of materials in three-dimensional (3D) geometries, such as voids, cracks and porosity. It was initially developed for medical applications to diagnose fractures and tumours, with resolutions in the submillimetre to millimetre range. Nowadays, micro-tomography (microCT), with micrometre resolution (voxel sizes $\geq 0.1\ \mu m^3$), and nano-tomography (nanoCT), achieving resolutions down to ~ 10 nm, are widely used in materials science, including battery research.[17, 18]

XCT works by utilizing the penetrating ability of X-rays to acquire a series of two-dimensional (2D) radiographs of the sample viewed from multiple angles, typically by rotating the sample over 180 degrees or 360 degrees. Each cross-sectional image is known as a CT scan or CT slice. Using computed reconstruction algorithms, a stack of 2D CT slices is then compiled into a 3D greyscale model, known as a tomogram, which enables detailed analysis of internal features. The quality and interpretability of the tomogram depend on the contrast observed in each projection, which is governed by how X-rays interact with the material. As X-rays pass through the sample, they undergo attenuation (intensity reduction) and a phase shift. These effects result in attenuation contrast and phase contrast, respectively, and are described by the refractive index, n:

$$n = 1 - \delta + i\beta \tag{2.3}$$

where the real part δ determines the phase shift, while the imaginary part β controls attenuation. The attenuation coefficient μ which quantifies the reduction in X-ray intensity after passing through a material, is directly related to β and can be expressed as below:

$$\mu = \frac{4\pi\beta}{\lambda} \tag{2.4}$$

where λ is the wavelength of the incident X-ray. Samples with greater thickness or higher atomic numbers absorb and scatter more X-rays, leading to a higher value of μ. The resulting intensity drop follows the Beer-Lambert Law:

$$I = I_0 e^{-\mu x} \tag{2.5}$$

where I_0 is the incident X-ray intensity, I is the transmitted X-ray intensity, and x is the path length through samples. In attenuation-based XCT, variations in μ across the sample generate attenuation contrast, enabling differentiation of materials with distinct X-ray absorption properties. In this thesis, all XCT results are derived from attenuation-based tomography, as the studied sulfide material shows clear attenuation differences with surrounding phases. Phase-contrast CT, on the other hand, is better suited for imaging objects with minimal attenuation contrast, such as soft biological tissues.[17]

2.3 Long-Range Structural Characterization

2.3.1 Powder X-ray Diffraction

Powder X-ray diffraction (PXRD) is used to identify the crystallographic structure of materials. It can also be used to quantify phase fractions in crystalline mixtures and determine the composition of each phase.[19]

X-ray diffraction occurs when X-rays are scattered by the periodic arrangement of atoms in a crystal, leading to constructive and destructive interference in the outgoing beam. This is possible because the wavelength of X-rays (typically 0.2 – 2 Å) is of the same length scale as the neighboring atomic planes within the crystal structure (~ 1 – 10 Å). In the PXRD experiment, a crystal is subjected to collimated and monochromatic (with single wavelength) X-rays. The incident beam of X-rays is subsequently scattered primarily by the electrons surrounding the atoms. Consequently, atoms with higher atomic numbers exhibit stronger scattering. The ordered atomic planes in the crystal cause this scattering to behave like reflections from parallel planes. These planes are indexed by Miller indices (h, k, l), which are derived from the inverse of the intercepts of the planes with the crystallographic axes a, b, and c, respectively. When the path-length difference between X-rays scattered from parallel planes equals an integer multiple of the wavelength, constructive interference occurs and a diffraction pattern is generated. This process is described by Bragg's Law,[20] shown in Figure 2.2 and Equation 2.6:

$$2d_{hkl}\sin(\theta) = n\lambda \tag{2.6}$$

where d_{hkl} is the interplanar spacing (also called d-spacing) for planes with Miller indices of (h, k, l), θ is the angle between the atomic plane and the incident X-ray, n is an integer and λ is the wavelength of the X-rays. The positions and number of peaks in a diffraction pattern are therefore governed by the space group and unit cell parameters, which determine the values of d_{hkl}. The intensity of each diffraction peak, $|I_{hkl}|$, is directly related to the scattering ability of the atoms in the (h, k, l) planes, which is described by the structure factor F_{hkl}, as described in Equation 2.7:

$$I_{hkl} \propto |F_{hkl}|^2 \tag{2.7}$$

The structure factor F_{hkl} is defined as:

$$F_{hkl\,=}\ \sum_j f_j exp[2\pi i(hx_j + ky_j + lz_j] \tag{2.8}$$

where the sum runs over all atoms in a particular (h, k, l) plane, f_j is the atomic scattering factor of the atom j, and x_j, y_j, and z_j are the coordinates of the j^{th} atom. The atomic scattering factor f_j is affected by the scattering ability of the atoms, the wavelength λ and the Bragg angle θ. In addition, the width of a diffraction peak can be used to estimate the average crystallite size, L, with smaller crystallite sizes showing broader peaks. This relationship is given by the Scherrer equation:

$$L = \frac{K\lambda}{\beta\cos\theta} \tag{2.9}$$

where K is the Scherrer constant, depending on the shape of the particle (~ 0.9) and β is the full width half maximum of the peak. Notably, peak broadening can also result from other factors, including instrumental broadening (from finite beam divergence and imperfect monochromator) and sample broadening (from lattice strain that can be induced by lattice distortion and stacking faults). The broadening from strain effects is often more pronounced at higher Bragg angles, while the crystallite size contribution is more significant at lower angles.

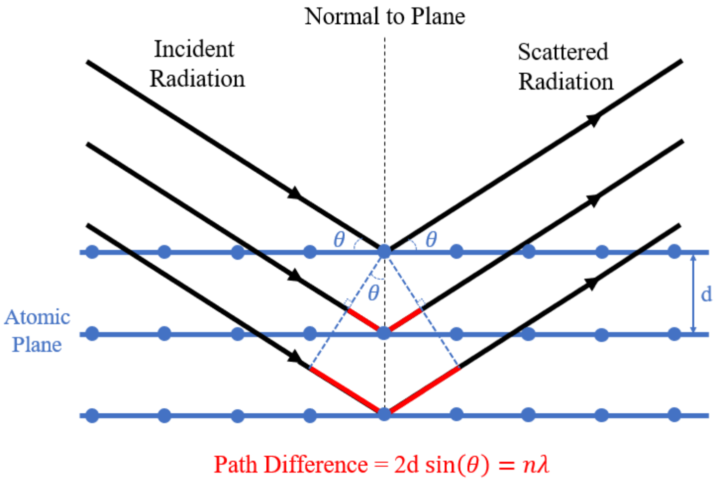

Figure 2.2: Schematic of Bragg's Law illustrating the relationship between interplanar spacing (d) with diffraction angle (θ) and the wavelength (λ) of the X-rays.

X-ray Sources

The X-ray diffraction experiment can be performed using either a laboratory-based diffractometer or a synchrotron radiation source. In lab setups, X-rays are generated by bombarding a metal anode (typically Cu, but also Ag or Co) with high-energy electrons. The resulting X-ray beam is then filtered by monochromators to isolate the most intense Cu $K_{\alpha 1}$ radiation ($\lambda = 1.5405$ Å), arising from the $2\,p_{3/2} \rightarrow 1\,s$ transition. Additional Cu K_{β} lines from other transitions can be effectively removed by using Ni foil.

Synchrotron-based radiation provides significantly higher intensity and highly collimated X-ray beams with tunable wavelength, enabling diffraction data to be collected with superior signal intensity in a short measuring time. Synchrotron X-rays are generated by accelerating electrons to near the speed of light and steering their trajectory by a complex array of magnets, including bending magnets and insertion devices (such as undulators or wigglers). This makes electrons undergo oscillating motion, leading them to emit X-ray radiation as they are forced to change direction. The X-rays are then directed to the beamline, where they are monochromated and collimated before being focused onto the sample. Unlike laboratory XRD, which typically operates in reflection mode, synchrotron XRD is commonly conducted in transmission mode using Debye–Scherrer geometry. In this setup, the X-ray beam remains stationary while the detector is scanned in 2θ.

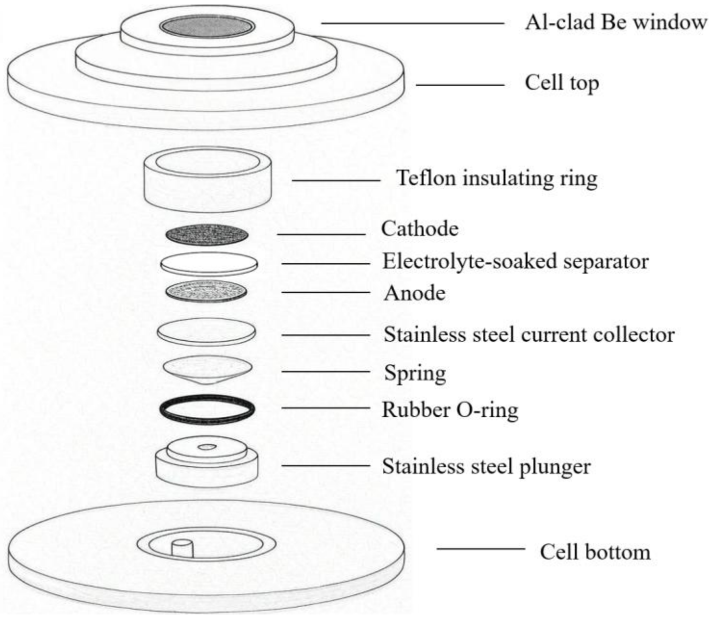

Figure 2.3: Schematic of the *operando* XRD cell used in this thesis for liquid cell systems. The cell was designed and provided by Rigaku.

Operando Experiments

Operando XRD experiments can be performed using both laboratory instruments and synchrotron sources, but require well-sealed cells equipped with X-ray transparent windows to allow the beam to penetrate the sample and reach the detector. Typically, materials like glassy carbon, beryllium metal, silicon nitride, and acetal with appropriate thickness can be applied as a cell window, due to their limited absorption of X-rays. These materials also show good mechanical strength and high chemical stability, ensuring proper cell cycling. In this thesis, two *operando* cell designs are applied, one for liquid cells (Figure 2.3) and the other for all-solid-state cells, tailored to accommodate differences in X-ray energy, experimental geometry and electrochemical system.

2.3.2 Neutron Diffraction

Neutron diffraction (ND) serves as a complementary technique to XRD for investigating both crystal structure and magnetic properties. Unlike X-rays, which interact with electron clouds, neutrons interact primarily with atomic nuclei.[21, 22] This results in their unique scattering characteristics, where the neutron coherent scattering length varies erratically with atomic number and even between isotopes. As a result, ND is particularly advantageous for detecting light elements such as Li, and distinguishing between atoms with similar electron numbers (like Co and Ni) and between isotypes of the same element (such as Ti^{46} and Ti^{48}). Another key benefit of ND is its minimal beam damage, as neutrons interact weakly with matter. However, this also means that relatively large sample quantities (normally > 1g) are required to achieve sufficient signal intensity in ND experiments.

Neutrons can be generated either by fission reaction in reactors or by spallation sources. In this thesis, all the neutron diffraction data were collected using spallation sources, where high-energy proton pulses impinge on the nuclei in a heavy metal target, producing pulses of neutrons. To fully utilize these discrete bursts of neutrons, ND measurements commonly employ a time-of-flight (TOF) diffractometer rather than selecting a specific wavelength using a monochromator.

The TOF is defined as the duration (usually in microseconds or milliseconds) between the moment a neutron is emitted from the source and the moment it is detected after interacting with the sample. In a TOF diffractometer, multiple banks of detectors are positioned at different scattering angles around the sample to record the arrival time of neutrons, enabling the measurement of neutron wavelengths. According to the de Broglie relation and Bragg’s Law, the spacing between adjacent atomic planes in the crystal is proportional to the TOF, as shown in Equation 2.10:

$$\lambda = \frac{h}{mv} = \frac{ht}{mL} = 2d_{hkl}\sin(\theta) \tag{2.10}$$

where h is Planck’s constant, m is the neutron mass, v and L are the velocity and the flight path length of the neutron, respectively, and t is the TOF. TOF powder diffraction data is typically presented as intensity versus d-spacing. For direct comparison with diffraction data from different X-ray or neutron sources, diffraction patterns can be converted into intensity versus the scattering vector Q, a wavelength-independent unit, which can be calculated using Equation 2.11:

$$Q = \frac{4\pi \sin\theta}{\lambda} = \frac{2\pi}{d_{hkl}} \tag{2.11}$$

2.3.3 Rietveld Refinement

Rietveld refinement is an analysis method developed to extract detailed crystallographic information from experimental diffraction data, whether obtained by X-ray or neutron sources.[23] It employs a least-squares approach to iteratively adjust a calculated diffraction pattern generated from an initial structural model to achieve the best possible fit with the measured diffraction pattern. The refinement is conducted by adjusting essential refinement parameters of the initial structure, including lattice parameters, site occupancies, atomic positions and thermal displacement parameters. Calculated peak positions, intensities and shapes are then generated and compared to the experimental data to assess the goodness of fit. These variables are then systematically and iteratively adjusted to minimize differences until a satisfactory fit is achieved. In this thesis, all Rietveld refinements were performed using the GSAS-II software suite.[24]

Three primary statistical metrics are used to assess the goodness of fit between the model and the data.[25, 26] The weighted profile factor, R_{wp}, is obtained by summing the squared differences between observed and calculated intensities, weighted by the observed peak intensities, as shown in Equation 2.12. The expected profile factor, R_{exp}, given in Equation 2.13, represents the lowest achievable value for R_{wp} based on the degrees of freedom in the refinement. Lastly, χ^2 in Equation 2.14 indicates how closely the refinement represents the experimental data.

$$R_{wp} = \left(\frac{\sum_i w_i[y_i(obs) - y_i(calc)]^2}{\sum_i w_i[y_i(obs)]^2}\right)^{1/2} \tag{2.12}$$

$$R_{exp} = \left(\frac{N - P + C}{\sum_i w_i[y_i(obs)]^2}\right)^{1/2} \tag{2.13}$$

$$\chi^2 = \frac{R_{wp}^2}{R_{exp}^2} \tag{2.14}$$

where w_i denotes the weighting factor, y_i is the peak intensity, N is the number of observations, P is the number of refined parameters and C is the number of applied constraints in the refinement.

2.4 Short-Range Structural Characterization

2.4.1 X-ray Pair Distribution Function

X-ray pair distribution function (PDF) analysis can be employed to probe the local structure at the atomic scale, regardless of the crystallinity of materials.[21, 27, 28] Unlike long-range and periodic structural features, which produce well-defined Bragg peaks, short-range atomic arrangements, such as local order/disorder, defects and amorphous regions, lead to diffuse scattering and low signals in diffraction patterns. In the PDF experiment, both Bragg and diffuse scattering can be collected as total scattering data. After carefully subtracting background scattering, this data in reciprocal space is transformed into real space by Fourier transform to obtain the Pair Distribution Function, as expressed in Equation 2.15:

$$G(r) = \frac{2}{\pi}\int_{Q_{min}}^{Q_{max}} Q[S(Q) - 1]\sin(Qr)dQ \qquad (2.15)$$

where $G(r)$ is referred to as the PDF, Q is the scattering vector as defined in Equation 2.11, $S(Q)$ is the normalized total scattering intensity, and $[Q_{min}, Q_{max}]$ define the Q range used for the Fourier transform. As an effect of the Fourier transform increasing Q_{max} gives rise to improved resolution, Δr, in real space, as described in Equation 2.16:

$$\Delta r \approx \frac{2\pi}{Q_{max}} \qquad (2.16)$$

The resulting PDF, $G(r)$, represents the distribution of atom-atom pairs as a function of distance r. Various atomic distances correspond directly to the peak positions. Peak intensity is determined by the amount of related atomic pairs and their respective scattering lengths. Peak broadening can arise from atomic displacements and thermal vibrations. In this thesis, to access data from higher Q value and higher resolution Δr, all X-ray PDFs were collected using synchrotron X-ray Sources.

2.4.2 Neutron Pair Distribution Function

PDF can also be obtained using neutron radiation. Combining X-ray and Neutron PDFs can offer a more comprehensive understanding of local atomic structure. As mentioned in Section 2.3.2, unlike X-ray scattering, the neutron scattering length (denoted as b) does not correlate with atomic number Z and can vary significantly, even between isotopes.[29] These characteristics offer neutron PDF access to the local environment of light elements like Li, and elements with similar electron densities but distinct neutron scattering lengths, for example, Fe (b = 9.45 fm) and Mn (b = –3.73 fm). Furthermore, due to the quantum mechanical nature of neutron-nucleus interaction, b values can either be positive or negative. A positive b indicates the scattered waves are in phase with the incident wave, while a negative b suggests an out-of-phase scattering. In contrast, the X-ray scattering factor of atoms is inherently positive, regardless of the phase in scattered waves. Correspondingly, a neutron PDF exhibits both positive and negative peaks due to the variable sign of neutron scattering length b, while X-ray PDF displays only positive peaks. For example, for two adjacent atoms, if one has a positive b value and the other a negative one, their interaction leads to destructive interference, causing a negative peak in the neutron PDF. This characteristic might be useful when two atomic pairs exist at similar distances: neutron PDF data may reveal one positive and one negative peak, whereas X-ray PDF data might show an overlapping positive peak. This distinction allows for more accurate assignments of atomic pairs in complex structures. In this thesis, neutron and X-ray PDFs were both collected for the studied samples to investigate the evolution of local structure in-depth. Joint refinements were conducted using the PDFgui software.[30]

2.5 Electrochemical Methods

2.5.1 Electrode Preparation

Once the cathode materials were synthesized, they were mixed and ground with conductive carbon powder and a polymer binder to form an electrode film for electrochemical tests. The added carbon additives (usually 10 wt%) bridge between cathode particles and offer more conductive pathways to transport electrons from the cathode particles to the current collector. The added polymer binder (usually 10 wt%), typically Polytetrafluorethylene (PTFE) or Polyvinylidene fluoride (PVDF), contains long chains that bind the separated cathode and carbon powders into a cohesive composite film. The mixing process can be performed using either a dry method, with a pestle and mortar, or a wet method, by dispersing the components into a uniform slurry using a solvent, such as N-Methyl-2-pyrrolidone (NMP). The slurry is then cast onto a current collector and dried to remove the solvent. PTFE is commonly used in the dry process, while PVDF is typically employed in the wet method.

In both approaches, the resulting electrode film is calendared to improve particle contact and film uniformity. Finally, the electrode film is cut to the desired size and weighed for subsequent experiments. In this thesis, all electrodes were prepared via the dry process inside an argon-filled glovebox to prevent sulfide from exposure to air and moisture. Most of the *ex situ* characterizations can be performed with the electrode film after electrochemical tests.

2.5.2 Coin Cell Assembly

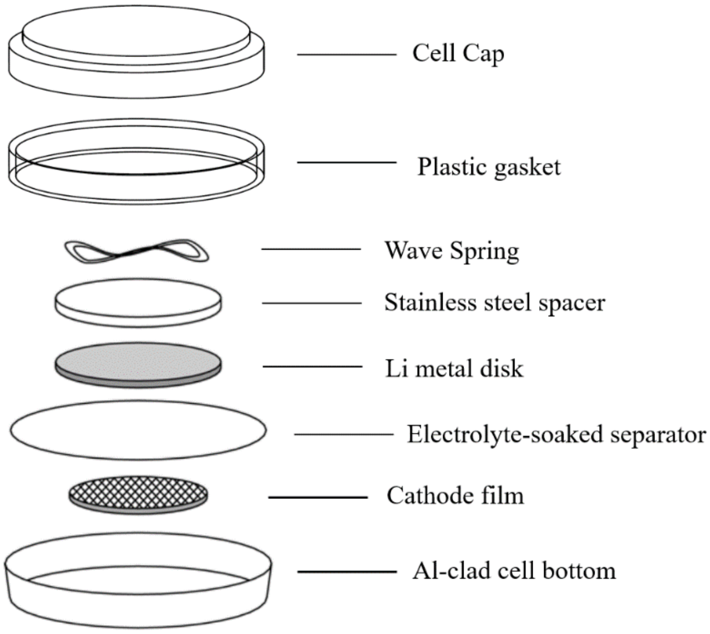

Figure 2.4: Schematic illustrating construction and components of a coin cell.

On the laboratory scale, coin cells are ideal for testing cathode materials in liquid electrolyte systems, as they are easy to assemble and require only a small amount of cathode material (usually 10 – 20 mg per cell).[31] Figure 2.4 illustrates the key components and how they are stacked to assemble a coin cell. The outer cases of the coin cell consist of a stainless-steel base and cap, which serve as current collectors and are electrically insulated from each other by a plastic ring gasket. Inside the cell, the cathode film is paired with an anode (typically a thin disk of Li metal) and separated by a glass fiber separator soaked with an ionically conductive electrolyte. This electrolyte typically consists of Li salts such as $LiPF_6$ dissolved in organic solvents like ethylene carbonate (EC) and dimethyl carbonate (DMC). A stainless-steel spacer and a spring are also included to ensure sufficient internal electrical contact and good electrolyte wetting. After all components are stacked in the order shown in Figure

2.4, the cell is hermetically sealed using a mechanical crimper. The entire assembly process is carried out in an argon-filled glovebox to prevent air and moisture exposure.

2.5.3 Solid-state Cell Assembly

To evaluate cathode performance in the ASSBs system, the liquid electrolyte is replaced with a solid electrolyte. This shift replaces solid-liquid interfaces with solid-solid interfaces, which can result in restricted kinetics such as sluggish ionic transport between cathode and solid-state electrolyte particles. To achieve sufficient inter-particle contact and enable efficient charge carrier transport, ASSBs require assembly under very high pressures (often > 100 MPa).[32] For this reason, electrochemical cell holders made of Polyether Ether Ketone (PEEK) are widely used for testing ASSBs in laboratories, due to their exceptional chemical resistance, mechanical strength and electrical insulation properties. As illustrated in Figure 2.5, the composite cathode, solid electrolyte and anode material are cold-pressed and assembled within the PEEK mould layer by layer using a hydraulic press. The composite cathode typically contains 70 – 80 wt% cathode materials, 20 – 30 wt% solid electrolyte, and 3 – 5 wt% conductive carbon.[33] The incorporated solid electrolyte offers more Li^+ transport pathways between particles, while the carbon additive improves electronic conductivity, collectively ensuring proper cell operation. For the central solid electrolyte layer, it serves as both an ionic conductor and a physical separator between electrodes. Lastly, a Li-In alloy with a composition close to $Li_{0.5}In$ is commonly employed as an anode, since it is less reductive than pure Li (0.6V vs Li/Li^+), offering improved interface stability.[34] This alloy is formed *in situ* by pressing appropriate amounts of lithium and indium foils together. Once the three-layer cell is put on top of each other, a desired pressure can be applied to the PEEK cell through stainless steel plungers to ensure intimate particle contact. In this thesis, all assembly steps were conducted inside an Ar-filled glovebox to prevent sulfide degradation.

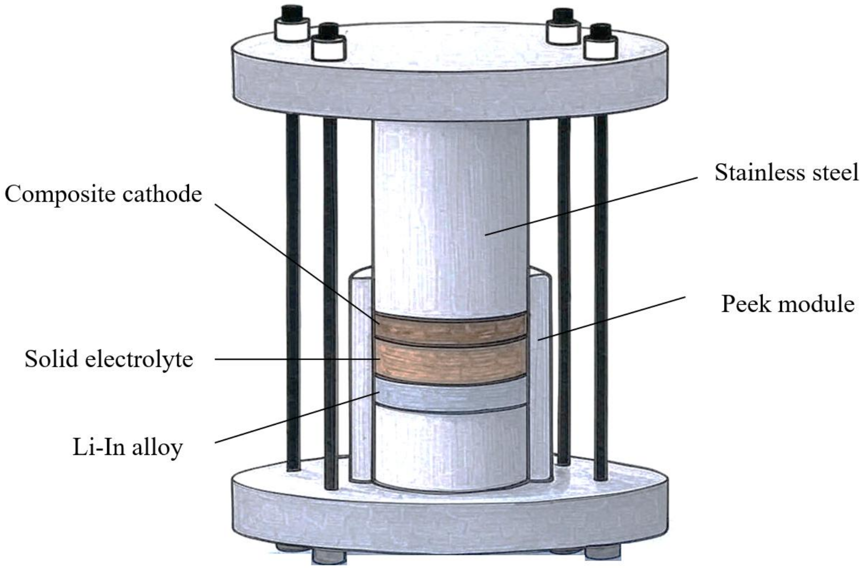

Figure 2.5: Schematic of an all-solid-state cell used in this thesis.

2.5.4 Cell Cycling

Cell cycling is the most fundamental method to access critical metrics in battery research, such as capacity, energy density, coulombic efficiency and cyclability. There are two primary cell cycling protocols, galvanostatic cycling and potentiostatic cycling. The former is the most common method, where the cell is charged and discharged at a constant current, while the voltage is monitored within the preset cutoffs. The constant current here can be determined in one of two ways: either calculated based on per unit mass or area of cathode (mA g^{-1} or mA cm^{-2}); or as a C-rate.[35] C-rate is defined as the current divided by the capacity of the cathode, and it is normally used in commercial cathodes with well-known capacity. A 1C rate means the current is set to achieve full charge or discharge state by one hour. This thesis aims to study the fundamental behaviors of some novel sulfide cathodes without a well-defined 1C current, so the current unit is selected as mA g^{-1} (in liquid cells) or mA cm^{-2} (in ASSBs). In addition, to ensure the electrochemical processes occur close to equilibrium conditions, a low current rate (usually 10 – 20 mA g^{-1} or 0.5 – 1 mA cm^{-2}) is applied during cycling. Cells can also be cycled using the other protocol, potentiostatic cycling, where a constant voltage is supplied and current is measured. This is particularly helpful for achieving a near-complete charge and reaching an equilibrium state at a specific voltage. In electronics and electric vehicles, a regime combining both cycling methods, known as CC-CV cycling (constant current-constant voltage), is commonly used. The battery is first charged to the upper cut-off voltage, and then it keeps charging by holding at this potential, until the current response decays to a certain fraction (like 1/20 – 1/10) of that used in the CC step. It improves capacity utilization without overcharging, alleviating capacity loss caused by overpotential in fast charging. Alternatively, other cycling methods, such as pulse charge and discharge, and multi-rate cycling, are utilized on different occasions.

2.5.5 Direct Current Polarization Measurements

The direct current (DC) polarization measurement is widely used to evaluate the ionic and electronic conductivities of materials.[36] The technique involves applying a constant electrical bias (voltage or current) across a sample and monitoring the resulting current (I) – voltage (V) response as a function of time.

The measurement is typically performed in a sandwich-type cell, where the material under study is placed between two electrodes. For determining electronic conductivity, ion-blocking electrodes (e.g., stainless steel or carbon paper) are employed to permit electronic transport while impeding ionic movement. Conversely, when evaluating ionic conductivity, electronically blocking electrodes (e.g., solid-state electrolytes) are used to isolate the ionic contribution.

In this thesis, DC polarization is applied to determine the electronic conductivity of sulfide-based materials. The samples were sandwiched between two stainless steel electrodes. A small DC voltage V (typically < 0.1 V) was applied, with the steady-state current I arising solely from electronic carriers once mobile ions had been polarized and the ionic flux had vanished. The electronic conductivity σ_e can be calculated using:

$$\sigma_e = d\frac{I}{A\times V} \tag{2.17}$$

where A is the electrode-sample contact area and d is sample thickness.

2.6 Spectroscopic Characterization

2.6.1 X-ray Photoelectron Spectroscopy

X-ray photoelectron spectroscopy (XPS) is a quantitative technique used to identify the composition, chemical state and electronic state at the topmost layer of the sample, typically within 10 nm.[37] In the XPS experiment, the sample is first irradiated with monochromatic X-rays (typically Al K_α).

When the X-ray photon energy exceeds the binding energy (E_b) of core-level electrons in the probed atoms within the sample, these electrons are excited and emitted from the sample surface. To minimize electron scattering during their transit to the analyzer and to prevent surface contamination, measurements are conducted under ultra-high vacuum (UHV) conditions, typically in the range of $10^{-9} – 10^{-10}$ mbar. Subsequently, the quantity of emitted electrons and their kinetic energies (E_k) are measured, enabling access to the binding energy (E_b) of emitted electrons using the photoelectric effect equation expressed as:

$$E_b = hv - E_k - \emptyset \tag{2.18}$$

where h is Planck's constant, v is the frequency of incident X-rays, and $\emptyset$ is the work function of the spectrometer, a value barely adjusted in practice. The obtained E_b value is a characteristic fingerprint for each atom. It is strongly affected by their oxidation state, chemical bonding, and environment, yet is independent of the X-ray source used. Notably, when measuring insulating or poorly conductive materials, charging effects can occur, leading to peak shifts. To minimize this, samples can be mixed with conductive compounds like carbon or mounted on a conductive substrate to facilitate charge dissipation. In cathode materials research, the XPS technique is widely employed to study surface composition and interfacial reactions between the cathode and electrolyte.[38]

2.6.2 X-ray Absorption Spectroscopy

X-ray absorption spectroscopy (XAS) is an indispensable element-specific technique used for investigating the oxidation state, electronic structure and local chemical environment of atoms.[39] XAS involves tuning the incident photon energy, typically using a crystalline monochromator, to excite core electrons from filled orbitals to empty states. This excitation process follows selection rules, allowing transitions between orbitals where the angular momentum changes by ± 1, corresponding to adjacent shells such as $s \rightarrow p$, $p \rightarrow d$, $d \rightarrow f$. According to the principal quantum numbers (n) of the excited core electron, the absorption edges are then classified as K-, L-, and M-edges, corresponding to n = 1, 2, and 3, respectively, as shown in Figure 2.6.

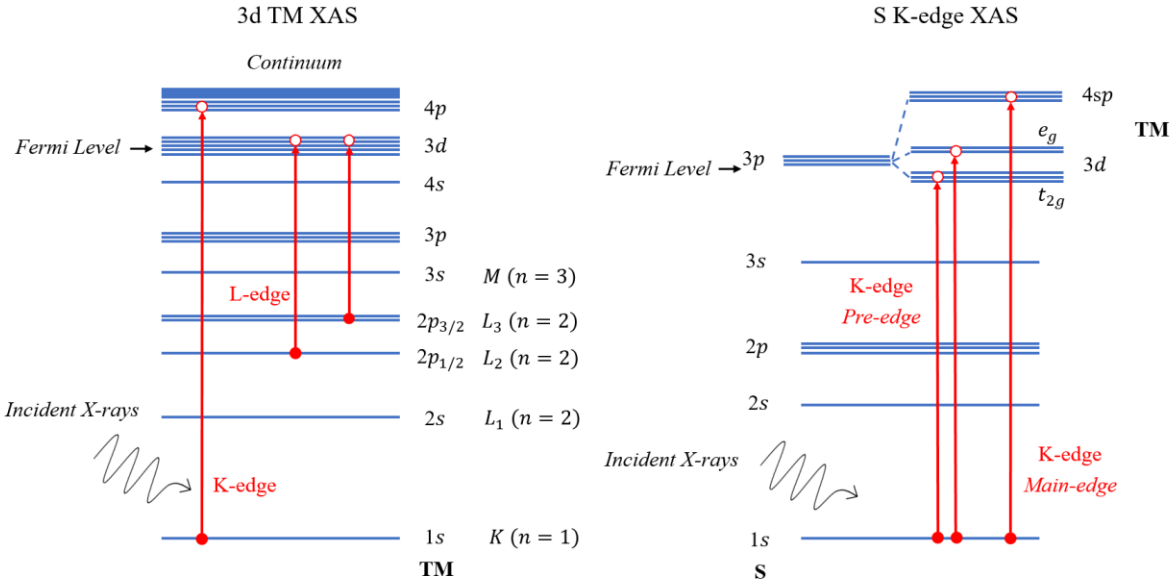

Figure 2.6: Schematic showing the XAS transitions relevant to this thesis, including the *3d* TM K- and L-edges and S K-edge.

The required X-ray energy varies depending on the element and the specific edge being probed. In this thesis, the primary focus is on the Mn and Ti K-edges, S, Cl, and P K-edges, along with Mn and Ti L-edges, which correspond to the hard (4 – 10 keV), tender (2 – 4 keV), and soft (100 – 1000 eV) X-ray regimes, respectively.[40] The energy of incident X-rays also determines their penetration depth into the sample. Hard X-rays, due to their greater penetration depth, are collected in transmission mode XAS, where the X-rays pass through the entire sample, providing information representative of the bulk material. In contrast, tender and soft XAS spectra are normally collected in fluorescence yield mode in a reflection geometry, which is inherently less bulk sensitive than transmission mode, as a great number of measured photons are contributed by the surface region. In both transmission and fluorescence modes, the absorption coefficient, μ, is measured and plotted as a function of energy, as shown in Figure 2.7. In transmission mode, μ is derived using the Beer-Lambert Law:

$$I_t = I_0 e^{-\mu x} \tag{2.19}$$

where I_0 and I_t are the measured intensities of the incident and transmitted beam, respectively, and x is the sample thickness. This relationship indicates that the transmitted beam intensity decays exponentially with increasing sample depth, and the absorption coefficient μ is proportional to $In\ (I_0/I_t)$. In fluorescence mode, μ is approximately proportional to I_f/I_0, where I_f is the intensity of the emitted fluorescence signal. When the incident X-ray energy is sufficiently high to excite electron transitions between orbitals, the absorption coefficient increases sharply, producing a characteristic absorption edge. The position and shape of this edge provide insights into the valence state of the absorbing atoms, with lower edge energies generally corresponding to more reduced systems.

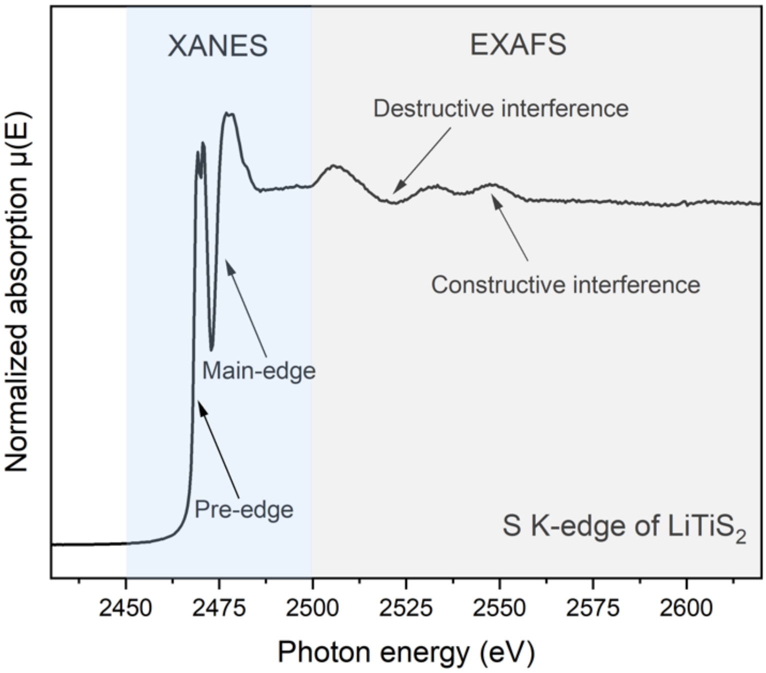

Figure 2.7: Normalized S K-edge XAS spectrum of $LiTiS_2$ with distinct spectral features labelled.

X-ray Absorption Near Edge Structure

The K-edge absorption for TM and S arises from the excitation of core $1s$ electrons to unoccupied $4p$ orbitals. The region around $\pm$ 50 eV of the main edge is known as X-ray absorption near-edge structure (XANES), as illustrated in Figure 2.7. In some TM K-edge XANES spectra, a pre-edge feature appears just before the main absorption edge. This feature is typically attributed to the dipole-forbidden $1s \rightarrow 3d$ transition, which is enabled by the hybridization between $3d$ and $4p$ orbitals. For S K-edge, it is strongly affected by orbital mixing with coordinated TM ions. The pre-edge arises from $1s \longrightarrow$ S $3p/$TM $3d$ transitions, while the main edge corresponds to 1s $\longrightarrow$ S $3p/$TM $4\,sp$ transitions. The shape, intensity, along with energy position of pre-edge and main edge in the XANES spectrum together offer valuable insights into the oxidation state, electronic structure and local environment of the probed atoms.[39] In practice, TM K-edge XAS are typically collected in air, while S, Cl and P K-edges, within tender X-ray regions, are measured using a He-filled environment. He gas attenuates incident X-rays significantly less than air, ensuring high-quality spectra collected in the tender X-ray regime.

Extended X-ray Absorption Fine Structure

Beyond the XANES region, the absorption profile shows oscillations extending up to ~ 1000 eV above the absorption edge, which is known as extended X-ray absorption fine structure (EXAFS).[41] At these energies, the incident X-ray has sufficient energy to excite the core 1s electrons into the continuum as free photoelectrons. These photoelectrons are subsequently scattered by adjacent atoms, causing interference between the outgoing photoelectrons and backscattered photoelectrons from absorbing atoms.[42] Constructive interferences increase the absorption coefficient, while destructive interferences reduce it, leading to characteristic oscillations in the EXAFS region (Figure 2.7). Therefore, these oscillations encode detailed information about the interatomic distances and local coordination numbers.[43, 44]

Before accessing the above structural information, data reduction must be performed.[45] The raw XAS spectrum is first normalized by fitting a pre-edge baseline (set to 0) and a post-edge line (set to 1) through the EXAFS region. Next, the background is subtracted to extract the oscillations, which are shown in k-space, where k represents the wavevector of the photoelectron. The resulting k-space data is typically multiplied by the k^2 or k^3 function to compensate for the natural damping of oscillations at higher energies. A window function is then applied to define the desired k range, effectively filtering out contributions from near-edge regions at low k range and noisy signals at high k. Finally, the processed k-space data is Fourier transformed into the real space (r-space), yielding a radial distribution function that displays peaks as a function of the radial distance r. Each peak corresponds to different adjacent atoms around the absorbing atom. The position of each peak (subject to a phase shift) reflects the interatomic distance, while the intensity provides information on the coordination number and scattering amplitude of neighboring atoms.

To achieve higher spatial resolution (Δr) in r space, it is essential to measure EXAFS over a wider k-range, which corresponds to collecting data at higher photon energies beyond the absorption edge. The spatial resolution is approximately given by Equation 2.20:

$$\Delta r \approx \frac{\pi}{\Delta k} \tag{2.20}$$

where Δk is the range of k-space included in the Fourier transform. For tender XAS, like S K-edge EXAFS, the usable energy region typically extends to ~ 500 – 700 eV above the edge, constrained by pronounced absorption of tender X-rays in both the sample and surrounding media.

Soft X-ray Absorption Spectroscopy

Soft X-ray absorption spectroscopy (sXAS) is employed to study the K-edges of light elements (such as C, N, O and S) and the L-edges of TM (such as Ti, Ni, Mn, Co, Fe).[40] Due to the intrinsically low energy of soft X-rays, sXAS measurements require UHV conditions to minimize substantial X-ray absorption and scattering caused by air. Fluorescence Yield is commonly used in sXAS, involving photon emission of a range of different photon energies. Summing all emitted photons gives rise to total fluorescence yield (TFY) data while integrating photons within an energy range produces partial fluorescence yield (PFY) data. PFY mode is particularly advantageous when two absorption edges overlap in TFY data. For example, measuring the S L-edge in a sulfide electrode using TFY mode is challenging, as the carbon added into the electrode film contributes an overwhelming background through the second-order harmonic of C K-edge (~ 140 eV), right below the S L-edge signal (~ 160 eV).[46] PFY mode helps isolate the S L-edge signal by selectively integrating the relevant fluorescence emissions, thereby enabling spectral interpretation. In addition to fluorescence yield with ~ 100 nm probing depth, the electrons emitted from the topmost ~ 10 nm of the samples can also be measured, producing a surface-sensitive total electron yield (TEY). As such, TEY data is especially valuable for studying surface features and surface reactions in cathode materials.

In this thesis, TM L-edges arising from $2p \rightarrow 3d$ electronic transitions are investigated. Due to spin-orbit coupling, which results from the interaction between the electron spin ($s = \pm 1/2$) and orbital angular momentum ($l = 1$ for $2p$ orbitals), the $2p$ orbitals split into two distinct, non-degenerate states: $2p_{1/2}$ and $2p_{3/2}$, associated with total angular momentum quantum numbers $j = 1/2$ and 3/2, respectively. As a result, the TM L-edge typically exhibit two edge features known as L_2 and L_3 edges.[47]

2.6.3 Resonant Inelastic X-ray Scattering

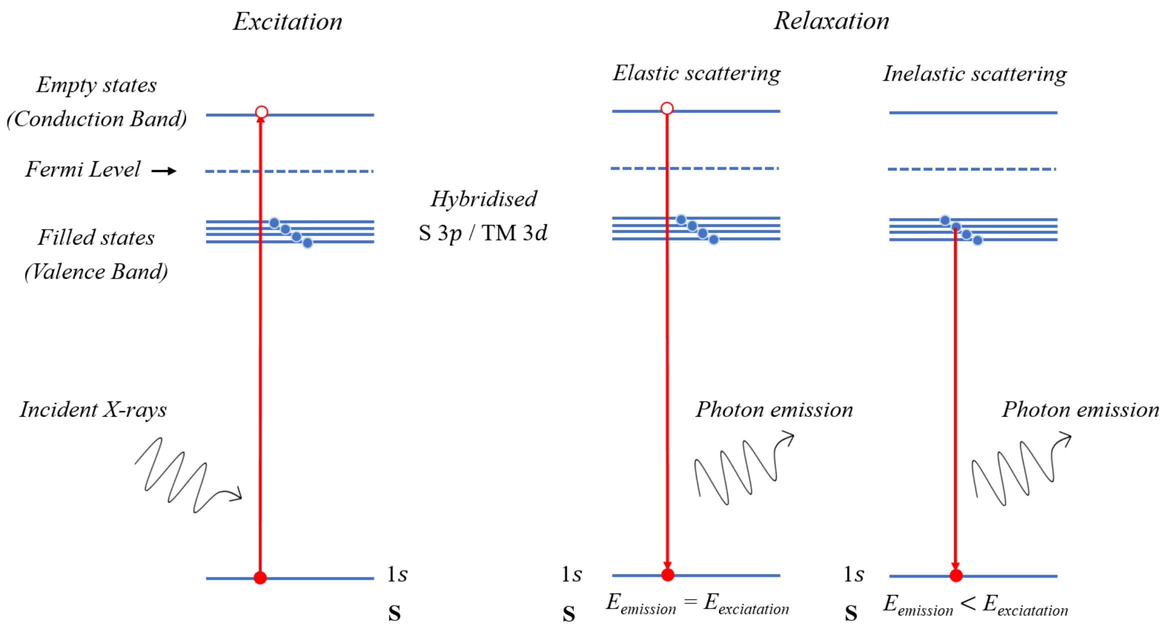

Figure 2.8: Schematic showing the key electronic transition processes involved in RIXS at the S K-pre-edge, with photon emission via elastic and inelastic scattering.

Resonant inelastic X-ray scattering (RIXS) is an element-specific technique that combines resonant X-ray absorption with X-ray emission spectroscopy.[48] In the RIXS experiment, a core-level electron is first excited to an unoccupied conduction band. Subsequently, the excited electron, or an electron from a filled valence state near the Fermi level, decays to fill the core hole, leading to either elastic or inelastic photon emission, as illustrated in Figure 2.8. The emitted photons during relaxation are then resolved by emission energy, rather than measuring photons with the same energy as the incoming beam (XAS with transmission mode) or all photons regardless of emission energy (XAS with TFY mode). The resulting emission spectrum at a given excitation energy is typically plotted as a function of energy loss relative to the incident energy, as shown before in Figure 1.7. The RIXS map can also be plotted by stacking obtained spectra across a range of excitation energies. In cathode materials research, RIXS at the Mn L-edge, Fe L-edge and O K-edge have been used to probe the local electronic structure and investigate the redox processes.[49-53] In particular, O K-edge RIXS has become a pivotal technique for studying O-redox behavior in Li-rich oxide cathodes.[53] Recent advances in synchrotron brightness and grating fabrication have significantly improved the energy resolution of O K-edge RIXS, now reaching ~ 30 meV at beamlines like I21 at the Diamond Light Source. Such advances in resolution have allowed for the resolution of phonon features associated with fundamental vibrational modes of oxidized oxygen species in the charged O-redox cathodes for the first time.[54]

In this thesis, S K-edge RIXS has been applied for the first time to study sulfide cathodes. Currently, the energy resolution at the S K-edge RIXS is limited to around 250 meV, leading to difficulties in fully resolving potential vibrational progressions arising from oxidized sulfur species.

2.6.4 Inelastic Neutron Scattering

Inelastic neutron scattering (INS) is a bulk-sensitive technique used to probe a range of different physical phenomena, including atomic diffusion or hopping, molecular vibrations, and magnetic or other quantum excitations.[55] In the INS experiment, a neutron beam interacts with the sample. During this process, both the energy and momentum of the neutron radiation and the internal state of the sample are changed by creating or annihilating excitations within the materials. The energy and momentum of the scattered neutrons are then recorded and analyzed to determine the energy transfer (ΔE) and momentum transfer (ΔQ) before a scattering function is constructed, providing a detailed picture of the vibrational density of states and phonon dispersion relations.

In this thesis, INS characterization is applied to investigate phonon modes and molecular vibrations within the sulfide cathodes. Compared to the most common light scattering techniques, Raman and infrared spectroscopy, INS spectra are not restricted to optical selection rules and the center of the Brillouin zone.[56] All vibrations are active and, in principle, measurable. Furthermore, signal intensities in INS results are proportional to the concentration of elements in the sample and their cross sections, enabling direct and accurate analytical calculation. However, due to the inherently weak interaction between neutrons and nuclei, relatively large sample amounts of typically several grams are required.

2.7 References

1. West, A. R., *Solid state chemistry and its applications*. John Wiley & Sons: 2022.

2. Murphy, D. W.; Trumbore, F. A., The Chemistry of TiS_3 and $NbSe_3$ Cathodes. *J. Electrochem. Soc.* **1976,** *123* (7), 960.

3. de la Llave, E. *et al.* Improving Energy Density and Structural Stability of Manganese Oxide Cathodes for Na-Ion Batteries by Structural Lithium Substitution. *Chem. Mater.* **2016,** *28* (24), 9064-9076.

4. Gao, A. *et al.* Topologically protected oxygen redox in a layered manganese oxide cathode for sustainable batteries. *Nat. Sustain.* **2021,** *5* (3), 214-224.

5. Saha, S. Exploration of ionic conductors and Li-rich sulfides for all-solid-state batteries. Sorbonne Université, **2020**.

6. Boldyrev, V. V., Mechanochemistry and mechanical activation of solids. *Solid State Ionics* **1993,** *63-65*, 537-543.

7. Takacs, L., Solid state reactions induced by ball milling. *Hyperfine Interact.* **1998,** *111* (1), 245-250.

8. Driscoll, L. L. *et al.* Under pressure: offering fundamental insight into structural changes on ball milling battery materials. *Energy Environ. Sci.* **2023,** *16* (11), 5196-5209.

9. Augustyn, V.; Manthiram, A., Effects of Chemical versus Electrochemical Delithiation on the Oxygen Evolution Reaction Activity of Nickel-Rich Layered $LiMO_2$. *J. Phys. Chem. Lett.* **2015,** *6* (19), 3787-3791.

10. Leube, B. T. *et al.* Activation of anionic redox in d0 transition metal chalcogenides by anion doping. *Nat. Commun.* **2021,** *12* (1), 5485.

11. Pennycook, S. J.; Nellist, P. D., *Scanning transmission electron microscopy: imaging and analysis*. Springer Science & Business Media: 2011.

12. Huang, R.; Ikuhara, Y., STEM characterization for lithium-ion battery cathode materials. *Curr. Opin. Solid State Mater. Sci.* **2012,** *16* (1), 31-38.

13. Lipson, A.; Lipson, S. G.; Lipson, H., *Optical physics*. Cambridge University Press: 2010.

14. Goldstein, J., Scanning electron microscopy and X-ray microanalysis: a text for biologists, materials scientists, and geologists. Plenum Press, **1992**.

15. Newbury, D. E.; Ritchie, N. W. M., Is Scanning Electron Microscopy/Energy Dispersive X-ray Spectrometry (SEM/EDS) Quantitative? *Scanning* **2013,** *35* (3), 141-168.

16. Zhong, X. *et al.* Comparing Xe^+ pFIB and Ga^+ FIB for TEM sample preparation of Al alloys: Minimising FIB-induced artefacts. *J. Microsc.* **2021,** *282* (2), 101-112.

17. Withers, P. J. *et al.* X-ray computed tomography. *Nat. Rev. Methods Primers* **2021,** *1* (1),

18. Pietsch, P.; Wood, V., X-Ray Tomography for Lithium Ion Battery Research: A Practical Guide. *Annu. Rev. Mater. Res.* **2017,** *47*, 451-479.

19. Klug, H. P.; Alexander, L. E., *X-ray diffraction procedures: for polycrystalline and amorphous materials*. 2nd, illustrated ed., *Wiley,* **1974**.

20. Bragg, W. H.; Bragg, W. L., The reflection of X-rays by crystals. *Proc. R. Soc. Lond. A* **1913,** *88* (605), 428-438.

21. Egami, T.; Billinge, S. J., *Underneath the Bragg peaks: structural analysis of complex materials*. Newnes: 2012; Vol. 16.

22. Copley, J. R., *NIST recommended practice guide: the fundamentals of neutron powder diffraction. NIST,* 2001, 960-2.

23. Rietveld, H. M., A profile refinement method for nuclear and magnetic structures. *J. Appl. Cryst.* **1969,** *2* (2), 65-71.

24. Toby, B. H.; Von Dreele, R. B., GSAS-II: the genesis of a modern open-source all purpose crystallography software package. *J. Appl. Cryst.* **2013,** *46* (2), 544-549.

25. McCusker, L. B.; Von Dreele, R. B.; Cox, D. E.; Louer, D.; Scardi, P., Rietveld refinement guidelines. *J. Appl. Cryst.* **1999,** *32* (1), 36-50.

26. Toby, B. H., R factors in Rietveld analysis: How good is good enough? *Powder Diffr.* **2006,** *21* (1), 67-70.

27. Chapman, K. W., Emerging *operando* and X-ray pair distribution function methods for energy materials development. *MRS Bull.* **2016,** *41* (3), 231-240.

28. Billinge, S. J. L., The rise of the X-ray atomic pair distribution function method: a series of fortunate events. *Philos. Trans. R. Soc. A: Math. Phys. Eng. Sci.* **2019,** *377* (2147), 20180413.

29. Billinge, S. J.; Thorpe, M., *Local structure from diffraction*. Springer Science & Business Media: 2006.

30. Farrow, C. L. *et al.* PDFfit2 and PDFgui: computer programs for studying nanostructure in crystals. *J. Phys.: Condens. Matter* **2007,** *19* (33), 335219.

31. Marks, T.; *et al.* A Guide to Li-Ion Coin-Cell Electrode Making for Academic Researchers. *J. Electrochem. Soc.* **2011,** *158* (1), A51.

32. Puls, S. *et al.* Benchmarking the reproducibility of all-solid-state battery cell performance. *Nat. Energy* **2024,** *9* (10), 1310-1320.

33. Minnmann, P. *et al.* Designing Cathodes and Cathode Active Materials for Solid-State Batteries. *Adv. Energy Mater.* **2022,** *12* (35), 2201425.

34. Santhosha, A. L. *et al.* The Indium−Lithium Electrode in Solid-State Lithium-Ion Batteries: Phase Formation, Redox Potentials, and Interface Stability. *Batteries Supercaps* **2019,** *2* (6), 524-529.

35. Lin, Z. *et al.* Aligning academia and industry for unified battery performance metrics. *Nat. Commun.* **2018,** *9* (1), 5262.

36. Maier, J., *Physical chemistry of ionic materials: ions and electrons in solids*. John Wiley & Sons: 2023.

37. Chastain, J.; King Jr, R. C., Handbook of X-ray photoelectron spectroscopy. *Perkin-Elmer Corp.* **1992,** *40* (221), 25.

38. Shutthanandan, V. *et al.* Applications of XPS in the characterization of Battery materials. *J. Electron Spectrosc. Relat. Phenom.* **2019,** *231*, 2-10.

39. Henderson, G. S.; De Groot, F. M.; Moulton, B. J., X-ray absorption near-edge structure (XANES) spectroscopy. *Rev. Mineral. Geochem.* **2014,** *78* (1), 75-138.

40. Lin, F. *et al.* Synchrotron X-ray Analytical Techniques for Studying Materials Electrochemistry in Rechargeable Batteries. *Chem. Rev.* **2017,** *117* (21), 13123-13186.

41. Newville, M., Fundamentals of XAFS. *Rev. Mineral. Geochem.* **2014,** *78* (1), 33-74.

42. Stern, E. A., Theory of the extended X-ray-absorption fine structure. *Phys. Rev. B* **1974,** *10* (8), 3027-3037.

43. Lee, P. A. *et al.* Extended X-ray absorption fine structure–its strengths and limitations as a structural tool. *Rev. Mod. Phys.* **1981,** *53* (4), 769-806.

44. Koningsberger, D. C.; Prins, R., X-ray absorption: principles, applications, techniques of EXAFS, SEXAFS and XANES. **1987**.

45. Teo, B. K., *EXAFS: basic principles and data analysis*. Springer Science & Business Media: 2012; Vol. 9.

46. Saha, S. *et al.* Exploring the bottlenecks of anionic redox in Li-rich layered sulfides. *Nat. Energy* **2019,** *4* (11), 977-987.

47. de Groot, *et al.* 2p X-ray absorption of 3d transition-metal compounds: An atomic multiplet description including the crystal field. *Phys. Rev. B* **1990,** *42* (9), 5459-5468.

48. Ament, L. J. P. *et al.* Resonant inelastic X-ray scattering studies of elementary excitations. *Rev. Mod. Phys.* **2011,** *83* (2), 705-767.

49. Chiu, C.-C. *et al.* Spectroscopic characterization of electronic structures of ultra-thin single crystal $La_{0.7}Sr_{0.3}MnO_3$. *Sci. Rep.* **2021,** *11* (1), 5250.

50. Abu-Samak, M. *et al.* RIXS, XES and XAS studies for electronic structure of rare earth and alkaline earth modified manganite. *Phys. B: Condens. Matter* **2022,** *628*, 413562.

51. Kaneshita, E.; Tsutsui, K.; Tohyama, T., Spin and orbital characters of excitations in iron arsenide superconductors revealed by simulated resonant inelastic X-ray scattering. *Phys. Rev. B* **2011,** *84* (2), 020511.

52. Hirsbrunner, M. *et al.* Vibrationally-resolved RIXS reveals OH-group formation in oxygen redox active Li-ion battery cathodes. *Phys. Chem. Chem. Phys.* **2024,** *26* (28), 19460-19468.

53. Zhou, D. *et al.* Exploring Anionic Redox Chemistry of Battery Cathodes with Resonant Inelastic X-Ray Scattering. *Adv. Mater.* **2025,** 2508246.

54. House, R. A. *et al.* The role of O_2 in O-redox cathodes for Li-ion batteries. *Nat. Energy* **2021,** *6* (8), 781-789.

55. Hu, Z. *et al.* Inelastic neutron scattering spectrometer and its applications. *Acta Phys. Sin.* **2025,** *74* (1), 012501-1-012501-13.

56. Hudson, B. S., Vibrational spectroscopy using inelastic neutron scattering: Overview and outlook. *Vib. Spectrosc.* **2006,** *42* (1), 25-32.

3

Understanding the S-redox Process in Li-rich Sulfide Cathodes

Contents

3.1 Introduction

Lithium-rich cathodes (i.e. those whereby the alkali metal/transition metal ratio > 1) offer one of the few routes available to increase the energy density of Li-ion batteries.[1, 2] They store more charge than conventional cathodes by invoking redox reactions on the anions. Compared to oxide-based Li-rich cathodes, sulfide-based Li-rich cathodes exhibit significantly reduced voltage hysteresis (~ 90% less than Li-rich oxide analogues), negligible first-cycle capacity loss and mitigated voltage fade.[3, 4] To understand the origin of these improved electrochemical characteristics compared to O-redox cathodes, it is essential to study the process of S-redox and determine the nature of the oxidized S^{2-}

species, which has been proven very challenging. In this chapter, O3-type $Li_{1.2}Ti_{0.8}S_2$ is investigated as a model Li-rich sulfide cathode, which is a direct analogue to the archetypal Li-rich layered oxides $Li_{1.2}TM_{0.8}O_2$ (TM = Ni, Co, Mn).[5-7] Through a suite of spectroscopic and structural characterization techniques, this chapter shows comprehensive direct evidence for the formation of S-S bonds in the form of S_2^{2-} in the bulk upon charging, instead of electron holes on S. These S_2^{2-} dimers are first revealed to be accommodated in vacancy clusters formed by in-plane TM migration, similar to the oxides. In contrast to Li-rich oxides, these defect-like S_2^{2-} dimers are coordinated to adjacent TM ions in the material, resulting in TM-S_2^{2-} coordination, which is absent for trapped molecular O_2 in Li-rich oxides.[6, 8, 9] The presence of the local TM-S_2^{2-} environment offers an explanation for the differing electrochemical characteristics between S- and O-redox chemistry.

3.2 Experimental

General synthesis: $Li_{1.2}Ti_{0.8}S_2$ was synthesized via solid-state reaction using stoichiometric amounts of Li_2S (99.98%, Sigma-Aldrich), TiS_2 (99.5%, Thermo Scientific) and elemental S (99.98%, Sigma-Aldrich). The precursor powders were thoroughly mixed by hand grinding and pelletized in an Ar-filled glove box. The resulting pellets were loaded into graphite crucibles and placed inside quartz tubes, which were then sealed under vacuum (~ 10^{-5} mbar). The sealed tubes were slowly heated to 750 °C over 25 hours, held for 36 hours, and then quenched in air. Air exposure was strictly avoided during the whole process, and the as-prepared samples were always handled in an Ar-filled glovebox. TiS_3 used as a reference compound was prepared similarly by reacting TiS_2 with elemental S (15 wt% excess) in a vacuum-sealed quartz tube at 550 °C for 4 days, using a heating and cooling rate of 1 °C min^{-1}.

Chemical delithiation of $Li_{1.2}Ti_{0.8}S_2$ was employed to prepare large quantities (~ 10g) of $Li_{0.1}Ti_{0.8}S_2$. $Li_{1.2}Ti_{0.8}S_2$ and I_2 (> 99.99%, Alfa Aesar) were mixed in a 2:1 mole ratio, dispersed in anhydrous acetonitrile and stirred at room temperature for 24 hours. The resulting powders were centrifuged, washed three times with anhydrous acetonitrile, and dried under vacuum at 50 °C for 12 hours.

SEM, EDS and STEM: SEM imaging and EDX analysis were performed on a Carl Zeiss Merlin high-resolution field emission gun SEM instrument. ADF-STEM micrographs were obtained using an aberration-corrected JEOL ARM-200F microscope operated at an accelerating voltage of 200 kV. The emission current was 5μA, and the beam current was 35pA. To prevent exposure to air, samples were always transferred using a vacuum transfer holder.

Electrochemistry characterization: Electrodes were prepared by mixing 80 wt% cathode material, 10 wt% acetylene black, and 10 wt% PTFE binder using a mortar and pestle, followed by calendaring to form self-supporting films with a thickness of approximately 100 μm. Electrochemical testing was carried out using CR2032 coin cells assembled in an Ar-filled glovebox with LP30 electrolyte (1 M $LiPF_6$ in a 1:1 volume ratio of ethylene carbonate and dimethyl carbonate), and Li metal disks as the counter electrode. Electrochemical charge-discharge measurements were all performed between 1.8 V and 3.0 V at a current density of 10 mA g^{-1} using a Maccor Series 4000.

X-ray and Neutron total scattering measurements: X-ray powder diffraction and total scattering measurements were conducted on the I15-1 beamline at Diamond Light Source (λ = 0.16167 Å). Neutron total scattering carried out on two sources, including the POLARIS diffractometer (ISIS, UK) and the NOMAD instrument (Oak Ridge National Laboratory, US) in TOF mode. Before conducting these measurements, silica was first measured as an internal calibration standard to obtain the instrumental parameters. The *operando* XRD data were measured using an in-house 9kW Rigaku Lab X-ray diffractometer equipped with a Cu source and a custom-built *operando* cell with an aluminium-coated beryllium window. Neutron and X-ray diffraction were jointly refined using the GSAS-II software.[10] PDFs were obtained from total scattering data using PDFgetX3, followed by co-refinement using PDFgui.[11, 12]

X-ray absorption spectroscopy: Ti and S K-edge XANES and EXAFS measurements were carried out on the B18 beamline at the Diamond Light Source. To collect high-quality EXAFS data, each spectrum was averaged over six scans and processed through energy calibration, background subtraction, and intensity normalization. The k^2-weighted EXAFS were then extracted using Athena over a k-range of 2.5 – 10.5 $Å^{-1}$ for Ti and 2 – 8.5 $Å^{-1}$ for S. Ti L-edge XAS data were collected in partial fluorescence yield mode on the BL27SU beamline at Spring8 in Japan.

3.2 Experimental

Resonant inelastic X-ray scattering: S K-edge RIXS measurements were conducted using the IRIXS instrument at P01 beamline of the PETRA III synchrotron radiation source at DESY. The incident photons (π-polarized) were monochromatized using a four-bounce inline high-resolution monochromator with a bandwidth of 60 meV. Scattered photons (π- and σ-polarized) from the sample were collected at an angle of $2\theta = 90$ degrees using a spherically bent and diced $LiNbO_3$ (110) analyser. This configuration resulted in a total resolution of ~ 250 meV (full width at half maximum), with the resolution varying between 200 and 300 meV across the S K-edge. The applied scattering geometry strongly suppresses the elastic charge (Thomson) scattering, thereby improving sensitivity to low-energy excitations. To prevent air exposure, samples were transferred using a vacuum transfer holder and subsequently pumped down to 10^{-7} mbar. RIXS maps were obtained with 1 eV excitation energy increments over the range of 2468 – 2472.5 eV. All measurements were performed at 20 K to minimize potential beam damage.

Inelastic neutron scattering: The INS spectra were recorded using the TOSCA spectrometer at the ISIS Neutron Source. Approximately 10 g of chemically delithiated sample was enclosed in a 4 × 4 cm^2 aluminium foil sachet, placed in an aluminium can, and then sealed under an inert atmosphere using indium wire. To minimize the thermal motion of the sample, measurements were conducted at 10 K. Data reduction was performed using the MANTID software package.

RMC Profile modelling analysis: Big-box modelling of the experimental PDF data was carried out using the reverse Monte Carlo (RMC) method, implemented in the RMCProfile software.[13, 14] The starting atomic configurations containing $15 \times 3 \times 9$ unit cells with an edge length of ~ 54 Å, and 9720 atoms, were derived from the average structures obtained by combining Rietveld refinement of neutron and X-ray diffraction data using the data2config tool in RMCProfile. RMC refinements were carried out by simultaneously fitting the Bragg and PDF data, allowing Ti-Li_{TM} (Li in the TM layer) and Ti-Li swaps with a probability of 0.05 and 0.02, respectively. In all RMC simulations, soft bond valence sum and atom-to-atom window distances (based on the experimentally observed PDF distances) restraints were applied to avoid unphysical bond lengths. In addition, the Ti and Li_{TM} atoms were rerandomized using at least 10^5 atom swaps before every run. Each RMC refinement was run for 10^6 moves, resulting in > 100 moves per atom. A total of five independent RMC configurations were produced for each sample, and their results were combined for further analysis.

3.3 Results and Discussion

3.3.1 Material Characterization

$Li_{1.2}Ti_{0.8}S_2$ was synthesized by the solid-state method as detailed in Section 3.2. The composition and structure of $Li_{1.2}Ti_{0.8}S_2$ were confirmed by synchrotron PXRD and neutron diffraction, with a minimal amount of impurities (2 wt%), as shown in Figure 3.1, A 3.1 and Table A3.1. The material crystallizes with an O3-type structure, where Li atoms occupy octahedral sites within the Li layer, and the sulfur layers exhibit an ABCABC stacking sequence, as shown in Figure 3.2. In the TM layer, Li and Ti ions are randomly distributed, as evidenced by the absence of superstructure Bragg peaks at around Q = 1.5 $Å^{-1}$.

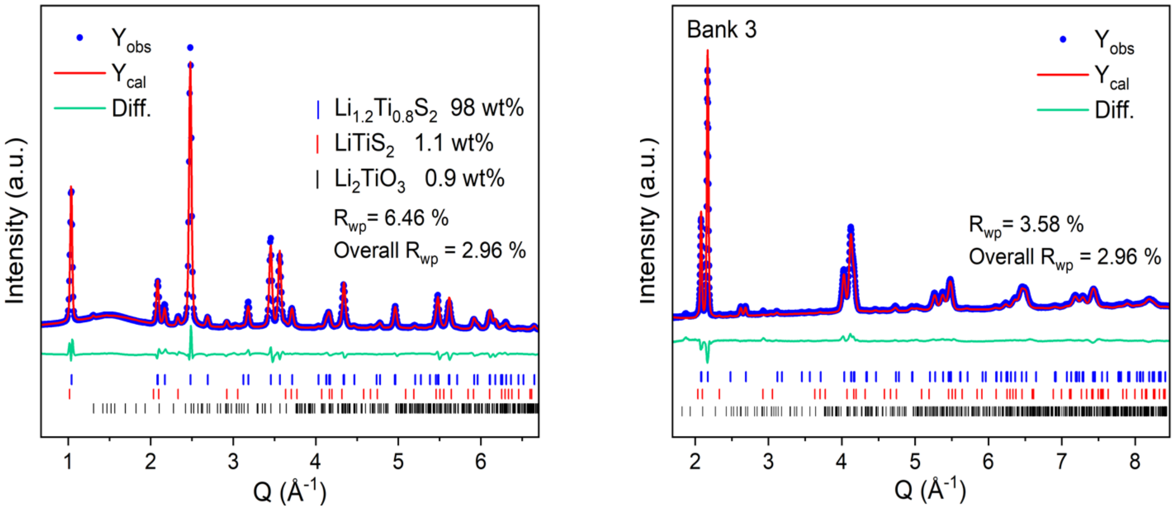

Figure 3.1: Joint Rietveld refinements of synchrotron PXRD and neutron diffraction of the pristine $Li_{1.2}Ti_{0.8}S_2$, using the $R\bar{3}m$ space group.

The structure of $Li_{1.2}Ti_{0.8}S_2$ was further confirmed using ADF-STEM. As shown in Figure 3.3, the obtained images are consistent with the refined model from diffraction data, revealing alternating stacking of LiS_2 and TMS_2 layers. Ti and S, being heavier scatterers, appear bright due to stronger electron scattering, while Li is barely visible.

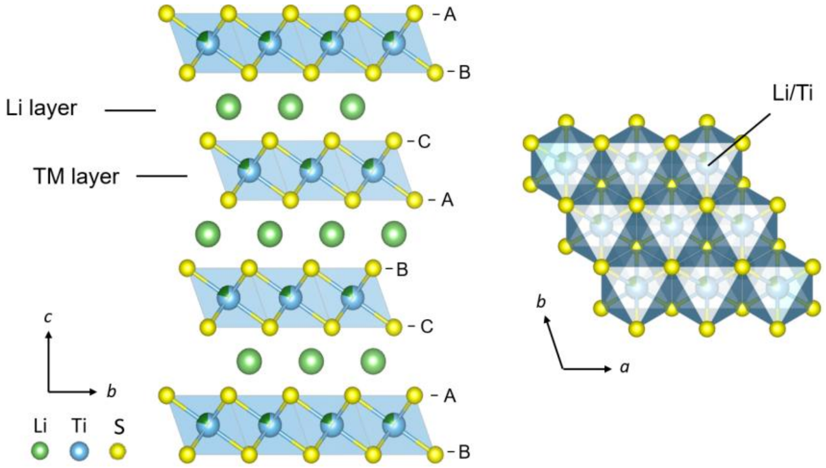

Figure 3.2: Schematic of the O3-type $Li_{1.2}Ti_{0.8}S_2$ structure, showing randomly distributed Li (green) and Ti (blue) atoms within the TM layer. S layers are stacked in an ABCABC arrangement.

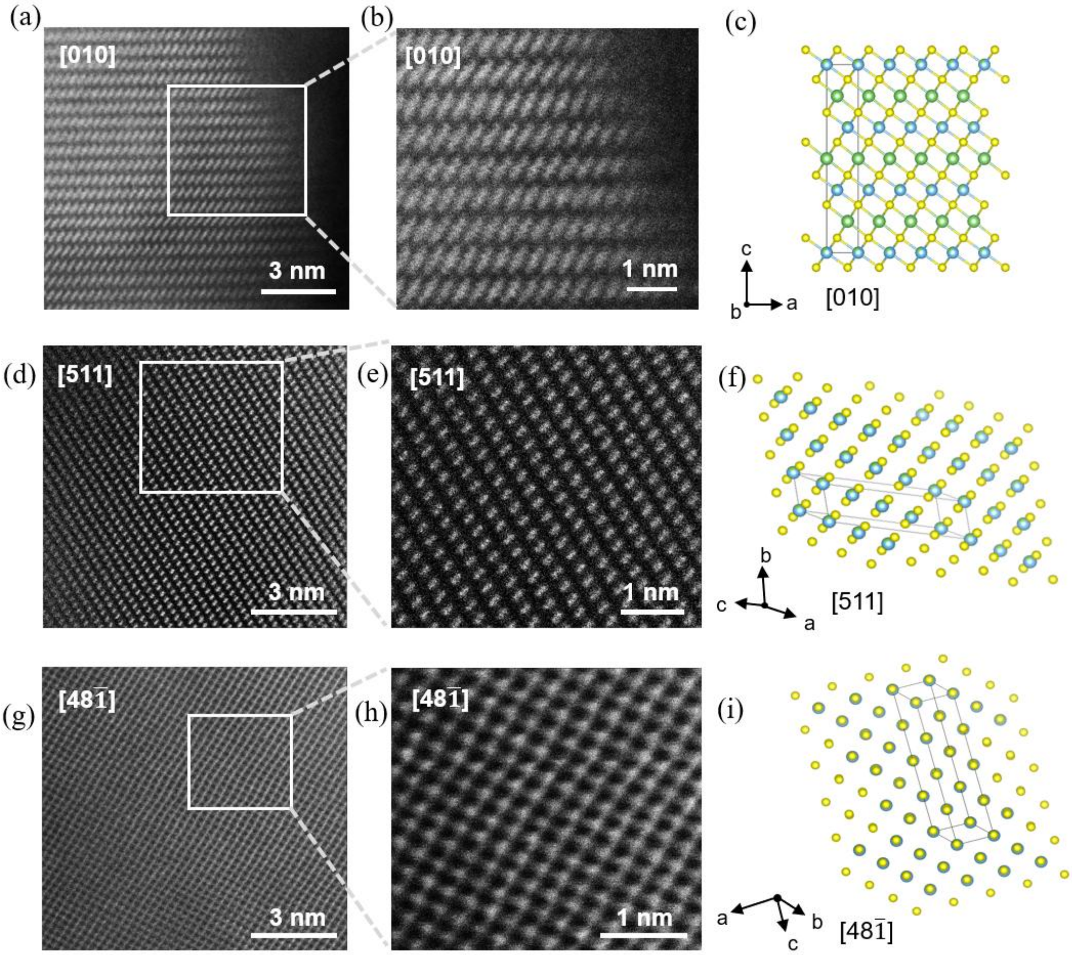

Figure 3.3: ADF-STEM images of $Li_{1.2}Ti_{0.8}S_2$. (a), (d), (g), ADF-STEM images acquired along the [010] (a), [511] (d) and [48$\bar{1}$] (g) zone axis. (b), (e), (h), Magnified views of the regions highlighted in (a), (d) and (g), respectively. (c), (f), (i), Structural models with matching orientations in (a), (d) and (g), respectively. Li atoms are almost invisible due to their weak electron scattering. ADF-STEM images were taken by Dr Jun Chen, and the material was prepared by me.

The particle morphology and elemental distribution were examined by SEM coupled with EDX. In Figure 3.4, primary particles ranging from 1 to 5 µm aggregate to form larger secondary particles of approximately 50 µm. In addition, the elemental distribution of Ti and S is homogeneous throughout the particles.

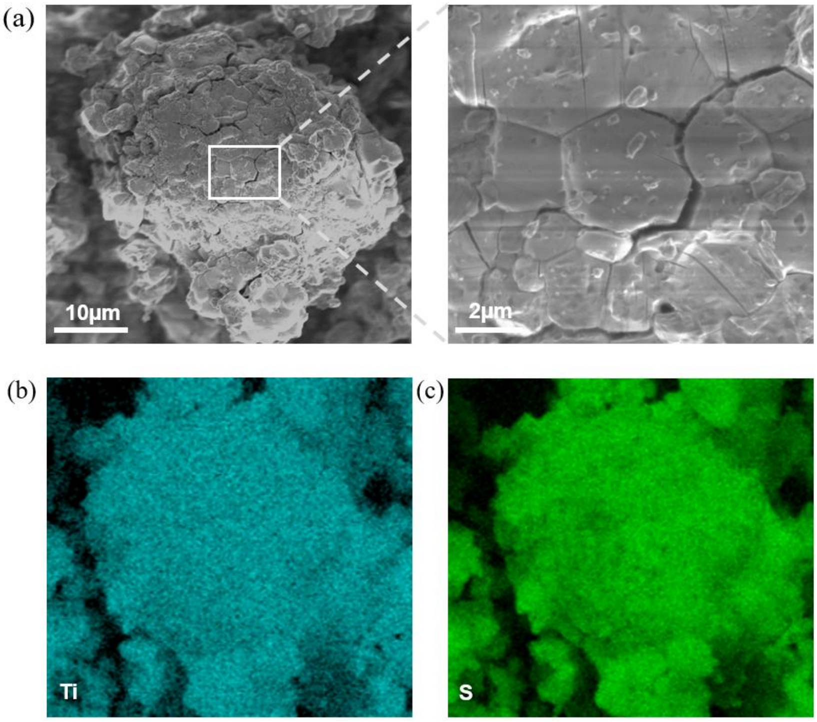

Figure 3.4: SEM and EDX images of pristine $Li_{1.2}Ti_{0.8}S_2$. (a) SEM image showing that the secondary particle consists of aggregated primary particles ranging between 1 – 5 µm in size. (b) and (c), EDX mapping confirms a homogenous distribution of elements within and between primary particles.

3.3.2 Electrochemical Characterization

The electrochemical behavior of $Li_{1.2}Ti_{0.8}S_2$ ($Li_{1.2}Ti_{0.4}^{+3}Ti_{0.4}^{+4}S_2$) was examined using galvanostatic cycling in a coin cell versus a Li metal anode, as shown in Figure 3.5. During the first charge, the voltage profile exhibits a sloping region from the open-circuit voltage (OCV) up to 2.6 V, corresponding to the extraction of approximately 0.4 moles of Li^+ per mole of $Li_{1.2}Ti_{0.8}S_2$. The sloping region is followed by a flat voltage plateau at around 2.75 V, associated with the removal of an additional 0.7 moles of Li^+ per formula unit. Upon discharge, almost all the extracted Li^+ is reinserted into the structure. However, the first charging plateau is not retained in subsequent discharge nor on the second cycle, exhibiting an S-shaped slope at a lower average voltage than the initial charging plateau. Notably, the total amount of extracted Li^+ (1.1 moles per formula unit) exceeds the theoretical capacity via the Ti^{3+}/Ti^{4+} redox in the compound (0.4 moles of Li^+ removal per formula unit), suggesting the contribution from sulfur redox activity. The detailed redox process is discussed in Section 3.3.3. Overall, $Li_{1.2}Ti_{0.8}S_2$ exhibits electrochemical profiles similar to those of Li-rich oxide cathodes, such as $Li_{1.2}Ni_{0.2}Mn_{0.6}O_2$, $Li_{1.2}Ni_{0.13}Co_{0.13}Mn_{0.54}O_2$ and $Li_2Ru_{0.75}Sn_{0.25}O_2$, where a distinct voltage plateau appears only in the first charge.[15-18] However, in sharp contrast to those Li-rich oxides, $Li_{1.2}Ti_{0.8}S_2$ shows nearly 100% first-cycle coulombic efficiency (~ 10 – 30% higher than Li-rich oxides) and significantly reduced voltage hysteresis (~ 90% less than Li-rich oxides).

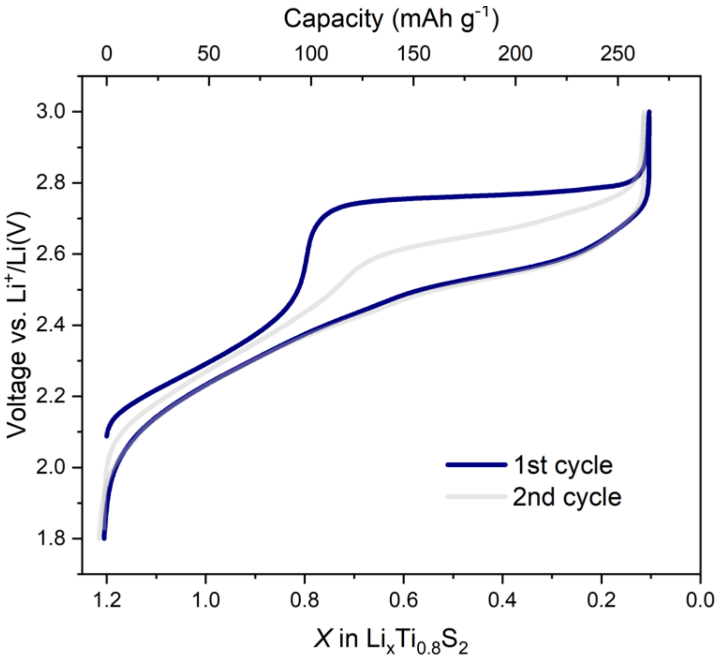

Figure 3.5: The load curves of $Li_{1.2}Ti_{0.8}S_2$ during the first two cycles. The cycling data was collected between 1.8V – 3V at a current density of 10 mA g^{-1}. After the first cycle, the distinct charging plateau diminishes, transitioning to a more sloping charge profile.

3.3.3 Charge Compensation Process

To investigate the redox process and confirm the participation of sulfur redox activity in $Li_{1.2}Ti_{0.8}S_2$, Ti K-edge and S K-edge XANES were measured on *ex situ* samples at different states of charge over the first cycle, as marked in Figure 3.6 (a). In Figure 3.6 (b), the main edge of the Ti K-edge for pristine material appears at ~ 4977eV, located between those of $LiTiS_2$ and TiS_2. This is consistent with an average Ti oxidation state of +3.5, as expected from the stoichiometric composition. During charging, across the initial sloping region up to 2.6V (before the S-redox plateau, denoted as BSP), the Ti K-edge shifts to higher energy, matching closely with the TiS_2 reference containing Ti^{4+}. Notably, no further energy shift is observed in the Ti K-edge throughout the subsequent charge plateau, despite 0.6 further moles of Li^+ extraction, suggesting that Ti remains redox inactive after being charged to Ti^{+4}. Upon discharge, the reduction of Ti^{4+} starts below 2.5V (half discharge, HD), with the Ti K-edge fully returning to the pristine state by 1.8V (full discharge, FD). Ti L-edge XAS (Figure A3.2) was also measured, showing the same Ti redox process evidenced by Ti K-edge XANES.

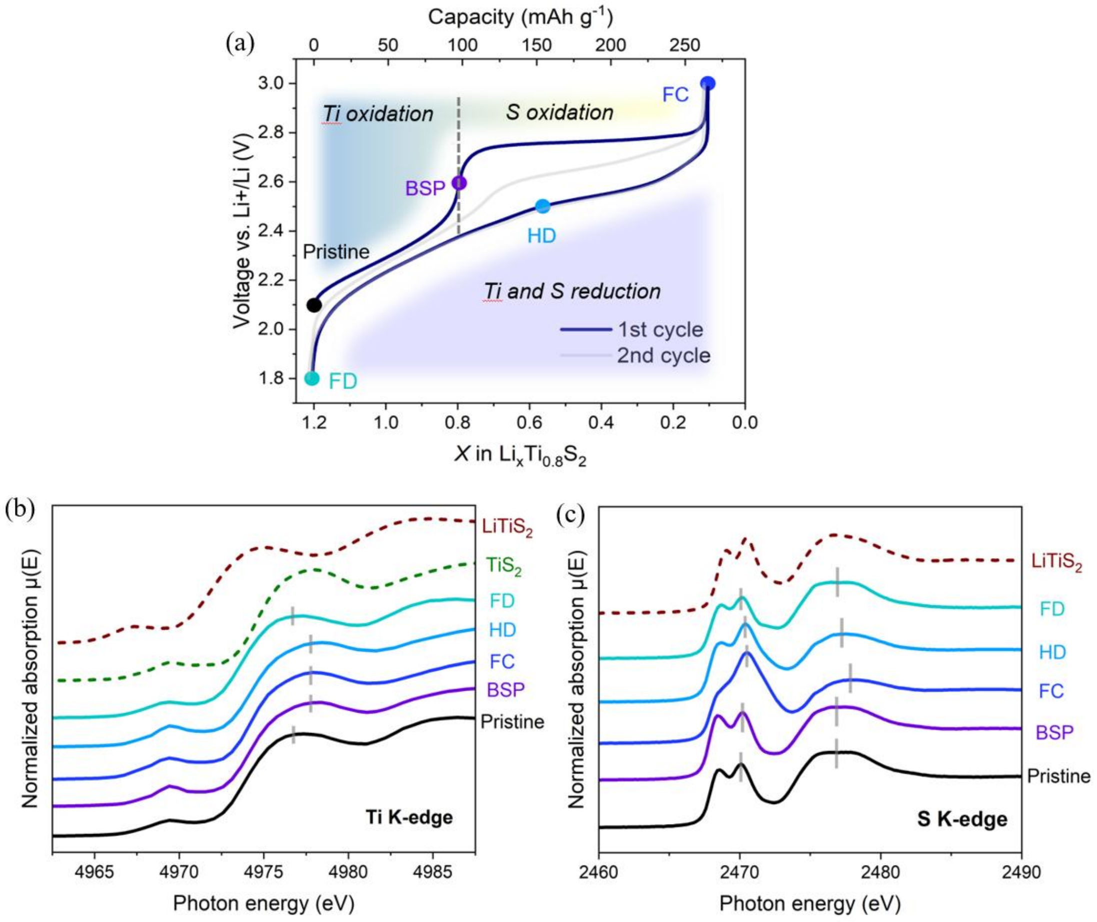

Figure 3.6: (a) Load profiles of the first cycle between 1.8V and 3V at 10 mA g^{-1}. Coloured markers denote specific states of charge selected for detailed study during the first cycle, including pristine (OCV), charge to before S redox plateau (BSP, 2.6V), fully charged (FC, 3V), half discharged (HD, 2.5V) and fully discharged (FD, 1.8V). (b), (c), Ti K-edge (b) and S K-edge (c) XANES spectra acquired at the states of charge highlighted in panel a.

The S K-edge XANES data presented in Figure 3.6 (c) show that the spectrum for pristine $Li_{1.2}Ti_{0.8}S_2$ consists of two distinct pre-edge features below 2475 eV and a broad edge centered at ~ 2477eV, closely resembling the reference $LiTiS_2$ containing S^{2-}. Upon charging to the BSP state, the position of the edges remains unchanged while the intensity of the first pre-edge at ~ 2469 eV increases, indicating an increased density of unoccupied states in the hybridized S 3*p*/Ti 3*d* band. This aligns well with the oxidation of Ti^{3+} during the sloped charging region. Further charging across the plateau results in a significant increase in the intensity of the second pre-edge feature at 2470.5 eV, along with a shift of around 0.2 eV towards higher energy. These observations cannot be attributed to Ti oxidation given that Ti^{4+} remains unchanged between the BSP and FC state. Additionally, a ~ 0.8 eV rightward shift of the broad main edge around 2477 eV is observed after reaching the FC state, further confirming the involvement of S-redox in the electrochemical cycling of the $Li_{1.2}Ti_{0.8}S_2$. The minimal evolution of the S K-edge before the BSP state suggests the Ti and S oxidation processes are well separated during the initial charging. On discharge, the Ti and S redox couples are less well separated than on charge. S reduction is more pronounced during the first half of the discharge, but continues to the FD state at 1.8 V, with the spectrum of the FD almost identical to that of the pristine state. The high reversibility of both Ti and S redox reactions indicates that the absence of the plateau feature in the second charge is more likely caused by irreversible structural changes occurring in the first cycle.

It is worth noting here that the peak shape and position changes at the S K-edge observed at the FC state reveal the formation of new hole states during sulfur oxidation. However, S K-edge XANES is not sensitive enough to uncover the nature of the oxidized sulfur species.

3.3.4 Long-range Structural Evolution

To understand the overall structural evolution of $Li_{1.2}Ti_{0.8}S_2$ during cycling, an *operando* PXRD experiment was carried out. As shown in Figure 3.7, diffraction peaks corresponding to the pristine O3-type phase exhibit continuous shifts during initial charging, without changing the overall crystal structure, indicative of a solid-solution mechanism. Across the S-redox plateau, the material undergoes a phase transition from an O3-type to an O1-type structure, where the sulfur layer stacking changes from ABCABC (O3) to ABAB (O1), a well-known behavior in layered Li-rich sulfide cathodes.[19] This transition is evidenced by the increased intensity of Bragg peaks at $2\theta = 15°$ and

33.8°, corresponding to the characteristic (001) and $(10\bar{1})$ reflections in the O1-type layered structure. During discharge, the O1-type phase fraction gradually diminishes, followed by a solid-solution region in which the material fully reverts to the original O3-type structure with all the extracted Li^+ ions reinserted. Throughout cycling, the material remains crystalline with well-preserved long-range layered crystal structures. In addition, a similar phase evolution is also observed in the second cycle, as depicted in Figure A3.3, though with almost half the voltage hysteresis of that in the first cycle. These findings suggest that changes in the load profiles between the first two cycles are not caused by differences in the long-range structural evolution.

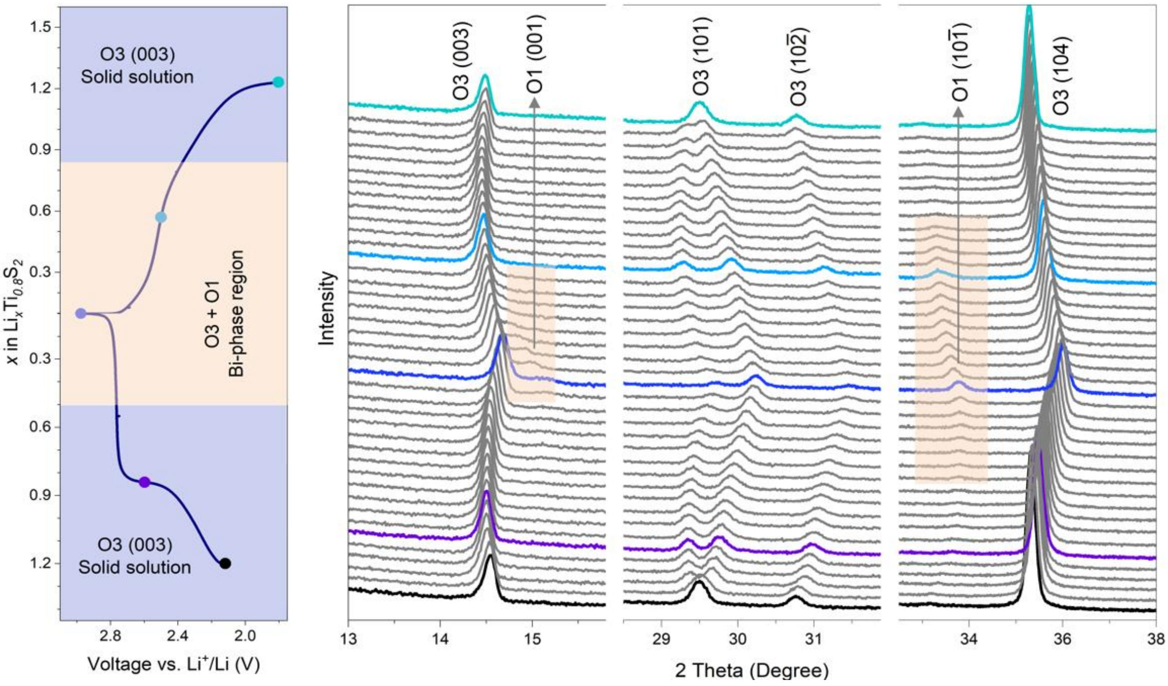

Figure 3.7: The first cycle load curve of $Li_{1.2}Ti_{0.8}S_2$ monitored by *operando* XRD with a Cu source diffractometer. The cell was cycled between 1.8V and 3V at 10 mA g^{-1}.

To access further detailed structure information at key states of charge, joint Rietveld refinements of synchrotron XRD and neutron diffraction data were performed on the *ex situ* BSP (Figure A3.4 and Table A3.2), FC (Figure A3.5 and Table A3.3) and FD samples (Figure A3.6 and Table A3.4). In line with *operando* XRD results, the O3-type structure is well maintained in the BSP, and the FC sample is fitted well by a mixture of 82.6 wt% O3 phase, 15.7 wt% O1 phase and a minor amount of impurity. At the FC state, the S-S distances in the long-range structure contract compared to the pristine material. However, the S-S distances remain above 3.4 Å, greatly larger than the typical bond length of persulfide S_2^{2-} which ranges between 2 – 2.2 Å.[20-22] Quantitative joint refinements of X-ray and neutron diffraction data further reveal that only the FC shows approximately 20% sulfur vacancies (Table A3.3). Notably, after the first cycle, the FD sample exhibits a complete occupancy of sulfur atoms at the 6c Wycoff positions (Table A3.4) in the $R\bar{3}m$ space group, almost identical to the pristine state. These observations indicate that although sulfur ions deviate from their equilibrium positions during the sulfur oxidation, they are not irreversibly lost from the material surface. This is further corroborated by the ADF-STEM image obtained for the FC sample (Figure A3.7), which reveals a well-preserved layered structure at the particle surface, contrasting with the densified surface layer commonly observed in Li-rich oxides due to the irreversible O_2 loss during charging.[1] Given the observations in the long-range structure evolution of $Li_{1.2}Ti_{0.8}S_2$ during cycling, three key questions arise:

1. Where are the off-position S atoms located within the fully charged sample?
2. What causes the first-cycle hysteresis, albeit much diminished compared to O-redox systems, given that a highly reversible long-range structure evolution and redox process has been evidenced.
3. Why does the second charging profile lose the plateau feature, even though both the FD and pristine samples exhibit nearly identical O3 phases, and the first two cycles follow similar long-range structural evolution?

To address these questions, it is essential to investigate the evolution of the local structure during electrochemical cycling.

3.3.5 Local Structural Evolution

X-ray and neutron PDFs

To investigate local structural changes of $Li_{1.2}Ti_{0.8}S_2$ in-depth, X-ray and neutron total scattering measurements were performed at key states of charge, including the pristine, BSP, FC and FD. Close fits to the PDFs over a broad length range, 1 – 20 Å, are obtained by joint refinements, employing the structure derived from diffraction data (Figure A3.8, A3.9 and Table A3.5 – A3.8). To focus on the local structure of a much shorter range, the PDFs in 1 – 4 Å are presented in Figure 3.8. In the pristine sample, both X-ray and neutron PDFs exhibit prominent peaks at approximately 2.45 Å and 3.51 Å, which are primarily attributed to Ti-S and S-S/Ti-Ti bonds within the TM layer, respectively. It is important to note that while all peaks in the X-ray PDF appear positive, peaks in the neutron PDF arise when the product of the scattering lengths of atom-atom pairs is positive and troughs when negative. In $Li_{1.2}Ti_{0.8}S_2$, Li (–1.9 fm) and Ti (–3.44 fm) have negative coherent scattering lengths, while S shows a positive coherent scattering length (2.85 fm). Upon charging to the BSP, the Ti-S bonds contract by ~ 0.5 Å, consistent with the oxidation of Ti^{3+} during the sloping region. Notably, after further charging to the FC state, a new positive peak appears at around 2.05 Å in both X-ray and neutron PDFs. This feature persists across PDFs generated using varying Q (scattering factor) ranges (Figure 3.9), ruling out the possibility of it being a Fourier transform artefact. Such a short distance with positive intensity strongly suggests the formation of new S-S atomic pairs, since Li^+ is nearly fully extracted and Ti remains in the TM layer at the FC state, as verified by joint Rietveld refinements of diffraction data (Figure A3.5, Table A3.3). Simulated PDFs of the reference TiS_3 compound, which contains S-S dimers with a bond length of ~ 2.05 Å,[22, 23] exhibit a closely matching peak, further supporting this assignment. Moreover, this new S-S distance is nearly 1.4 Å shorter than that presented in the long-range structure, indicating that some sulfur atoms are significantly displaced from their original lattice sites, in agreement with the sulfur vacancies observed in the FC sample. These short S-S pairs act as local defects as they are detectable via total scattering but not by powder diffraction, which is only sensitive to long-range periodic structures. At the end of discharge, the peak at ~ 2.05 Å disappears as sulfur ions are reduced back to S^{2-}, demonstrating the reversible nature of the S-redox process during cycling.

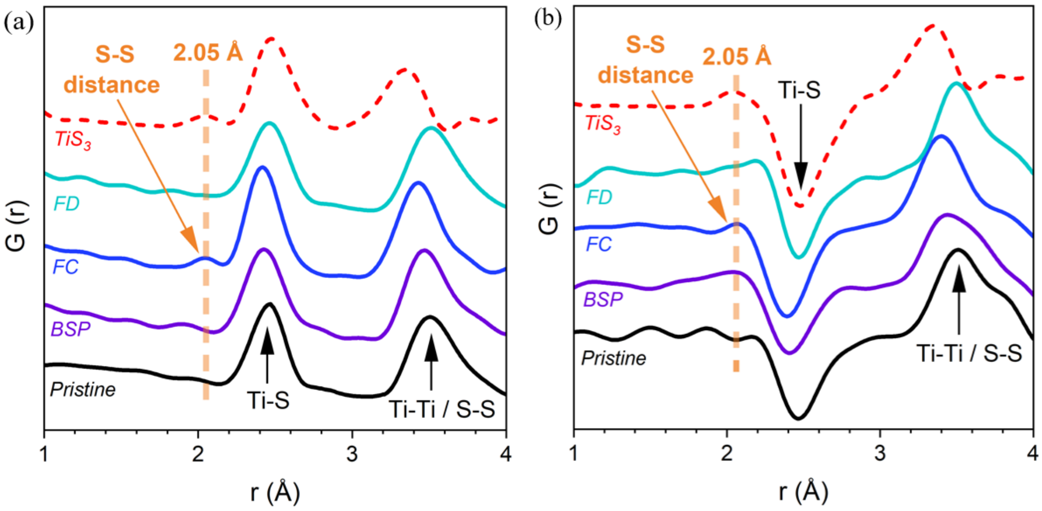

Figure 3.8: (a), (b), X-ray PDF (a) and Neutron PDF (b) results of $Li_{1.2}Ti_{0.8}S_2$ in the 1 – 4 Å region at various states of charge, generated from total scattering data measured at room temperature, Q_{max} = 23 Å. A new peak emerges exclusively in the FC sample at 2.05 Å (highlighted in orange), corresponding to the formation of the S-S distance attributed by S_2^{2-}. Simulated PDF data for TiS_3, a reference compound containing S-S dimers with a bond length of 2.05 Å, exhibits a peak at the same radial distance.

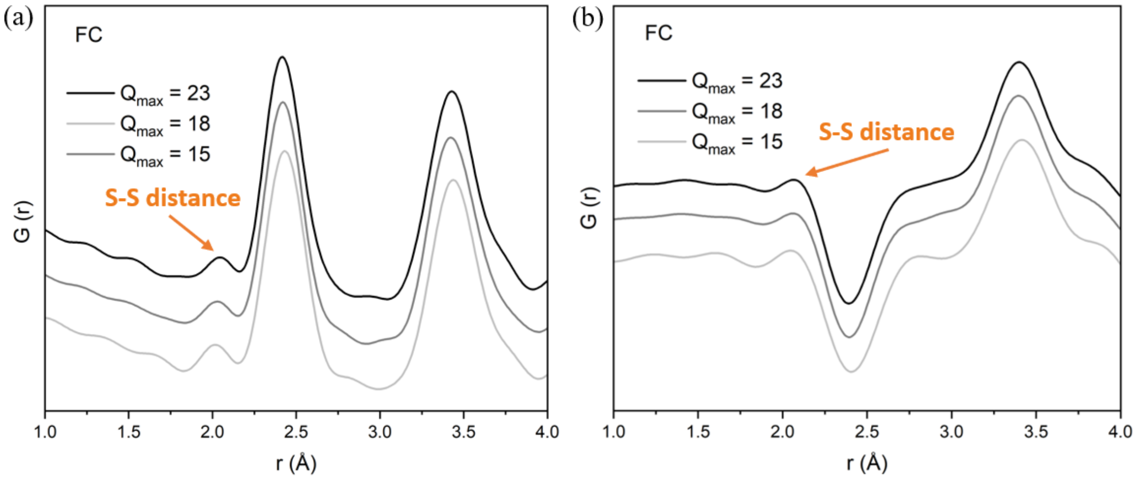

Figure 3.9: Additional PDF data of fully charged $Li_{1.2}Ti_{0.8}S_2$. (a), (b), X-ray (a) and neutron (b) PDF data of the FC sample in the 1 – 4 Å region, generated using different Q_{max} values for the Fourier transform. Across all Q_{max} values, the peak at around 2 Å appears consistently, confirming the presence of a short distance in the FC sample rather than an artefact from Fourier ripples. For further analysis, a Q_{max} of 23 Å was used to ensure optimal real-space resolution.

S and Ti K-edge EXAFS

S and Ti K-edge EXAFS measurements were also employed to probe the local structure changes. As shown in Figure 3.10, both S and Ti K-edge EXAFS reveal a shortening of the Ti–S bond from pristine to the BSP state, consistent with the PDFs. At the FC state, a distinct shoulder emerges at a low radial distance in the S K-edge EXAFS, while the Ti K-edge EXAFS remains almost the same as the BSP sample. The shoulder, located at ~ 2 Å, is in good accord with the new peak at ~ 2.05 Å observed in the PDFs (Figure 3.8 and Figure 3.9). Thanks to the element-specific nature of EXAFS, the contrasting evolution at the S and Ti K-edges unequivocally confirms that the new short distance originates exclusively from the formation of a new shorter S-S distance, rather than contraction of Ti-S bonds. In addition, all EXAFS spectra within the first two coordination shells were well fitted (Figure A3.10, A3.11 and Table A3.9, A3.10), revealing an S-S distance of 2.08 Å in the FC state (Table A3.10), closely matching the observations in PDFs (2.05 Å). The minor discrepancy is attributed to the limited resolution (~ 0.24 Å) of the S-K edge EXAFS measurements. A slight increase in the coordination number n(r) of neighboring Ti-Ti after the first cycle is also captured (Table A3.9), indicative of Ti aggregation with the TM layer, which will be further discussed later in this Section. However, a short S-S distance in the FC material does not necessarily indicate that they are bonded; what then is the nature of oxidized S ions in $Li_{1.2}Ti_{0.8}S_2$?

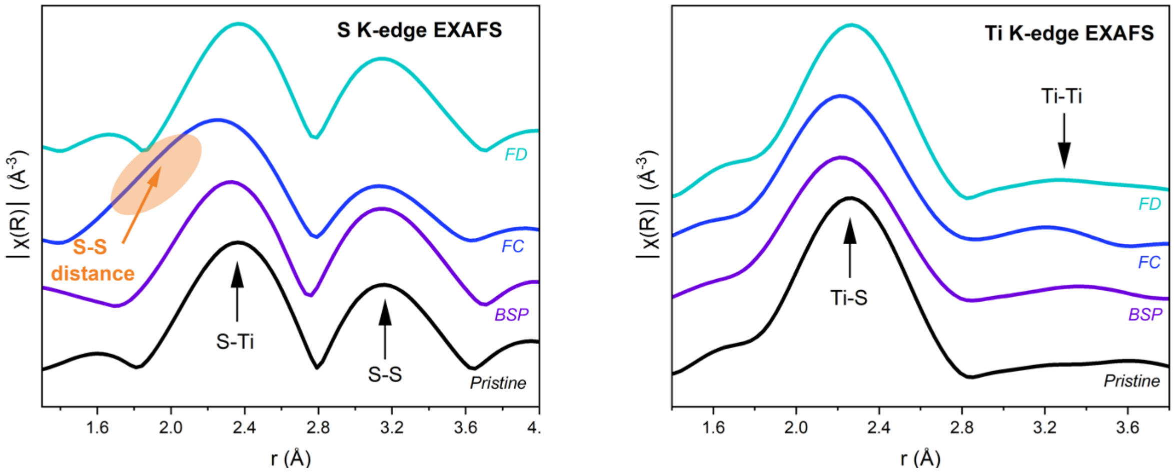

Figure 3.10: S and Ti K-edge EXAFS spectra at different states of charge. The appearance of a shoulder at a low radial distance in the first shell (highlighted in orange) of the S K-edge EXAFS spectrum is consistent with the formation of short S-S distances associated with the oxidation of S ions. The r value in the x-axis has been corrected by the phase correction function.

RIXS and INS

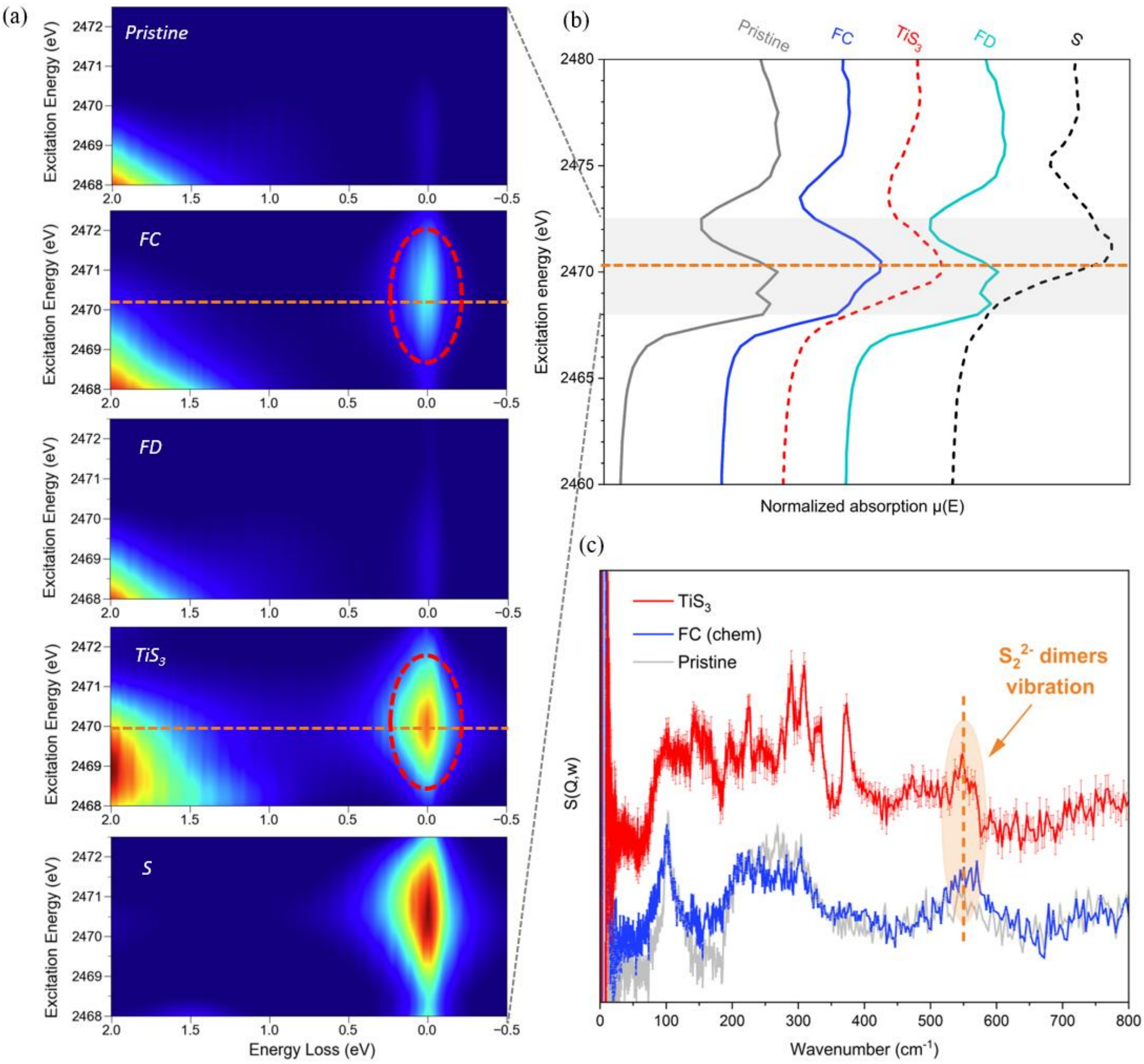

Figure 3.11: Spectroscopic evidence of S_2^{2-} formation. (a) S K-edge RIXS maps for pristine $Li_{1.2}Ti_{0.8}S_2$, FC, FD samples, and reference TiS_3 and elemental S. The scans were performed over an excitation energy range of 2468 – 2472.5 eV, as indicated by the shaded grey area in (b). In the FC sample, a distinct feature arises near the elastic line (marked by a red circle), with maximum intensity at 2470.25 eV (highlighted by the orange line), corresponding to the top of its S K-edge XANES. This feature closely resembles the characteristics signal (highlighted by a red circle) observed in the RIXS map of TiS_3, which is attributed to S-S dimers. (b) S K-edge XNAES data over a broader energy range for $Li_{1.2}Ti_{0.8}S_2$ at different states of charge, along with TiS_3 and elemental sulfur as references. (c) INS spectra for the pristine, FC (chem) and TiS_3 samples. The FC (chem) sample is prepared by the chemically delithiated method and shows nearly the same structure and composition as the FC sample obtained by charging pristine to 3V at 10 mA g^{-1}.

To confirm the presence of S-S dimers in the form of S_2^{2-}, RIXS and INS were both employed in this study. S K-edge RIXS offers a probe of the electronic states on S sensitive to depths of approximately 100 nm into the sample, and the INS complements it by providing a bulk-average measurement of the vibrational modes associated with interatomic bonds in the material. Previously, O K-edge RIXS has been applied to study the O-redox cathodes, where the emission signals arise in the low-energy loss region due to the electronic transitions of molecular O_2. Herein, RIXS on the S K-edge was first applied on the Li-rich sulfide cathodes. The RIXS maps for the pristine, BSP, FC and FD samples, along with reference TiS_3 and elemental S, are presented in Figure 3.11 (a). In S K-edge RIXS, incident X-rays excite the 1s core electrons on sulfur into unoccupied 3p orbitals. The subsequent photon emission arises from the relaxation of electrons from filled sulfur valence states back into the core-hole levels (S 1*s*), thus providing direct access to the valence states on sulfur. To further highlight emission signals in the low energy-loss region, the elastic peak has been suppressed, as described in Section 3.2. The XANES spectra over a broader excitation energy range for all the samples are shown in Figure 3.11 (b), with the grey-shaded area showing the energy range scanned for the RIXS maps.

In the XANES spectra in Figure 3.11 (b), compared to the pristine, no extra signal appears before the S K pre-edge (below 2468 eV) in the FC sample, where electron holes on S^{2-} (that is S^{n-}, $n < 2$) just above the Fermi energy are expected to be detected.[21] In addition, extra hole states located at 2470.3 eV emerge in the FC due to sulfur oxidation (dashed line in Figure 3.11 (b)), which also appears in TiS_3 at 2470.3 eV. At the same excitation energy, the RIXS map for the FC sample exhibits distinct features, marked by the dotted circle (Figure 3.11 (a)), revealing the formation of new sulfur valence states. Notably, these new features closely resemble the energy loss features observed in TiS_3 within the incident energy range of 2470.3 ± 2 eV (dotted circle in TiS_3 RIXS map), which are attributed to the electronic transitions of S_2^{2-} dimers. The close similarities of both the hole states in the sulfur conduction band and filled states in the sulfur valence band between the FC and TiS_3 strongly suggest the formation of S_2^{2-} during the sulfur oxidation in $Li_{1.2}Ti_{0.8}S_2$.

The RIXS map and associated XANES spectrum were also collected for the elemental S. As shown in Figure 3.11 (a), the emission features near the elastic line caused by S^0-S^0 bonds appear significantly more asymmetric and exhibit peak intensities at a higher excitation energy than 2470.3 eV. Accordingly, the absorption edge of elemental sulfur occurs at a higher energy than the FC and TiS_3 samples (Figure 3.11 (b)). These different features rule out the formation of the elemental S at the FC state in the bulk. At the end of discharge, the spectral signature relevant to S_2^{2-} is absent, indicating a reversible reduction back to S^{2-}. Overall, the close agreement in the RIXS and XANES data between the FC and TiS_3 corroborates the formation of S_2^{2-} in the charged state, although the sharp vibrational peak progressions observed in oxides in the low energy-loss region are not fully resolved here (dotted circles in Figure 3.11 (a)) for sulfides due to the energy resolution limitations.

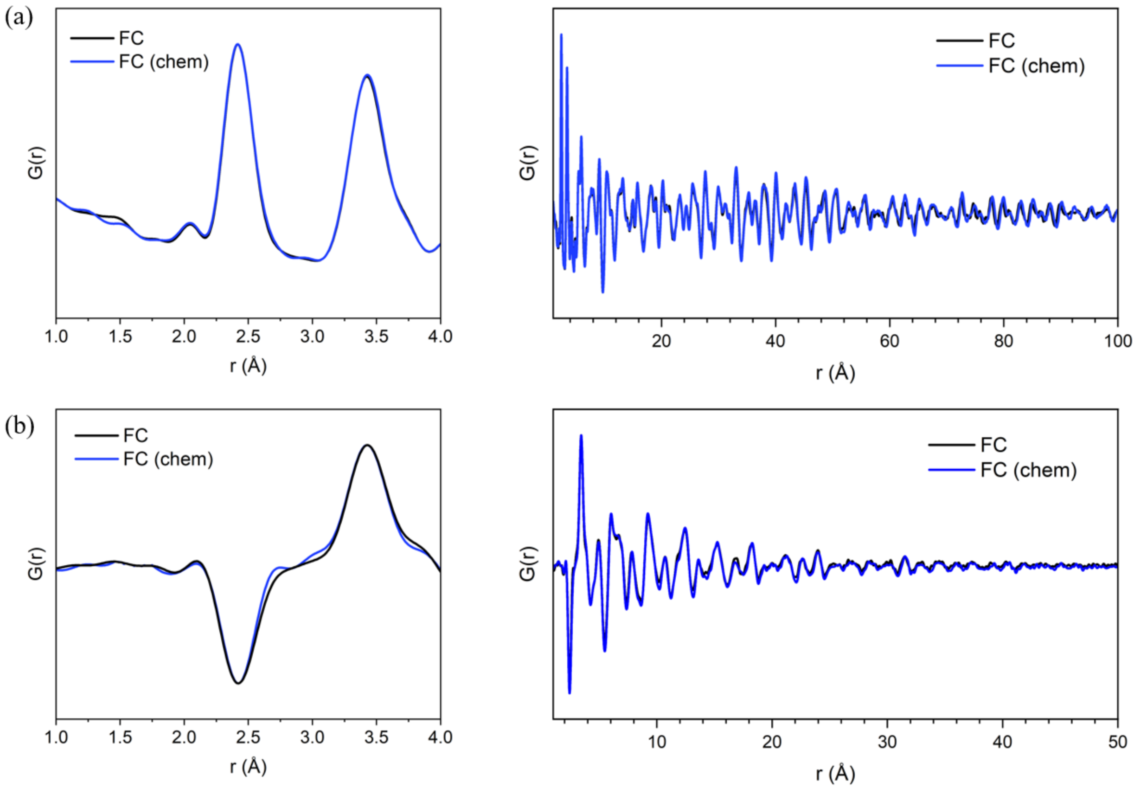

Figure 3.12: PDF data of chemically and electrochemically delithiated $Li_{1.2}Ti_{0.8}S_2$**.** (a), (b), X-ray (a) and neutron (b) PDF data comparing chemically and electrochemically delithiated $Li_{1.2}Ti_{0.8}S_2$, with Q_{max} = 23 Å. The chemically delithiated sample, FC (chem), was prepared via oxidation using I_2, as described in the synthesis methods section. Across both short range (1 – 4 Å) and long range, the FC (chem) sample closely matches the FC sample, including the characteristic short S-S peak at 2.05 Å. The faster decay of peak intensity with increasing r in the neutron PDF is attributed to lower Q resolutions inherent to the instrument.

To further confirm the formation of S_2^{2-} following sulfur oxidation, INS measurements were performed on the pristine, chemically delithiated sample (denoted as FC (chem)) and TiS_3, as shown in Figure 3.11 (c). INS data were collected using a large sample volume (~ 10g) at 10 K to achieve a good signal-to-noise ratio and minimize thermal motion effects. The chemical delithiation method, as detailed in Section 3.2, is used here to prepare ~ 10g of delithiated $Li_{1.2}Ti_{0.8}S_2$. Importantly, the FC (chem) and FC samples exhibit nearly identical structural features at both short-range (1 – 4 Å) and long-range (1 – 100 Å) scales, as verified by X-ray and neutron PDFs presented in Figure 3.12. This structure equivalence validates that the FC (chem) is a representative sample for probing vibrational features associated with S_2^{2-} using INS. The INS spectra in Figure 3.11 (c) reveal a new vibrational mode (highlighted by a dashed line) in the FC (chem) sample compared with the pristine, and the other spectral features remain largely unchanged, in agreement with the well-preserved layered structure. A peak at the same position, with a vibrational frequency of 553 cm^{-1}, is also observed in TiS_3, which matches the fundamental vibrational mode of S_2^{2-} measured by Raman spectroscopy at 556 cm^{-1}.[24] These observations further confirm the formation of S_2^{2-} dimers at the top of the charge. Notably, the peak associated with S_2^{2-} in TiS_3 is much sharper than that in FC (chem). This is most likely because all the S_2^{2-} dimers in TiS_3 are in the equivalent environment and orientation, while in the fully charged $Li_{1.2}Ti_{0.8}S_2$, S_2^{2-} are randomly dispersed through the solid as localized defects. Moreover, the primary vibrational frequency of the elemental S, located at 473 cm^{-1}, is absent in the FC (chem), consistent with RIXS results.[25] The use of INS provides bulk average structural information and is also free from possible beam damage, adding valuable confirmation of the S_2^{2-}dimer formation during S-redox in layered Li-rich sulfide cathodes.

S_2^{2-} formation accompanied by vacancy clustering

The observations discussed in the previous section show that, during charging across the plateau, sulfur oxidation produces S_2^{2-} dimers with a bond length of 2.05 Å, embedded within a long-range ordered layered structure where S–S distances exceed 3.4 Å. If both sulfur atoms within the dimers remained bonded with Ti, the formation of such short S_2^{2-} would typically induce significant distortions in the corresponding Ti-S bond lengths and surrounding Ti–S distances. However, Ti–S distances remain largely unchanged during S oxidation, suggesting that S_2^{2-} dimer formation most likely involves partial de-coordination of the S_2^{2-} from Ti. This is consistent with the S vacancies observed in joint X-ray and neutron refinements of the FC sample. The 20% vacant occupation of S sites is roughly half the number of S_2^{2-} species anticipated from the charge passed (0.7 electrons per formula unit or 35% of all S), which could indicate the persulfide species remains singly coordinated to a Ti atom.

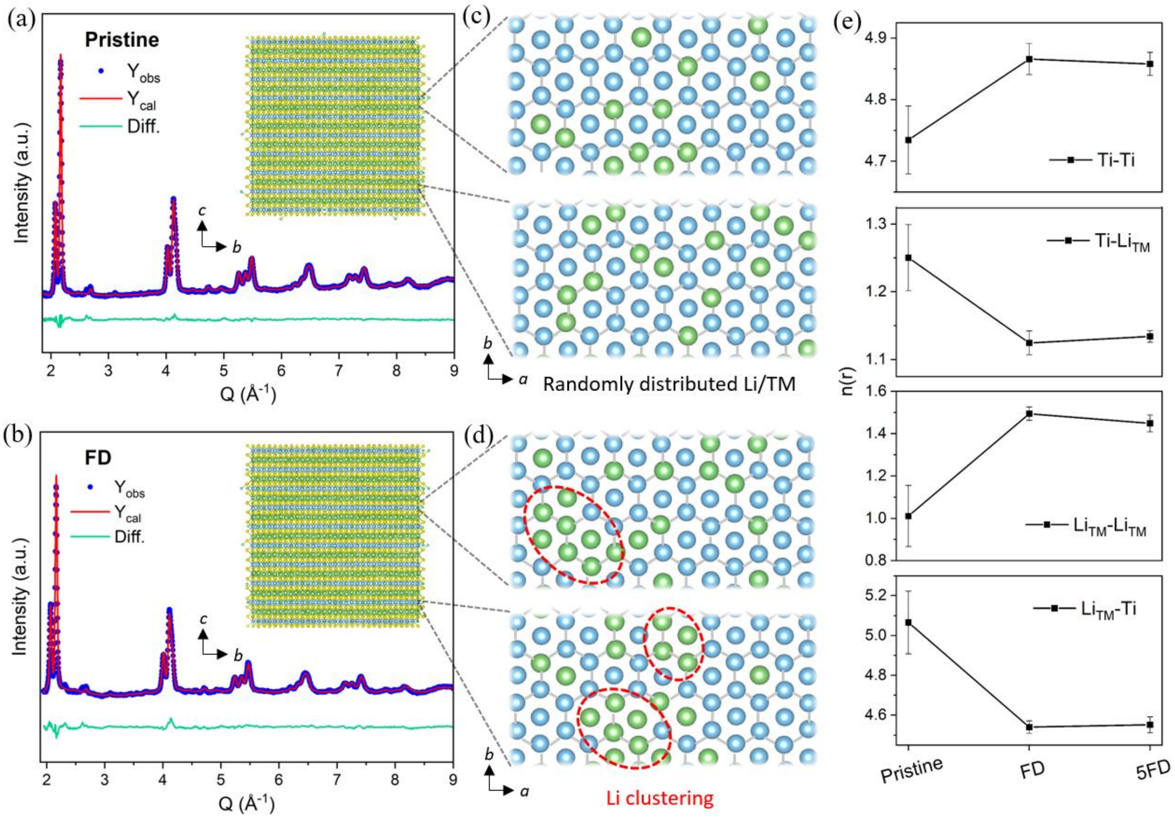

Figure 3.13: In-plane Ti migration and vacancy clustering during S redox. (a), (b), Neutron diffraction fitting results of the (a) pristine and (b) FD sample, obtained from RMC profile modelling using a supercell containing 9720 atoms, as illustrated in the insets. (c), (d), Enlarged local slices from the RMC analysis illustrating the spatial distribution of Li (green) and Ti (blue) atoms within the TM layer for the (c) pristine and (d) FD samples. The grey hexagons illustrate the neighboring six cations around the center cation within the TM layer. (e) Evolution of the coordination number, n(r), for neighboring atomic pairs in the TM layer, including Ti-Ti, Ti-Li_{TM}, Li_{TM}-Li_{TM}, and Li_{TM}-Ti across the pristine, FD and 5FD (full discharged sample after 5 cycles) samples. Li_{TM} refers to the Li ions in the TM layer. The RMC modelling analyses were conducted by Dr Javier Castells-Gil, and the sample was prepared by me.

In Li-rich layered oxides, the molecular O_2 that is formed from TM-O de-coordination is trapped within vacancy clusters in the TM layer. These appear after Li^+ vacates the TM layer during charge, permitting in-plane TM ions migration.[5] To investigate whether a similar mechanism of vacancy clustering occurs in layered Li-rich sulfides to accommodate the S_2^{2-}, RMC modelling analysis of the neutron total scattering data was performed on the pristine, FD and 5FD (FD state after 5 cycles) samples. To access local structural features with a reliable statistical analysis, a supercell model based on the O3-type $Li_{1.2}Ti_{0.8}S_2$ with 9720 atoms was built for all three samples. In the analysis, both neutron diffraction and neutron PDF are fitted simultaneously, allowing the iterative displacement and swapping of all Ti and Li atoms in the supercell until there is no further improvement in fit quality. Figure 3.13 (a) and (b) display the final RMC fits to the neutron diffraction for the pristine and FD samples, respectively, with the corresponding refined supercells shown as insets. The associated PDF fittings are presented in Figure A3.12. Overall, the neutron total scattering data for both samples are well fitted, suggesting that the final supercell models accurately capture both the short-range and long-range structural features. Figure 3.13 (c) and (d) present zoomed-in local slices along the TM layers from the refined large supercells of the pristine and FD, respectively, enabling direct visualization of the cation distribution in the TM layers. In pristine, Li and Ti ions are randomly distributed with minimal Li clusters. In contrast, distinct local domains with Li aggregation (dotted circles) are observed after the first cycle, despite the TM layers remaining disordered over long range, based on Bragg diffraction data. These newly formed Li clusters correspond to vacancy clusters formed at the delithiated state, before the re-intercalation of Li^+ during discharge, suggesting the formation of uncoordinated S at the FC state.

A detailed statistical analysis on the local coordination environment across the pristine, FD and 5FD samples was also conducted, as summarized in Figure 3.13 (e). In an ideally disordered TM layer, the theoretical coordination numbers n(r) are 4.8 for neighboring Ti-Ti and 1.2 for adjacent Ti-Li_{TM}, according to the composition stoichiometry, where Li_{TM} refers to the Li ions in the TM layer. These values are very close to those obtained from the RMC analysis of the pristine state, aligning well with the fully disordered TM layer in the as-prepared material. In the FD sample, the Ti-Ti coordination number increases, and that for Li_{TM}-Li_{TM} pairs also rises, further suggesting the vacancy clustering at the FC state. These results are consistent with coordination numbers obtained from Ti K-edge EXAFS (Table A3.9), for the pristine (4.8), and FC and FD states (both 5.0).

After five cycles, coordination numbers of Ti-Ti and Li_{TM}-Li_{TM} remain comparable to those in the FD sample, indicating that Ti aggregation is irreversible and persists in the following cycles. As a control, a sample cycled 5 times only within the Ti redox region (below the voltage of the BSP) was also examined by RMC analysis, which showed essentially unchanged coordination numbers compared to the pristine state (Figure A3.13 and A3.14). These results collectively reveal that the formation of the S_2^{2-} dimer is accompanied by in-plane migration of the TM ions to generate vacancy clusters and uncoordinated S, in a similar process to that reported in layered Li-rich oxides.

Discussion

Bringing together the spectroscopic and structural characterizations, it is evident that the oxidation of S^{2-} results in the formation of S_2^{2-} in the bulk upon charging. These S_2^{2-} dimers are accommodated within the vacancy clusters formed by TM in-plane migration, analogous to the process observed in Li-rich layered oxides.

When comparing the S-redox and O-redox processes in analogues Li-rich layered structures, the intrinsic properties of different anions fundamentally shape the anionic redox behavior. In both cases, the oxidized anions tend to dimerize. However, sulfur, being inherently softer and more polarizable than oxygen, more readily exists as a partially oxidized S_2^{2-} species than oxygen. Such S_2^{2-} dimers have been well-studied in TM sulfides, such as FeS_2 (Fe^{2+} S_2^{2-}), VS_4 ($V^{4+}(S_2^{2-})_2$) and TiS_3, as well as in more ionic alkali metal sulfides, like Na_2S_2.[20, 26-28] In contrast, oxide oxidation tend to form fully oxidized molecular O_2.[6, 29-31] Therefore, during charge, each oxidized sulfur contributes one electron through the formation of S_2^{2-} dimers, enabling a more distributed electron reservoir across the anion sublattice, compared to the trapped O_2 in Li-rich oxides. The local environment of the oxidized anions is also different. In Li-rich oxides, the relatively ionic nature of oxygen and weaker TM-O covalency result in the irreversible O_2 loss from the surface and formation of more isolated molecular O_2 trapped in the bulk.[9] In contrast, the strong TM-S covalency in Li-rich sulfides stabilizes the S_2^{2-}

dimers, which remain coordinated to adjacent TM ions rather than becoming free species. This may help explain why sulfides do not exhibit first-cycle irreversibility and retain well-preserved, undensified surface. It may also account for the faster kinetics observed in Li-rich sulfides than Li-rich oxides, as coordination with the TM will aid electron transfer between S_2^{2-} and the host structure.

3.3.6 Voltage Hysteresis in Li-rich sulfides

Based on the discussions in the preceding sections, the mechanism underlying voltage hysteresis in Li-rich sulfides is summarized schematically in Figure 3.14. RMC modelling analyses of neutron total scattering data reveal that S_2^{2-} dimers are accommodated within vacancy clusters formed by in-plane TM migration. During the first discharge, with the S_2^{2-} being reduced to S^{2-}, Li^+ ions reinsert into the TM layers and fill the sites from which the Ti ions migrated (Figure 3.14(b)). As a result, in the initial cycle, although both the redox process and long-range structure evolution are highly reversible, the local cation rearrangement in the TM layer is not, which results in a sloping discharge curve at lower voltage, similar to Li-rich oxides. These findings elucidate the origin of the residual voltage hysteresis in Li-rich sulfide cathodes. However, in contrast to the Li-rich oxides, where the formation of isolated trapped O_2 requires complete disruption of adjacent TM-O bonds,[8] Li-rich sulfides require less breaking and forming of the TM-S bonds during cycling due to the presence of TM–S_2^{2-} coordination, which results in fewer bulk structural changes during S-redox. Thanks to the reduced bulk structure rearrangement, minimal surface densification, and more delocalized electron contribution throughout particles, Li-rich sulfides exhibit significantly suppressed voltage hysteresis.

In the FD sample, increased Li^+ clustering results in more S^{2-} ions being coordinated exclusively by Li^+ ions, compared to the pristine state. This weakened ionic interaction shifts the S 3*p* states closer to the Fermi level, raising their energy relative to the S 3*p* states in the pristine structure, where sulfur is randomly coordinated by Ti and Li ions. Consequently, in the second cycle, those newly formed ionic S^{2-}, coordinated by Li^+ alone, will be oxidized at lower voltages, explaining the diminished plateau feature during the second charge. In addition, based on the in-plane Ti migration in the first cycle, less structure rearrangement is required to form vacancy clusters in the second cycle, as shown in Figure 3.14 (d), which explains the much reduced hysteresis in the second cycle. Meanwhile, the reversible formation and reduction of the S_2^{2-} recurs, similar to that observed in the first cycle, as the X-ray PDFs shown in Figure 3.14 (c). After five cycles, vacancy clusters that accommodate S_2^{2-} dimers remain largely unchanged, further explaining that the most pronounced diminution of the charging plateau is observed after the first charge, as shown in Figure A3.15.

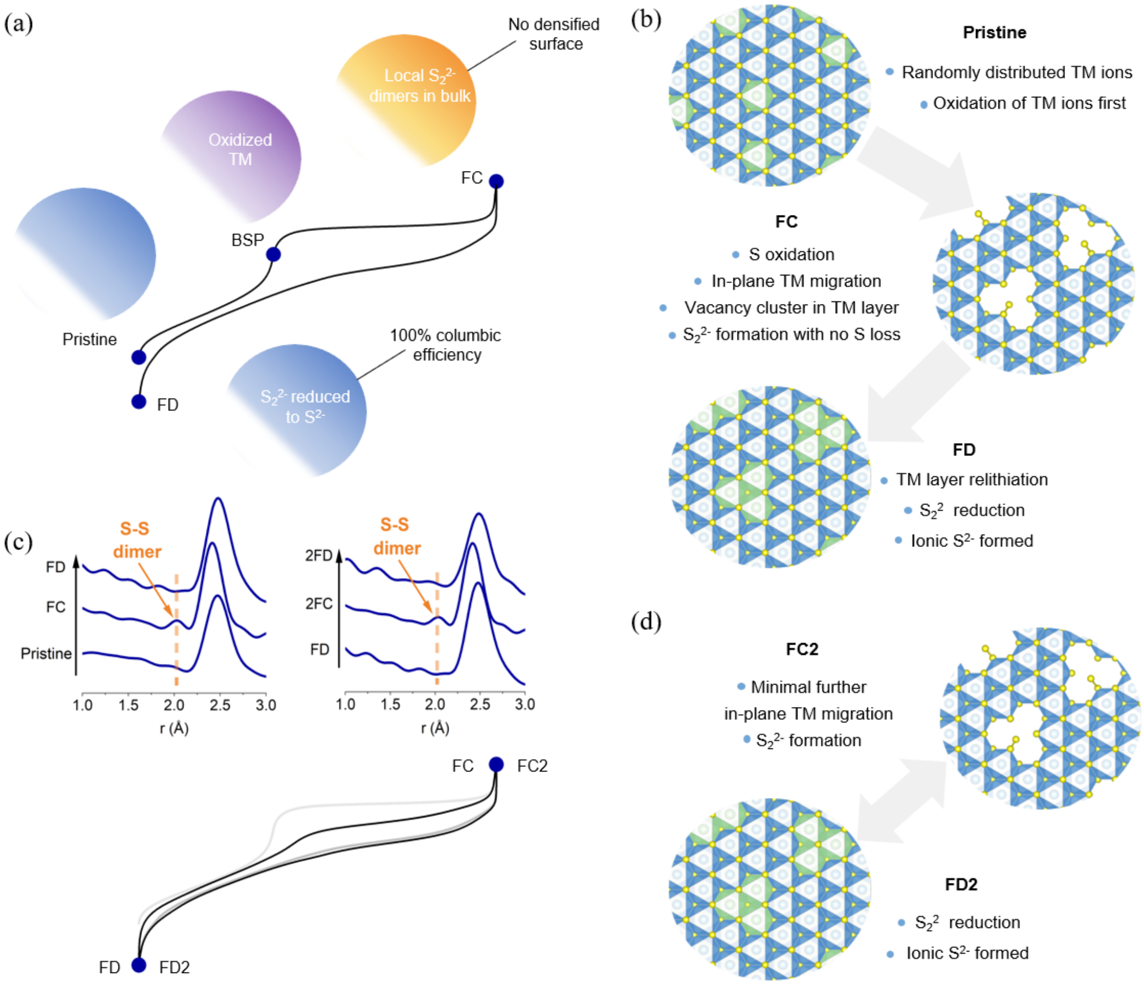

Figure 3.14: Mechanism of S_2^{2-} formation and first-cycle hysteresis. (a) Macroscale evolution of cathode particles during cycling: Across the plateau, S^{2-} is oxidized to form S_2^{2-}, which remains within the particle rather than being irreversibly lost at the surface. The S_2^{2-} dimers are reversibly reduced back to S^{2-} upon discharge. (b) Atomic-scale changes within the TM layer: oxidation of S^{2-} triggers in-plane migration of TM ions into the sites vacated by Li^+, leading to the formation of local vacancy clusters. On subsequent discharge, Li^+ reinserts into the TM layers, occupying sites previously taken by TM ions. (c) X-ray PDFs showing reversible reduction and formation of S_2^{2-} throughout the first cycle (left) and second cycle (right). Corresponding electrochemical profiles are displayed below, with the first cycle in grey and the second cycle in blue. (d) Atomic-scale evolution of the TM layer after the first cycle. Vacancy clusters formed in the TM layer persist after the first cycle, enabling S_2^{2-} formation and reduction without requiring further substantial TM migration.

Interestingly, moderately heating the FD sample partially restores the voltage plateau in subsequent charging (Figure A3.16). It indicates that by providing mild thermal energy, the materials can be driven to a more thermodynamically favourable state that is close to pristine, resulting in voltage recovery. RMC analysis on the reheated sample supports this further (Figure A3.13 and A3.14), revealing reduced cation aggregation in the TM layer. Notably, under similar mild annealing conditions, cycled Li-rich oxides commonly show more pronounced voltage recovery.[32] This contrast suggests that Li-rich sulfides experience a higher kinetic barrier for in-plane TM migration during thermal treatment compared to their oxide counterparts, consistent with the retention of a fully occupied TM layer in cycled Li-rich sulfides due to their high coulombic reversibility.

3.4 Conclusion

An in-depth investigation of the layered Li-rich sulfide, $Li_{1.2}Ti_{0.8}S_2$, reveals that sulfur oxidation during charging is associated with the formation of the S_2^{2-} dimers, rather than hole states on the oxidized sulfur ions or elemental S. The formation of persulfide S_2^{2-} is collectively identified by a suite of complementary techniques, including X-ray and neutron total scattering, S and Ti K-edge EXAFS, S K-edge RIXS and INS. Quantitative joint X-ray and neutron refinements further show that 20% of sulfur is displaced from the lattice structure, corresponding to nearly half of the S in the S_2^{2-} dimers, which suggests that S_2^{2-} remain partially coordinated to Ti ions in the layered structure, in stark contrast with the more isolated trapped molecular O_2 in Li-rich oxides. These S_2^{2-} dimers, behaving like local defects, are accommodated in the vacancy clusters formed by in-plane TM migration, similar to that in Li-rich oxides, albeit in a less dramatic manner than in Li-rich oxides. The results in this chapter confirm that the presence of strong TM–S_2^{2-} coordination leads to key improvements in electrochemical characteristics in Li-rich sulfides compared with their oxide analogues, including low voltage hysteresis, high coulombic reversibility, and fast kinetics.

The fundamental understanding gained from S-redox chemistry in this work offers a more complete picture of the anionic redox mechanism. To combine the reversibility of S-redox and energy density of O-redox, preparing Li-rich oxysulfide cathodes is a promising strategy. In addition, exploring the sulfides with a higher Li/TM ratio is essential to achieve more competitive energy densities against

Li-rich oxides. Future investigations into other Li-rich sulfides with different structural frameworks are crucial to examine if the same S-redox mechanism occurs and further broaden the design routes for high-energy-density Li-rich cathodes.

3.5 References

1. Zuo, W. *et al.* Li-rich cathodes for rechargeable Li-based batteries: reaction mechanisms and advanced characterization techniques. *Energy Environ. Sci.* **2020,** *13* (12), 4450-4497.

2. Chen, M. *et al.* Lithium-rich sulfide/selenide cathodes for next-generation lithium-ion batteries: challenges and perspectives. *Chem. Commun.* **2022,** *58* (22), 3591-3600.

3. Saha, S. *et al.* Exploring the bottlenecks of anionic redox in Li-rich layered sulfides. *Nat. Energy* **2019,** *4* (11), 977-987.

4. Li, J.-C. *et al.* From Oxygen Redox to Sulfur Redox: A Paradigm for Li-Rich Layered Cathodes. *J. Am. Chem. Soc.* **2024,** *146* (11), 7274-7287.

5. House, R. A. *et al.* First-cycle voltage hysteresis in Li-rich 3d cathodes associated with molecular O_2 trapped in the bulk. *Nat. Energy* **2020,** *5* (10), 777-785.

6. House, R. A. *et al.* The role of O_2 in O-redox cathodes for Li-ion batteries. *Nat. Energy* **2021,** *6* (8), 781-789.

7. Armstrong, A. R. *et al.* Demonstrating oxygen loss and associated structural reorganization in the lithium battery cathode $Li[Ni_{0.2}Li_{0.2}Mn_{0.6}]O_2$. *J. Am. Chem. Soc.* **2006,** *128* (26), 8694-8698.

8. McColl, K. *et al.* Phase segregation and nanoconfined fluid O_2 in a lithium-rich oxide cathode. *Nat. Mater.* **2024,** *23* (6), 826-833.

9. Marie, J.-J. *et al.* Trapped O_2 and the origin of voltage fade in layered Li-rich cathodes. *Nat. Mater.* **2024,** *23* (6), 818-825.

10. Toby, B. H.; Von Dreele, R. B., GSAS-II: the genesis of a modern open-source all purpose crystallography software package. *J. Appl. Cryst.* **2013,** *46* (2), 544-549.

11. Farrow, C. L. *et al.* PDFfit2 and PDFgui: computer programs for studying nanostructure in crystals. *J. Phys.: Condend. Matter* **2007,** *19* (33), 335219.

12. Juhas, P.; Davis, T.; Farrow, C. L.; Billinge, S. J. L., PDFgetX3: a rapid and highly automatable program for processing powder diffraction data into total scattering pair distribution functions. *J. Appl. Cryst.* **2013,** *46* (2), 560-566.

13. Tucker, M. G.; Keen, D. A.; Dove, M. T.; Goodwin, A. L.; Hui, Q., RMCProfile: reverse Monte Carlo for polycrystalline materials. *J. Phys.: Condens. Matter* **2007,** *19* (33), 335218.

14. Zhang, Y.; Eremenko, M.; Krayzman, V.; Tucker, M. G.; Levin, I., New capabilities for enhancement of RMCProfile: instrumental profiles with arbitrary peak shapes for structural refinements using the reverse Monte Carlo method. *J. Appl. Cryst.* **2020,** *53* (6), 1509-1518.

15. Boivin, E. *et al.* The Role of Ni and Co in Suppressing O-Loss in Li-Rich Layered Cathodes. *Adv. Funct. Mater.* **2021,** *31* (2), 2003660.

16. Liu, T. *et al.* Origin of structural degradation in Li-rich layered oxide cathode. *Nature* **2022,** *606* (7913), 305-312.

17. Li, B. *et al.* Decoupling the roles of Ni and Co in anionic redox activity of Li-rich NMC cathodes. *Nat. Mater.* **2023,** *22* (11), 1370-1379.

18. Sathiya, M. *et al.* Reversible anionic redox chemistry in high-capacity layered-oxide electrodes. *Nat. Mater.* **2013,** *12* (9), 827-835.

19. Louis, J. *et al.* Effect of the Nature of Both Cation and Anion Substitution on the Structural Symmetry of Li-Rich 3d-Metal Chalcogenide Electrodes. *Adv. Energy Mater.* **2023**, *13* (45), 2302158.

20. Zak, J. J.; Kim, S. S.; Laskowski, F. A. L.; See, K. A., An Exploration of Sulfur Redox in Lithium Battery Cathodes. *J. Am. Chem. Soc.* **2022,** *144* (23), 10119-10132.

21. Wang, T. *et al.* Anionic redox reaction in layered $NaCr_{2/3}Ti_{1/3}S_2$ through electron holes formation and dimerization of S–S. *Nat. Commun.* **2019,** *10* (1), 4458.

22. Furuseth, S. *et al.* On the Crystal Structures of TiS_3, ZrS_3, $ZrSe_3$, $ZrTe_3$, HfS_3, and $HfSe_3$. *Acta Chem. Scand.* **1975**, *29* (6), 623-631.

23. Saha, S. Exploration of ionic conductors and Li-rich sulfides for all-solid-state batteries. Sorbonne Université, 2020.

24. Wu, K. *et al.* Unusual lattice vibration characteristics in whiskers of the pseudo-one-dimensional titanium trisulfide TiS_3. *Nat. Commun.* **2016,** *7* (1), 12952.

25. Nims, C. *et al.* Low frequency Raman Spectroscopy for micron-scale and in vivo characterization of elemental sulfur in microbial samples. *Sci. Rep.* **2019,** *9* (1), 7971.

26. Rouxel, J., Some solid state chemistry with holes: Anion–cation redox competition in solids. *Curr. Sci.* **1997,** *73* (1), 31-39.

27. Rouxel, J., Anion–Cation Redox Competition and the Formation of New Compounds in Highly Covalent Systems. *Chem. Eur. J.* **1996,** *2* (9), 1053-1059.

28. Britto, S. *et al.* Multiple Redox Modes in the Reversible Lithiation of High-Capacity, Peierls-Distorted Vanadium Sulfide. *J. Am. Chem. Soc.* **2015,** *137* (26), 8499-8508.

29. McColl, K. *et al.* Transition metal migration and O_2 formation underpin voltage hysteresis in oxygen-redox disordered rocksalt cathodes. *Nat. Commun.* **2022,** *13* (1), 5275.

30. Boivin, E. *et al.* Bulk O_2 formation and Mg displacement explain O-redox in $Na_{0.67}Mn_{0.72}Mg_{0.28}O_2$. *Joule* **2021,** *5* (5), 1267-1280.

31. House, R. A. *et al.* Delocalized electron holes on oxygen in a battery cathode. *Nat. Energy* **2023,** *8* (4), 351-360.

32. Singer, A. *et al.* Nucleation of dislocations and their dynamics in layered oxide cathode materials during battery charging. *Nat. Energy* **2018,** *3* (8), 641-647.

4

Applying S-redox Chemistry in All-Solid-State Batteries

Contents

4.1 Introduction

Compared to conventional Li-ion batteries, ASSBs using non-flammable SEs are considered a promising route for next-generation batteries due to their potential for enhanced safety and higher energy density. However, the operating voltage (> 4 V) of conventional oxide cathodes (e.g., $LiCoO_2$, $LiNi_{0.8}Mn_{0.1}Co_{0.1}O_2$) generally exceeds the electrochemical stability window (~ 1.7 – 2.3 V) of sulfide electrolytes, resulting in the formation of highly resistive interfacial layers that severely impair battery performance.[1, 2] Considerable efforts have therefore been devoted to introducing a chemically compatible and stable buffer layer between oxide cathodes and SEs, but such coating processes are usually time-consuming and costly.[3-6] An alternative approach is to replace the oxide cathodes with sulfide cathodes operating at moderate voltages yet offering high specific capacities, thereby enabling comparable energy densities to oxides without significant electrolyte degradation. Early studies have shown that sulfide cathodes such as TiS_2 and TiS_3 can effectively minimize interfacial resistances.[7-10] Nevertheless, these TM sulfides typically suffer from either limited capacity or rapid capacity fading.

In Chapter 3, the archetype Li-rich sulfide, O3-type $Li_{1.2}Ti_{0.8}S_2$ has been studied in-depth in liquid cells, where it achieved a competitive energy density of ~ 600 Wh kg^{-1} enabled by highly reversible S-redox chemistry. In this Chapter, $Li_{1.2}Ti_{0.8}S_2$ was directly applied into the ASSBs and paired with the widely employed sulfide (thiophosphate) SE, Li_6PS_5Cl (LPSC). At room temperature, ASSBs with a CAM loading of ~ 12 mg cm^{-2} exhibit a capacity of ~ 2.8 mAh cm^{-2} (> 230 mAh g^{-1} at 0.5 mA cm^{-2}) with a capacity retention of above 99% over 200 cycles under a low stack pressure of 2 MPa. At a higher CAM loading of ~ 25 mg cm^{-2}, the ASSBs achieve a capacity of ~ 6 mAh cm^{-2} (> 220 mAh g^{-1} at 1mA cm^{-2}) and maintain over 85% capacity retention for 200 cycles at 60 °C, also under 2 MPa. These results highlight a great potential of applying Li-rich sulfides with S-redox chemistry for high-performance ASSBs. To elucidate the origin of this superior electrochemical performance, this chapter investigated the electrochemical behavior, interfacial reactivity, as well as the structural and mechanical stability of $Li_{1.2}Ti_{0.8}S_2$ within ASSBs.

4.2 Experimental

General synthesis: $Li_{1.2}Ti_{0.8}S_2$ was synthesized by solid-state reaction, following the procedure described in Section 3.2. In this chapter, ball milling was applied to the as-prepared $Li_{1.2}Ti_{0.8}S_2$ to reduce the particle size. Approximately 0.6 g of $Li_{1.2}Ti_{0.8}S_2$ and 5 mm zirconia balls were loaded into a 20 mL zirconia jar at a ball-to-powder ratio of 20:1, and then sealed inside an Ar-filled glove box. Ball-milling was carried out at 200 rpm for 1, 3, 5 and 8 hours, respectively, using a Fritsch Pulverisette 7 planetary ball mill.

Electrochemical measurements: ASSBs were assembled in a customized PEEK module (5 mm inner diameter) with stainless steel plunger as current collectors. Li_6PS_5Cl powder (~ 20 mg) was first pelletised inside the module cylinder under a uniaxial pressure of 100 MPa for 1 min. The composite cathode was prepared by hand-grinding $Li_{1.2}Ti_{0.8}S_2$, Li_6PS_5Cl (MSE Supplies), and carbon nanofibers (Sigma Aldrich, > 99.9%) at a mass ratio of 70:27:3, unless otherwise specified, using an agate mortar for 30 min. Ketjenblack carbon (EC600JD, Lion Speciality Chemicals) was also explored as an alternative conductive additive. 3 – 3.5 mg (or 6 – 7 mg for the high-loading tests) of composite cathode mixture was uniformly distributed on one side of the SE pellet before being pressed at 400 MPa for 5 min. Following this, a 0.2 mm-thick indium foil (Alfa Aesar, 99.99%) disc of 5 mm diameter and a 0.2 mm-thick lithium foil (China Energy Lithium) disc of 4 mm diameter were successively placed on the other side of the SE pellet and pressed at 200 MPa for 3 min. For high-loading cells, the amount of Li-In anode was increased accordingly. The Li: In mole ratio was maintained close to the composition $Li_{0.5}In$, which can provide a stable potential of ~ 0.6 V vs. Li^+/Li as the counter electrode.[11] During operation, a sustained stack pressure of 2 MPa was applied to the cell using the screw of the stainless-steel framework. Galvanostatic cycling was performed using a Bio-Logic BCS-805 in the voltage range of ~ 1.8 – 3 V (vs. Li^+/Li) at a current density of 0.5 mA cm^{-2} (or 1 mA cm^{-2}). The voltage range was calibrated via a three-electrode cell with a lithium reference electrode. All cell assembly and electrochemical measurements are conducted in an Ar-filled glovebox with H_2O and O_2 levels below 0.1 ppm.

PFIB-SEM: PFIB-SEM was conducted on a ThermoFisher Helios G4 Plasma-FIB instrument to measure the cross-section of the composite layers. All samples were transferred from the glove box to the instrument using an airtight transfer holder to prevent exposure to moisture and air.

XPS: XPS measurement was conducted using a PHI Versaprobe (Ulvac-PHI, INC.) under ultrahigh vacuum (< 10^{-6} Pa) with Al Kα radiation. A pass energy of 55 eV was set to acquire core-level spectra. All spectra were calibrated to the carbon 1s peak at 284.8 eV and fitted using CASAXPS software.

X-ray absorption spectroscopy: Ti, P, S and Cl K-edge XANES were measured on B18 beamline at Diamond Light Source. The Ti K-edge was recorded in transmission mode. The P, S and Cl K-edges were collected using both total fluorescence yield and total electron yield, with the sample chamber filled with helium gas. Each spectrum was averaged over three repetitions.

***Operando* XRD and *in situ* X-ray CT:** *Operando* XRD and *in situ* X-ray CT experiments were performed on the I12 (JEEP) beamline at the Diamond Light Source using a custom-built airtight acetal tube cell. A 5 mm ASSB full cell (composite cathode | LPSC | $Li_4Ti_5O_{12}$), was sealed within the tube and then electrochemically cycled using a Gamry potentiostat at 30 °C under a controlled pressure of 2 MPa. Before collecting diffraction data, X-ray radiography was applied to locate the sample, ensuring that the incident X-ray beam passed through the centre of the composite cathode. Upon cycling, the PXRD was continuously collected in transmission mode with a wavelength of 0.23405 Å and an X-ray spot size of 500 × 50 μm. The sample-to-detector distance was 1200 mm. At key states of charge, tomography was conducted using optical module 4, providing a field of view (FOV) of 3.3 × 2.8 mm and a spatial resolution corresponding to a pixel size of 1.3 μm.

4.3 Results and Discussions

4.3.1 Material Characterization

$Li_{1.2}Ti_{0.8}S_2$ was synthesized by the solid-state method as outlined in Section 4.2. $Li_{1.2}Ti_{0.8}S_2$ exhibits an O3-type structure, as confirmed by joint refinement of X-ray and neutron diffraction in the last Chapter (Figure 3.1). The primary particles of $Li_{1.2}Ti_{0.8}S_2$ range from 1 to 5 µm in size and aggregate into secondary particles of around 20 – 50 µm, as shown in Figure 3.4.

In ASSBs, the cathode layer typically comprises a composite of CAM, SE and often carbon. In this Chapter, except otherwise stated, the composite cathode consists of 70 wt% $Li_{1.2}Ti_{0.8}S_2$, 27 wt% LPSC, and 3 wt% CNFs, as discussed in the next section. LPSC has been widely used as SEs due to its combination of high ionic conductivity and good ductility.[12] CNFs are commonly employed in ASSBs as a conductive additive because they can provide an efficient and interconnected electronic conduction network while not causing severe side reactions at the cathode interface.

Figure 4.1 presents a cross-sectional image of a composite cathode with 70 wt% $Li_{1.2}Ti_{0.8}S_2$, 27 wt% LPSC and 3 wt% CNFs, obtained using PFIB-SEM. The CAM and LPSC were differentiated as the darker and lighter greyscale in the image, respectively. It reveals a ~ 100 μm thick cathode layer with uniformly distributed Ti, P and Cl elements, confirming a homogeneous composite microstructure. The absence of cracking in the CAM is confirmed, and minor voids can be observed within the monolithic secondary particles. The upright curtain-shaped lines in the PFIB-SEM image were formed by the ion beam for milling. This is due to the soft nature of the sulfide materials and the lowest limitation of ion beam current.[13] The bright dots are possibly associated with the variations in surface roughness or local topography of the sample, which could increase the probability of secondary electrons reaching the detector.

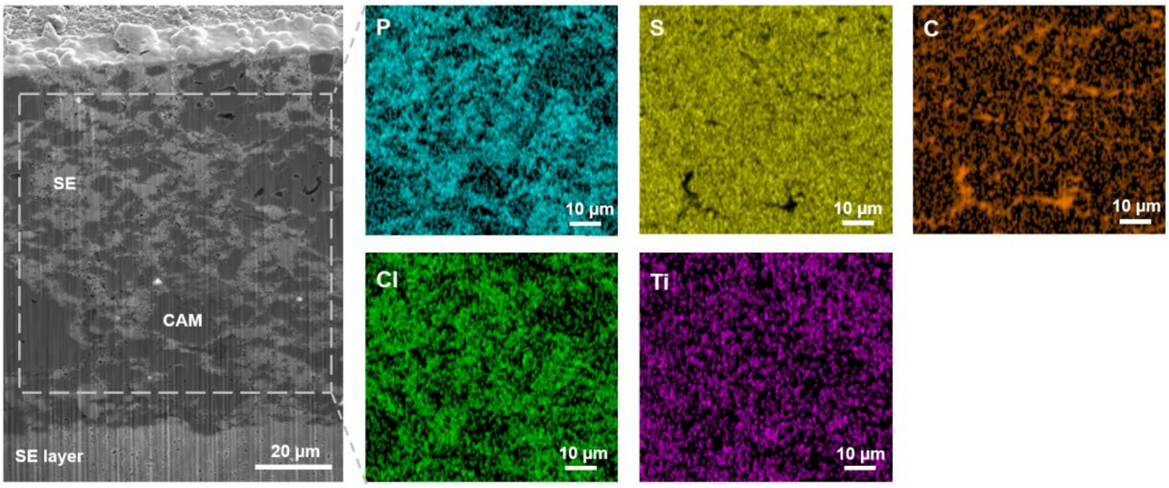

Figure 4.1: Cross-sectional PFIB-SEM image and EDX of the pristine composite cathode. The composite cathode consists of 70 wt% $Li_{1.2}Ti_{0.8}S_2$, 27 wt% LPSC and 3 wt% CNFs. The CAM and LPSC were differentiated as the darker and lighter greyscale in the PFIB-SEM image, respectively.

4.3.2 Electrochemical Characterization

The electrochemical behavior of $Li_{1.2}Ti_{0.8}S_2$ in ASSBs was examined against a Li-In alloy anode. Compared to the pure Li anode, the Li-In anode reduces interfacial reactions with the SE due to its less reductive potential (0.6 V vs. Li/Li^+), and allows cycling at a current density of > 0.5 mA cm^{-2} without dendrite formation.[11, 14, 15] Together, the use of Li-In alloy ensures the electrochemical behaviors are primarily focused on the $Li_{1.2}Ti_{0.8}S_2$. In addition, to approach more practical operating conditions, most cells in this chapter were tested under a low pressure of 2 MPa and at 30 °C.

Composite cathode manipulation

To maximize the energy density, a higher areal capacity (mAh cm^{-2}) of the CAM is desirable. As a result, optimizing the SE and carbon content in the composite cathode is important, which is strongly dependent on the properties of the materials used. In ASSBs with oxide cathodes, composite cathodes typically contain 70 – 75 wt% CAM.[16, 17] Additionally, sulfides generally exhibit higher electronic conductivity than their analogue oxide cathodes, due to the softer and more polorizable sulfur ions.[18] Therefore, to start with, a composite cathode comprising 70 wt% $Li_{1.2}Ti_{0.8}S_2$ and 30 wt% LPSC was examined within the voltage range of 1.2 – 2.4 V vs. InLi/Li^+ (~ 1.8 – 3 V vs. Li/Li^+) at a current density of 0.5 mA cm^{-2}, as shown in Figure 4.2 (a). The cell delivered a sloping load curve with a charge capacity of only 88.8 mAh g^{-1}, close to the theoretical capacity associated with the Ti^{3+}/Ti^{4+} redox (~ 97 mAh g^{-1}). This is most likely because once all Ti reaches Ti^{4+} the resulting empty conduction band with d^0 electronic configuration hinders efficient electron transport through the resistive CAM particles to the current collector. To address this, CNF was added, yielding a composite cathode with 70 wt% $Li_{1.2}Ti_{0.8}S_2$, 27 wt% LPSCl and 3wt % CNF. Under identical test conditions, the CNF-containing sample displayed a flat S-redox plateau at near 2.15 V (~ 2.75 V vs. Li/Li^+), consistent with the behavior observed in liquid cells, as shown in Section 3.3.2. The overlapping sloping regions in the charge profiles, with and without CNF, indicate that the electronic conductivity of $Li_{1.2}Ti_{0.8}S_2$ indeed drops markedly after Ti oxidation, which will be discussed further in the following Chapter. Overall, a reversible capacity of 232 mAh g^{-1} can be achieved with a CAM loading of ~ 12.5 mg cm^{-2} and current density of 0.5 mA cm^{-2} (under 2MPa, at 30 °C) in the ASSBs. The utilization (capacity) of the CAM is slightly lower than the ~ 250 mAh g^{-1} obtained in liquid cells under equivalent conditions (CAM loading, current density and test temperature), as depicted in Figure A4.1. Further increasing the CNFs to 8 wt% resulted in greater polarization and reduced capacity, suggesting that the ionic pathways might be disrupted in the composite cathode (Figure 4.2 (a)).

For subsequent optimization, the composite cathode with 70wt% $Li_{1.2}Ti_{0.8}S_2$, 27wt% LPSC and 3wt% CNF was used as the baseline (black curve), with only one parameter varied (red curve) in each test to isolate its effect on $Li_{1.2}Ti_{0.8}S_2$ behavior in ASSBs. As shown in Figure 4.2 (b), a modest increase in the CAM loading from 70 to 75 wt% significantly raised overpotentials, even in the Ti oxidation region, indicating ionic percolation limitations. In Figure 4.2 (c), similar behavior was observed when doubling the CAM loading to 25 mg cm^{-2}, attributed to the longer and sluggish ionic diffusion within a thick composite cathode layer.

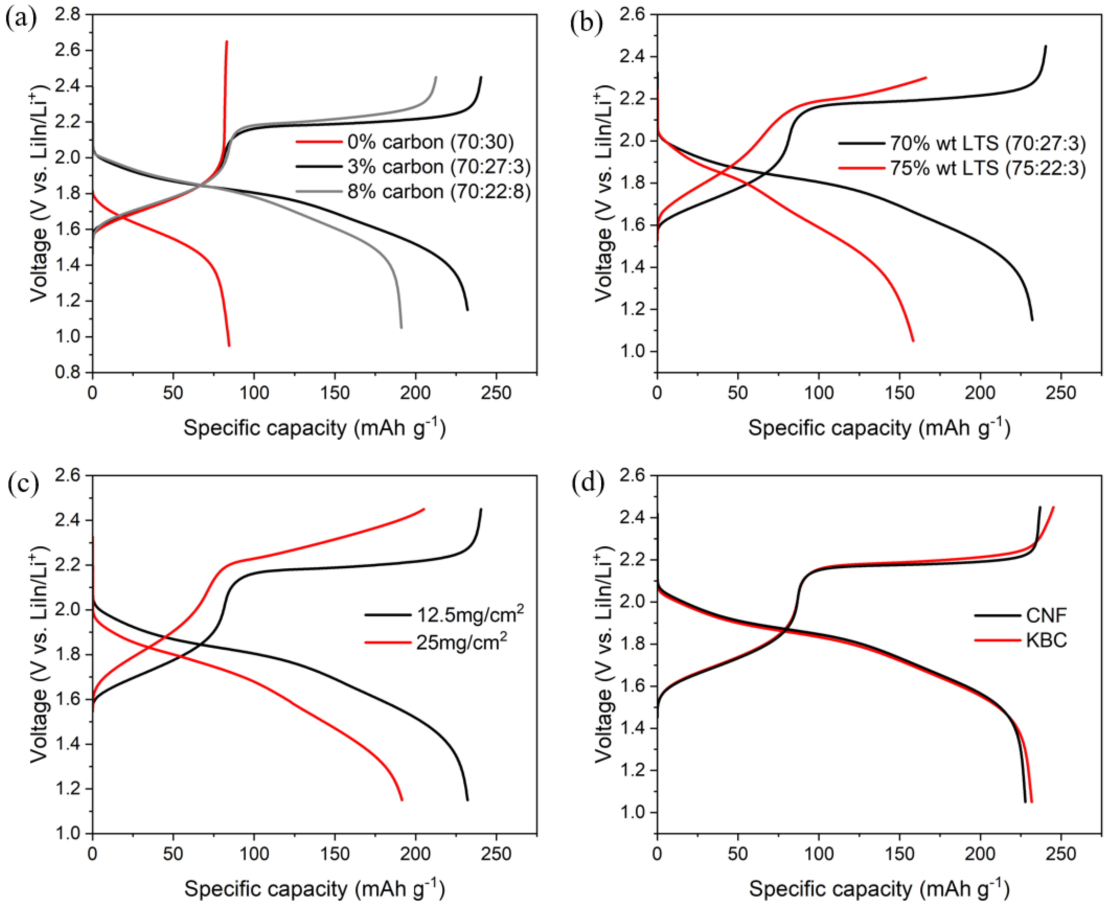

Figure 4.2: First-cycle load curves for different composite cathodes. All cells were measured at 0.5 mA cm^{-2}, 30 °C, under 2 MPa. The black curves correspond to a composite ratio of 70 wt% CAM: 27 wt% LPSC: 3 wt% CNFs, with a CAM loading of 12.5 mg cm^{-2}. In each panel, one parameter was varied to evaluate CAM behavior in ASSBs: (a) carbon content, (b) CAM content, (c) CAM loading, and (d) carbon type.

In addition, Ketjenblack carbon (KBC), which possesses a specific surface area approximately 50 times higher than that of CNF,[19] was explored as an alternative conductive additive. Previous studies on oxide-based cathodes ASSBs have reported that high-surface-area carbons, particularly KBC, can accelerate SE decomposition during charging, leading to capacity loss and reduced cyclability.[20, 21] Given the moderate cycling voltage of Li-rich sulfides, we wondered whether KBC could enhance electron percolation and CAM utilization without adversely affecting the battery performance. As shown in Figure 4.2 (d), the cell containing 3 wt% KBC delivered slightly higher discharge capacity (~ 4 mAh g^{-1}) but ~ 2% lower coulombic efficiency, with the end of charge profile being more sloping, which deviates from the behavior of the cell using CNF and the liquid cell. These results suggest that the additional charge capacity above 2.3 V (vs. LiIn/Li^{+}) most likely arises from interfacial side reaction, exacerbated by the increased contact between KBC and SE. Therefore, in the subsequent experiment, CNF is retained as the conductive additive.

Furthermore, the particle size of the CAM has a significant effect on its kinetic behavior, because smaller cathode particles generally prompt mass transport of Li^+ by shortening the diffusion pathway. Herein, the pristine $Li_{1.2}Ti_{0.8}S_2$ was ball-milled for 1, 3, 5 and 8 hours, respectively. To minimize extra structural changes, a relatively mild ball-milling speed of 200 rpm was applied, as described in Section 4.2. As shown in Figure 4.3 (a), all ball-milled samples retained the $R\overline{3}m$ structure, with no evidence of additional crystalline phase. However, progressive peak broadening was observed with increasing ball milling time, primarily attributed to the reduced crystallite size and increased lattice strain. SEM images in Figure A4.2 revealed that even after 1 hour of milling, most primary particles were reduced to below 0.5 µm, smaller than the LPSC (~ 1 – 3 µm) used in this chapter. Longer milling time leads to a further reduced particle size with irregular morphologies.

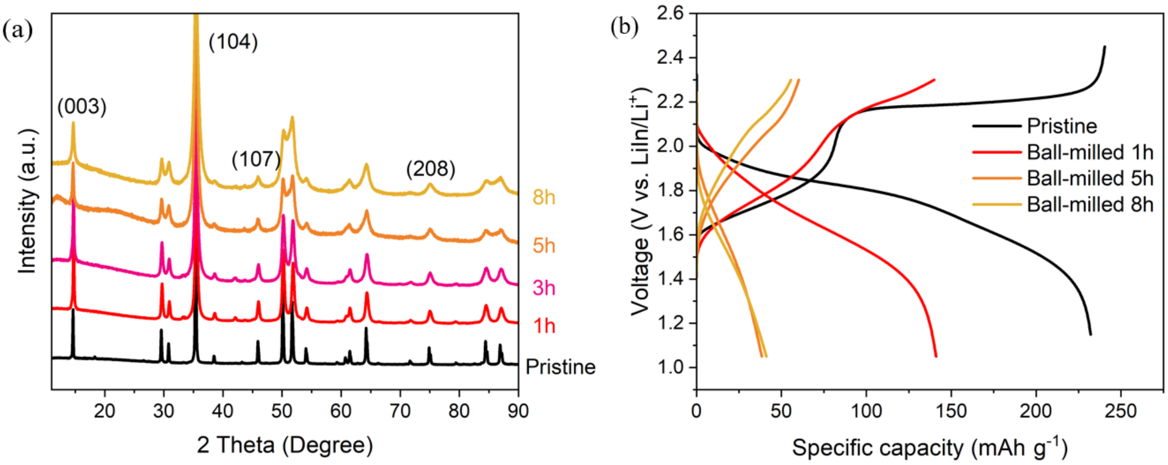

Figure 4.3: (a) XRD patterns and (b) first-cycle load curves of composite cathodes using $Li_{1.2}Ti_{0.8}S_2$ with different ball-milling times. All cells were tested at 0.5 mA cm^{-2}, 30 °C, under 2 MPa. The composite cathodes contained 70 wt% CAM, 27 wt% LPSC, and 3 wt% CNFs, with a CAM loading of 12.5 mg cm^{-2}.

As shown in Figure 4.3 (b), with the same 70:27:3 wt% ratio, the 1h ball-milled sample exhibited a discharge capacity of only 140 mAh g^{-1}, accompanied by substantially higher polarization compared to the pristine. For the 5h and 8h ball-milled samples, the capacity dropped below 50 mAh g^{-1}. These inferior electrochemical performances are likely due to the significant drop in the CAM-to-SE particle size ratio, which lowers the probability of direct CAM-SE contact and thereby disrupts the ionic percolation network.[22] As a result, more CAM particles become inactive, or Li^+ ions must diffuse through the less conductive CAM particles, leading to reduced capacity and increased overpotential observed in Figure 4.3 (b). These results suggest that in ASSBs, optimizing particle size requires consideration of both CAM and SE dimensions. More gentle methods, like cryo ball-milling or sonication, could be explored to break apart the secondary particles of $Li_{1.2}Ti_{0.8}S_2$ without reducing the primary particle size. Based on the above investigations, in the following experiment, the as-prepared $Li_{1.2}Ti_{0.8}S_2$ remains as the CAM material, and 70:27:3 wt% ratio was confirmed to be used as a composite cathode.

Varied measurement conditions

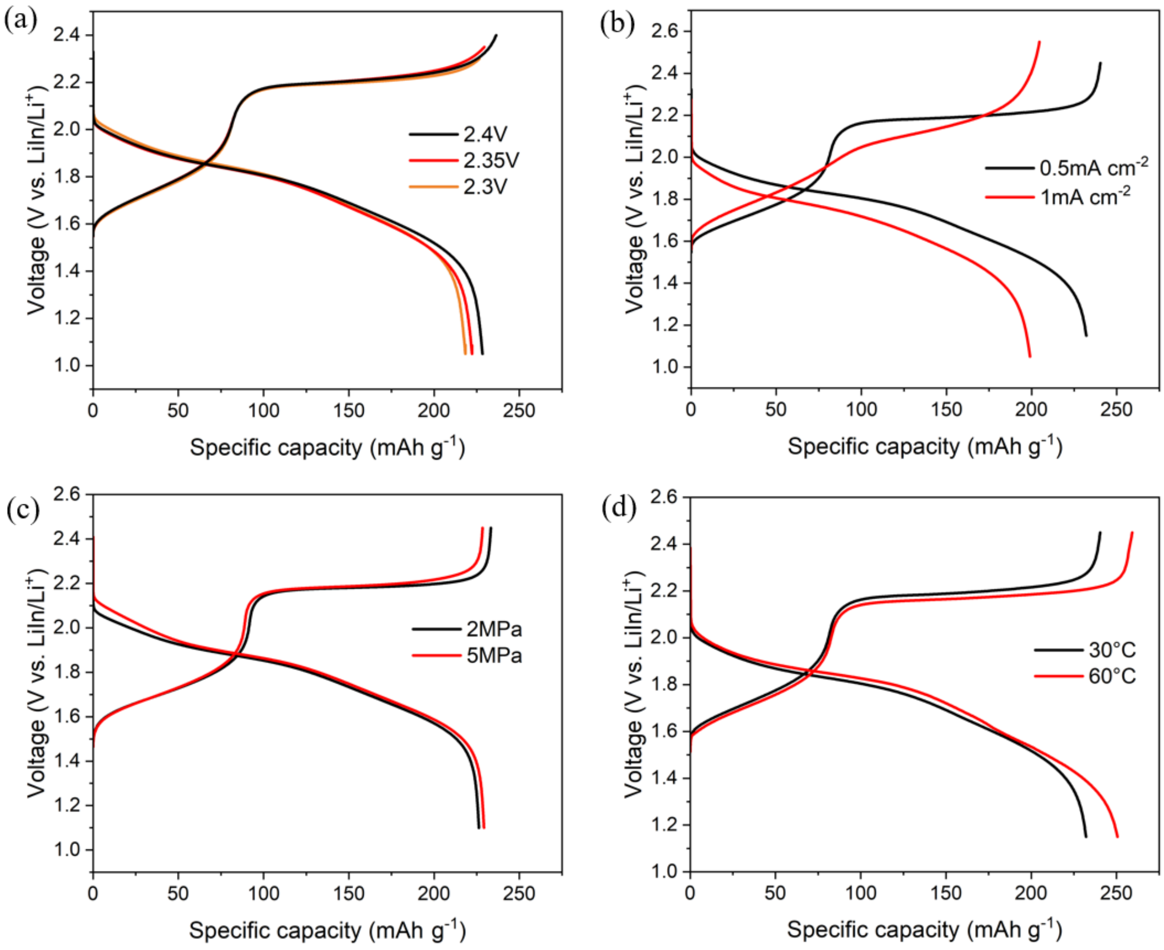

Figure 4.4: First-cycle load curves of the composite cathodes (70 wt% CAM: 27 wt% LPSC: 3 wt% CNFs, with a CAM loading of 12.5 mg cm^{-2}) measured under different operated conditions. The black curves correspond to measurements at 0.5 mA cm^{-2}, 30 °C, under 2 MPa, with a top cut-off voltage of 2.4 V. In each panel, one parameter was varied to evaluate CAM behavior in ASSBs: (a) top cut-off voltage, (b) current density, (c) applied pressure, and (d) operating temperature.

To further assess the behavior of $Li_{1.2}Ti_{0.8}S_2$ in ASSBs, different operated conditions were applied. First, to minimize potential interfacial side reactions in composite cathodes, a lower upper cut-off voltage is always preferred. However, the results in Figure 4.4 (a) suggest that charging to 2.4 V (~ 3 V vs. Li/Li^+) is necessary to achieve a higher reversible capacity. Second, after doubling the current density to 1 mA cm^{-2}, the CAM utilization decreased as expected, while a capacity of ~ 200 mAh g^{-1} was still achievable (Figure 4.4 (b)). Increasing the external pressure to 5 MPa, however, produced negligible improvement, as shown in Figure 4.4 (c). Interestingly, raising the temperature from 30 °C to 60 °C (Figure 4.4 (d)) enabled a reversible capacity of ~ 250 mAh g^{-1} at 0.5 mA cm^{-2} under 2 MPa, nearly the same as that in liquid electrolyte cells at 30 °C (Figure A 4.1), suggesting that the improved ionic transport within the composite cathode at 60 °C facilitates full capacity delivery.

Cycling stability

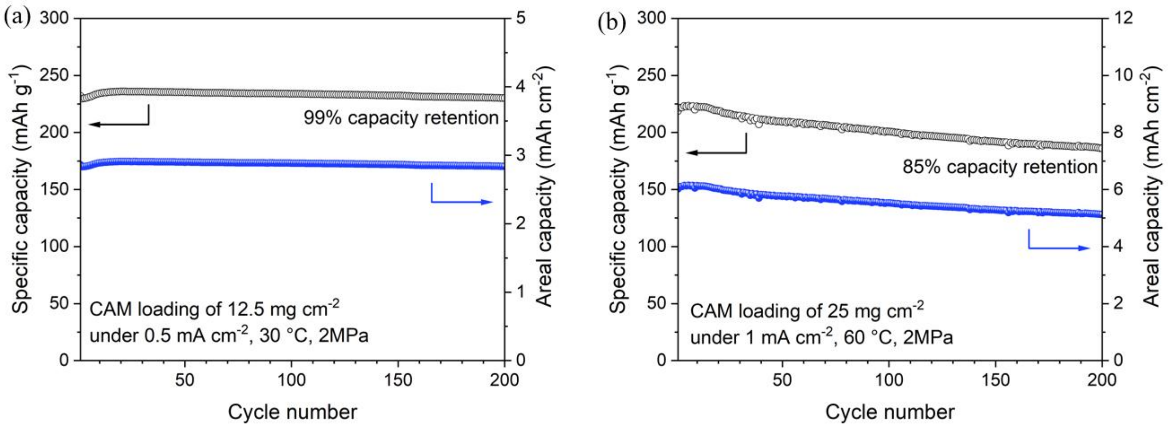

Figure 4.5: The cycling performance of the composite cathode (70 wt% CAM: 27 wt% LPSC: 3 wt% CNFs) under 2 MPa.

Excitingly, $Li_{1.2}Ti_{0.8}S_2$ with a CAM loading of ~ 12 mg cm^{-2} exhibits a superior capacity retention of ~ 99% after 200 cycles at 0.5 mA cm^{-2}, while maintaining a satisfactory areal capacity of ~ 2.8 mAh cm^{-2}, as shown in Figure 4.5 (a). Even at a high loading of ~ 25 mg cm^{-2}, the ASSB delivers an areal capacity of ~ 6 mAh cm^{-2} and outstanding cycling stability (> 85%) over 200 cycles at 60°C under a current density of 1 mA cm^{-2} (Figure 4.5 (b)). Importantly, this excellent cyclability was achieved without any surface coating, particle size refinement, or composition optimization, highlighting that Li-rich sulfides with S-redox chemistry could be an attractive possibility yet to be explored in ASSBs. In sharp contrast, $Li_{1.2}Ti_{0.8}S_2$ in liquid cells under comparable conditions (12 mg cm^{-2}, 0.5 mA cm^{-2}

and 30 °C) shows a capacity retention of only 16.3% after 200 cycles, as shown in Figure A4.3. Such a rapid capacity decay is primarily caused by the dissolution of sulfur ions into electrolyte solutions with polar solvents,[23, 24] which is inherently suppressed by using SE. Nevertheless, similar to $Li_{1.2}Ti_{0.8}S_2$ in liquid cells (Figure 3.5), in ASSBs, the material exhibited a diminished charging plateau from the second cycle (Figure A4.4), due to the irreversible in-plane Ti aggregation within the bulk structure, as discussed in Chapter 3. With extended cycling, progressive voltage decay and disappearance of the charging plateau are observed in both systems, regardless of electrolyte type, suggesting that the cycling profile evolution primarily originates from irreversible bulk structural changes. The continued growth of vacancy clusters and Ti migration over the cycling offers a likely explanation, analogous to the processes observed in O-redox cathodes.[25]

4.3.3 Charge Compensation Process

To follow how charge compensation is achieved in $Li_{1.2}Ti_{0.8}S_2$ within ASSBs, Ti K-edge and S K-edge XANES were employed on *ex situ* samples collected at different states of charge, as shown in Figure 4.6 (a). The Ti K-edge of the pristine composite cathode (PCC) lies between that of the Ti^{3+} reference compound $LiTiS_2$ and the Ti^{4+} standard in TiS_2, consistent with the nominal +3.5, as shown in Figure 4.6 (b). At the point just before the S-redox plateau (BSP, 2.1 V vs. $LiIn/Li^+$), the Ti K-edge spectrum closely matches that of the Ti^{4+} standard, suggesting Ti has reached +4. After charging across the plateau to the fully charged state (2.4 V vs. $LiIn/Li^+$), Ti XANES data remain unchanged, implying that a different charge compensation mechanism, S-redox, is taking place. Upon discharge, the Ti K-edge starts to shift back from around the half discharge (HD) point at 1.8 V (vs. $LiIn/Li^+$) and is reversibly recovered to nearly the PCC state by the fully discharged point (FD, 1.2 V vs. $LiIn/Li^+$). These results clearly suggest that the Ti redox of $Li_{1.2}Ti_{0.8}S_2$ in ASSBs follows the same behavior as in liquid electrolyte cells, as studied in Section 3.3.3.

Turning now to the S K-edge XANES in Figure 4.6 (c), the spectra of all composite cathode samples show contributions from both the sulfide cathode and the LPSC electrolyte. Compared to the pristine pure cathode (PPC), the PCC displays a much more intense edge feature at ~ 2470.6 eV, arising from the pronounced peak of LPSC at a very similar position, ~ 2470.7 eV. In the FC sample, an additional shoulder emerges on the right side of the original edge at ~2470.6 eV in the PCC, as highlighted in light beige, and disappears after full discharge. As revealed in Chapter 3, this extra signal originates from oxidized S species in $Li_{1.2}Ti_{0.8}S_2$, specifically S_2^{2-}, although its intensity is partially masked by overlapping contributions from LPSC. By contrast, the S main K-edge feature at approximately 2477 eV remains dominated by the cathode, which shifts to higher energy after passing the BSP state and continuously shifts back to nearly the pristine state throughout the discharge, similar to that in liquid cells (Section 3.3.3).

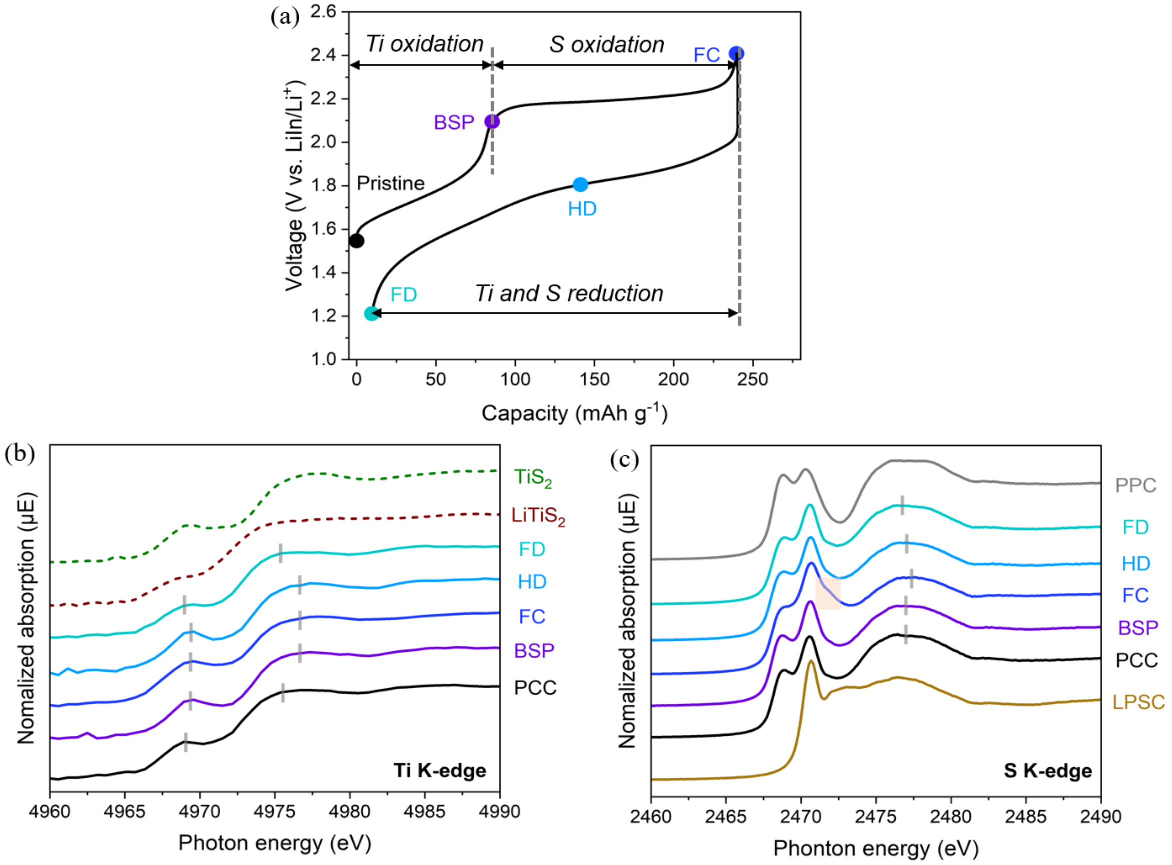

Figure 4.6: (a) Load profiles of the first cycle at 0.5 mA cm^{-2}. Coloured markers denote specific states of charge selected for detailed study during the first cycle, including pristine composite cathode (PCC), charge to before S redox plateau (BSP, 2.1V), fully charged (FC, 2.4V), half discharged (HD, 1.8V), fully discharged (FD, 1.2V), along with reference samples. (b), (c), Ti K-edge (b) and S K-edge (c) XANES spectra acquired at the states of charge highlighted in panel a, along with reference compounds (TiS_2, $LiTiS_2$, LPSC and pristine pure cathode (PPC)).

4.3.4 Surface Reactivity

Ti and P XPS

To investigate the origin of the superior cyclability of $Li_{1.2}Ti_{0.8}S_2$ in ASSBs, *ex situ* Ti 2*p* and P 2*p* XPS spectra were first collected to examine the interficial compatibility between $Li_{1.2}Ti_{0.8}S_2$ and the LPSC upon cycling. Quantitative analysis on the evolution of S 2*p* XPS spectra in this case is difficult due to overlapping contributions from multiple species, including S^{2-} and S_2^{2-} in the cathode, S^{2-} and PS_4^{3-} from the SE, and possible sulfur-containing side products such as Li_2S and sulphites, which have been reported previously in oxide-cathode-based ASSBs.[26-28]

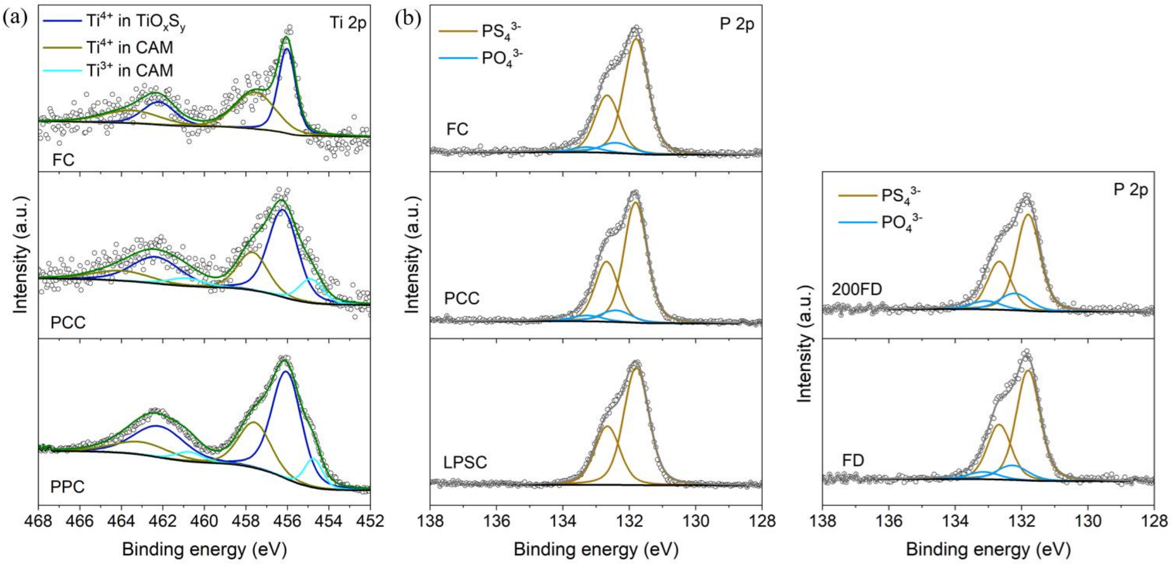

Figure 4.7: Ti 2*p* (a) and P 2*p* (b) XPS data for a composite cathode at different states of charge, including PCC, FC, FD and 200FD (fully discharged state in the 200th cycle). The PPC and LPSC were also included as references.

The Ti 2*p* core-level XPS spectra are shown in Figure 4.7 (a). For $Li_{1.2}Ti_{0.8}S_2$ (PPC), three doublets ($2p_{3/2}/2p_{1/2}$) are observed, which can be attributed to the Ti^{3+} (Ti $2p_{3/2}$ at 454.8 eV) and Ti^{4+} (Ti $2p_{3/2}$ at 457.6 eV) species in the $Li_{1.2}Ti_{0.8}S_2$ structure, along with the Ti^{4+} (Ti $2p_{3/2}$ at 456.1 eV) component in an oxygen or mixed oxygen/sulfur environment. The presence of the latter Ti^{4+} (Ti $2p_{3/2}$ at 456.1 eV) species is due to the strong affinity of Ti for trace oxygen during synthesis, which is challenging to eliminate even under strict experimental atmosphere conditions.[29, 30] After PPC is in contact with LPSC and CNFs, the proportions of these surface components remain largely unchanged, as shown in the Ti 2*p* spectrum of PCC, indicating the high chemical stability of $Li_{1.2}Ti_{0.8}S_2$ toward LPSC. This behavior contrasts with the commonly observed spontaneous decomposition reaction between Ni-rich oxides and LPSC/CNFs, which results in pronounced Ni reduction on the cathode surface.[26] At the FC state, the Ti^{3+} signal disappears with Ti oxidation, in line with the Ti K-edge XANES results discussed in Section 4.3.3.

Turning to the P 2*p* XPS data in Figure 4.7 (b), LPSC exhibits a single doublet corresponding to PS_4^{3-} tetrahedra units of the LPSC (P $2p_{3/2}$ at 131.8 eV). In the PCC, when LPSC is in contact with $Li_{1.2}Ti_{0.8}S_2$ /CNFs, a minor amount of PO_4^{3-} is detected,[31] probably because of the interfacial reactions between residual oxygen species on the cathode surface and LPSC. Notably, in both the FC and FD samples, even in the discharged state after 200 cycles (200 FD), the P 2*p* spectrum does not change much compared to the PCC, suggesting that the phosphorus environment in LPSC remains largely stable during cycling. Moreover, no P_2S_x species are detected in any of the states, indicating that the typical decomposition pathway of LPSC, reported for ASSBs employing oxide cathodes (even with surface coatings) is effectively suppressed in this system.[26, 32] These observations highlight the better chemical stability of the Li-rich sulfide/sulfide electrolyte interface compared to the oxide/sulfide electrolyte interface.

P, Cl and S K-edge XANES

To further assess the interficial stability between $Li_{1.2}Ti_{0.8}S_2$ and LPSC, P, Cl and S K-edge XANES spectra were collected at the PCC, FD, and 200FD states under both TEY and TFY modes. Similar to XPS, TEY-XANES is surface-sensitive (~ 5 – 10 nm), while TFY-XANES probes deeper into the bulk (~ 50 – 100 nm).

The TEY spectra are shown in Figure 4.8 (a). At the P K-edge, both the spectral shape and intensity remain nearly unchanged upon extended cycling, consistent with the P 2*p* XPS results, confirming the stable thiophosphate environments. Similarly, the Cl K-edge spectra show negligible variations across the three samples. However, the S K-edge spectrum exhibits increased intensities near 2472 eV and 2482 eV after the first cycle, which typically correspond to Li_2S and sulphite/sulfate species, respectively. Additionally, the pre-edge feature at 2468.8 eV, associated with hybridized S 3*p*/Ti 3*d* states in the CAM, decreases slightly in intensity, indicating changes in the chemical states or local structural environments at the cathode surface. These observations show that, even for Li-rich sulfide cathodes, interfacial side reactions occur between the CAM and LPSC/CNFs interfaces. After 200 cycles, these new features evolve further, pointing to progressive interfacial reactions. Overall, the interfacial reactions involve S more significantly than P or Cl in LPSC, similar to that observed in oxide-cathode-based ASSBs.[26, 27]

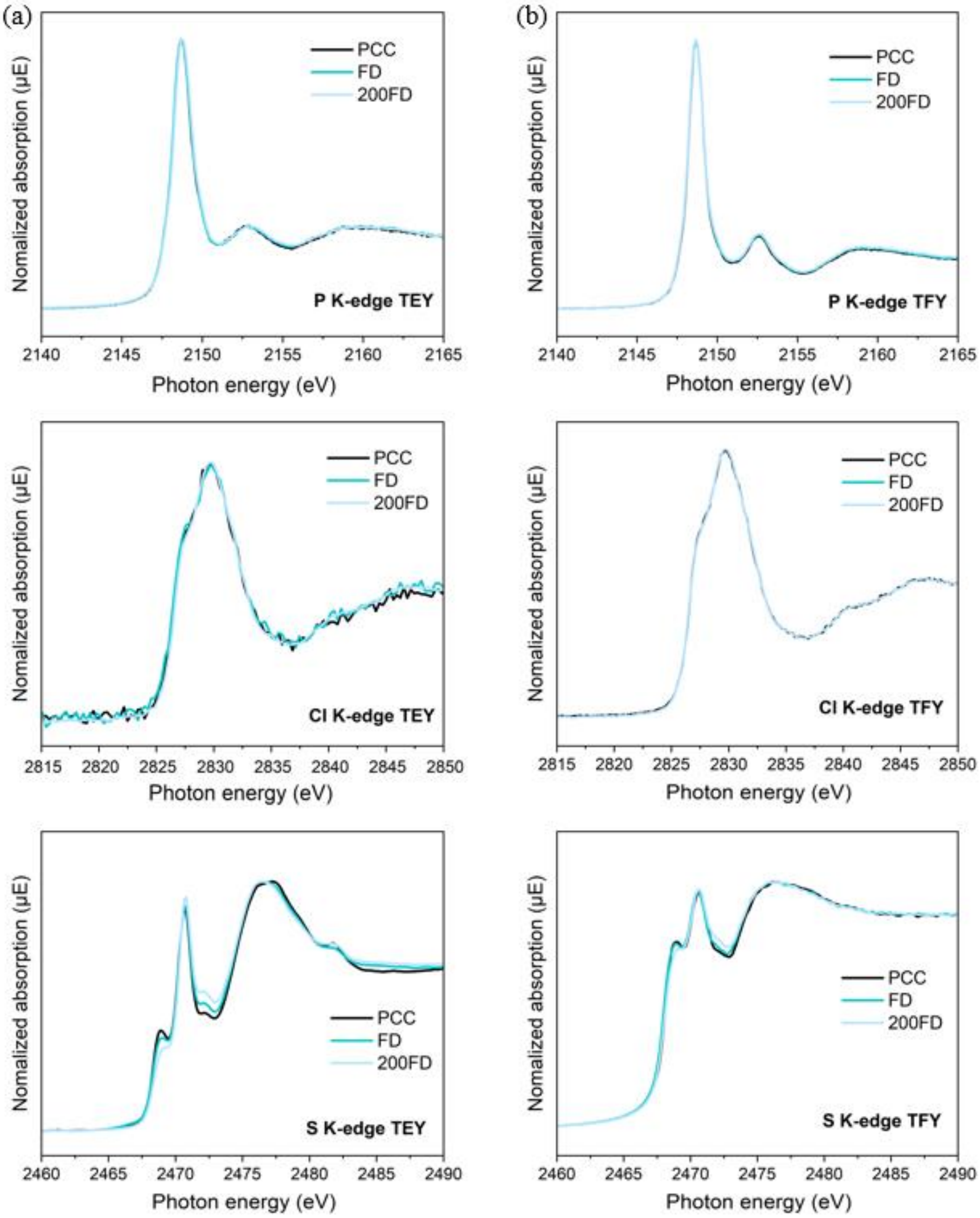

Figure 4.8: TEY-XANES (a) and TFY-XANES (b) spectra at the P, Cl and S K-edge for composite cathode at the PCC, FD and 200FD states.

To probe deeper into the bulk, TFY-XANES spectra of the P, Cl, and S K-edges were recorded after 200 cycles, as shown in Figure 4.8 (b). Under TFY mode, both the P and Cl K-edge spectra remain largely unchanged after prolonged cycling, in agreement with the TEY results, and also remain stable at the charged state (Figure A4.5). By contrast, the S K-edge TFY spectra display far less evolution compared to the surface-sensitive TEY results. The FD sample exhibits a spectrum nearly identical to that of the PCC state, and the 200FD sample displays only minor spectral evolutions. Notably, the sulfide/sulfate feature at ~ 2482 eV, detected under TEY mode, is absent in TFY-XANES even after 200 cycles. This contrast between S K-edge TEY and TFY measurements indicates that interfacial side reactions are largely confined to the very top surface region and do not significantly penetrate the bulk of the LPSC. Such behavior differs sharply from that of Ni-rich oxides/LPSC interfaces, where S K-edge shifts and strong sulphite/sulfate signals typically develop in TFY-XAMES spectra after cycling, suggesting much deeper interfacial degradation.[26]

Taken together, the XPS and XANES spectra (collected under both TEY and TFY modes) provide compelling evidence of the superior chemical compatibility at the $Li_{1.2}Ti_{0.8}S_2$/LPSC interface, in line with the excellent cyclability shown in Section 4.3.2. In this system, the P and Cl in LPSC remain chemically stable throughout prolonged cycling, and S-related interfacial side reactions are largely limited to the near-surface region, in stark contrast to the extensive interfacial degradation observed at oxide cathodes/LPSC interfaces.[2, 26, 33]

4.3.5 Long-range Structural Evolution

In addition to interfacial side reactions, the volume changes of the CAM particles during cycling can induce microscopic CAM/SE interfacial delamination due to rigid mechanical contact, thus resulting in CAM particle isolation, increased interfacial resistance, and ultimately degraded performance.[13, 34] To evaluate the volume changes of $Li_{1.2}Ti_{0.8}S_2$ under operating conditions (~ 12.5 mg cm^{-2}, 30 °C, 2 MPa), *operando* XRD was conducted over the initial two cycles. To minimize the influence of the counter electrode and focus on the behavior of the composite cathode, $Li_4Ti_5O_{12}$ was used as the anode due to its negligible volume change during lithiation/delithiation.[35] In addition, *in situ* X-ray CT and *ex situ* PFIB-SEM were employed to further probe the mechanical stability of the CAM and the composite cathode microstructure upon cycling.

Operando XRD

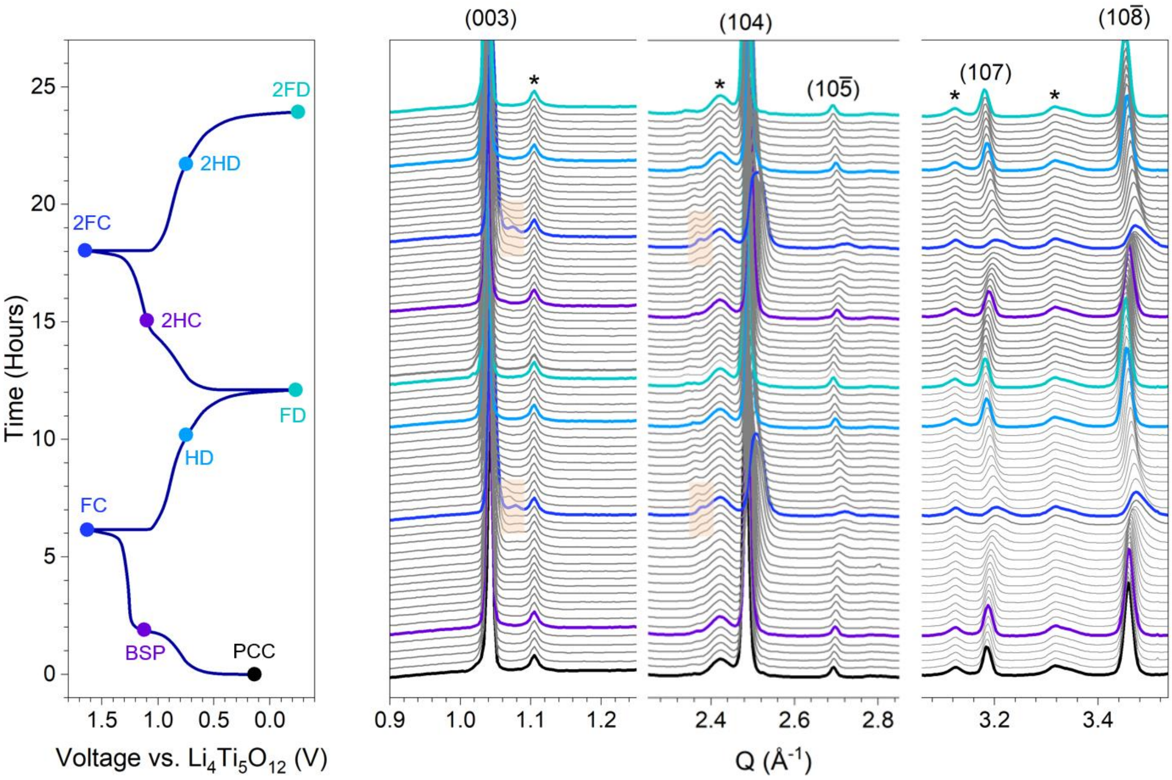

Figure 4.9: Structure evolution of the composite cathode during the first two cycles. $Li_{1.2}Ti_{0.8}S_2$ predominantly retains the O3 phase, with only a minor O1 phase (< 5 wt%, highlighted in light beige) at highly delithiated states. Asterisks mark Bragg peaks originating from LPSC and the acetyl cell. The left panel shows the corresponding cycling profile for the first two cycles at 0.5 mA cm $^{-2}$, 30 °C, under 2 MPa.

The *operando* XRD results during the first two cycles are shown in Figure 4.9. The structure at key states of charge, including the PCC, BSP, FC, FD, 2FC (fully charged states in the second cycle) and 2FD (fully discharged states in the second cycle), was further examined by Rietveld refinement, as shown in Figure 4.10 and Figure A4.6. Upon the first charge, the (003) peak position remains largely invariant, while the (104), (10$\bar{5}$) and (107) peaks continuously shift to higher angles. Compared to the PCC, the BSP state shows a slight contraction of the *a* lattice parameter and expansion of *c*. At later stages of charge, an O3-O1 phase transition occurs, evidenced by the appearance of new Bragg peaks at ~ 1.08 and 2.36 Å^{-1} (as highlighted) corresponding to the (001) and (10$\bar{1}$) reflections of the O1-type structure, respectively. At the top of charge, the cathode remains dominated by the O3-type phase (> 95 wt%), with only a minor contribution from the O1 phase. In addition, within the charged

O3 structure, both *a* and *c* parameters contract, and the minor O1 structure exhibits similar interlayer and intralayer S–S distances to those of the O3 phase (Table A4.1). Upon discharge, the structural evolution proceeds in a reverse manner, with the FD sample almost identical to the pristine state, showing no residual O1 phase. Overall, the O3 phase undergoes only minor lattice changes in the first cycle, with $\Delta a = 1.42\ \%$, $\Delta c = 0.61\%$, and a corresponding volume change of $\Delta V = 3.3\ \%$, consistent with its excellent cyclability. During the second cycle, the structural evolution and lattice parameter change mirror that of the first, as shown in Figure 4.10 and Figure A4.6, further confirming overall structural stability and highly reversible phase evolution. Similar O3-O1 structural evolution was observed in liquid cells (Section 3.3.3), though with ~ 10 wt% more O1 phase formation, likely due to more Li^+ extraction.

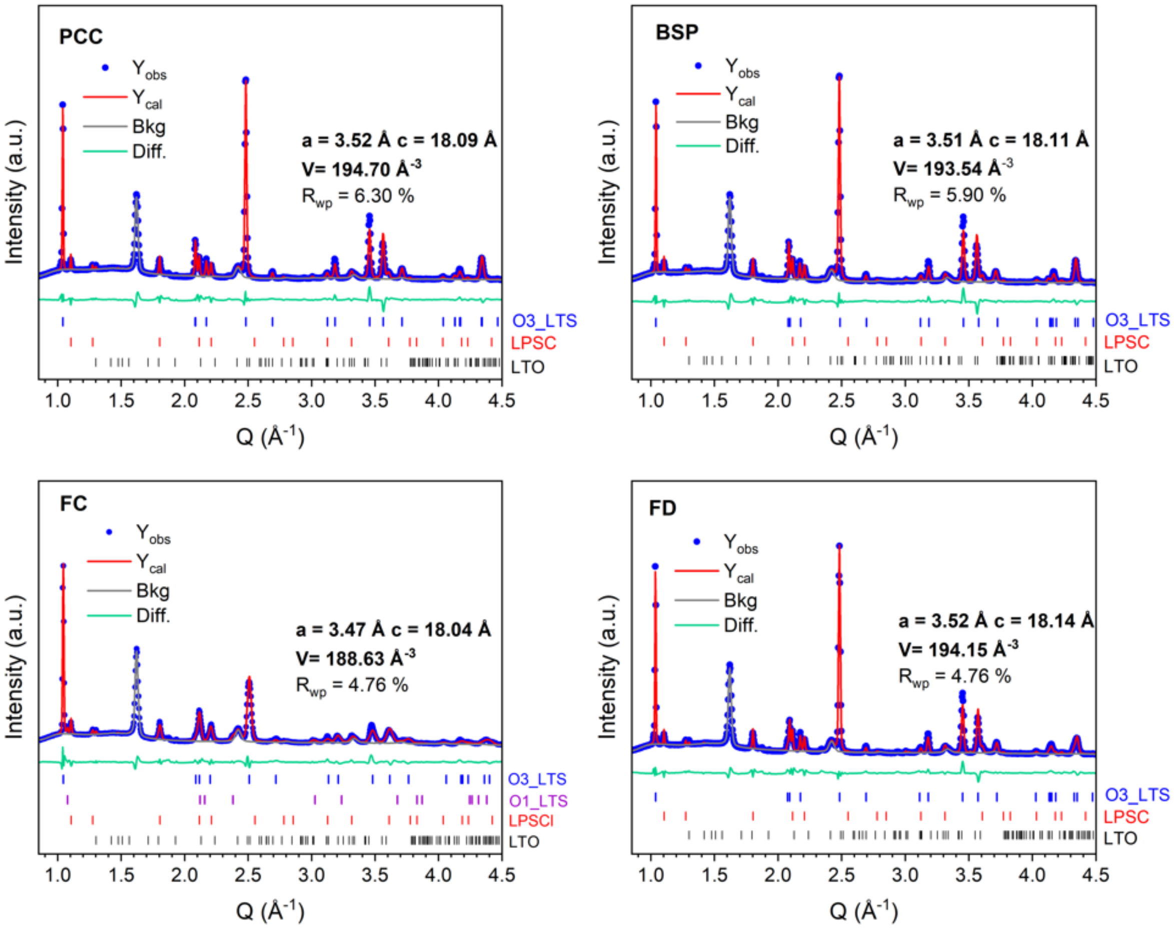

Figure 4.10: Rietveld refinement of the key states of charge, including PCC, BSP, FC and FD during the first cycle. For the dominant O3 phase, lattice variations are $\Delta a = 1.42\ \%; \Delta c = 0.61\ \%;\ \Delta V = 3.3\ \%$ across the cycle.

Notably, the small overall volume change arises primarily from the minimal variation in the *c* lattice parameter, despite nearly one mole of Li^+ being (de)intercalated per formula unit. This stability is consistent with the minimal change in the (003) peak position, which reflects the interslab spacing. Such behavior contrasts greatly with Ni-rich layered oxides, where the *c* parameter initially expands during delithiation due to reduced screening effect and enhanced O-O repulsion in the LiO_2 layer, but collapses in the latter stage of charging when severe Li depletion destabilises the original layered framework, leading to slab gliding and large volume changes typically exceeding 6% (after charging to 4.3 V vs. Li^+/Li).[36]

In terms of $Li_{1.2}Ti_{0.8}S_2$, a slight expansion of the *c* parameter before the BSP state is also attributed to Li^+ extraction and resultant increased S–S repulsion between LiS_2 layers. However, across the S-redox plateau, the (003) peak remains stable without collapse. As established in Chapter 3, S^{2-} ions are oxidized to S_2^{2-} dimers that are accommodated in the vacancy cluster formed in the TM layer, accompanied by partial S atoms being displaced from their original lattice site. This process reduces the net negative charge density on sulfur layers, thereby minimizing repulsions between LiS_2 layers and stabilizing the *c* lattice throughout cycling. Similar suppression of the *c* lattice variation has also been observed in O-redox cathodes, such as $Na_{0.72}Li_{0.24}Mn_{0.76}O_2$, and $Li_{1.2}Ni_{0.36}Mn_{0.44}O_2$.[37, 38]

In situ **X-ray CT**

The microstructural evolution of the composite cathode was investigated using synchrotron *in situ* X-ray CT at nine key states of charge, including PCC, BSP, FC, HD, and FD states in the first cycle, and half charge, full charge, half discharged and fully discharged states in the second cycle (denoted as 2HC, 2FC, 2HD and 2FD, respectively). Figure 4.11 (a) and (b) show the 3D-rendered composite cathode at pristine and FC states, respectively, where the CAM (purple), LPSC (yellow) and voids (green) are clearly distinguished. The spatial resolution corresponds to a pixel size of 1.3 μm, below which the CNFs can not be resolved. The images of rendered structures for the other seven states are provided in Figure A4.7. This phase differentiation in the X-ray CT data is enabled by absorption contrast, as illustrated in the top-down slices of the pristine and FC samples (Figure 4.11 (c) and (d)). The brighter regions (highlighted in red) correspond to $Li_{1.2}Ti_{0.8}S_2$ particles with higher relative electron density. The darker regions (green) represent voids, and the surrounding grey regions correspond to LPSC/CNF. The non-uniform greyscale within LPSC particles arises from the intrinsic microstructural inhomogeneity and imaging noise. The X-ray CT 2D slices for the other seven states are shown in Figure A4.7.

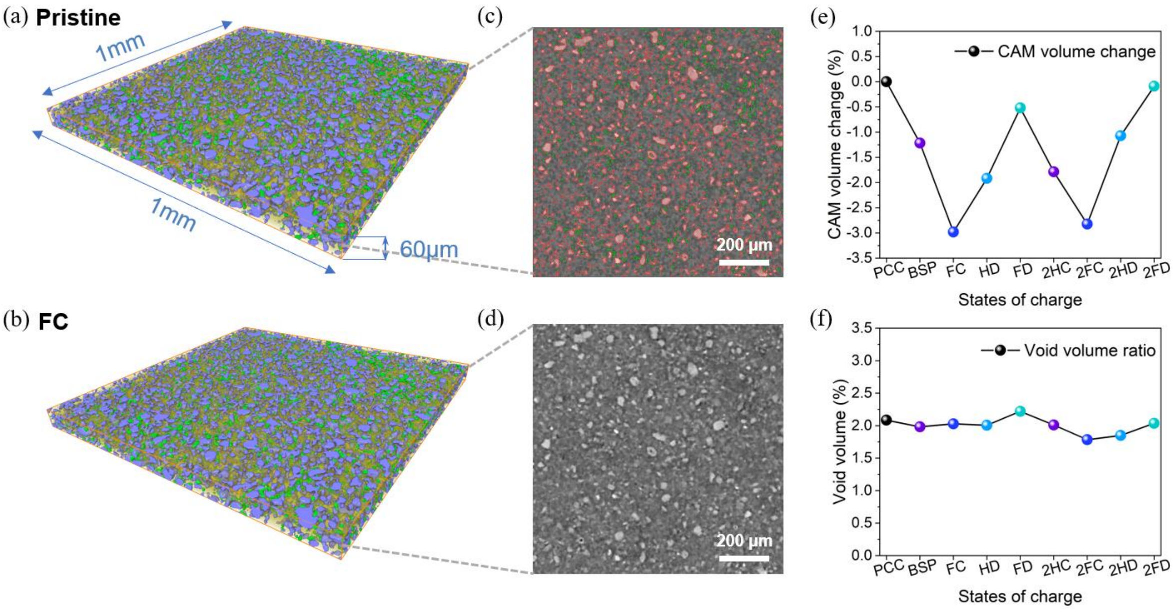

Figure 4.11: *In situ* X-ray CT analysis of the composite cathode during operation. The cell was cycled at 0.5 mA cm^{-2} at room temperature under a stack pressure of 2 MPa, with an areal capacity of ~ 3 mAh cm^{-2}. (a), (b), 3D-rendered structures of the composite cathode in the pristine (a) and FC (b) states. Purple region denotes CAM particles, green represents voids, and the remaining volume corresponds to the LPSC electrolyte and CNF domain. The reconstructed volume is 1mm × 1mm × 60 μm. (c), (d), 2D X-ray CT virtual cross-sections of the pristine (c) and FC (d) states, illustrating the segmentation of CAM (red), voids (green), and LPSC/CNF (grey) based on grey scale variations in different regions. (e), (f), Evolution of CAM volume change (e) and void fraction (f) at key states of charge (as indicated in the left panel of Figure 4.9), derived from the 3D reconstructed composite cathodes. The X-ray CT data were processed by Dr Bingkun Hu, and the sample was prepared by me.

Quantitative analysis of the reconstructed structures reveals the evolution of CAM and void volumes across the key states of charge, as summarized in Figure 4.11 (e) and (f). Upon charging, the CAM volume decreases progressively, contracting by ~ 3% at full charge, consistent with *operando* XRD results. During the first discharge, the volume of CAM particles expands reversibly. In the second cycle, a similar contraction–expansion sequence occurs, with the CAM volume nearly fully returning to its pristine value, again in agreement with *operando* XRD observations. Benefiting from the small volume change of CAM, the void volume remains largely constant, and no visible cracks or CAM/SE delamination are detected during the first two cycles. Overall, the limited CAM volume evolution and the preservation of microstructural integrity suggest intimate interparticle contact, consistent with the negligible capacity fade observed over long cycling.

PFIB-SEM

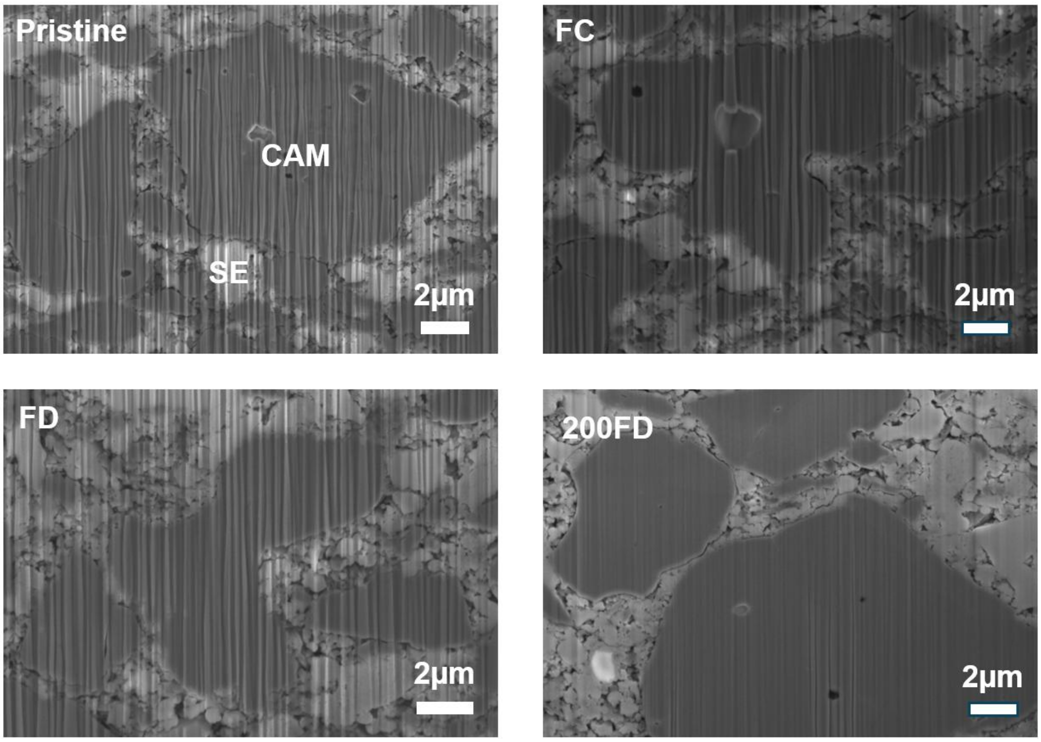

Figure 4.12: Cross-sectional PFIB-SEM images of the composite cathode in the pristine, FC, FD and 200FD states. The darker regions represent the $Li_{1.2}Ti_{0.8}S_2$ cathode, while the brighter regions correspond to the LPSC electrolyte.

To further investigate the microstructural evolution of the composite cathode, high-resolution cross-sectional SEM images of the PCC, FC, FD and 200 FD samples, obtained by PFIB-SEM, are shown in Figure 4.12. Before cycling, the PCC exhibits continuous physical contact throughout. At the FC and FD states in the first cycle, the CAM and LPSC remain in intimate contact with minimal changes, consistent with *operando* XRD and *in situ* CT results. Even after 200 cycles, the 200FD sample displays a well-preserved microstructure, showing no clear evidence of cracking or delamination at the CAM/LPSC interface, in accord with the excellent capacity retention achieved under a low stack pressure of 2 MPa.

Overall, these results demonstrate that the low volume change of $Li_{1.2}Ti_{0.8}S_2$ during operation greatly contributes to the structural and mechanical stability of the composite cathode, thereby providing a distinct advantage in cyclability under low-pressure conditions.

4.3.6 Advantages of Li-rich Sulfide Cathodes

Based on the above results, the $Li_{1.2}Ti_{0.8}S_2$ cathode in ASSBs delivered outstanding cycling stability and satisfactory capacity at room temperature under a low stack pressure of 2 MPa, without requiring any post-treatments. A detailed study of the fundamental electro-chemo-mechanical relationships in this Chapter demonstrates several intrinsic advantages of layered Li-rich sulfides over conventional oxide systems, summarized as below:

1. Improved chemical compatibility. Oxide cathodes tend to readily oxidize sulfide electrolytes even in the absence of an applied potential.[39] In contrast, Li-rich sulfides do not undergo spontaneous interfacial reactions, probably because the shared sulfide framework reduces the driving force for side reactions. Moreover, their narrower cycling range (1.8 – 3 V vs. Li^+/Li) aligns more closely with the electrochemical stability window of sulfide electrolytes (generally < 2.3 V vs. Li^+/Li)[1], preventing electrolyte oxidation that typically occurs with high-voltage oxide cathodes (cycling at 3 – 4.3 V vs. Li^+/Li). This difference is caused by the lower energy of S 3*p* valence bands relative to O 2*p* orbitals, which lowers the cathode redox potential. While this lower voltage is often considered a penalty for energy density, it provides clear benefits in chemical compatibility and long-term stability when paired with sulfide SE.
2. Satisfactory energy density. Earlier sulfide cathodes such as TiS_2 and $LiTiS_2$ suffered from limited capacity (< 220 mAh g^{-1} in liquid cells) and low average voltage (< 2.2 V vs. Li^+/Li).[40, 41] By contrast, layered Li-rich sulfides studied in this Chapter exhibit both Ti and S-redox processes. This results in significantly improved performance, with a discharge capacity typically exceeding 250 mAh g^{-1} (in liquid cell) and an average discharge voltage of ~ 2.5 V (vs. Li^+/Li), achieving energy densities comparable to some oxide cathodes.[42] While $Li_{1.2}Ti_{0.8}S_2$ itself does not yet rival state-of-the-art Ni-rich layered oxide cathodes, the

vast compositional and structural tunability of Li-rich sulfides offers substantial potential for further improvements in energy density.

3. Reduced structural changes. S-redox chemistry in layered Li-rich sulfides not only improves energy density but also suppresses volume changes during cycling. *Operando* XRD results presented in this chapter suggest that sulfur oxidation minimizes the increased electrostatic repulsion between LiS_2 slabs upon Li^+ extraction. As a result, the *c* lattice parameter remains largely unchanged, suppressing overall volume change. Importantly, this structural stability is not universal among other cathodes with active S-redox reactions. For example, transition metal disulfides (like FeS_2) and trisulfides (like TiS_3), containing S_2^{2-} dimers in their pristine state, experience repeated breaking and reforming of nearly all S_2^{2-} bonds during cycling.[43-47] This process induces large hysteresis, significant volume changes, and rapid capacity decay. Conversion-type systems, such as Li-S batteries, are even more severely affected, due to complete structural rearrangement, sluggish kinetics, and the formation of insulating pure sulfur.[48] By contrast, Li-rich sulfides engage only partial sulfur oxidation by an intercalation-type mechanism, preserving structural integrity and enabling long-term cyclability.[49]
4. Better ductility. The well-preserved microstructure of the $Li_{1.2}Ti_{0.8}S_2$ composite cathode can be attributed to both the relatively smaller volume change and inherently greater ductility of Li-rich sulfides compared with oxides. Sulfur ions are larger, softer, and more polarizable than oxygen ions, resulting in more covalent bonding and more delocalized electronic states. Consequently, sulfide lattices experience reduced electrostatic repulsion under mechanical stresses, facilitating plastic deformation.[50] In contrast, the more ionic O^{2-} ions form stronger and more directional TM-O bonds, which promote rigidity and brittleness. In ASSBs, the higher deformability of Li-rich sulfides improves interfacial contact with SE particles upon initial pelletization and better accommodates CAM volume changes during cycling, thereby suppressing voids and crack formation.

4.4 Conclusion

In this Chapter, a model layered Li-rich sulfide, $Li_{1.2}Ti_{0.8}S_2$, with S-redox activity, has been applied as a cathode material for ASSBs. Compared with conventional layered oxides, Li-rich sulfides show reduced surface reactivity with sulfide electrolytes and limited volume changes upon cycling. These intrinsic advantages suppress the continuous accumulation of side products and mitigate contact loss at the CAM/SE interface, and also improve the mechanical integrity of the composite electrode. As a result, the as-prepared $Li_{1.2}Ti_{0.8}S_2$ show a high areal capacity (~ 6 mAh cm^{-2}), a high specific capacity (> 220 mAh g^{-1} at 1mA cm^{-2}), and superior cycling stability (with > 85% capacity retention after 200 cycles) at 30 °C under a low stack pressure of 2 MPa. This work demonstrates that Li-rich sulfides can be extended to practical ASSBs applications, highlighting their potential to overcome critical limitations of oxide-based cathodes. More broadly, it aims to raise awareness of exploring the largely untapped Li-rich sulfides with S-redox chemistry as attractive cathodes for the development of next-generation high-performance ASSBs.

4.5 References

1. Zhu, Y.; He, X.; Mo, Y., Origin of Outstanding Stability in the Lithium Solid Electrolyte Materials: Insights from Thermodynamic Analyses Based on First-Principles Calculations. *ACS Appl. Mater. Interfaces* **2015,** *7* (42), 23685-23693.

2. Koerver, R. *et al.* Redox-active cathode interphases in solid-state batteries. *J. Mater. Chem. A* **2017,** *5* (43), 22750-22760.

3. Xiao, Y. *et al.* Understanding interface stability in solid-state batteries. *Nat. Rev. Mater.* **2020,** *5* (2), 105-126.

4. Xi, L. *et al.* Interface Engineering of All-Solid-State Batteries Based on Inorganic Solid Electrolytes. *ChemSusChem* **2023,** *16* (9), e202202158.

5. Cao, D. *et al.* Stable Thiophosphate-Based All-Solid-State Lithium Batteries through Conformally Interfacial Nanocoating. *Nano Lett.* **2020,** *20* (3), 1483-1490.

6. Matsuyama, T. *et al.* Electrochemical properties of all-solid-state lithium batteries with amorphous titanium sulfide electrodes prepared by mechanical milling. *J. Solid State Electrochem.* **2013,** *17* (10), 2697-2701.

7. Lu, P. *et al.* Realizing long-cycling all-solid-state Li-In||TiS_2 batteries using $Li_{6+x}M_xAs_{1-x}S_5I$ (M = Si, Sn) sulfide solid electrolytes. *Nat. Commun.* **2023,** *14* (1), 4077.

8. Kim, J. Y. *et al.* Revisiting TiS_2 as a diffusion-dependent cathode with promising energy density for all-solid-state lithium secondary batteries. *Energy Storage Mater.* **2021,** *41*, 289-296.

9. Matsuyama, T. *et al.* Improved electrochemical performance of amorphous TiS_3 electrodes compared to its crystal for all-solid-state rechargeable lithium batteries. *J. Ceram. Soc. Jpn.* **2016,** *124* (3), 242-246.

10. Tanibata, N. *et al.* All-solid-state sodium batteries using amorphous TiS_3 electrode with high capacity. *J. Power Sources* **2015,** *275*, 284-287.

11. Santhosha, A. L. *et al.* The Indium−Lithium Electrode in Solid-State Lithium-Ion Batteries: Phase Formation, Redox Potentials, and Interface Stability. *Batteries Supercaps* **2019,** *2* (6), 524-529.

12. Wang, C. *et al.* All-solid-state lithium batteries enabled by sulfide electrolytes: from fundamental research to practical engineering design. *Energy Environ. Sci.* **2021,** *14* (5), 2577-2619.

13. Liu, B. *et al.* The effect of volume change and stack pressure on solid-state battery cathodes. *SusMat* **2023,** *3* (5), 721-728.

14. Kasemchainan, J. *et al.* Critical stripping current leads to dendrite formation on plating in lithium anode solid electrolyte cells. *Nat. Mater.* **2019,** *18* (10), 1105-1111.

15. Doux, J.-M. *et al.* Stack Pressure Considerations for Room-Temperature All-Solid-State Lithium Metal Batteries. *Adv. Energy Mater.* **2020,** *10* (1), 1903253.

16. Minnmann, P. *et al.* Designing Cathodes and Cathode Active Materials for Solid-State Batteries. *Adv. Energy Mater.* **2022,** *12* (35), 2201425.

17. Marchini, F. *et al.* Li-Rich Layered Sulfide as Cathode Active Materials in All-Solid-State Li–Metal Batteries. *ACS Appl. Mater. Interfaces* **2020,** *12* (13), 15145-15154.

18. Li, M. *et al.* Dense All-Electrochem-Active Electrodes for All-Solid-State Lithium Batteries. *Adv. Mater.* **2021,** *33* (26), 2008723.

19. Randau, S. *et al.* On the Additive Microstructure in Composite Cathodes and Alumina-Coated Carbon Microwires for Improved All-Solid-State Batteries. *Chem. Mater.* **2021,** *33* (4), 1380-1393.

20. Strauss, F. *et al.* Influence of electronically conductive additives on the cycling performance of argyrodite-based all-solid-state batteries. *RSC Adv.* **2020,** *10* (2), 1114-1119.

21. Ren, D. *et al.* Challenges and opportunities of practical sulfide-based all-solid-state batteries. *eTransportation* **2023,** *18*, 100272.

22. Shi, T. *et al.* High Active Material Loading in All-Solid-State Battery Electrode via Particle Size Optimization. *Adv. Energy Mater.* **2020,** *10* (1), 1902881.

23. Shinoda, M. *et al.* Activation of Anionic Redox for Stoichiometric and Li-Excess Metal Sulfides through Structural Disordering: Joint Experimental and Theoretical Study. *J. Am. Chem. Soc.* **2025,** *147* (30), 26238-26253.

24. Wang, T. *et al.* Anionic redox reaction in layered $NaCr_{2/3}Ti_{1/3}S_2$ through electron holes formation and dimerization of S–S. *Nat. Commun.* **2019,** *10* (1), 4458.

25. Marie, J.-J. *et al.* Trapped O_2 and the origin of voltage fade in layered Li-rich cathodes. *Nat. Mater.* **2024,** *23* (6), 818-825.

26. Wang, L. *et al.* High-energy all-solid-state lithium batteries enabled by Co-free $LiNiO_2$ cathodes with robust outside-in structures. *Nat. Nanotechnol.* **2024,** *19* (2), 208-218.

27. Deng, S. *et al.* Insight into cathode surface to boost the performance of solid-state batteries. *Energy Storage Mater.* **2021,** *35*, 661-668.

28. Ma, Y. *et al.* Advanced Nanoparticle Coatings for Stabilizing Layered Ni-Rich Oxide Cathodes in Solid-State Batteries. *Adv. Funct. Mater.* **2022,** *32* (23), 2111829.

29. Flamary-Mespoulie, F. *et al.* Lithium-rich layered titanium sulfides: Cobalt- and Nickel-free high capacity cathode materials for lithium-ion batteries. *Energy Storage Mater.* **2020,** *26*, 213-222.

30. Caspar, M. *et al.* Study of the Cathode/Electrolyte Interface in an All-Sulfide-Solid-State Battery Using Lithium-Rich Transition Metal Sulfide. *ACS Appl. Mater. Interfaces* **2025,** *17* (4), 7142-7150.

31. Walther, F. *et al.* Visualization of the Interfacial Decomposition of Composite Cathodes in Argyrodite-Based All-Solid-State Batteries Using Time-of-Flight Secondary-Ion Mass Spectrometry. *Chem. Mater.* **2019,** *31* (10), 3745-3755.

32. Banerjee, A. *et al.* Interfaces and Interphases in All-Solid-State Batteries with Inorganic Solid Electrolytes. *Chem. Rev.* **2020,** *120* (14), 6878-6933.

33. Auvergniot, J. *et al.* Interface Stability of Argyrodite Li_6PS_5Cl toward $LiCoO_2$, $LiNi_{1/3}Co_{1/3}Mn_{1/3}O_2$, and $LiMn_2O_4$ in Bulk All-Solid-State Batteries. *Chem. Mater.* **2017,** *29* (9), 3883-3890.

34. Gao, X. *et al.* Solid-state lithium battery cathodes operating at low pressures. *Joule* **2022,** *6* (3), 636-646.

35. Ohzuku, T. *et al.* Zero-Strain Insertion Material of $Li[Li_{1/3}Ti_{5/3}]O_4$ for Rechargeable Lithium Cells. *J. Electrochem. Soc.* **1995,** *142* (5), 1431.

36. Park, G.-T. *et al.* Single-Crystal vs Polycrystalline Cathodes for Lithium-Ion Batteries. *Chem. Rev.* **2025,** 5c00441.

37. Rong, X. *et al.* Anionic Redox Reaction-Induced High-Capacity and Low-Strain Cathode with Suppressed Phase Transition. *Joule* **2019,** *3* (2), 503-517.

38. Liu, H. *et al.* Tailoring superstructure units for improved oxygen redox activity in Li-rich layered oxide battery's positive electrodes. *Nat. Commun.* **2024,** *15* (1), 9981.

39. Jung, S.-K. *et al.* Understanding the effects of chemical reactions at the cathode–electrolyte interface in sulfide based all-solid-state batteries. *J. Mater. Chem. A* **2019,** *7* (40), 22967-22976.

40. Whittingham, M. S.; Gamble, F. R., The lithium intercalates of the transition metal dichalcogenides. *Mater. Res. Bull.* **1975,** *10* (5), 363-371.

41. Clark, S. J.; Wang, D.; Armstrong, A. R.; Bruce, P. G., $Li(V_{0.5}Ti_{0.5})S_2$ as a 1 V lithium intercalation electrode. *Nat. Commun.* **2016,** *7* (1), 10898.

42. Chen, M. *et al.* Lithium-rich sulfide/selenide cathodes for next-generation lithium-ion batteries: challenges and perspectives. *Chem. Commun.* **2022,** *58* (22), 3591-3600.

43. Holleck, G. L.; Driscoll, J. R., Transition metal sulfides as cathodes for secondary lithium batteries—II. titanium sulfides. *Electrochim. Acta* **1977,** *22* (6), 647-655.

44. Saha, S. Exploration of ionic conductors and Li-rich sulfides for all-solid-state batteries. Sorbonne Université, 2020. NNT : 2020SORUS041. tel-03153280.

45. Gard, P.; Sourisseau, C.; Ouvrard, G.; Brec, R., Infrared study of lithium intercalated phases in the Li_xFeS_2 system ($0 \leq x \leq 2$). Characterization of a new iron disulfide. *Solid State Ionics* **1986,** *20* (3), 231-238.

46. Murphy, D. W.; Trumbore, F. A., The Chemistry of TiS_3 and $NbSe_3$ Cathodes. *J. Electrochem. Soc.* **1976,** *123* (7), 960.

47. Whittingham, M. S., Chemistry of intercalation compounds: Metal guests in chalcogenide hosts. *Prog. Solid State Chem.* **1978,** *12* (1), 41-99.

48. Manthiram, A. *et al.* Rechargeable Lithium–Sulfur Batteries. *Chem. Rev.* **2014,** *114* (23), 11751-11787.

49. Zak, J. J. *et al.* An Exploration of Sulfur Redox in Lithium Battery Cathodes. *J. Am. Chem. Soc.* **2022,** *144* (23), 10119-10132.

50. Sakuda, A. *et al.* High Reversibility of "Soft" Electrode Materials in All-Solid-State Batteries. *Front. Energy Res.* **2016,** *4*, 19.

5

S-redox Chemistry with Tunable Transition Metal-S Covalency

Contents

5.1 Introduction

The TM-anion covalency can be modulated by composition tuning in both Li-rich oxides and Li-rich sulfides, a route widely employed to explore novel anionic redox cathodes. In oxide systems, moving down from 3*d* TM (e.g., Ni, Co, Mn) to 4*d* and 5*d* TM (e.g., Ru and Ir) with greater covalency has enabled the preparation of cathodes like Li_2RuO_3, $Li_2Ru_{0.75}Sn_{0.25}O_3$, $Li_2Ir_{0.75}Sn_{0.25}O_3$.[1,2] However, the resulting more covalent TM-O bonding does not suppress the formation of molecular O_2 during O oxidation.[3] In chapter 3, it was established that replacing the O with more covalent S still favors the dimerization of anions in the layered Li-rich sulfide, $Li_{1.2}Ti_{0.8}S_2$, resulting in the formation of the S_2^{2-} dimers coordinated to adjacent TM ions in the structure. Nevertheless, within the Li-rich sulfides system, the effect of TM-S covalency on the S-redox process remains poorly understood.

In this chapter, another model Li-rich sulfide, $Li_{1.2}Mn_{0.2}Ti_{0.6}S_2$ with the same O3-type structure as $Li_{1.2}Ti_{0.8}S_2$, is studied in depth. Compared to the $Ti^{3+/4+}$ band in $Li_{1.2}Ti_{0.8}S_2$, the 3*d* band of $Mn^{2+/3+}$ in $Li_{1.2}Mn_{0.2}Ti_{0.6}S_2$ is located at lower-energy states, just above the S 3*p* orbitals, resulting in higher hybridization between the S 3*p* and Mn 3*d* states and stronger Mn-S covalency.[4] Like-for-like comparison of these two sulfides reveals that increased TM-S covalency promotes the participation of S-redox in the earlier delithiation process and significantly improves electronic conductivity of the material during charging. These findings suggest that tailoring TM-S covalency is a promising approach to facilitate faster electrochemical kinetics in the S-redox process, which could further advance the application of Li-rich sulfides in ASSBs, as discussed in Chapter 4. Moreover, both PDFs and EXAFS data on the Mn-doped sulfide suggest that the enhanced TM-S covalency can not prevent the formation of S_2^{2-} dimers.

5.2 Experimental

Materials preparation: $Li_{1.33-2y/3}Mn_yTi_{0.67-y/3}S_2$ samples were prepared by solid-state reaction between stoichiometric amounts of Li_2S (99.98%, Sigma-Aldrich), TiS_2 (99.5%, Thermo Scientific), Mn (99%, Sigma-Aldrich) and elemental S (99.98%, Sigma-Aldrich). The precursor was hand-ground, pressed into pellets, and then placed into graphite crucibles before being transferred into quartz tubes. These tubes were subsequently sealed under vacuum (~ 10^{-5} mbar) and heated to 900 °C for 36 hours with a heating rate of 1 °C min^{-1}, followed by quenching in air. In the whole process, air exposure was avoided, and the as-prepared materials were collected and stored in an Ar-filled glovebox.

Chemical delithiation of $Li_{1.2}Ti_{0.8}S_2$ and $Li_{1.2}Mn_{0.2}Ti_{0.6}S_2$ was performed to obtain materials equivalent to the electrochemically charged samples. Based on desired delithiated states, appropriate mole ratios of the sulfide material and I_2 (> 99.99%, Alfa Aesar) were dispersed in anhydrous acetonitrile and stirred at room temperature for 24 hours. The resulting products were then centrifuged, washed three times with anhydrous acetonitrile, and dried under vacuum at 50 °C for 12 hours.

Electrochemistry characterization: Self-supporting electrodes were fabricated by mixing the active material with acetylene black and PTFE binder in a mass ratio of 8:1:1, unless otherwise specified. Electrochemical measurements were performed in coin cells using Li metal foil as the anode and LP30 as the electrolyte. For *ex situ* characterizations, cells were disassembled at various states of charge, and the cathodes were subsequently rinsed twice with anhydrous DMC before being dried under vacuum.

DC polarization measurements were performed to determine the electronic conductivity of the sulfide materials at various delithiated states. The material was cold-pressed into a 5 mm diameter pellet under a pressure of 400 MPa inside a PEEK module. Stainless steel current (SUS) collectors, serving as ion-blocking electrodes, were then inserted into the PEEK module on both sides of the pellet. Subsequently, chronoamperometry was performed on the pellet under various voltage steps in 5-minute intervals with SUS/sulfide material/SUS cell configuration, and the current response was recorded using Bio-Logic BCS-805.

X-ray absorption spectroscopy: Mn, Ti and S K-edge XANES and EXAFS data were collected on the B18 beamline at the Diamond Light Source. The Mn and Ti K-edges were measured in transmission mode, while the S K-edge was measured in fluorescence mode with the sample chamber filled with helium gas. Each spectrum was averaged over five measurements, calibrated, background subtracted, and normalized. The k^2-weighted EXAFS were then extracted using the k-range of 2 – 10 $Å^{-1}$ for Mn, 2.5 – 10.5 $Å^{-1}$ for Ti and 2 – 8.5 $Å^{-1}$ for S with the Athena software. Mn and Ti L-edge XAS were collected in partial fluorescence yield mode on the BL27SU beamline at Spring8 in Japan.

X-ray and Neutron total scattering measurements: X-ray powder diffraction and total scattering measurements were acquired on the I15-1 beamline at Diamond Light Source, using a wavelength of 0.16167 Å, except otherwise specified. Neutron diffraction and total scattering data were recorded on the NOMAD instrument at the Neutron Spallation Source, Oak Ridge National Laboratory.

Before conducting these measurements, silica was first measured as an internal calibration standard to obtain the instrumental parameters. *Operando* PXRD measurements were performed using a Cu-source Rigaku 9 kW diffractometer with a beryllium window electrochemical cell provided by Rigaku. Joint Rietveld refinements of X-ray and neutron diffraction data were performed using the GSAS-II software.[5] PDF data were obtained using PDFgetX3 within the xPDFsuite package,[6] and joint refinements of X-ray and neutron PDFs were conducted using PDFgui.[7]

5.3 Results and Discussion

5.3.1 Material Characterization

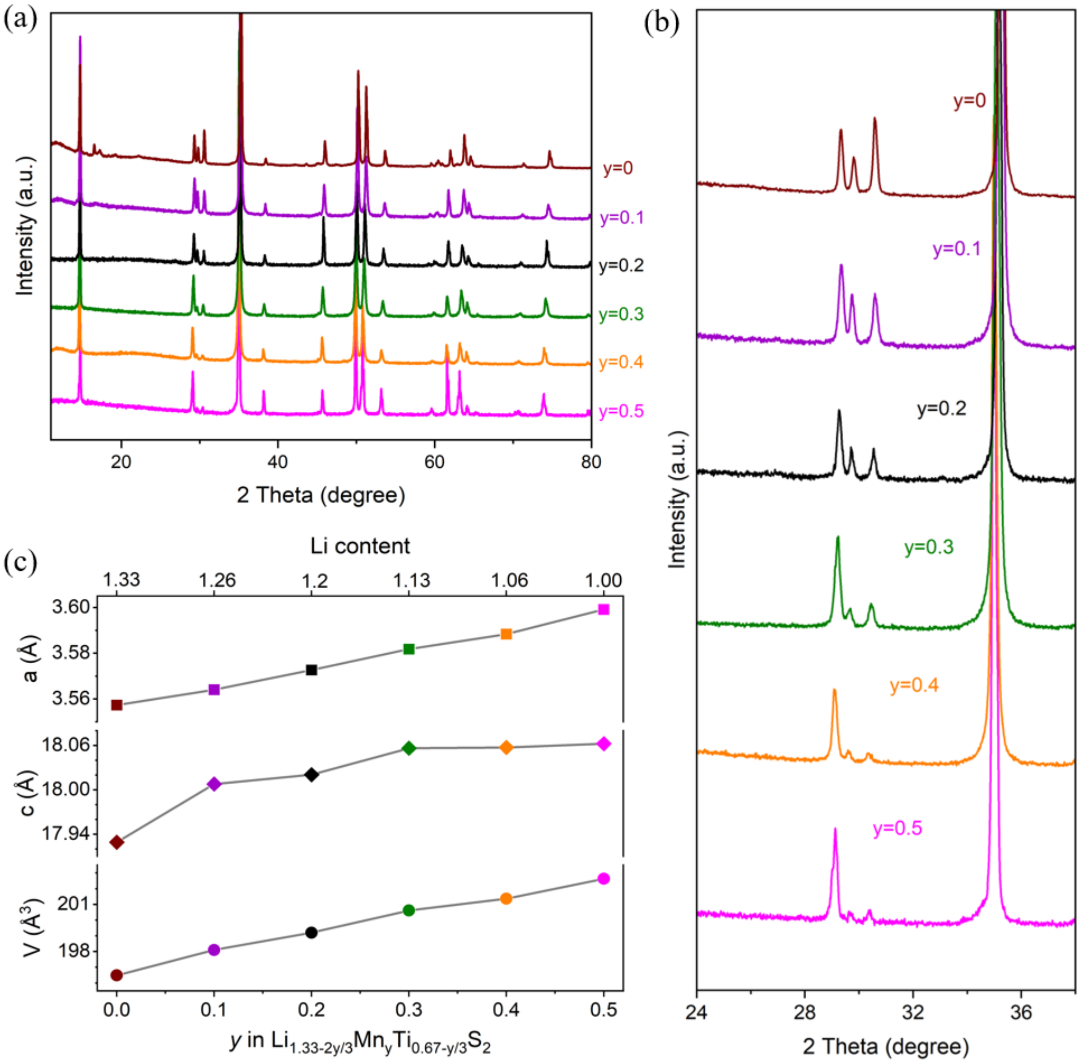

Figure 5.1: Structural behavior of the $Li_{1.33-2y/3}Mn_yTi_{0.67-y/3}S_2$ series. (a) The XRD patterns and (b) the magnified region of the XRD patterns. (c) The variation of lattice parameters obtained from Rietveld Refinement. Increasing Mn content leads to a monotonic increase in the *a*, *c*, and cell volume *V*.

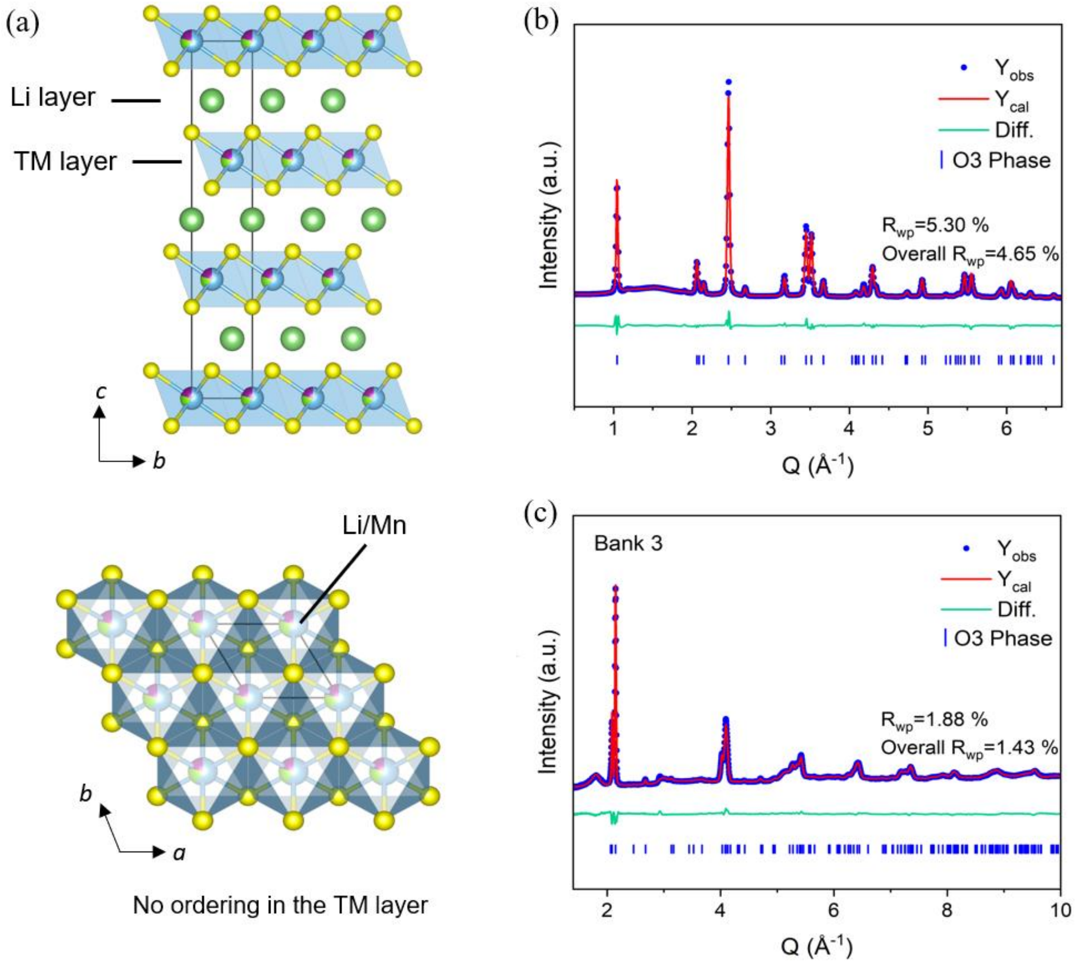

Figure 5.2: (a) Schematic of the O3-type $Li_{1.2}Mn_{0.2}Ti_{0.6}S_2$ structure, with Li (green) and Ti (blue) atoms randomly distributed within the TM layer, and S atoms are shown in yellow. (b), (c) Joint Rietveld refinements of synchrotron PXRD (b) and neutron diffraction (c) of the pristine $Li_{1.2}Mn_{0.2}Ti_{0.6}S_2$, using the $R\bar{3}m$ space group.

To substitute Ti^{3+} in $Li_{1.2}Ti_{0.8}S_2$ with Mn^{2+}, which has lower-lying 3*d* states, nominal compositions of $Li_{1.33-2y/3}Mn_yTi_{0.67-y/3}S_2$ ($y = 0 – 0.5$), corresponding to the $Li_{1.33}Ti_{0.67}S_2$-$LiMn_{0.5}Ti_{0.5}S_2$ tie-line, were synthesized as outlined in Section 5.2. The PXRD patterns of these samples are presented in Figure 5.1. As the Mn content increases, no impurity peaks are observed (Figure 5.1 (a)), and a progressive shift of the Bragg peaks is evident (Figure 5.1 (b)), indicating the formation of a continuous solid solution across all composition stoichiometries. This is further supported by Rietveld refinements using the $R\bar{3}m$ space group, which reveal a linear evolution in both lattice parameters and unit cell volume with increasing Mn content, as shown in Figure 5.1 (c). Among these compounds, $Li_{1.2}Mn_{0.2}Ti_{0.6}S_2$ ($y = 0.2$) is the primary focus in this chapter, as it is structurally and compositionally analogous to O3-type $Li_{1.2}Ti_{0.8}S_2$, ensuring that the key variable under investigation is the difference in TM-S covalency.

The structure of $Li_{1.2}Mn_{0.2}Ti_{0.6}S_2$ was examined by joint refinement of synchrotron XRD and neutron diffraction, as shown in Figure 5.2, Figure A5.1 and Table A5.1. $Li_{1.2}Mn_{0.2}Ti_{0.6}S_2$ possesses an O3-type structure with randomly distributed cations in the TM layer, closely similar to $Li_{1.2}Ti_{0.8}S_2$.

5.3.2 Electrochemical Characterization

The electrochemical behavior of $Li_{1.33-2y/3}Mn_yTi_{0.67-y/3}S_2$ was examined against a Li metal anode, as shown in Figure A5.2. For the Mn-free composition (y = 0), $Li_{1.33}Ti_{0.67}S_2$ is almost electrochemically inactive, as the empty $Ti^{3+/4+}$ band lies far above the S 3*p* band, rendering S oxidation inaccessible.[8, 9] Upon Mn substitution, the electrochemical capacity substantially increases, reaching nearly 260 mAh g^{-1} in $Li_{1.2}Mn_{0.2}Ti_{0.6}S_2$ (y = 0.2). Further increases in Mn content (y = 0.3, 0.4 and 0.5) lead to a reduced Li^+ reservoir in the formula, which result in a decrease in capacity.

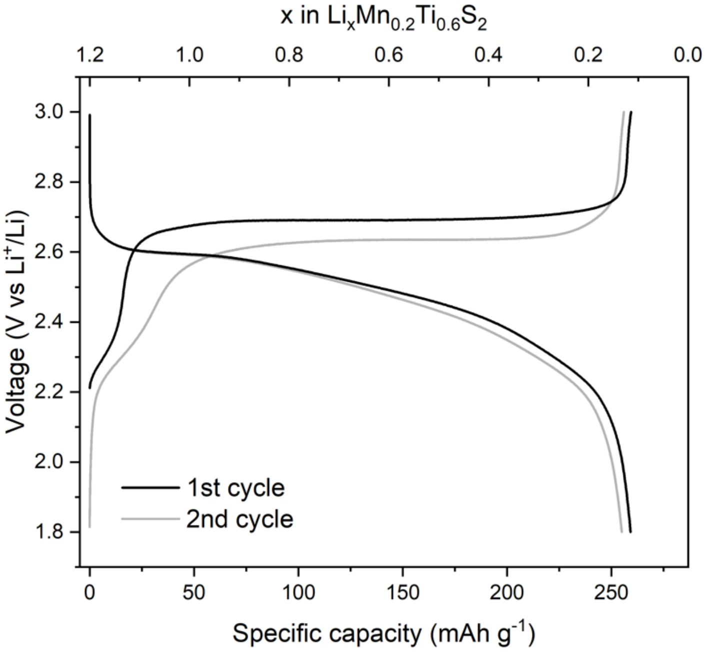

Figure 5.3: Load curves of $Li_{1.2}Mn_{0.2}Ti_{0.6}S_2$ during the first two cycles. Cycling was performed between 1.8 – 3V at a current density of 10 mA g^{-1}. Following the first charge, the discharge curve evolves into a sloping profile at a lower average voltage than the initial charging plateau. The second cycle exhibits reduced voltage hysteresis compared to the first cycle.

The load curves of $Li_{1.2}Mn_{0.2}Ti_{0.6}S_2$ for the first two cycles are plotted in Figure 5.3. During the initial charge, the material shows a long flat voltage plateau at approximately 2.7V, preceded by a brief sloping region. It contrasts with the first charge profile of $Li_{1.2}Ti_{0.8}S_2$, which features a more pronounced sloping region and a shorter plateau, as discussed in Chapters 3 and 4. At the top of charge, nearly 1.1 moles of Li^+ per formula unit are extracted from $Li_{1.2}Mn_{0.2}Ti_{0.6}S_2$, similar to that observed in $Li_{1.2}Ti_{0.8}S_2$, as shown in Section 3.3.2. In $Li_{1.2}Mn_{0.2}Ti_{0.6}S_2$, the extracted Li^+ amount is well beyond the limitation of Mn redox, even assuming a multielectron $Mn^{2+/4+}$ process, which is unlikely in a sulfide framework where sulfur oxidation occurs at lower voltages than $Mn^{3+/4+}$ redox.[4] It suggests that the S-redox reaction indeed contributes to the charge compensation process in $Li_{1.2}Mn_{0.2}Ti_{0.6}S_2$. On subsequent discharge down to 1.8V, the material is nearly fully relithiated to its pristine state. However, the discharge profile evolves into an S-shaped curve with much lower average voltage than the charge plateau. In the second cycle, the sloping region during delithiation becomes more prominent, and the plateau shifts to a lower voltage, resulting in reduced voltage hysteresis. These electrochemical behaviors closely resemble those observed in $Li_{1.2}Ti_{0.8}S_2$, which likewise shows more pronounced hysteresis in the first cycle and reduced hysteresis in following cycles, accompanied by evolved charge and discharge profiles.

5.3.3 Charge Compensation Process

To follow the charge compensation process that accompanies cycling in $Li_{1.2}Mn_{0.2}Ti_{0.6}S_2$, Mn, Ti and S K-edge XANES were employed on *ex situ* samples at various states of charge, as shown in Figure 5.4 and Figure A5.3. To further investigate how TM-S covalency affects the redox process, the evolution of the Mn, Ti and S K-edge positions along the initial cycle in both $Li_{1.2}Mn_{0.2}Ti_{0.6}S_2$ and $Li_{1.2}Ti_{0.8}S_2$ was extracted from the first derivative of their main absorption edges, as summarized in Figure 5.4 (a) and (b). Shifts in the main edge energy can serve as a reliable indicator of oxidation state variations, as the outer orbitals are sensitive to electronic structure changes driven by electron shielding effects.[10]

In $Li_{1.2}Ti_{0.8}S_2$, during the first charge, the Ti K-edge only shifts before reaching the plateau (BP, 2.6V), corresponding to the oxidation of Ti^{3+}. Beyond this point, further charging across the half plateau (HP) and to the fully charged state (FC, 3.0 V) results in continued edge shifts observed exclusively in the S K-edge XANES, indicating a well-separated Ti and S oxidation process, as discussed in Sections 3.3.3 and 4.3.3. During discharge, Ti reduction occurs only after the half discharge (HD, 2.5V), suggesting limited Ti 3*d*-S 3*p* hybrid character throughout the cycling.

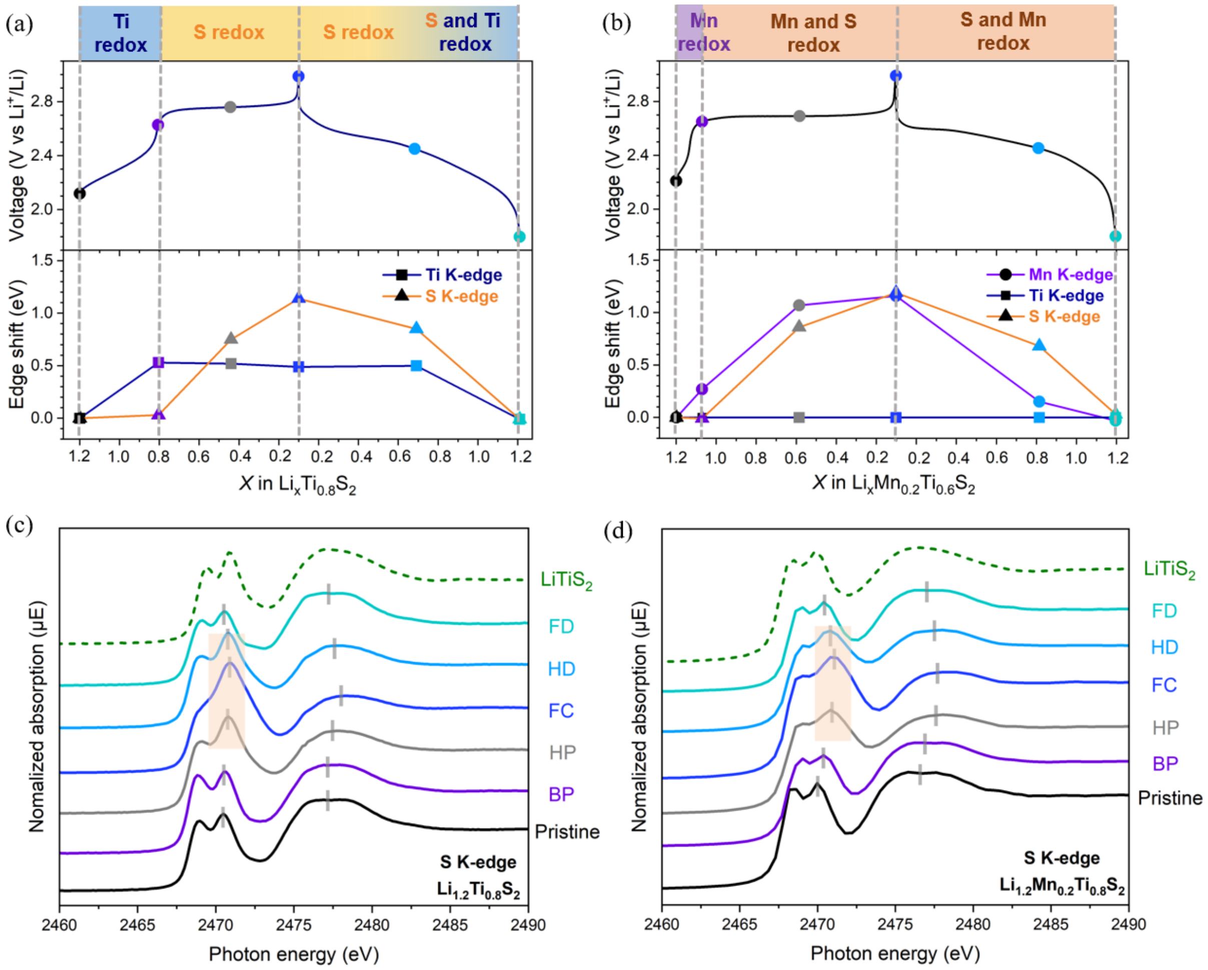

Figure 5.4: Galvanostatic curves of $Li_{1.2}Ti_{0.8}S_2$ (a) and $Li_{1.2}Mn_{0.2}Ti_{0.6}S_2$ (b) together with the evolution of the Ti, Mn and S K-edges energy position, defined as the absorption edge energy (E_0), which is the maximum of the first derivative of μ(E). (c), (d), The corresponding S K-edge spectra for $Li_{1.2}Ti_{0.8}S_2$ (c) and $Li_{1.2}Mn_{0.2}Ti_{0.6}S_2$ (d). $Li_{1.2}Mn_{0.2}Ti_{0.6}S_2$ exhibits a broader pre-edge than $Li_{1.2}Ti_{0.8}S_2$, as highlighted, suggesting a wider distribution of Mn 3*d*-S 3*p* hybridized states. The corresponding Mn and Ti K-edge XANES spectra are displayed in Figure A5.3.

As for $Li_{1.2}Mn_{0.2}Ti_{0.6}S_2$, Mn^{2+} substitution drives Ti to a nominal Ti^{4+} oxidation state from the beginning. Ti K-edge energy remains unchanged throughout the whole cycle, indicating that Ti^{4+} acts as a spectator species. Upon the initial charge before the plateau (BP, 2.65V), only $Mn^{2+/3+}$ redox is active. Across the plateau, notably, both Mn and S K-edges shift concurrently, exhibiting a concerted redox process, consistent with the long plateau profile and distinct from the discrete Ti and S oxidation in $Li_{1.2}Ti_{0.8}S_2$. This simultaneous Mn and S redox suggests that the $Mn^{2+/3+}$ 3*d* band indeed overlaps more with the S 3*p* states than the $Ti^{3+/4+}$ 3*d* band does, indicating stronger Mn-S covalency relative to Ti-S interactions. During discharge, both Mn and S are reduced simultaneously as well. These continuous Mn redox and inactive Ti redox in the first cycle are also observed by Mn L-edge and Ti L-edge XAS, as shown in Figure A5.4. At the fully discharged state (FD, 1.8V), all edge shifts are reversed in both Li-rich sulfides, consistent with their high coulombic efficiency.

The stronger Mn-S covalency is further supported by the evolution of the S K pre-edge in these two materials, as shown in Figure 5.4 (c) and (d). Upon charging of both compounds, the pre-edge intensity appears to increase, attributed to the oxidation of both the TM and S ions, which leads to the formation of electron holes in S 3*p*/TM 3*d* hybridized orbitals. Notably, the pre-edge in the charged Mn-substituted samples is greatly broader (light beige region), indicating a wider distribution of Mn 3*d*-S 3*p* hybridized states and thus a stronger Mn–S covalency. Moreover, at the top of charge, both compositions exhibit the formation of new hole states at around 2470.3 eV. This feature closely resembles the S K pre-edge of reference TiS_3, which contains S_2^{2-} dimers, as discussed in Section 3.3.4. The effect of TM-S covalency on the oxidized S species will be discussed later in Section 5.3.6.

5.3.4 Electronic Conductivity Evolution

Stronger TM-S covalency arises from increased overlap between TM 3*d* and S 3*p* orbitals, which alters the electronic band structures and affects the electronic conductivity of materials. To further investigate the influence of TM-S covalency on the electron transfer process during S-redox, both compounds were cycled at a current density of 5 mA g^{-1} with varying carbon additive contents, from 0 wt% to 3 wt%, 5 wt%, and 10 wt%, as shown in Figure 5.5. The use of such a low current density minimizes the impact of differences in Li^+ diffusivity between these two materials, thereby isolating the effects of electronic conductivity associated with TM-S covalency.

As illustrated in Figure 5.5 (a), in the absence of carbon, only the $Ti^{3+/4+}$ redox is active in $Li_{1.2}Ti_{0.8}S_2$, corresponding to nearly 0.4 electrons (e^-) transferred per formula unit during charging (dashed vertical line). The first-cycle curve matches closely with that observed in SSBs using $Li_{1.2}Ti_{0.8}S_2$ without carbon additives, as discussed in Section 4.3.2. These results indicate that, following full oxidation of Ti^{3+} to Ti^{4+} with d^0 electronic configuration, the electronic resistance of the material significantly increases. By adding 3 wt% carbon, S redox becomes accessible, but exhibits considerable polarization compared to the 5 wt% carbon sample. After increasing the carbon amount to 10 wt%, the S-redox plateau shifts downward to below 2.8V, as indicated by the horizontal dashed line, suggesting further improved kinetics. The cycling comparison between the 5 wt% and 10 wt% carbon samples, as shown in Figure 5.5 (c), further demonstrates the importance of sufficient carbon content in fully accessing the S-redox capacity of $Li_{1.2}Ti_{0.8}S_2$.

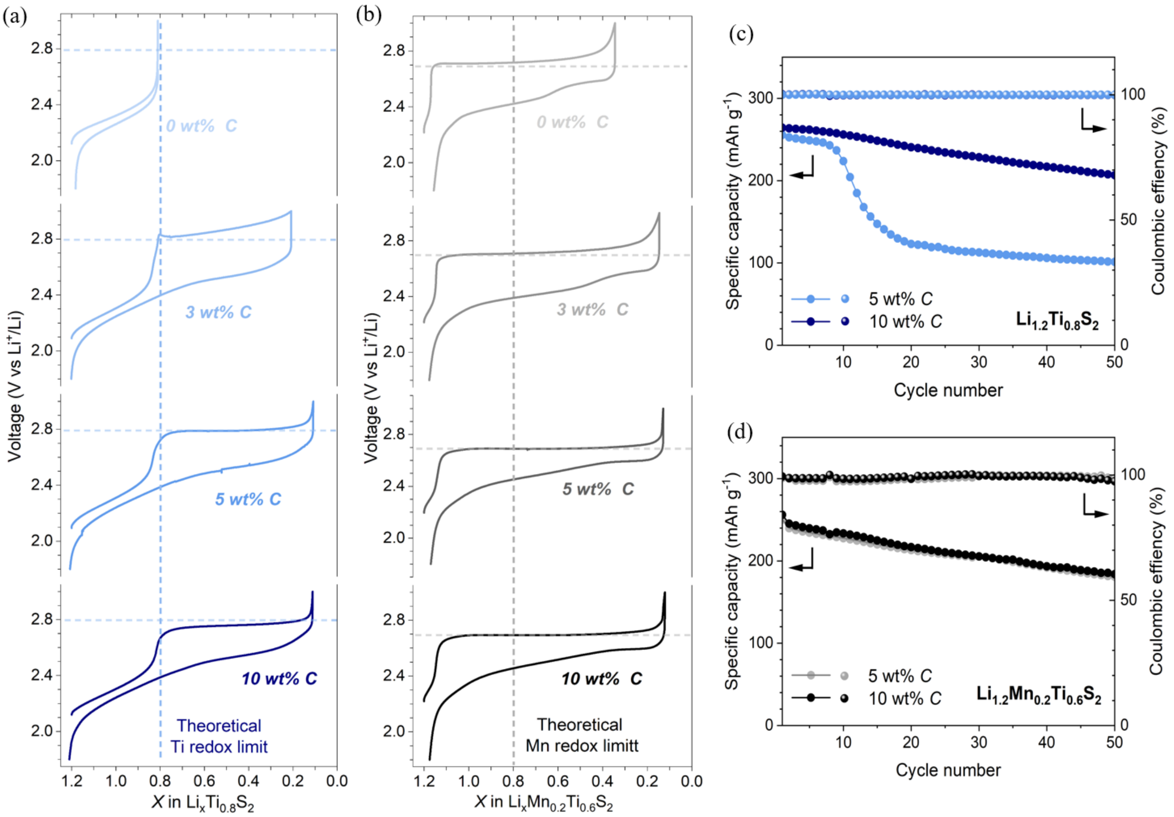

Figure 5.5: Electrochemical performance of $Li_{1.2}Ti_{0.8}S_2$ and $Li_{1.2}Mn_{0.2}Ti_{0.6}S_2$ with different carbon contents. (a), (b), The first cycle profiles of $Li_{1.2}Ti_{0.8}S_2$ (a) and $Li_{1.2}Mn_{0.2}Ti_{0.6}S_2$ (b) with 0, 3, 5, 10 wt% carbon at a current density of 5 mA g^{-1} between 1.8 – 3V. (c), (d), Cycling performance of $Li_{1.2}Ti_{0.8}S_2$ (c) and $Li_{1.2}Mn_{0.2}Ti_{0.6}S_2$ (d) at 20 mA g^{-1} between 1.8 – 3V with 5% and 10% carbon. Overall, $Li_{1.2}Mn_{0.2}Ti_{0.6}S_2$ requires less carbon to access S-redox capacity and to maintain stable operation.

In stark contrast, $Li_{1.2}Mn_{0.2}Ti_{0.8}S_2$ exhibits S oxidation even at carbon-free conditions, greatly extending the limit of Mn redox (dashed vertical line), as shown in Figure 5.5 (b). The sample with 3 wt% carbon exhibits a similar amount of Li^+ extraction as those with 5 and 10 wt% carbon.

Furthermore, $Li_{1.2}Mn_{0.2}Ti_{0.6}S_2$ with just 5 wt% carbon achieves nearly identical electrochemical behavior to that with 10 wt% carbon, in terms of initial cycle load curve, voltage hysteresis and cyclability, as depicted in Figure 5.5 (b) and (d), highlighting its inherently higher electronic conductivity throughout cycling. This enhanced electronic conductivity is in line with greater Mn 3*d*-S 3*p* orbital hybridization, which results in more delocalized electronic states and more facile electron transfer from the S 3*p* band during charging. On the contrary, the weaker Ti-S covalency in $Li_{1.2}Ti_{0.8}S_2$ leads to more localized electronic states, hindering electron mobility through the material, particularly after the Ti oxidation.

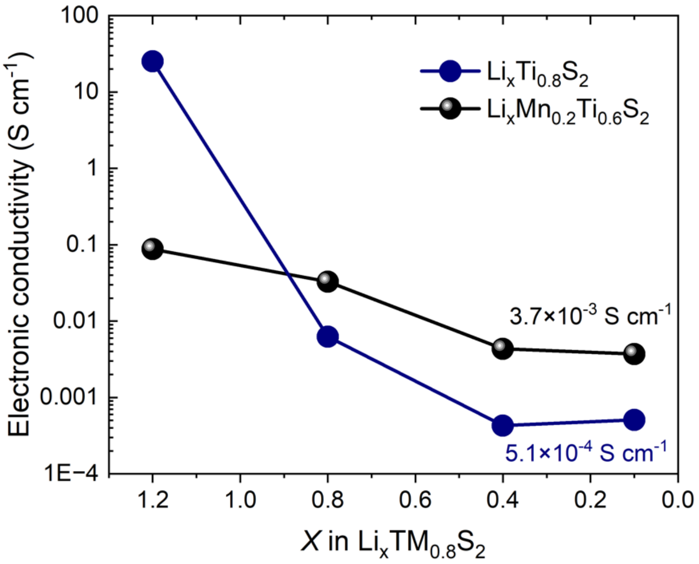

Figure 5.6: Electronic conductivity of $Li_xTi_{0.8}S_2$ and $Li_xMn_{0.2}Ti_{0.6}S_2$ at different delithiated states (x = 1.2, 0.8, 0.4 and 0.1). The delithiated samples were prepared by the chemical delithiation method to avoid the introduction of carbon, as detailed in Section 5.2. Except for the pristine state, the Mn-substituted compound exhibits approximately one order of magnitude higher electronic conductivity across most states of charge.

To further track the evolution of electronic conductivity (σ_e) during charging in both materials, DC polarization measurements were conducted on a series of delithiated samples, as shown in Figure A5.5 and A5.6. To eliminate interference from conductive carbon, chemical delithiation was employed to achieve states equivalent to those obtained by electrochemical charging, as detailed in Section 5.2. As present in Figure 5.6, pristine $Li_{1.2}Ti_{0.8}S_2$ shows a significnatly higher electronic conductivity (~ 25 S cm^{-1}) compared to $Li_{1.2}Mn_{0.2}Ti_{0.6}S_2$ (~ 0.08 S cm^{-1}), consistent with the highly conductive $Ti^{3+/4+}$ redox band. This disparity also confirms the Ti 3*d* band lies much closer to the

Fermi level than the Mn 3d band, which corresponds well to the lower OCV observed for $Li_{1.2}Ti_{0.8}S_2$ (~ 2.1V) than the Mn-substituted sample (~ 2.2V), as shown in Figure 5.5. Accordingly, the Mn 3*d* bands are positioned closer to the top of the S 3*p* bands, aligning with stronger hybridization between Mn-S compared to Ti-S bonds.

Upon deintercalation of 0.4 moles of Li^+ per formula unit, the electronic conductivity of $Li_{0.8}Ti_{0.8}S_2$ drops significantly to 6.2×10^{-3} S cm^{-1}, primarily due to the depletion of Ti^{3+} after Ti oxidation. Further delithiation, leaving 0.4 and 0.1 moles of Li^+ per formula unit, results in additional decreases in σ_e to 4.3×10^{-4} and 5.1×10^{-4} S cm^{-1}, respectively. In sharp contrast, the Mn-substituted samples exhibit only a moderate decline in σ_e during delithiation. Specifically, the electronic conductivity drops to 3.3×10^{-2}, 4.3×10^{-3} and 3.7×10^{-3} S cm^{-1} after extracting 0.4, 0.8 and 1.1 moles of Li^+ per formula unit, respectively. These values remain an order of magnitude higher than those observed in corresponding $Li_xTi_{0.8}S_2$ (x = 0.8, 0.4, 0.1). Together, these findings reveal that enhanced TM-S orbital hybridization significantly promotes electron mobility during sulfur oxidation, highlighting modulating TM-S covalency as a promising strategy to enable S-redox with faster kinetics. Moreover, the monotonic drop in electronic conductivity upon delithiation indicates that no delocalized electron holes are formed on the S ions. Otherwise, an increase in electronic conductivity would be expected after S oxidation.

5.3.5 Long-range Structural Evolution

To investigate the structural evolution of $Li_{1.2}Mn_{0.2}Ti_{0.6}S_2$, *operando* XRD during galvanostatic cycling was carried out. As shown in Figure 5.7, upon initial charge until approximately 0.3 mol e^- is extracted, the material shows a continuous left shift of the (003) peak and right shift of the (104) peak, suggesting an expansion of interlayer distance (*c* lattice parameter) and a contraction of the in-plane atomic distance (*a* lattice parameter), respectively. The increase in *c* arises from reduced electrostatic screening between adjacent sulfur layers upon Li removal, and the decrease in *a* is attributed to the shortening of the TM-S bond, associated with the Mn oxidation.

Upon further charging across the plateau, a new Bragg peak appears at around $2\theta = 36.8°$ (highlighted in light beige) at the expense of the original (104) peak at approximately $2\theta = 35.5°$.

Simultaneously, the intensity of the pristine (003) reflection decreases, alongside the emergence of a new peak at a higher 2θ (also highlighted), suggesting a two-phase process. In the FC sample, the newly formed phase dominates, retaining the O3-type structure but exhibiting a smaller unit cell compared to the pristine state, due to overall lattice contraction during charging. A similar behavior is commonly observed in Ni-rich layered oxides, where phase evolution (preserving the hexagonal layered framework but different lattice parameters) occurs upon lithium extraction.[1] Joint Rietveld refinements of X-ray and neutron diffraction, as shown in Figure A5.7 and Table A5.2, confirm that the fully charged $Li_{1.2}Mn_{0.2}Ti_{0.6}S_2$ consists of a mixture of 76.6 wt% of the contracted O3-type phase and 23.4 wt% of the O3-type phase structurally closer to pristine $Li_{1.2}Mn_{0.2}Ti_{0.6}S_2$. During discharge, the contracted O3 phase quickly fades, followed by a solid-solution behavior. At the FD state, the material is nearly identical to the pristine state with well-maintained crystallinity, as confirmed by joint refinement results in Figure A5.8 and Table A5.3. A similar structural change is also observed in the second cycle, as shown in Figure A5.9.

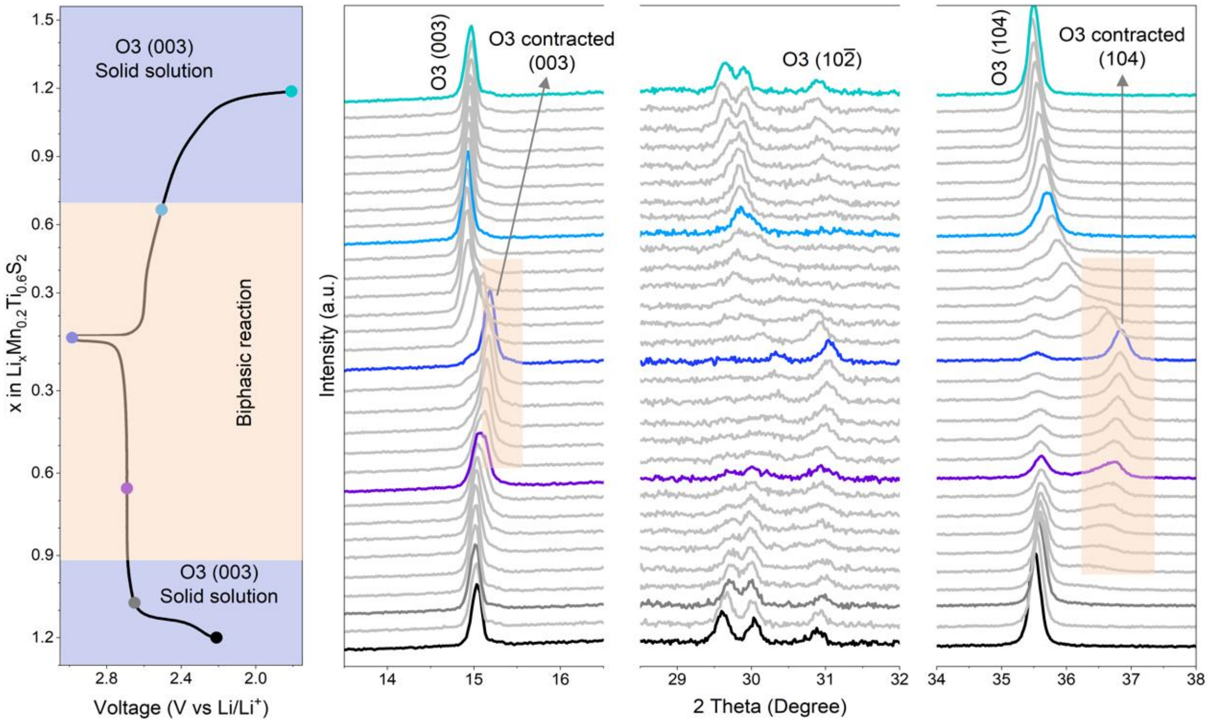

Figure 5.7: The first cycle load curve of $Li_{1.2}Mn_{0.2}Ti_{0.6}S_2$ monitored by *operando* XRD with a Cu-source diffractometer. The cell was cycled between 1.8V and 3V at 10 mA g^{-1}. A more contracted O3 phase with reduced lattice parameters emerges during charging and reversibly disappears during discharge.

In comparison to $Li_{1.2}Ti_{0.8}S_2$, although the O1 phase has not been observed in fully charged $Li_{1.2}Mn_{0.2}Ti_{0.6}S_2$, both sulfides almost fully return to their pristine long-range structure at the end of the first discharge and exhibit reduced voltage hysteresis in the following cycles. As revealed in Chapter 3, $Li_{1.2}Ti_{0.8}S_2$ undergoes in-plane Ti aggregation accompanied by S_2^{2-} dimer formation, thus resulting in the evolved charge and discharge profiles. To determine whether a similar process occurs in $Li_{1.2}Mn_{0.2}Ti_{0.6}S_2$, it is essential to examine its local structure evolution during cycling.

5.3.6 Local Structural Change

To investigate whether stronger TM-S covalency would favor different oxidized S species, such as localized hole states on S, and prevent the dimerization of oxidized sulfur ions, once again, PDFs and EXAFS data were obtained to study the local structure change in charged $Li_{1.2}Mn_{0.2}Ti_{0.6}S_2$.

X-ray and neutron PDFs

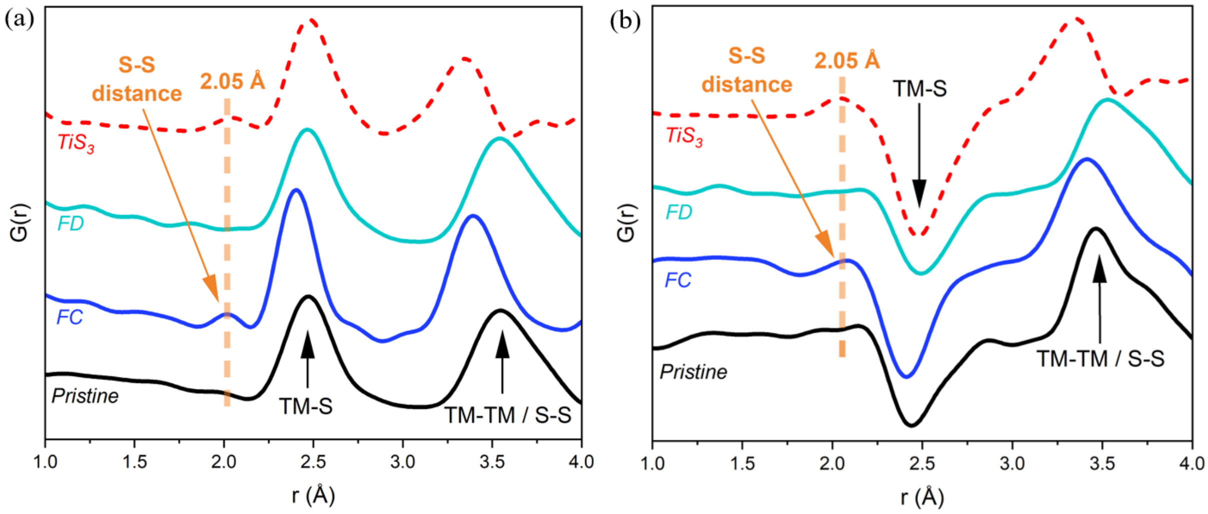

Figure 5.8: (a), (b), X-ray PDF (a) and Neutron PDF (b) results of $Li_{1.2}Mn_{0.2}Ti_{0.6}S_2$ in the 1 – 4 Å region at various states of charge, generated from total scattering data measured at room temperature, Q_{max} = 22 Å. A new peak emerges exclusively at the FC state at 2.05 Å (highlighted in orange), corresponding to the formation of the S-S distance attributed to S_2^{2-} dimers. Simulated PDF data for TiS_3, a reference compound containing S-S dimers with a bond length of 2.05 Å, exhibits a peak at the same radial distance.

The X-ray and neutron PDFs for the pristine, FC, and FD states were collected and fitted well over the 1 – 20 Å using structural models derived from joint Rietveld refinement of the corresponding diffraction data, as shown in Figure A5.10 and Table A5.4 – A5.6. To investigate any short S-S distance formation, the PDFs are presented over a short range, 1 – 4 Å, as shown in Figure 5.8. In the pristine sample, peaks located at approximately 2.45 Å and 3.52 Å correspond to TM-S and S-S/TM-TM bond lengths, respectively. Upon charging, both atomic distances decrease, consistent with the formation of a more contracted O3-type structure. In addition, the fully charged $Li_{1.2}Mn_{0.2}Ti_{0.6}S_2$ exhibits a new positive peak at around 2.05 Å, closely resembling that previously seen in charged $Li_{1.2}Ti_{0.8}S_2$, as discussed in Section 3.3.5. This positive peak persists across PDFs generated using different Q ranges, as present in Figure 5.9, confirming it as an intrinsic structural feature rather than a Fourier transform artefact.

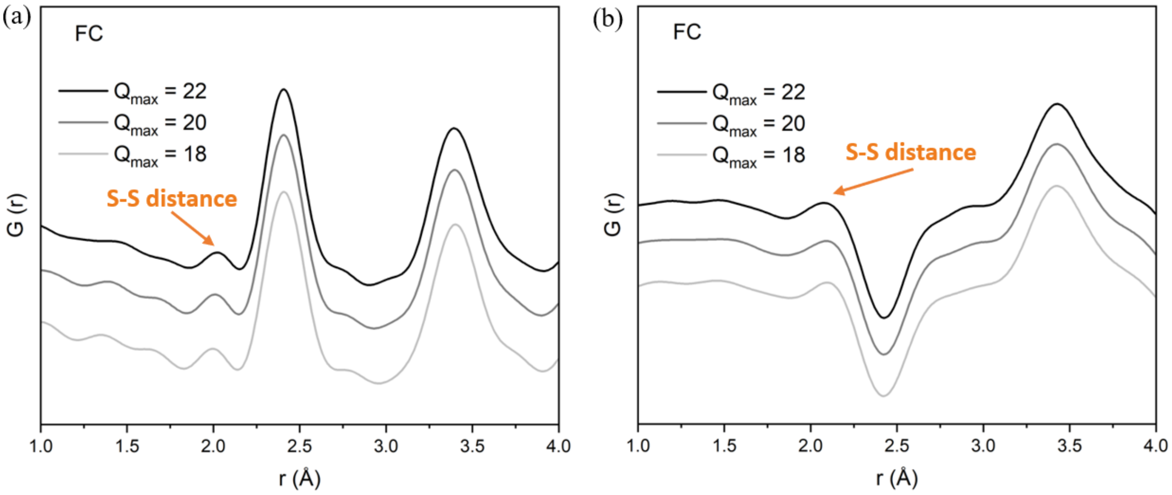

Figure 5.9: Additional PDF data of fully charged $Li_{1.2}Mn_{0.2}Ti_{0.6}S_2$. (a), (b), X-ray (a) and neutron (b) PDF data of the FC sample in the 1 – 4 Å region, generated using different Q_{max} values for the Fourier transform. Across all Q_{max} values, the peak at around 2 Å consistently appears, confirming the presence of a short distance in the FC sample rather than an artefact from Fourier ripples. For further analysis, a Q_{max} of 22 Å was used to ensure optimal real-space resolution.

Unlike X-ray PDFs, where all peaks are positive due to the nature of the scattering process, the neutron PDF can exhibit both positive and negative features depending on the product of the neutron scattering lengths of atom pairs. A positive product yields a peak, while a negative product results in a trough. In $Li_{1.2}Mn_{0.2}Ti_{0.6}S_2$, Li (–1.9 fm), Ti (–3.44 fm) and Mn (–3.73 fm) all exhibit negative scattering lengths, whereas S possesses a positive scattering length (2.85 fm). This strongly suggests that the new positive signal at ~ 2.05 Å is attributed to the formation of new S-S atomic pairs, as in the FC state, minimal Li^+ is retained, and TM ions are retained in the TM layer, as confirmed by joint Rietveld refinement results in Figure A5.7 and Table A5.2. This ~ 2.05 Å peak also aligns well with the S-S bond length of S_2^{2-} dimers in TiS_3,[11, 12] as evidenced by the simulated PDFs of TiS_3.

Moreover, as shown in Figure 5.4 and Figure 3.11, the FC states of both $Li_{1.2}Ti_{0.8}S_2$ and $Li_{1.2}Mn_{0.2}Ti_{0.6}S_2$ show the formation of new hole states on S K pre-edge at 2470.3 eV, nearly identical to that seen in TiS_3. Together, these observations strongly suggest the formation of S_2^{2-} dimers in both $Li_{1.2}Mn_{0.2}Ti_{0.6}S_2$ and $Li_{1.2}Ti_{0.8}S_2$ during charging. In the FD sample, the peak associated with S_2^{2-} in PDFs disappears. In the second cycle, the reversible formation and reduction of the ~ 2.05 Å peak is also observed, as shown in Figure A5.11, in line with its highly reversible S-redox process.

S, Ti and Mn K-edge EXAFS

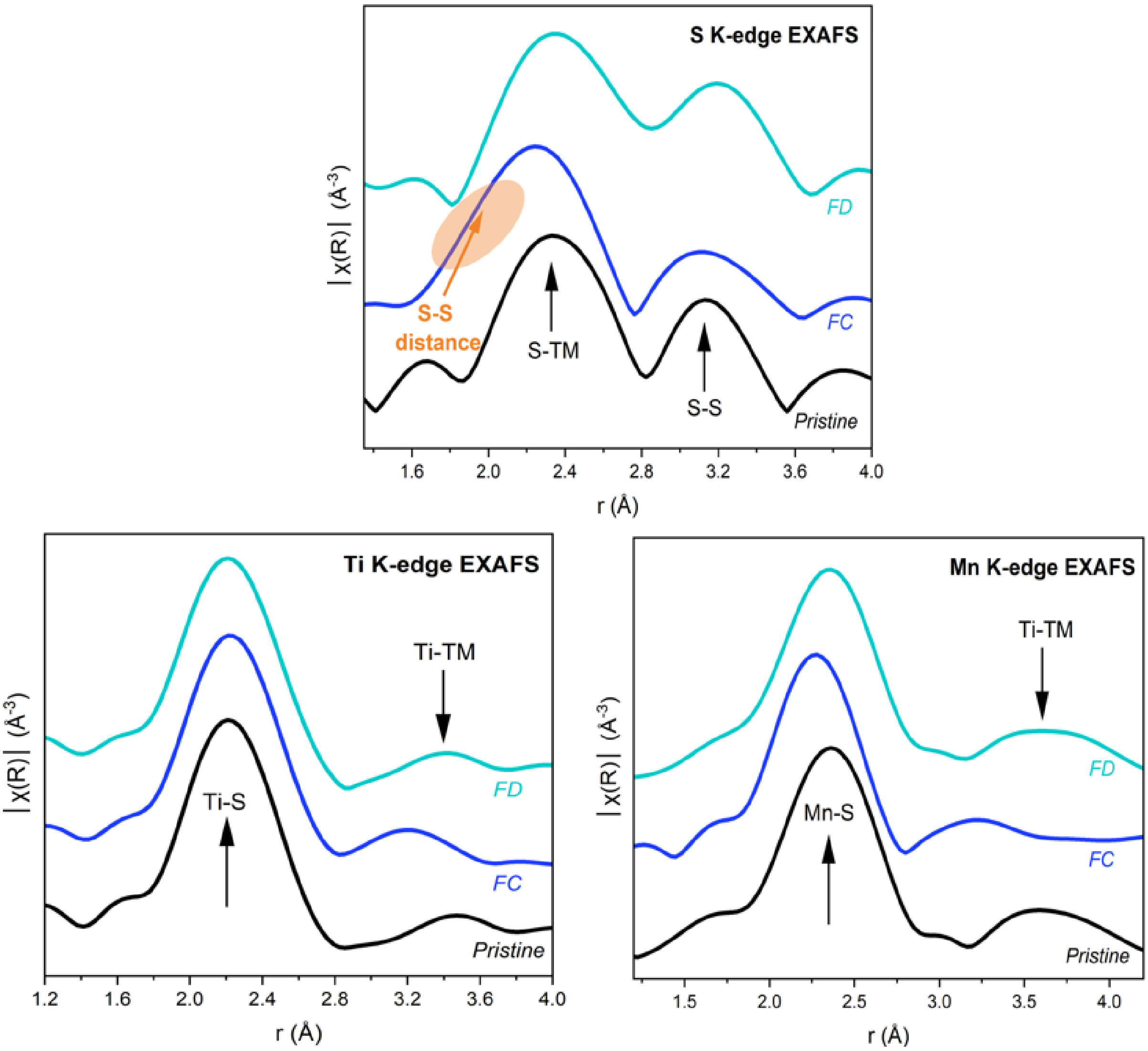

Figure 5.10: S, Ti and Mn K-edge EXAFS spectra at different states of charge. The appearance of a shoulder at a low radial distance in the first shell (highlighted in orange) of the S K-edge spectrum is consistent with the formation of short S-S distances associated with the oxidation of S ions. The phase correction function has corrected the r-value in the x-axis.

To further confirm the S_2^{2-} formation in $Li_{1.2}Mn_{0.2}Ti_{0.6}S_2$, S, Ti, and Mn K-edge EXAFS were collected on the pristine, FC and FD samples, as shown in Figure 5.10. At the FC state, S K-edge EXAFS shows significant changes in the first coordination sphere with the appearance of a new shoulder at low radial distance (~ 2 Å), as well as intensity decrease in the second shell associated with the original S-S bonds (≈ 3.1 – 3.2 Å), suggesting further the formation of short S_2^{2-} dimers, as observed in PDFs. In contrast, the Ti-S environment in Ti K-edge EXAFS remains nearly the same throughout cycling, consistent with the redox-inactive Ti^{4+}. A slight shortening of the Mn-S distance is observed at the top of charge, arising from the Mn oxidation, which is far less pronounced than the low-r shoulder seen in S K-edge EXAFS. Together, the exclusive appearance of the shoulder at ~ 2 Å in the S K-edge EXAFS strongly supports the formation of S_2^{2-} dimers within the bulk of charged $Li_{1.2}Mn_{0.2}Ti_{0.6}S_2$. At the FD state, the evolutions of S and Mn K-edge EXAFS spectra are largely reversible, with the spectra being very similar to the pristine $Li_{1.2}Mn_{0.2}Ti_{0.6}S_2$.

Discussion

The above PDF and EXAFS results indicate that the more covalent compound, $Li_{1.2}Mn_{0.2}Ti_{0.6}S_2$, which exhibits greater Mn 3*d*-S 3*p* overlap, also favors formation of S_2^{2-} dimers during S oxidation, bearing a close resemblance to $Li_{1.2}Ti_{0.8}S_2$. In Chapter 3, it has been revealed that S_2^{2-} formation in $Li_{1.2}Ti_{0.8}S_2$ is accompanied by in-plane Ti migration to form vacancy clusters within the TM layer, accounting for the degree of voltage hysteresis observed. Furthermore, this local TM rearrangement can be partially restored by mildly heating the cycled material.

To examine whether a similar mechanism accommodates S_2^{2-} dimers in the Mn-substituted sample, the FD sample was reheated in an Ar atmosphere at various temperatures for two hours. As discussed earlier, although both the pristine and FD samples can be refined well using the same O3 structure, the second cycle exhibits much reduced hysteresis compared to the first, indicating irreversible local structural changes during the first cycle. After mild heating the FD compound at 300 °C, as shown in Figure 5.11, the XRD pattern remains nearly unchanged. However, the reheated sample shows voltage recovery in both charge and discharge processes, with load curves approaching that of the first cycle. Moreover, with increasing annealing temperature, the electrochemical behavior further resembles the initial cycle, suggesting the material is progressively driven to a more thermodynamically stable, pristine-like state. All these observations closely mirror those observed in $Li_{1.2}Ti_{0.8}S_2$ (Figure A3.16), supporting the conclusion that S_2^{2-} dimers formed in charged $Li_{1.2}Mn_{0.2}Ti_{0.6}S_2$ are also accommodated within vacancy clusters generated by in-plane TM aggregation. As a result, after the first cycle, more S ions become coordinated primarily with Li^+, resulting in a lower voltage S oxidation plateau in subsequent cycles, similar to the behavior seen in $Li_{1.2}Ti_{0.8}S_2$.

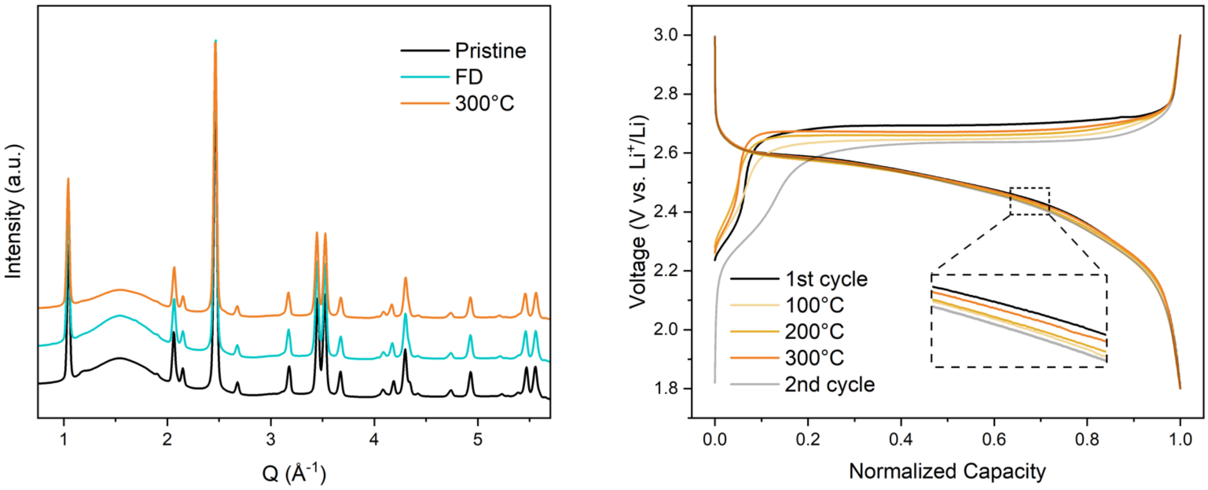

Figure 5.11: Comparison of XRD patterns and electrochemical profiles of pristine $Li_{1.2}Mn_{0.2}Ti_{0.6}S_2$, the FD sample, and reheated FD samples. The reheated samples were obtained by sintering the FD sample under Ar for 2 hours at moderate temperatures. Mild heating does not change the long-range structure but partially restores the original cycling profile, while higher reheating temperatures (100 °C, 200 °C and 300 °C) result in electrochemical load curves increasingly similar to the first cycle of pristine $Li_{1.2}Mn_{0.2}Ti_{0.6}S_2$.

This structural metastability of the cycled material is observed in both Li-rich sulfide and Li-rich oxide cathodes, where dimerized anions are accommodated within the vacancy clusters in the TM layer.[13-15] In layered Li-rich oxides, vacancy clustering disrupts the initial cation ordering in the TM layer, as directly indicated by the loss of superstructure Bragg peaks.[15] In contrast, in layered Li-rich sulfides, the TM layer remains long-range disordered from the pristine compound, making it very challenging to capture such subtle reorganization in the TM layer. Heating cycled Li-rich cathodes at an intermediate temperature offers access to highlight the local structural evolution associated with the anionic redox process.

5.3.7 Outlook for Controlling Metal-S Covalency

Since the discovery of layered Li-rich sulfide cathodes exhibiting S-redox behavior, design strategies have primarily focused on pinning the TM 3*d* band with available 3*d* electrons on top of S 3*p* bands. This is typically achieved by introducing active TM redox couples, such as $Ti^{3+/4+}$, $Fe^{2+/3+}$ and $Mn^{2+/3+}$, into the electrochemically inactive $Li_{1.33}Ti_{0.67}S_2$ framework.[9, 16-19] This Chapter, through a comparative study of O3-type $Li_{1.2}Mn_{0.2}Ti_{0.6}S_2$ and $Li_{1.2}Ti_{0.8}S_2$, demonstrates that compositional tuning can greatly enhance the TM 3*d*-S 3*p* orbital hybridization, as shown in Figure 5.12, thereby improving electronic conductivity during the S-redox activity.

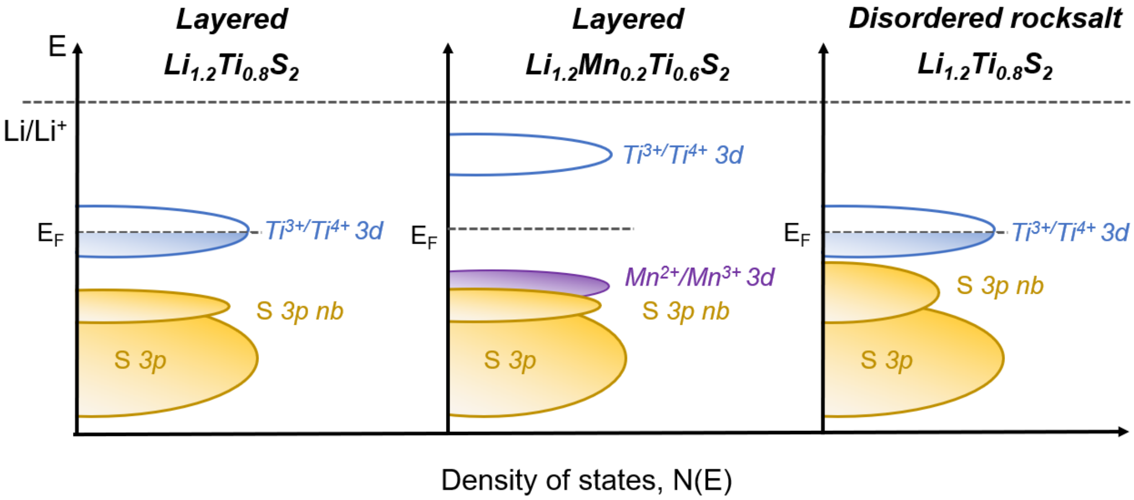

Figure 5.12: Schematic of the electronic structures for layered $Li_{1.2}Ti_{0.8}S_2$, $Li_{1.2}Mn_{0.2}Ti_{0.6}S_2$ and disordered rocksalt $Li_{1.2}Ti_{0.8}S_2$. Introducing the lower-lying Mn^{2+}/Mn^{3+} redox center or introducing cation disorder in layered $Li_{1.2}Ti_{0.8}S_2$ can both enhance the TM-S hybridization, which decreases the band gap of its electronic structure, thus promoting electron delocalization and improving electronic conductivity. The label *nb* denotes non-bonding states.

In addition to composition modifications, structural tuning via disorder was also explored. A disordered rocksalt phase of $Li_{1.2}Ti_{0.8}S_2$ was synthesized by ball milling the layered O3-type $Li_{1.2}Ti_{0.8}S_2$ under an Ar atmosphere for 2 hours, as shown in Figure 5.13 (a) and Table A5.7. Interestingly, this disordered polymorph achieves the extraction of up to 1.1 moles of Li^+ per formula without introducing carbon, comparable to the capacity delivered with 10 wt% carbon, as shown in Figure 5.13 (b). Furthermore, in contrast with the more discrete Ti and S redox processes in layered $Li_{1.2}Ti_{0.8}S_2$, concurrent Ti and S redox were clearly observed during both charge and discharge in disorder rocksalt $Li_{1.2}Ti_{0.8}S_2$. As shown in Figure 5.13 (c) and (d), the Ti and S K-edges shift simultaneously towards higher energies during oxidation and return close to their pristine position by the end of discharge. All these behaviors are very similar to those observed in $Li_{1.2}Mn_{0.2}Ti_{0.6}S_2$, suggesting that Ti 3*d*-S 3*p* hybridization is significantly improved within the disordered structure. This is most likely because the disorder provides variable local environments around sulfur sites (for example, a S ion is coordinated with six Li^+ ions), which broadens the dispersion of the S 3*p* states,[20-22] as schematically shown in Figure 5.12.

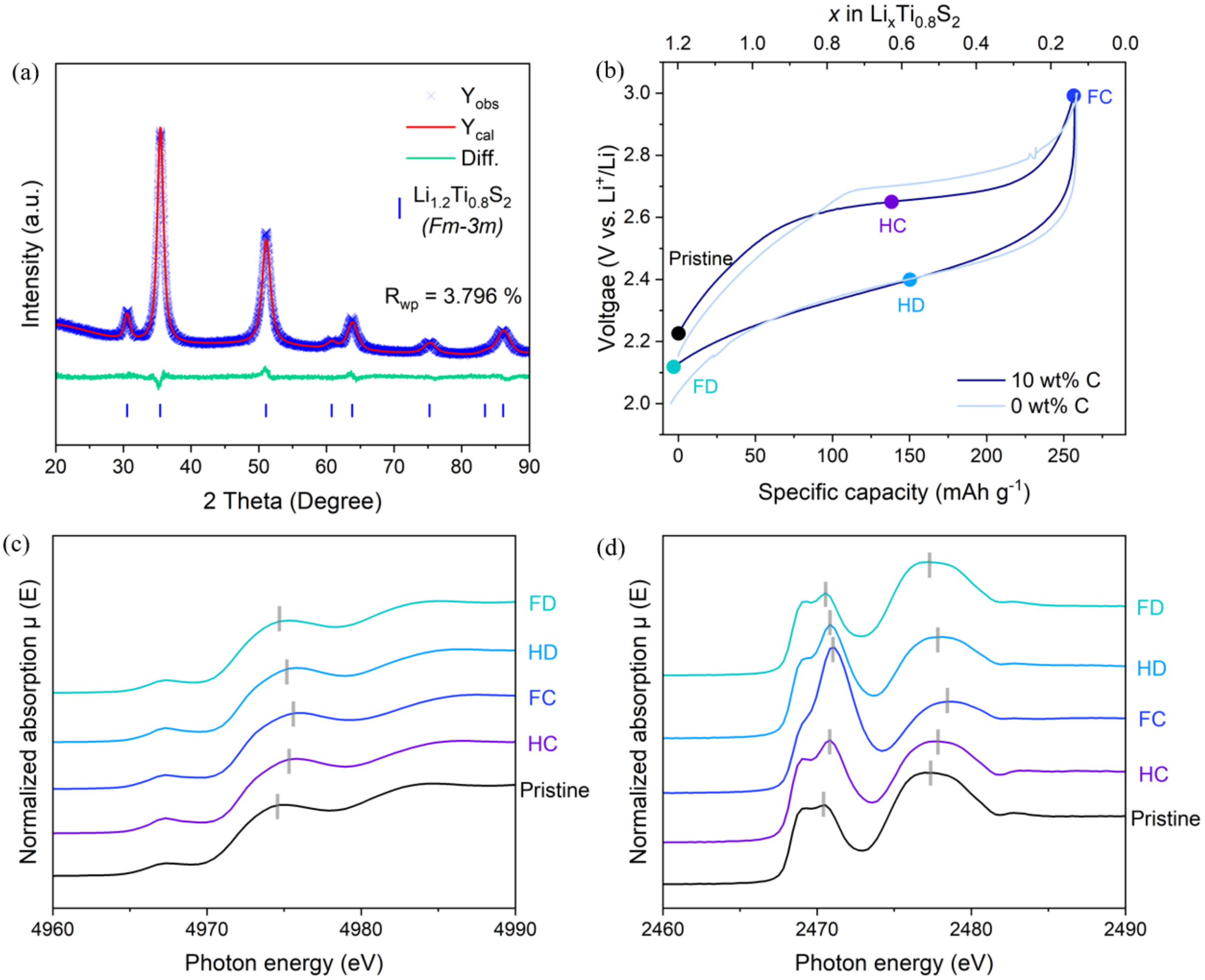

Figure 5.13: (a) Rietveld refinement of disordered rocksalt $Li_{1.2}Ti_{0.8}S_2$ with Fm-3m space group. (b) Load profiles of the first cycle between 1.8V and 3V at 10 mA g^{-1}. Coloured markers denote specific states of charge selected for detailed study during the first cycle, including pristine (OCV), half charged (HC, 2.65V), fully charged (FC, 3V), half discharged (HD, 2.4V) and fully discharged (FD, 1.8V). (c), (d), Ti K-edge (c) and S K-edge (d) XANES spectra acquired at the states of charge highlighted in panel b.

Overall, both compositional and structural tuning can play critical roles in modulating TM-S orbital mixing and covalency in Li-rich sulfides, an area that remains largely unexplored. The findings in this chapter also further highlight the potential of Li-rich sulfide cathodes for application in SSBs, provided that sufficient electronic conductivity can be maintained during cycling to minimize the use of carbon and thereby improve energy density.

5.4 Conclusion

The S-redox process in Li-rich sulfides can be effectively tuned through controlling the TM-S covalency. Compared to Ti 3*d*-S 3*p* interactions in $Li_{1.2}Ti_{0.8}S_2$, stronger Mn 3*d*-S 3*p* mixing in $Li_{1.2}Mn_{0.2}Ti_{0.6}S_2$ leads to more dispersive bands and enhanced electron delocalization, which enables more facile electron transfer during sulfur oxidation and simultaneous TM and S redox during cycling. However, much like $Li_{1.2}Ti_{0.8}S_2$, $Li_{1.2}Mn_{0.2}Ti_{0.6}S_2$ shows more pronounced voltage hysteresis in the initial cycle and partial voltage recovery after annealing the cycled material. The X-ray and neutron PDFs, along with EXAFS spectra, confirm that S_2^{2-} dimers also form in $Li_{1.2}Mn_{0.2}Ti_{0.6}S_2$, very similar to observations in $Li_{1.2}Ti_{0.8}S_2$. These results suggest that while TM–S covalency affects electronic structure, it has a limited effect on the nature of the oxidized sulfur species in the bulk of Li-rich sulfides. Further investigations involving other 4d or 5d TMs (like Zr and Nb) are warranted to examine if different oxidized sulfur products occur. To further improve the kinetics during the S-redox activity, future research on Li-rich sulfides could focus on leveraging metal-ligand covalency, via compositional and structural modifications.

5.5 References

1. Sathiya, M. *et al.* Reversible anionic redox chemistry in high-capacity layered-oxide electrodes. *Nat. Mater.* **2013,** *12* (9), 827-835.

2. McCalla, E. *et al.* Visualization of O-O peroxo-like dimers in high-capacity layered oxides for Li-ion batteries. *Science* **2015,** *350* (6267), 1516-1521.

3. House, R. A. *et al.* Covalency does not suppress O_2 formation in 4d and 5d Li-rich O-redox cathodes. *Nat. Commun.* **2021,** *12* (1), 2975.

4. Li, X.; *et al.* Reducing Voltage Hysteresis in Li-Rich Sulfide Cathodes by Incorporation of Mn. *Chem. Mater.* **2024,** *36* (11), 5687-5697.

5. Toby, B. H.; Von Dreele, R. B., GSAS-II: the genesis of a modern open-source all purpose crystallography software package. *J. Appl. Cryst.* **2013,** *46* (2), 544-549.

6. Juhas, P.; Davis, T.; Farrow, C. L.; Billinge, S. J. L., PDFgetX3: a rapid and highly automatable program for processing powder diffraction data into total scattering pair distribution functions. *J. Appl. Cryst.* **2013,** *46* (2), 560-566.

7. Farrow, C. L.; Juhas, P.; Liu, J. W.; Bryndin, D.; Božin, E. S.; Bloch, J.; Proffen, T.; Billinge, S. J. L., PDFfit2 and PDFgui: computer programs for studying nanostructure in crystals. *J. Phys.: Condens. Matter* **2007,** *19* (33), 335219.

8. Hayashi, F. *et al.* Crystal Growth and Structural Analysis of Layered Lithium Titanium Sulfide. *Inorg. Chem.* **2025,** *64* (4), 1711-1717.

9. Saha, S. *et al.* Exploring the bottlenecks of anionic redox in Li-rich layered sulfides. *Nat. Energy* **2019,** *4* (11), 977-987.

10. Boivin, E.; House, R. A.; Marie, J.-J.; Bruce, P. G., Controlling Iron Versus Oxygen Redox in the Layered Cathode $Na_{0.67}Fe_{0.5}Mn_{0.5}O_2$: Mitigating Voltage and Capacity Fade by Mg Substitution. *Adv. Energy Mater.* **2022**, *12* (30), 2200702.

11. Saha, S. Exploration of ionic conductors and Li-rich sulfides for all-solid-state batteries. Sorbonne Université, 2020.

12. Furuseth, S. *et al.* On the Crystal Structures of TiS_3, ZrS_3, $ZrSe_3$, $ZrTe_3$, HfS_3, and $HfSe_3$. *Acta Chem. Scand.* **1975**, *29* (6), 623-631.

13. Qiu, B. *et al.* Metastability and Reversibility of Anionic Redox-Based Cathode for High-Energy Rechargeable Batteries. *Cell Rep. Phys. Sci.* **2020,** *1* (3), 100028.

14. Qiu, B. *et al.* Negative thermal expansion and oxygen-redox electrochemistry. *Nature* **2025,** *640*, 941–946.

15. House, R. A. *et al.* First-cycle voltage hysteresis in Li-rich 3d cathodes associated with molecular O_2 trapped in the bulk. *Nat. Energy* **2020,** *5* (10), 777-785.

16. Louis, J. *et al.* Effect of the Nature of Both Cation and Anion Substitution on the Structural Symmetry of Li-Rich 3d-Metal Chalcogenide Electrodes. *Adv. Energy Mater.* **2023,** *13* (45), 2302158.

17. Flamary-Mespoulie, F. *et al.* Lithium-rich layered titanium sulfides: Cobalt- and Nickel-free high capacity cathode materials for lithium-ion batteries. *Energy Storage Mater.* **2020,** *26*, 213-222.

18. Jiang, Z. *et al.* Metal–Ligand Spin-Lock Strategy for Inhibiting Anion Dimerization in Li-Rich Cathode Materials. *J. Am. Chem. Soc.* **2025,** *147* (4), 3062-3071..

19. Li, J.-C. *et al.* From Oxygen Redox to Sulfur Redox: A Paradigm for Li-Rich Layered Cathodes. *J. Am. Chem. Soc.* **2024,** *146* (11), 7274-7287.

20. Marchandier, T. *et al.* Triggering Anionic Redox Activity in Li_3NbS_4 Through Cationic Disordering or Substitution. *Adv. Energy Mater.* **2022,** *12* (41), 2201417.

21. Shinoda, M. *et al.* Activation of Anionic Redox for Stoichiometric and Li-Excess Metal Sulfides through Structural Disordering: Joint Experimental and Theoretical Study. *J. Am. Chem. Soc.* **2025,** *147* (30), 26238-26253.

22. Kwon, D.; Kim, D., Structural factors for activating anionic redox in Li-rich Ti-based cathodes. *J. Mater. Chem. A* **2023,** *11* (28), 15140-15146.

6

Conclusion

Contents

6.1 Conclusion

Invoking anionic redox chemistry is a compelling strategy to overcome the limitations imposed by transition metals on storing charge in cathode materials for Li-ion batteries. In oxide-based Li-rich cathodes, oxidation of O^{2-} leads to the formation of molecular O_2 trapped in nano-sized pores within the cathode particles and the irreversible O_2 loss from the particle surface. These processes cause pronounced voltage hysteresis and voltage fade, low first-cycle coulombic efficiency, as well as sluggish kinetics. Despite extensive optimization efforts in Li-rich oxides, these practical problems remain largely unresolved. Recent studies, however, have revealed that replacing O ions with S ions to make Li-rich sulfides enables S-redox, which largely mitigates most of the undesired anionic redox behaviors. The work presented in this thesis focuses on elucidating the fundamental mechanism of S-redox, comparing and contrasting it with O-redox in analogous layered Li-rich structures, and exploring strategies to harness S-redox more effectively.

6.1 Conclusion

In Chapter 3, a model Li-rich sulfide, $Li_{1.2}Ti_{0.8}S_2$, which is a direct analogue of the archetypal O3-type Li-rich layered oxides $Li_{1.2}TM_{0.8}O_2$ (TM = Ni, Co, Mn) has been investigated. Employing a suite of spectroscopic and structural characterization techniques, it was revealed that S-redox is associated with the formation of S-S bonds in the form of S_2^{2-} in the bulk upon charging, rather than elemental S or electron holes on S. RMC Profile modelling of the neutron total scattering data reveals, for the first time, that the S_2^{2-} dimers are accommodated in vacancy clusters formed by in-plane TM migration, similar to that observed Li-rich oxides, explaining the residual first-cycle hysteresis in Li-rich sulfide cathodes. Furthermore, quantitative joint PXRD and neutron diffraction refinements show that approximately 20% of the sulfur atoms are displaced from their original lattice sites to form S_2^{2-} after charging, roughly half the amount of S_2^{2-} species anticipated from the charge passed, indicating that the persulfide dimers remain partially coordinated to Ti atoms. This behavior contrasts sharply with Li-rich oxides, where the relatively ionic nature of oxygen and weaker TM-O covalency result in the irreversible O_2 evolution from the surface and formation of more isolated molecular O_2 trapped in the bulk. In Li-rich sulfides, the strong TM-S covalency stabilizes the S_2^{2-} dimers, which remain coordinated to adjacent TM ions rather than becoming free species. This rationalizes why Li-rich sulfides do not exhibit first-cycle irreversibility and retain well-preserved, undensified surface structures. It may also account for the faster kinetics observed in Li-rich sulfides than Li-rich oxides, as coordination with the TM will aid electron transfer between S_2^{2-} and the host structure.

In Chapter 4, beyond conventional liquid electrolyte cells, the S-redox behavior of $Li_{1.2}Ti_{0.8}S_2$ was also investigated in ASSBs. When paired with Li_6PS_5Cl SEs, the as-prepared $Li_{1.2}Ti_{0.8}S_2$ can deliver nearly 99% capacity retention after 200 cycles at room temperature under 2MPa pressure, with the areal capacity of ~ 2.8 mAh cm^{-2}. This outstanding electrochemical performance arises from the excellent chemical compatibility between Li-rich sulfide and sulfide SE, the limited volume change of the Li-rich sulfide, and the well-preserved mechanical integrity of the composite cathode. These results highlight the potential of Li-rich sulfides in ASSBs as a promising cathode to achieve high energy density beyond the landscape of high-voltage oxide-based cathodes. Nevertheless, to offer true competitiveness against state-of-the-art Ni-rich oxides in ASSBs, novel sulfide cathodes with higher capacity and faster kinetics are required to overcome the inherent energy density penalty associated with sulfur as a ligand.

In Chapter 5, another layered Li-rich sulfide cathode, $Li_{1.2}Mn_{0.2}Ti_{0.6}S_2$, was successfully synthesized. Compared to $Li_{1.2}Ti_{0.8}S_2$, this compound exhibits stronger TM–S covalency, arising from the lower-lying $Mn^{2+/3+}$ bands relative to the $Ti^{3+/4+}$ states, which enhances hybridization between TM 3*d* and S 3*p* orbitals. Local structural probes confirm that S_2^{2-} dimers persist as the oxidized products of S ions in the charged $Li_{1.2}Mn_{0.2}Ti_{0.6}S_2$. However, the stronger TM–S covalency enables S oxidation at earlier stages of charging and significantly enhances electron mobility during the S-redox process. Accordingly, S-redox capacity can be fully accessed with reduced carbon additive content. These results demonstrate that faster S-redox kinetics can be achieved by tailoring composition to strengthen TM–S covalency, thereby further advancing the development of Li-rich sulfides for ASSBs.

Overall, the insights provided by the results and discussion in this thesis offer renewed optimism for exploiting anionic redox in the design of higher-energy-density cathode materials. Although the Li-rich sulfides investigated in this thesis are unlikely to be technologically viable materials in their current forms, their detailed study offers a fundamental understanding of the chemistry of S-redox and contributes to a more comprehensive picture of anionic redox behavior.

6.2 Further Work

6.2.1 Further Understanding S-redox Chemistry

The present work in this thesis has advanced the understanding of S-redox processes in layered Li-rich sulfides through the combined use of inelastic spectroscopies and local structural probes. Nevertheless, the current knowledge of S-redox lags significantly behind that of O-redox, which has been extensively investigated in various Li-rich compositions and structures as well as in Na-ion cathodes. Future investigations into a broader range of Li-rich sulfides with diverse electrochemical behaviors and structures are therefore essential. Such studies will clarify whether other alternative

S-redox mechanisms are operative and may provide new design principles for high-energy-density Li-rich cathodes.

For example, systematic comparisons of compounds with the same $Li_{1.2}Ti_{0.8}S_2$ composition but in layered and disordered rocksalt structures, together with direct parallels between S-redox and O-redox behaviors within the same disordered rocksalt framework, would offer a more comprehensive understanding of anionic redox behavior in cathode materials.

Beyond Li-ion systems, S-redox activity has also been observed in Na-based sulfides, with some distinct behaviors relative to Li-rich sulfides. For example, the S-redox reaction is active in non-Na-rich sulfides, like $NaCrS_2$.[1] In addition, unlike the electrochemically inert layered Li_2TiS_3, the Na-based analogue Na_2TiS_3 exhibits pronounced S-redox activity.[2] The mechanism of these intriguing behaviors remains poorly understood. Extending the methodologies developed in this thesis to probe the oxidized S species and their associated structural evolution in these Na-based sulfides would provide valuable insights.

From a methodological perspective, characterizing oxidized S species remains a challenge. In O-redox cathodes, high-resolution O K-edge RIXS has successfully distinguished between oxidized O species, such as O_2^{-}, O_2^{2-}, and O_2.[3] In contrast, different oxidized S species may possess very similar bond lengths, making them more challenging to differentiate. The development and application of complementary techniques, such as S L-edge RIXS, *operando* PDF, and scanning transmission X-ray microscopy (STXM), might prove critical in disentangling the complex S-redox processes.

6.2.2 Synthesizing New Sulfide and Oxysulfide Cathodes

The promising electrochemistry of Li-rich sulfides present in this thesis raises the exciting prospect of novel Li-rich sulfides using S-redox. To achieve higher energy density, Li-rich sulfides with a higher Li/TM ratio must be explored, such as Li_3NbS_4.

Extending this concept to Na-ion systems is equally important. For instance, the Na-based analogue, $Na_{1.2}Ti_{0.8}S_2$, of the model compound studied in this thesis, $Li_{1.2}Ti_{0.8}S_2$, has not been reported yet.

Another promising direction lies in the design of Li-rich oxysulfide cathodes, which could combine the reversibility of S-redox with the high energy density characteristic of O-redox. Such materials might be synthesized via direct solid-state synthesis by incorporating an appropriate amount of oxide precursors (e.g., Li_2O or TM oxides) into sulfide-based frameworks.

6.2.3 Promoting the Energy Density of All-solid-state Batteries by Li-rich Sulfides

Building on superior cyclability and satisfactory areal capacity demonstrated by layered $Li_{1.2}Ti_{0.8}S_2$, it is essential to explore new compositions and processing routes that can further raise ASSB energy density to levels competitive with state-of-the-art Ni-rich oxides. Because sulfides generally operate at lower voltages than oxides, achieving Li-rich sulfides with higher specific capacities (> 300 mAh g^{-1}) is particularly desirable. As shown in this thesis, the electronic conductivity of Li-rich sulfides can be significantly improved by tuning both composition and crystal structure, thereby reducing the required carbon additive content in composite cathodes and improving energy density. Moreover, processing methods play a key role. Given the excellent interfacial compatibility between Li-rich sulfides and sulfide SEs demonstrated in this thesis, hot pressing the composite cathodes at moderate temperatures (< 200 °C) may provide a promising approach to achieve denser electrode architectures, thus minimizing porosity, improving particle–particle contact, and boosting the performance of Li-rich sulfides in ASSBs.

6.3 References

1. Shadike, Z. *et al.* Antisite occupation induced single anionic redox chemistry and structural stabilization of layered sodium chromium sulfide. *Nature Communications* **2017,** *8* (1), 566.

2. Leube, B. T. *et al.* Layered Sodium Titanium Trichalcogenide Na_2TiCh_3 Framework (Ch = S, Se): A Rich Crystal and Electrochemical Chemistry. *Chemistry of Materials* **2022,** *34* (5), 2382-2392.

3. House, R. A. *et al.* Covalency does not suppress O_2 formation in 4d and 5d Li-rich O-redox cathodes. *Nature Communications* **2021,** *12* (1), 2975.

Appendices

Contents

Appendices for Chapter 3

Appendices Figures

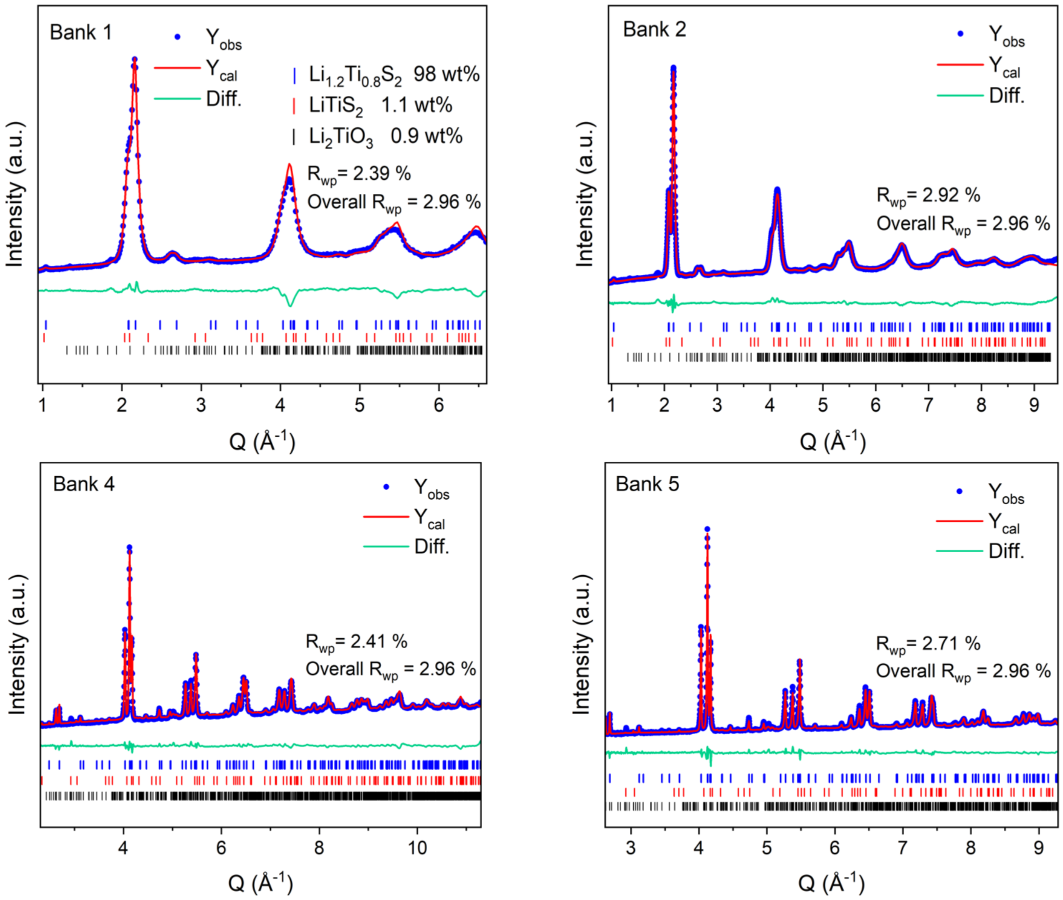

Figure A3.1: Rietveld refinements of the time-of-flight neutron diffraction for $Li_{1.2}Ti_{0.8}S_2$. Neutron diffraction data from five detector banks are jointly refined along with the PXRD data presented in Figure 3.1.

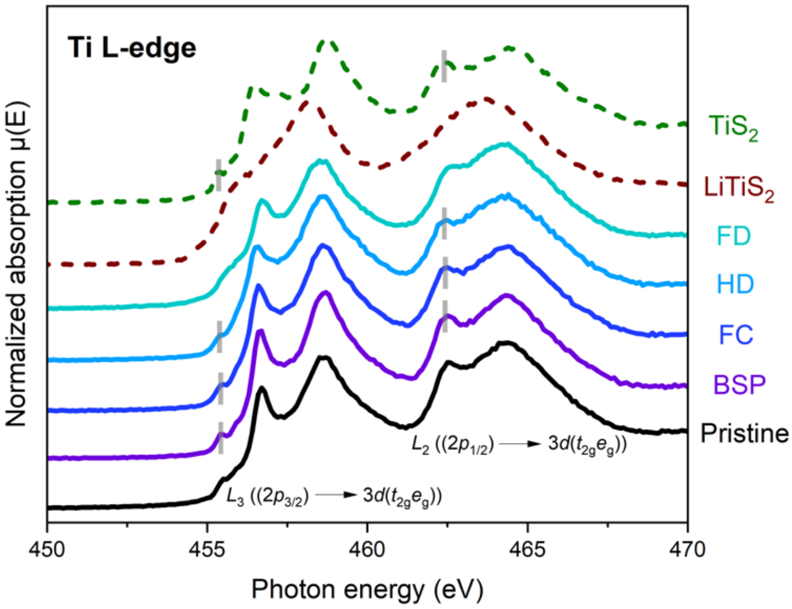

Figure A3.2: Ti L-edge XAS spectra for $Li_{1.2}Ti_{0.8}S_2$ at different states of charge during the first cycle. The Ti $L_{2,3}$-edge XAS spectra were collected under fluorescence PFY mode, offering bulk sensitivity to a depth of approximately 100 nm. The spectra exhibit two primary peaks corresponding to the $2p_{3/2} \rightarrow 3d$ (L_3) and $2p_{1/2} \rightarrow 3d$ (L_2) transitions. From the BSP to HD states, the Ti L-edge features (highlighted by grey lines) remain largely unchanged and closely resemble those Ti^{4+} in TiS_2, consistent with the Ti K-edge XANES data shown in Figure 3.6 (b).

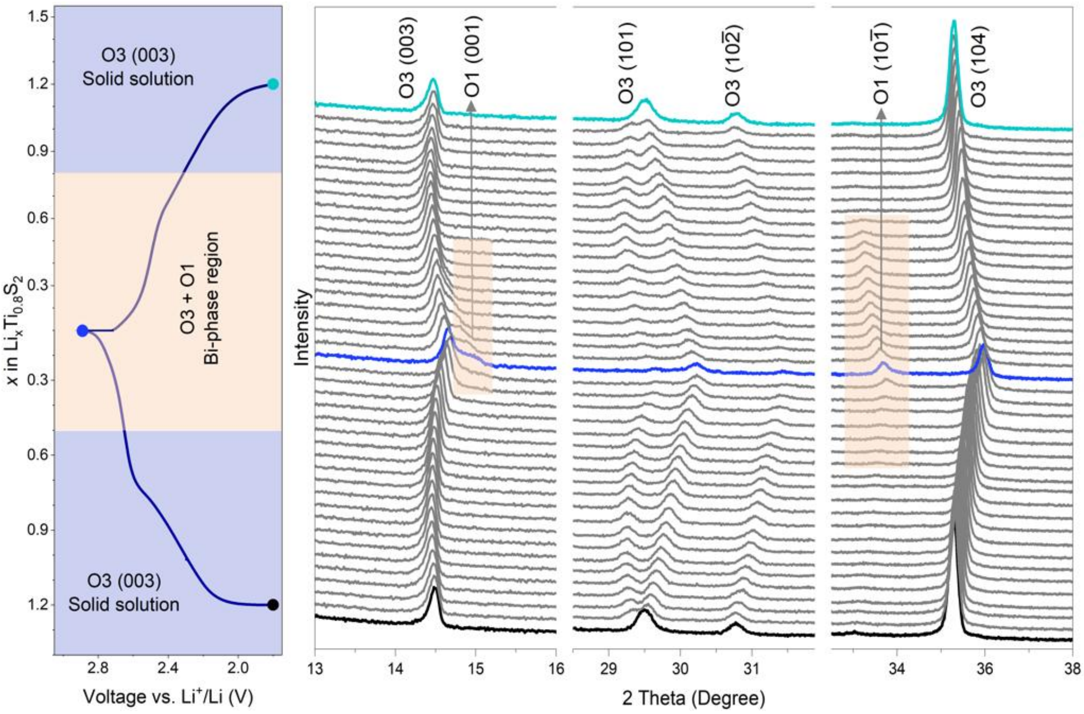

Figure A3.3: Structural evolution of $Li_{1.2}Ti_{0.8}S_2$ during the second cycle. $Li_{1.2}Ti_{0.8}S_2$ undergoes the same O3-O1 phase evolution observed in the initial cycle. The left panel shows the corresponding cycling profile for the second cycle between 1.8V and 3V at 10 mA g^{-1}.

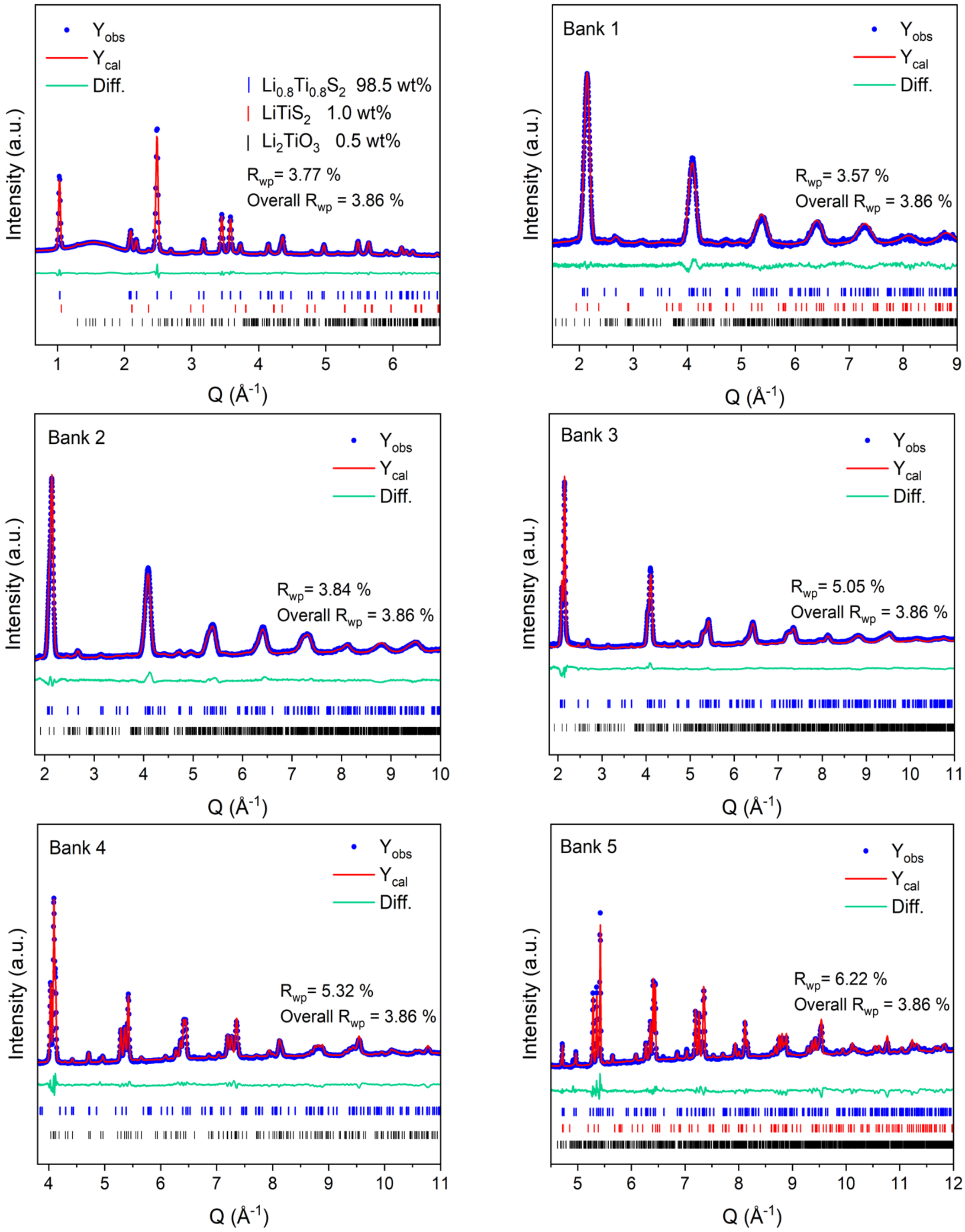

Figure A3.4: Rietveld refinements of the BSP sample ($Li_{1.2}Ti_{0.8}S_2$ charged to 2.6V). Joint Rietveld refinements of the PXRD (top left) and neutron diffraction data from five detector banks. The BSP sample retains the O3-type structure with $R\bar{3}m$ space group.

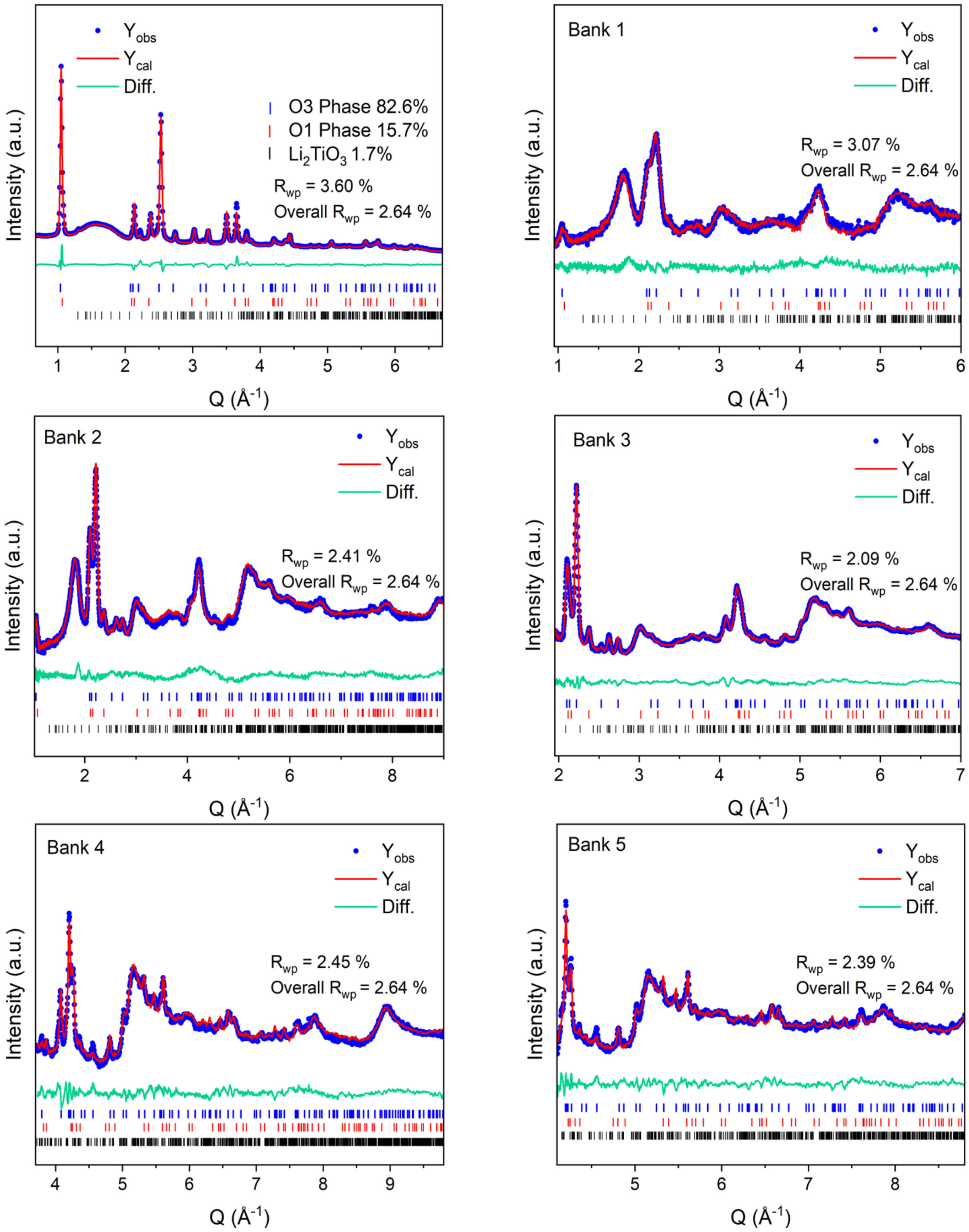

Figure A3.5: Rietveld refinements of the FC sample ($Li_{1.2}Ti_{0.8}S_2$ charged to 3V). Joint Rietveld refinements of the PXRD (top left) and neutron diffraction data from five detector banks. The FC sample exhibits a biphasic mixture of O3- and O1- phases, consistent with the *operando* XRD results presented in Figure 3.7.

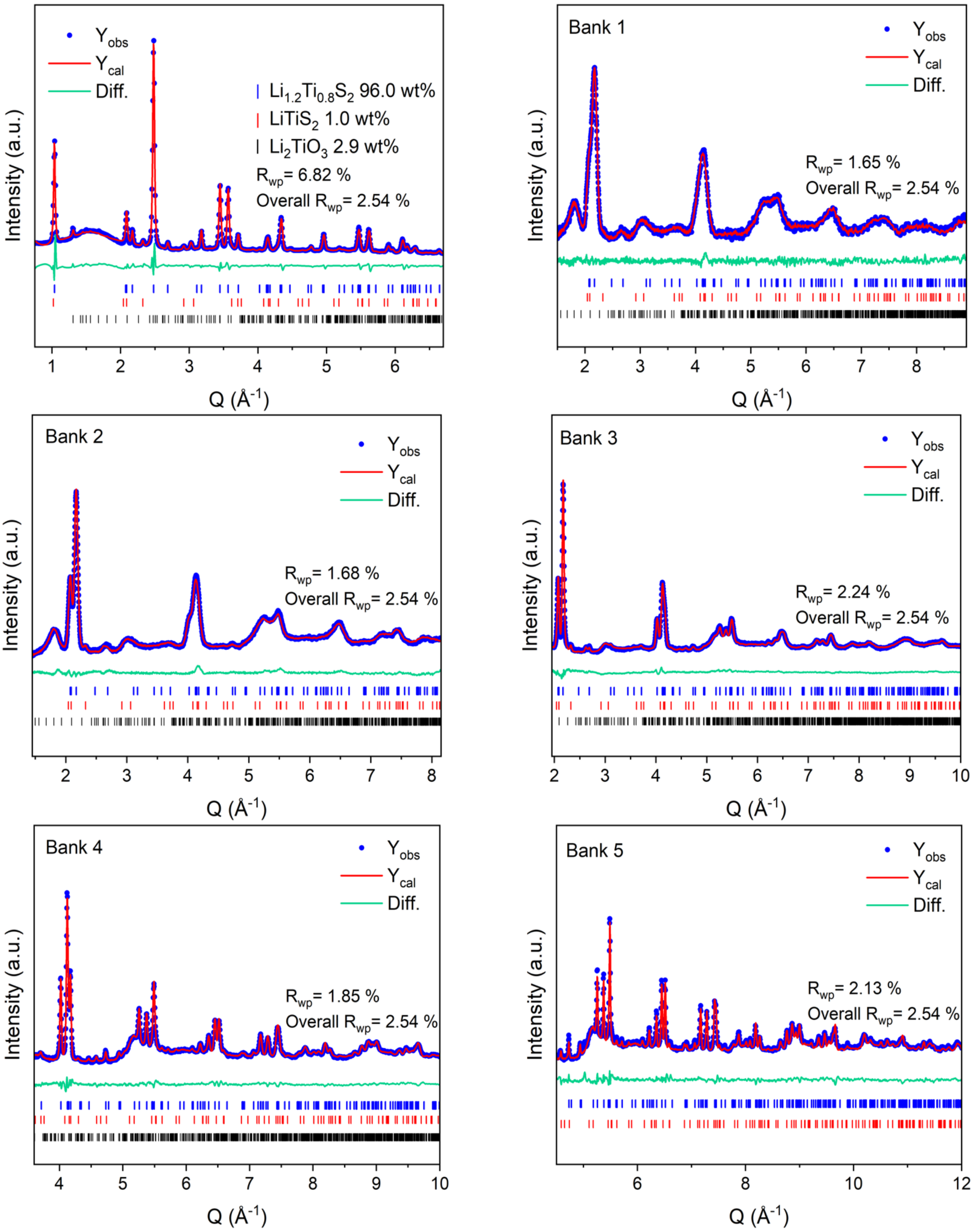

Figure A3.6: Rietveld refinements of the FD sample (Li$_{1.2}$Ti$_{0.8}$S$_2$ discharged to 1.8V). Joint Rietveld refinements of the PXRD (top left) and neutron diffraction data from five detector banks. Following a full cycle, the FD sample remains the O3-type layered structure with lattice parameters closely matching the pristine state, suggesting a highly reversible long-range structural evolution during cycling.

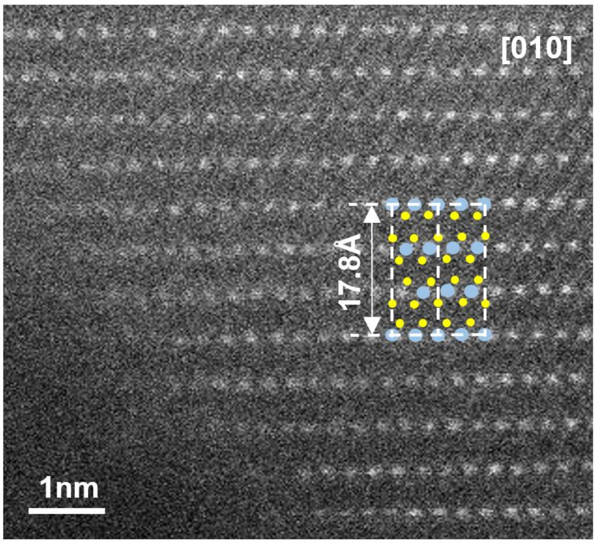

Figure A3.7: The ADF-STEM image of the FC sample. The STEM image, taken along with the [010] zone axis, aligns with the O3-type layered structure. No densification layer is observed on the surface. ADF-STEM images were taken by Dr Jun Chen, and the material was prepared by me.

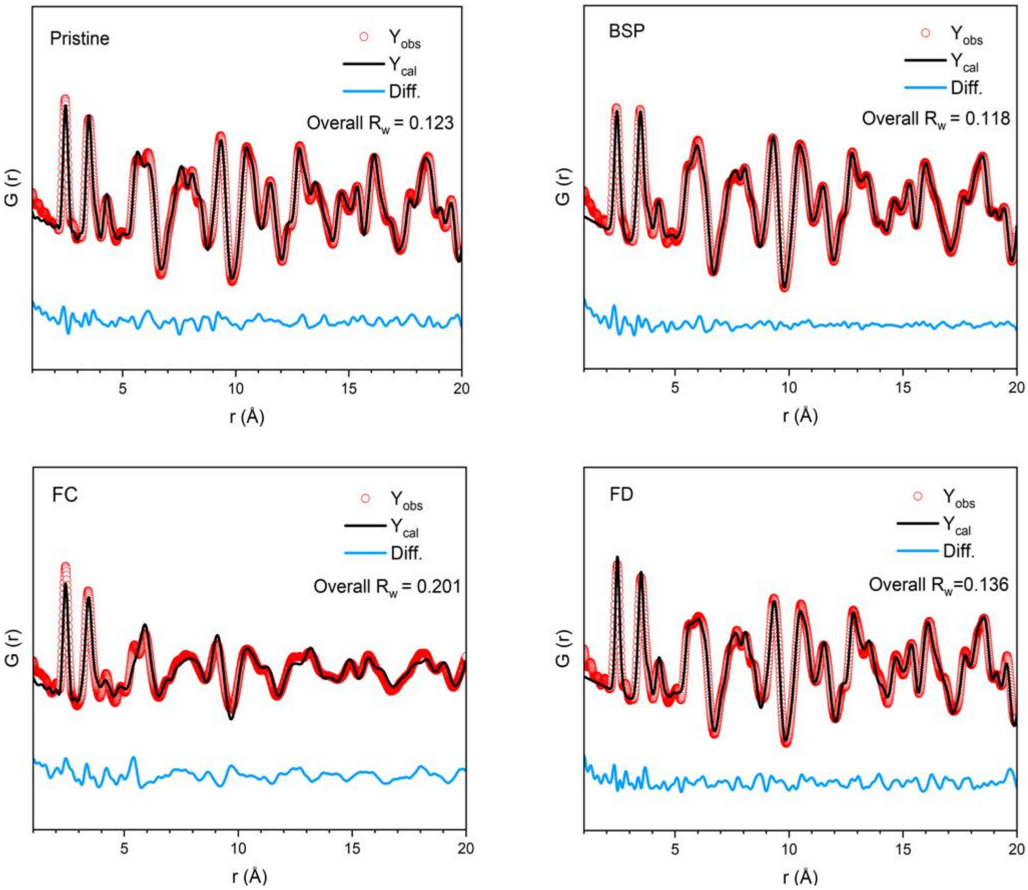

Figure A3.8: Fitting results of X-ray PDFs. X-ray PDFs of $Li_{1.2}Ti_{0.8}S_2$ at various states of charge, with Q_{max} = 23 Å. At each state of charge, the X-ray and Neutron PDFs (Figure A3.9) were jointly refined between 1 – 20 Å using PDFgui. The PDF of the FC sample was refined using a biphasic O3/O1 structural model, while the others were refined using a single-phase O3-type structure, consistent with diffraction results.

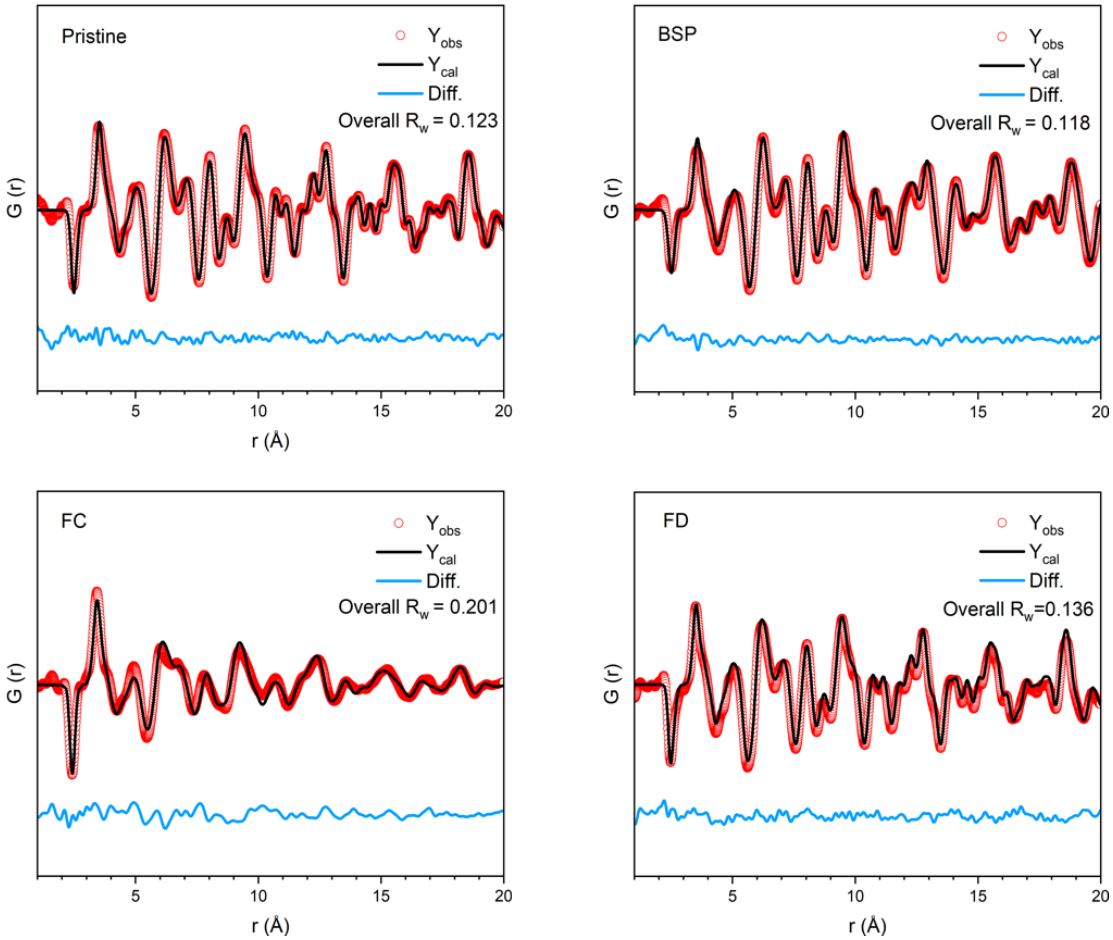

Figure A3.9: Fitting results of neutron PDFs. Neutron PDFs of $Li_{1.2}Ti_{0.8}S_2$ at various states of charge, with Q_{max} = 23 Å. At each state of charge, the neutron and X-ray PDFs (Figure A3.8) were jointly refined between 1 – 20 Å using PDFgui. The PDF of the FC sample was refined using a biphasic O3/O1 structural model, while the others were refined using a single-phase O3-type structure, consistent with diffraction results.

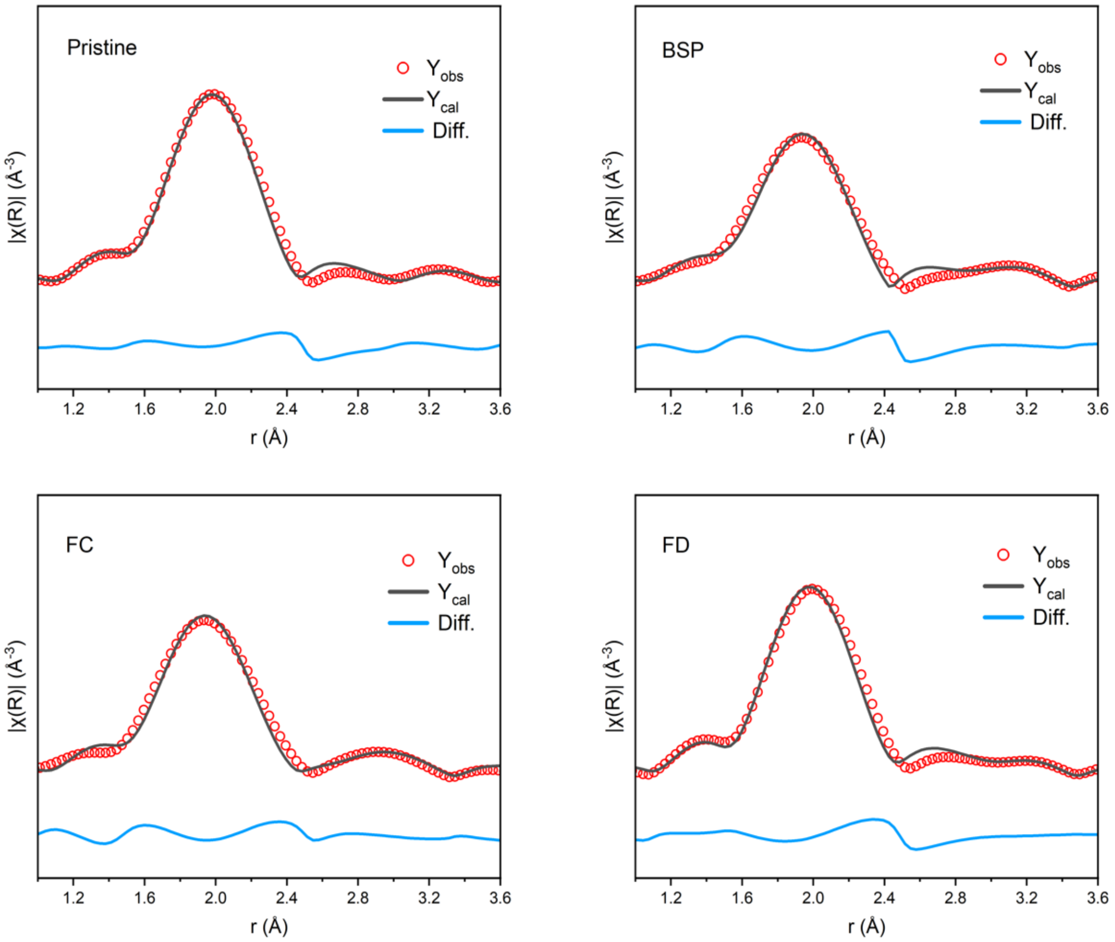

Figure A3.10: Fitting of S K-edge EXAFS for $Li_{1.2}Ti_{0.8}S_2$ at different states of charge. The description of the model used and the fitting parameters are listed in Table A3.9.

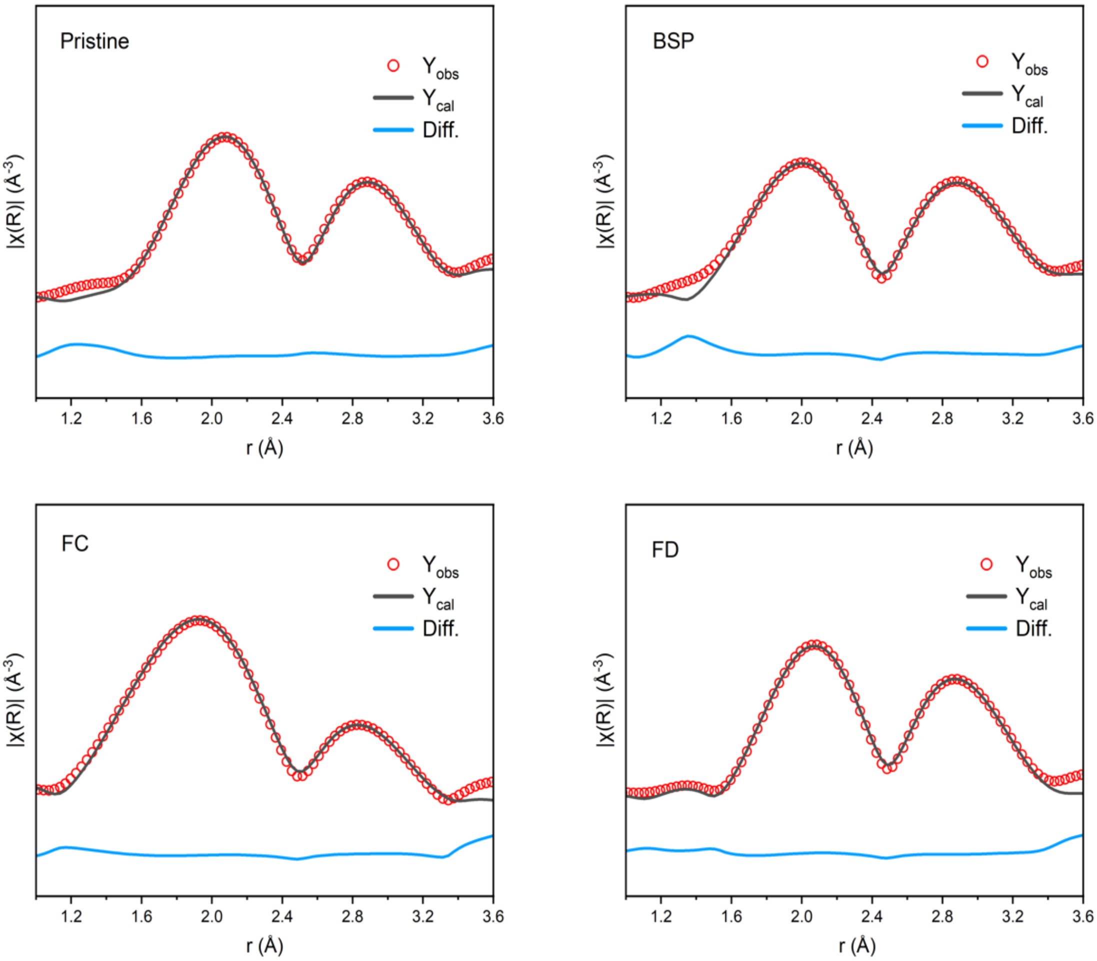

Figure A3.11: Fitting of Ti K-edge EXAFS for $Li_{1.2}Ti_{0.8}S_2$ at different states of charge. The description of the model used and the fitting parameters are listed in Table A3.10.

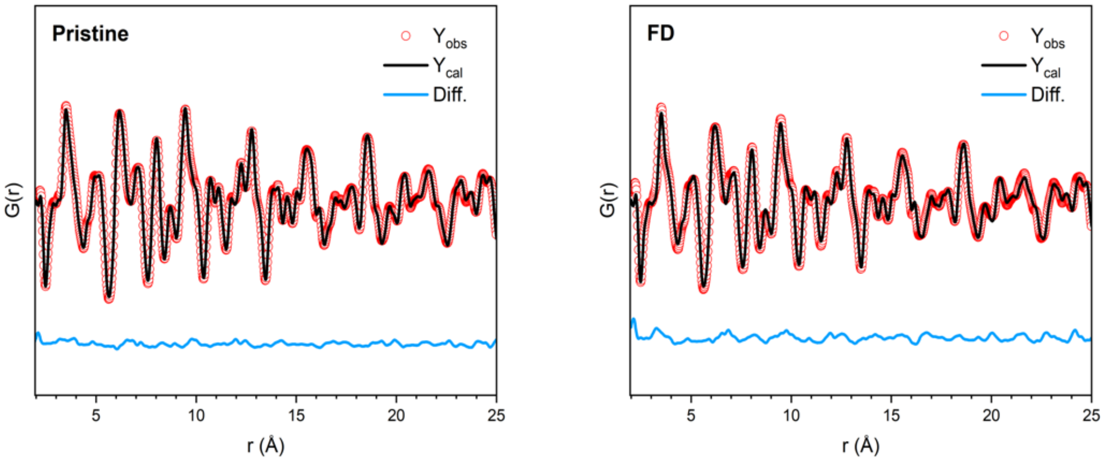

Figure A3.12: Neutron PDF fitting results of the pristine and FD sample, obtained from the RMC profile modelling analysis.

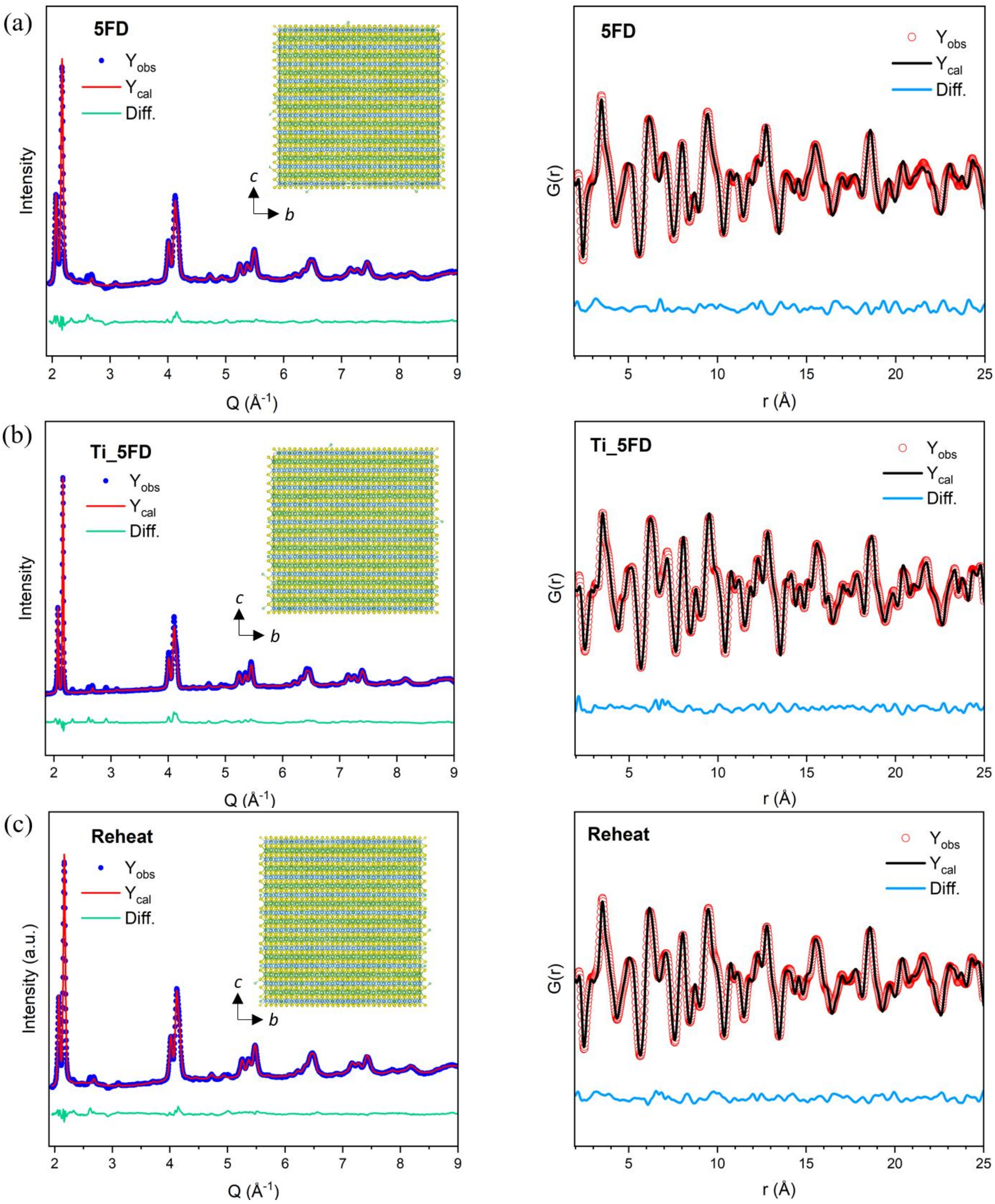

Figure A3.13: Neutron total scattering data fitting of the (a) 5FD sample (after 5 cycles) (b) Ti_5FD sample (cycled within the Ti redox window for 5 cycles) and (c) Reheated sample (Reheated the FD sample at 200 °C for 2 hours), obtained from the RMC profile modelling analysis.

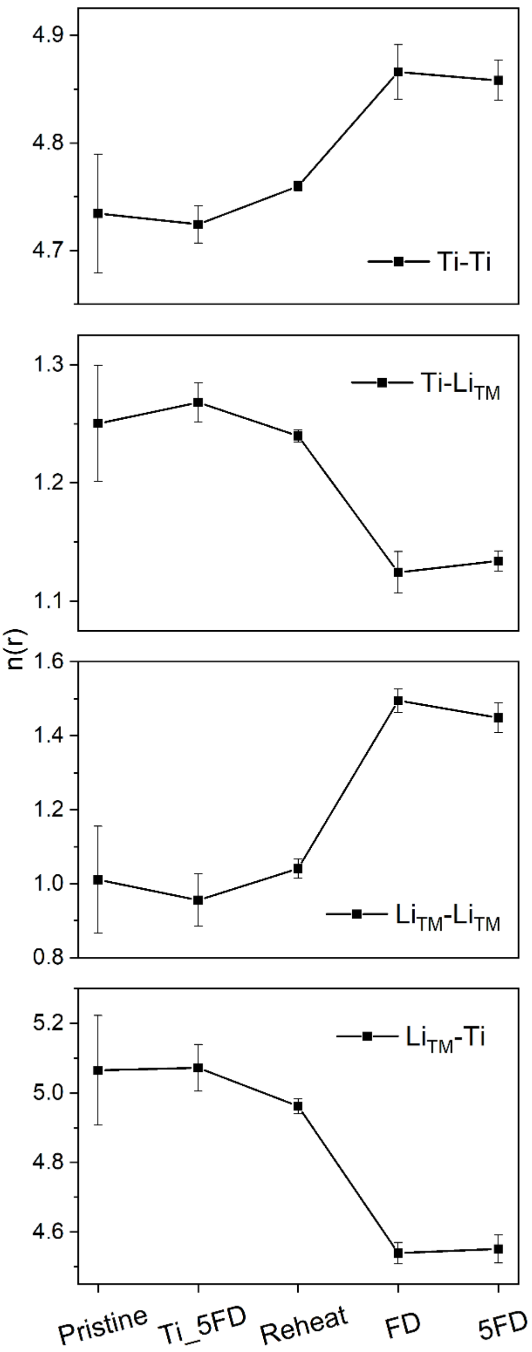

Figure A3.14: Evolution of the coordination number, n(r), for neighboring atomic pairs in the TM layer, including Ti-Ti, Ti-Li$_{TM}$, Li$_{TM}$-Li$_{TM}$, and Li$_{TM}$-Ti across the pristine, Ti_5FD, Reheated_FD, FD, and 5FD samples. All these statistical analyses are extracted from RMC profile modelling.

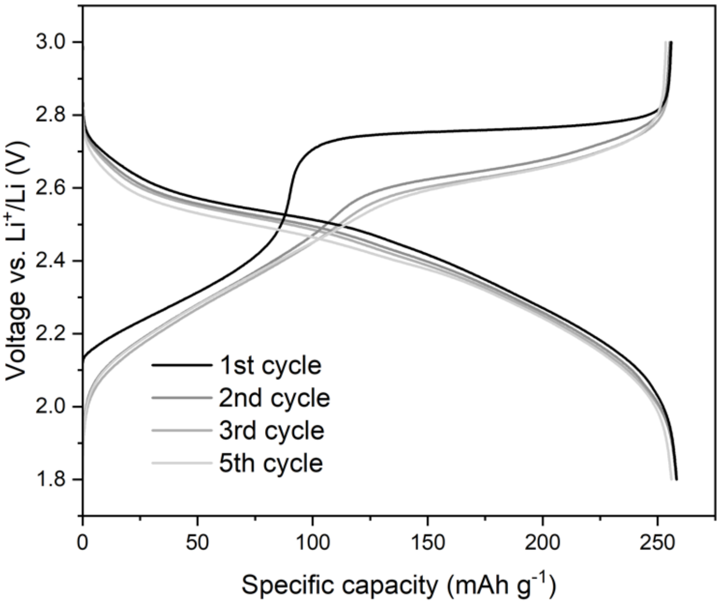

Figure A3.15: Additional electrochemical cycling for $Li_{1.2}Ti_{0.8}S_2$. The first five cycles collected between 1.8 – 3V at a current density of 10 mA g^{-1}. After the first cycle, the distinct charging plateau diminishes, transitioning to a more sloping charge profile.

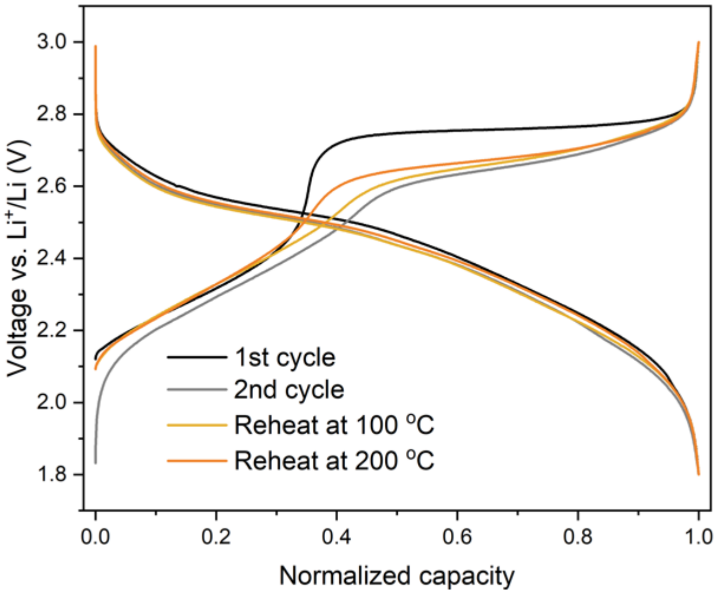

Figure A3.16: Comparison of electrochemical profiles after reheating the FD sample. After the first cycle, the FD sample was reheated in Ar for 2 hours at 100 °C and 200 °C, respectively. Thermal treatment partially restores the original charging plateau and prompts the average discharge voltage. Higher reheating temperatures result in electrochemical profiles that more closely resemble those of the first cycle for pristine. However, sintering at a temperature above 250 °C would lead to Li loss.

Appendices Tables

Table A3.1: Refined structural parameters for the pristine $Li_{1.2}Ti_{0.8}S_2$ sample obtained from joint Rietveld refinement of PXRD and neutron diffraction data.

Atom	Wyckoff	x	y	z	Occupancy	Uiso
Li1	3b	0	0	0.5	1	0.0156(9)
Li2	3a	0	0	0	0.2	0.0156(9)
Ti	3a	0	0	0	0.8	0.0041(6)
S	6c	0	0	0.2546(0)	1	0.0070(4)
Space group $R\bar{3}m$, a = 3.5251(3) Å, c = 18.1123(2) Å, Overall R_{wp} = 2.96%						

Table A3.2: Refined structural parameters for the BSP sample (~ $Li_{0.8}Ti_{0.8}S_2$) obtained from joint Rietveld refinement of PXRD and neutron diffraction data.

Atom	Wyckoff	x	y	z	Occupancy	Uiso
Li1	3b	0	0	0.5	0.6	0.0231(1)
Li2	3a	0	0	0	0.2	0.0231(1)
Ti	3a	0	0	0	0.8	0.0130(9)
S	6c	0	0	0.2567(0)	1	0.0099(8)
Space group $R\bar{3}m$, a = 3.5113(4) Å, c = 18.1860(3) Å, Overall R_{wp} = 3.86%						

Table A3.3: Refined structural parameters for (a) O3 phase and (b) O1 phase in the fully charged sample, ~ $Li_{0.1}Ti_{0.8}S_2$, obtained from joint Rietveld refinement of PXRD and neutron diffraction data.

(a)

Atom	Wyckoff	x	y	z	Occupancy	Uiso
Li1	3b	0	0	0.5	0.05	0.05
Li2	3a	0	0	0	0.05	0.05
Ti	3a	0	0	0	0.8	0.0586(4)
S	6c	0	0	0.2559(9)	0.780(4)	0.0215(6)
Space group $R\bar{3}m$, a = 3.4444(6) Å, c = 17.9564(8) Å, Overall R_{wp} = 2.64%						

(b)

Atom	Wyckoff	x	y	z	Occupancy	Uiso
Li1	1b	0	0	0.5	0.05	0.05
Li2	1a	0	0	0	0.05	0.05
Ti	1a	0	0	0	0.8	0.0586(4)
S	2d	0.33333	0.66667	0.25000	0.857(8)	0.0215(6)
Space group $R\bar{3}m$, a = 3.4287(8) Å, c = 5.8278(7) Å, Overall R_{wp} = 2.64%						

Table A3.4: Refined structural parameters for the FD sample, $Li_{1.2}Ti_{0.8}S_2$ obtained from joint Rietveld refinement of PXRD and neutron diffraction data.

Atom	Wyckoff	x	y	z	Occupancy	Uiso
Li1	3b	0	0	0.5	1	0.0153(0)
Li2	3a	0	0	0	0.2	0.0153(0)
Ti	3a	0	0	0	0.8	0.0110(9)
S	6c	0	0	0.2556(9)	1	0.0105(0)
Space group $R\overline{3}m$, a = 3.5220(4) Å, c = 18.1724(9) Å, Overall R_{wp} = 2.54%						

Table A3.5: Refined structural parameters for the pristine $Li_{1.2}Ti_{0.8}S_2$ sample obtained from joint Rietveld refinement of X-ray and neutron PDFs.

Atom	Wyckoff	x	y	z	Occupancy	Uiso
Li1	3b	0	0	0.5	1	0.0160(6)
Li2	3a	0	0	0	0.2	0.0160(6)
Ti	3a	0	0	0	0.8	0.0144(0)
S	6c	0	0	0.2558(5)	1	0.0093(4)
Space group $R\overline{3}m$, a = 3.535 Å, c = 18.034 Å r = 1-20 Å, Q_{max} = 23 Å, Overall R_w = 0.123						

Table A3.6: Refined structural parameters for the BSP sample (~ $Li_{0.8}Ti_{0.8}S_2$) obtained from joint Rietveld refinement of X-ray and neutron PDFs.

Atom	Wyckoff	x	y	z	Occupancy	Uiso
Li1	3b	0	0	0.5	0.6	0.0195(8)
Li2	3a	0	0	0	0.2	0.0195(8)
Ti	3a	0	0	0	0.8	0.0134(7)
S	6c	0	0	0.2568(8)	1	0.0095(3)
Space group $R\overline{3}m$, a = 3.516 Å, c = 18.157 Å r = 1-20 Å, Q_{max} = 23 Å, Overall R_w = 0.118						

Table A3.7: Refined structural parameters for (a) O3 phase and (b) O1 phase in the fully charged sample (~ $Li_{0.1}Ti_{0.8}S_2$) obtained from joint Rietveld refinement of X-ray and neutron PDFs

(a)

Atom	Wyckoff	x	y	z	Occupancy	Uiso
Li1	3b	0	0	0.5	0.05	0.05
Li2	3a	0	0	0	0.05	0.05
Ti	3a	0	0	0	0.8	0.0186(3)
S	6c	0	0	0.2565(7)	1	0.0349(4)

Space group $R\bar{3}m$, a = 3.437 Å, c = 18.093 Å
r = 1-20 Å, Q_{max} = 23 Å, Overall R_w = 0.201

(b)

Atom	Wyckoff	x	y	z	Occupancy	Uiso
Li1	1b	0	0	0.5	0.05	0.05
Li2	1a	0	0	0	0.05	0.05
Ti	1a	0	0	0	0.8	0.0122(2)
S	2d	0.33333	0.66667	0.25000	1	0.0436(8)

Space group $R\bar{3}m$, a = 3.369 Å, c = 5.689 Å
r = 1-20 Å, Q_{max} = 23 Å, Overall R_w = 0.201

Table A3.8: Refined structural parameters for the FD sample ($Li_{1.2}Ti_{0.8}S_2$) obtained from joint Rietveld refinement of X-ray and neutron PDFs.

Atom	Wyckoff	x	y	z	Occupancy	Uiso
Li1	3b	0	0	0.5	1	0.0236(7)
Li2	3a	0	0	0	0.2	0.0236(7)
Ti	3a	0	0	0	0.8	0.0155(4)
S	6c	0	0	0.2563(3)	1	0.0121(1)

Space group $R\bar{3}m$, a = 3.520 Å, c = 18.189 Å
r = 1-20 Å, Q_{max} = 23 Å, Overall R_w = 0.136

Table A3.9: The fitting parameters of the Ti K-edge EXAFS spectrum for $Li_{1.2}Ti_{0.8}S_2$ at Pristine, BSP, FC and FD states of charge. Good fits are achieved based on the initial structure model obtained from the joint refinement of diffraction data. $d_{i\text{-}j}$ is the refined distance between i and j atoms. σ^2 is the Debye-Waller factor and [n] is the coordination number of j atoms around i. Due to the limited resolution in r space (~ 0.24 Å), the slight bond-length differences between O3 and O1-type phases at the fully charged state are not distinguishable. Therefore, the FC sample was fitted using the dominant O3-type layered phase.

	Ti-S			Ti-Ti			R-factors (%)
	d_{i-j} (Å)	σ^2 (Å^{-2})	[n]	d_{i-j} (Å)	σ^2 (Å^{-2})	[n]	
Pristine	2.43(0)	0.0060(6)	6.0	3.50(4)	0.0207(9)	4.80	0.905
BSP	2.40(6)	0.0083(5)	6.0	3.49(8)	0.0158(1)	4.80	1.427
FC	2.40(9)	0.0070(6)	6.0	3.41(5)	0.0207(9)	5.0(9)	1.647
FD	2.43(2)	0.0049(7)	6.0	3.49(6)	0.0155(5)	5.0(3)	1.27

Table A3.10: Fitting parameters of the S K-edge EXAFS spectra for $Li_{1.2}Ti_{0.8}S_2$ at the Pristine, BSP, FC and FD states of charge. Good fits were achieved using the initial structural model obtained by joint Rietveld refinement of diffraction data. In the below table, $d_{i\text{-}j}$ refers to the refined distance between atoms i and j. σ^2 is the Debye-Waller factor and [n] denotes the coordination number of j atoms around i. Due to the limited resolution in r space (~ 0.24 Å), S-S distances within the ab plane and between the TiS_2 interlayers cannot be differentiated. Similarly, the slight bond-length differences between O3- and O1-type phases at the fully charged state are not distinguishable. Therefore, the FC sample was fitted using the majority O3-type layered phase.

	S-Ti			S-S in LiS_2 interlayer			S-S in ab plane and TiS_2 interlayer			S-S dimer			R-factors (%)
	d_{i-j} (Å)	σ^2 (Å^{-2})	[n]	d_{i-j} (Å)	σ^2 (Å^{-2})	[n]	d_{i-j} (Å)	σ^2 (Å^{-2})	[n]	d_{i-j} (Å)	σ^2 (Å^{-2})	[n]	
Pristine	2.41(1)	0.0039(2)	6.0	3.79(5)	0.0024(6)	3.0	3.45(9)	0.0105(6)	9.0				0.462
BSP	2.37(3)	0.0039(6)	6.0	3.77(5)	0.0065(3)	3.0	3.42(5)	0.0072(4)	9.0				0.768
FC	2.37(3)	0.0053(7)	6.0	3.74(6)	0.0240(5)	3.0	3.41(0)	0.0151(8)	7.0(4)	2.07(9)	0.00272	1	0.177
FD	2.41(2)	0.0103(8)	6.0	3.86(0)	0.0267(5)	3.0	3.41(5)	0.0099(7)	9.0				0.169

Appendices for Chapter 4

Appendices Figures

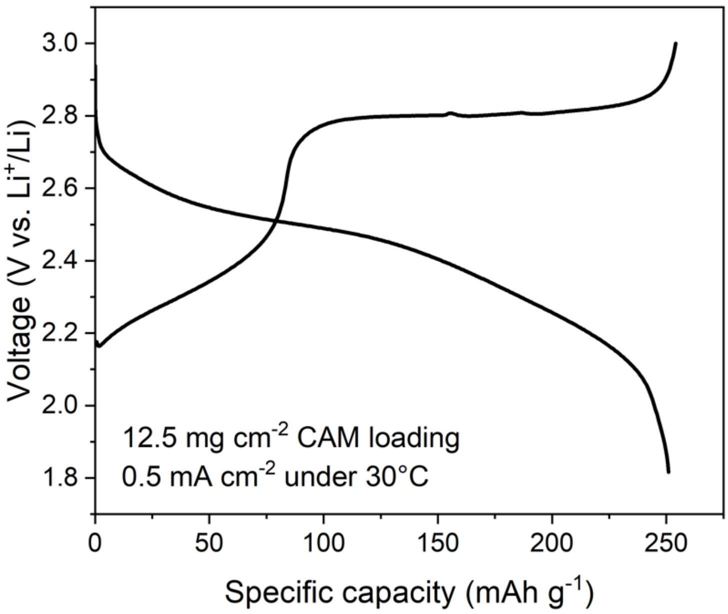

Figure A4.1: The first cycle of $Li_{1.2}Ti_{0.8}S_2$ in the liquid electrolyte cells at 0.5 mA cm^{-2}, 30 °C, with a CAM loading of 12.5 mg cm^{-2}.

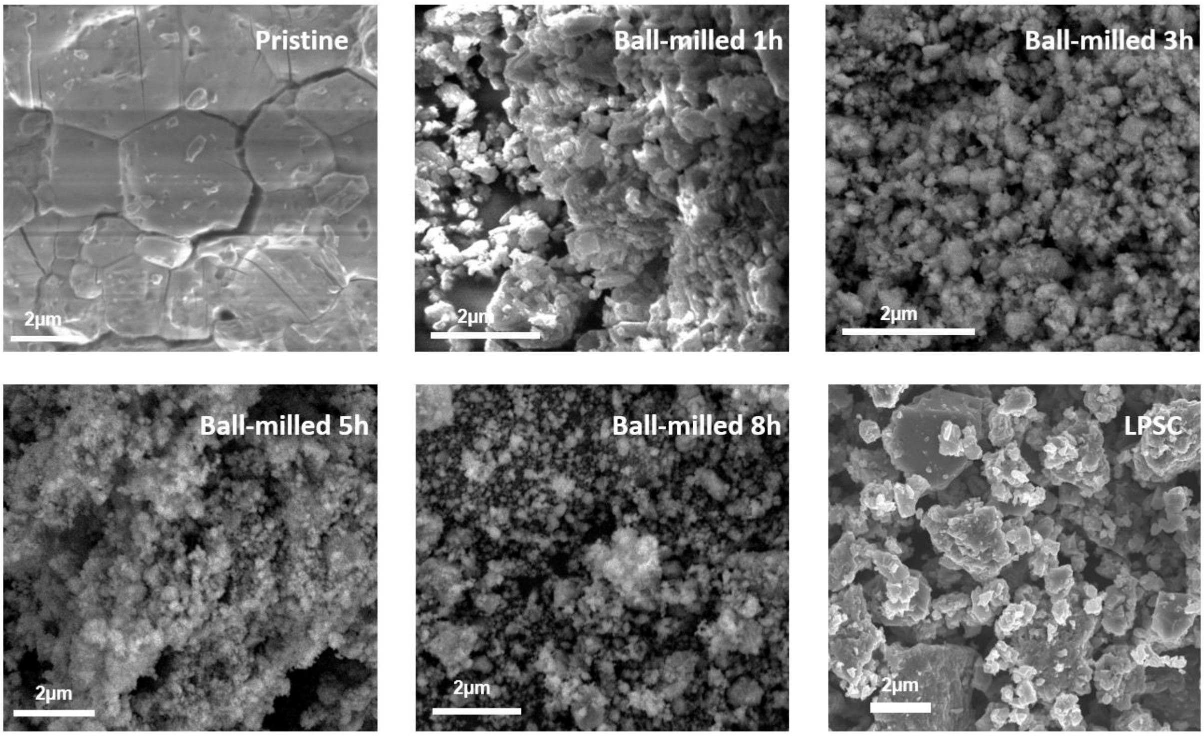

Figure A4.2: SEM images of the CAM $Li_{1.2}Ti_{0.8}S_2$ after different ball-milling durations at 200 rpm, along with the LPSC used in the composite cathode.

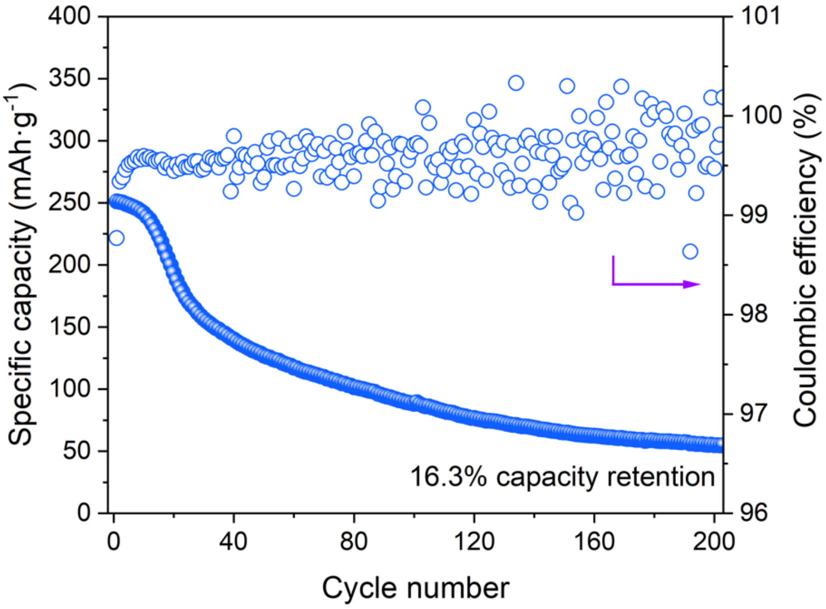

Figure A4.3: The cycling performance of $Li_{1.2}Ti_{0.8}S_2$ in the liquid electrolyte cells at 0.5 mA cm^{-2}, 30 °C, with a CAM loading of 12.5 mg cm^{-2}.

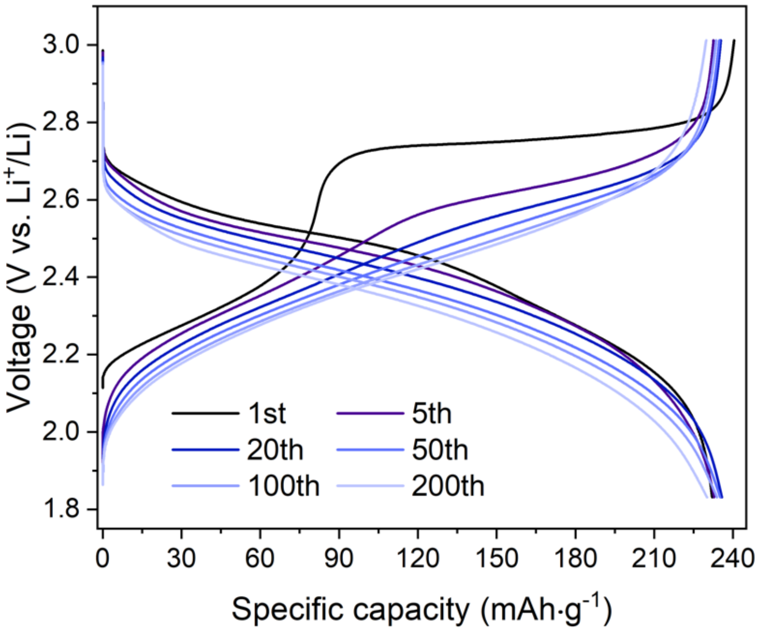

Figure A4.4: The load curves of $Li_{1.2}Ti_{0.8}S_2$ in the liquid electrolyte cells at 0.5 mA cm^{-2}, 30 °C, with a CAM loading of 12.5 mg cm^{-2}. The voltage present here was calibrated using a three-electrode reference method.

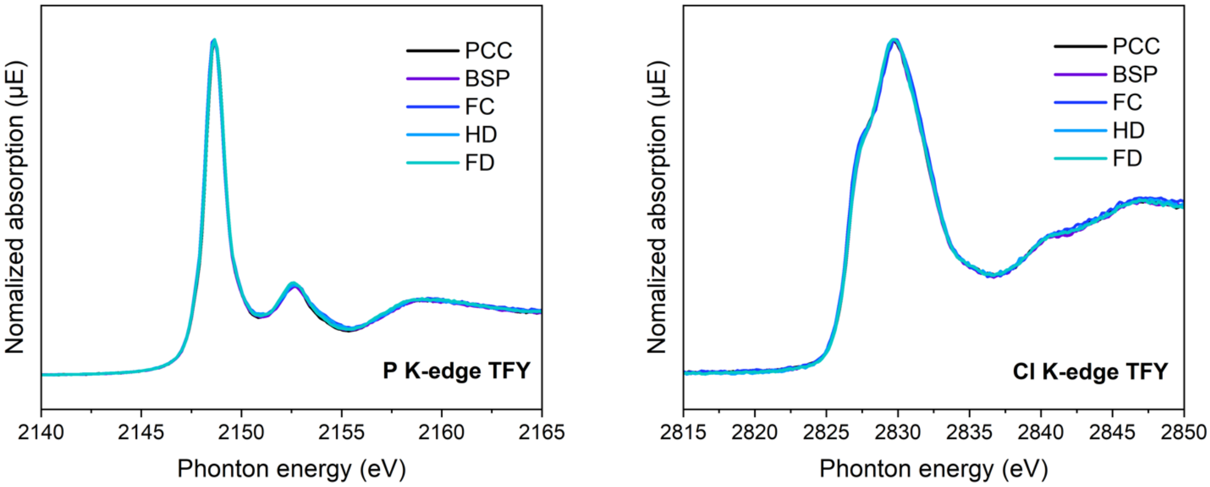

Figure A4.5: The TFY-XANES spectra at the P and Cl K-edge for the composite cathode at the PCC, BSP, FC, HD and FD states in the first cycle.

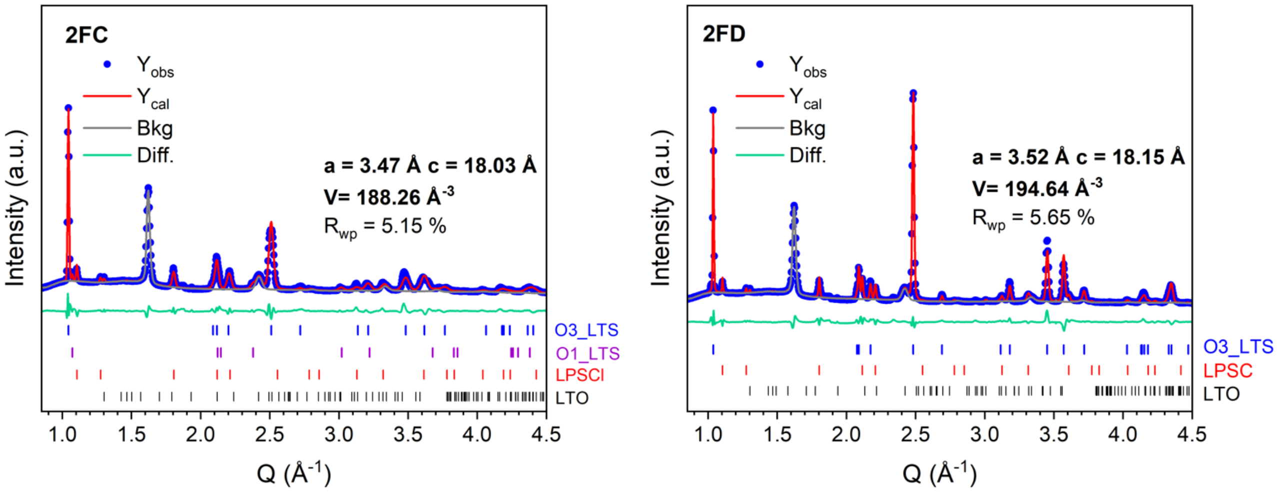

Figure A4.6: Rietveld refinement of the FC and FD states during the second cycle. $Li_{1.2}Ti_{0.8}S_2$ shows nearly identical phase evolution and lattice parameter changes to those observed in the first cycle.

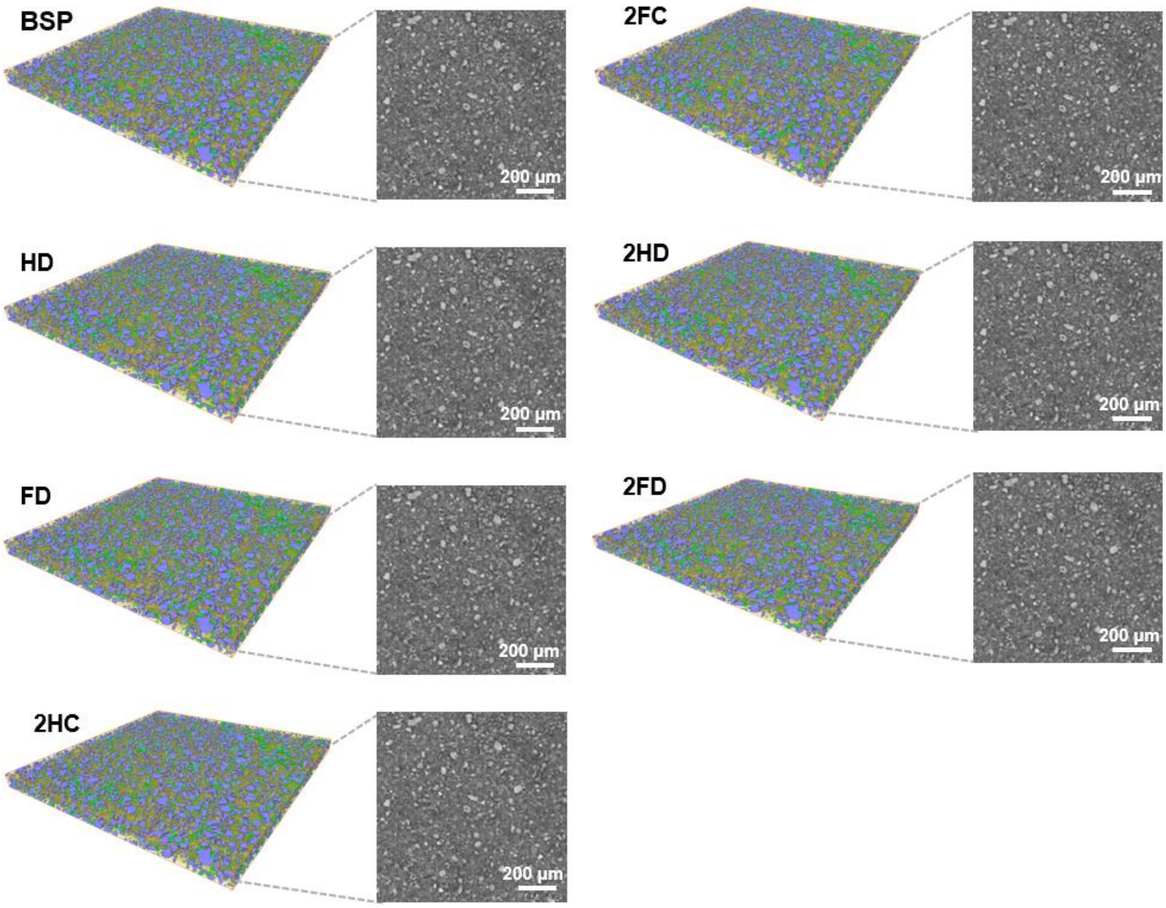

Figure A4.7: *In situ* X-ray CT analysis of the composite cathode during cycling. The cell was cycled at 0.5 mA cm^{-2} at room temperature under a stack pressure of 2 MPa, with an areal capacity of ~ 3 mAh cm^{-2}. 3D rendered images of the composite cathode are shown on the left side. Purple denotes CAM particles, green represents voids, and the remaining volume corresponds to the LPSC and CNF. 2D X-ray CT virtual cross-section of each state is displayed on the right.

Appendices Tables

Table A4.1: Refined structural parameters for (a) O3 phase and (b) O1 phase in the fully charged composite cathode, obtained from Rietveld refinement of synchrotron XRD diffraction data.

(a)

Atom	Wyckoff	x	y	z	Occupancy	Uiso
Li1	3b	0	0	0.5	0.15	0.05
Li2	3a	0	0	0	0.05	0.05
Ti	3a	0	0	0	0.8	0.0340(3)
S	6c	0	0	0.2580(3)	1.0	0.0415(6)
Space group $R\bar{3}m$, a = 3.4744(8) Å, c = 18.0425(7) Å, Overall R_{wp} = 4.76%						

(b)

Atom	Wyckoff	x	y	z	Occupancy	Uiso
Li1	1b	0	0	0.5	0.15	0.05
Li2	1a	0	0	0	0.05	0.05
Ti	1a	0	0	0	0.8	0.0254(0)
S	2d	0.33333	0.66667	0.25000	1.0	0.0546(0)
Space group $R\bar{3}m$, a = 3.4177(8) Å, c = 5.8227(5) Å, Overall R_{wp} = 4.76%						

Appendices for Chapter 5

Appendices Figures

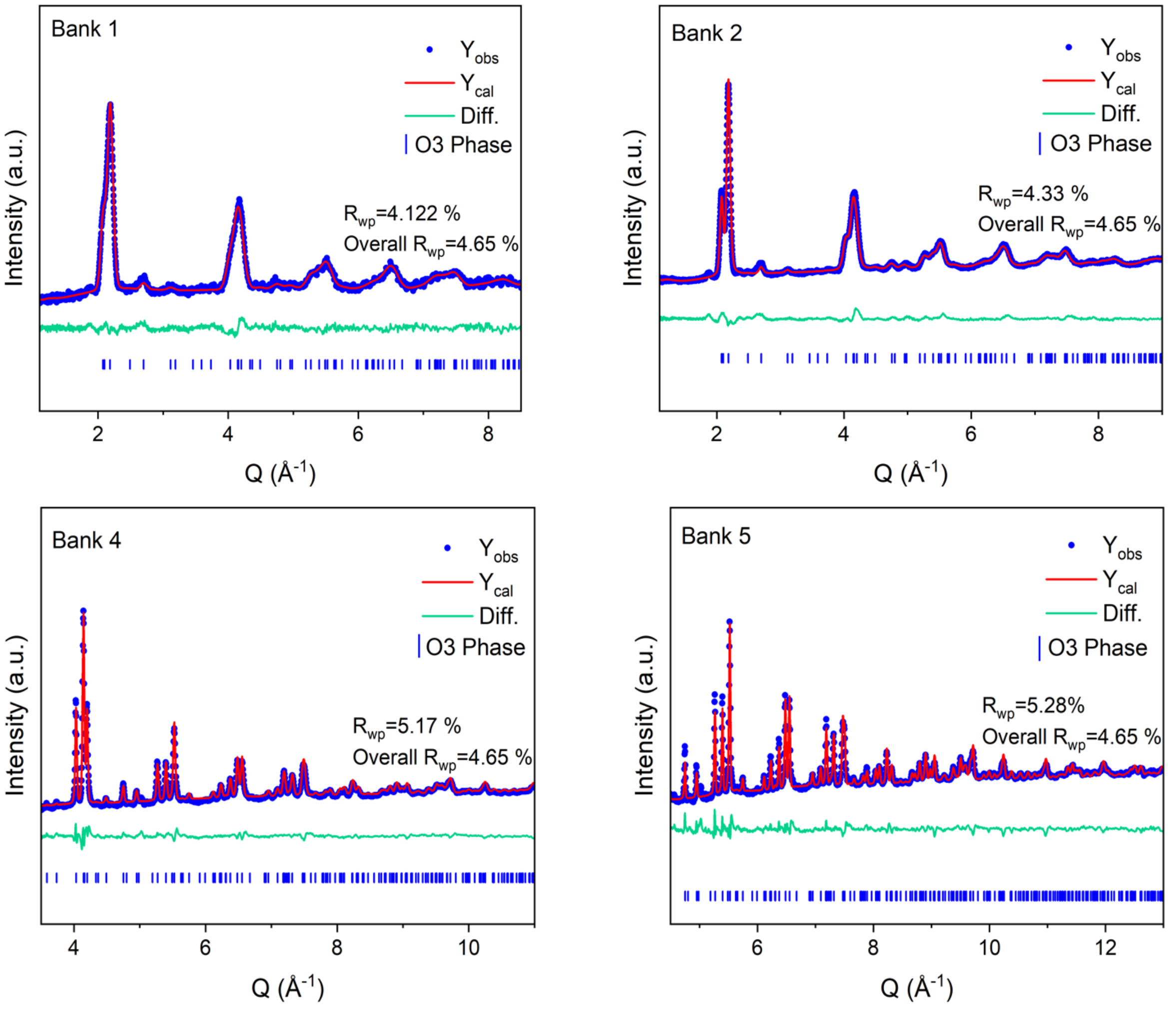

Figure A5.1: Rietveld refinements of the pristine $Li_{1.2}Mn_{0.2}Ti_{0.6}S_2$. Joint refinements of the PXRD (presented in Figure 5.2) and neutron diffraction data from five detector banks.

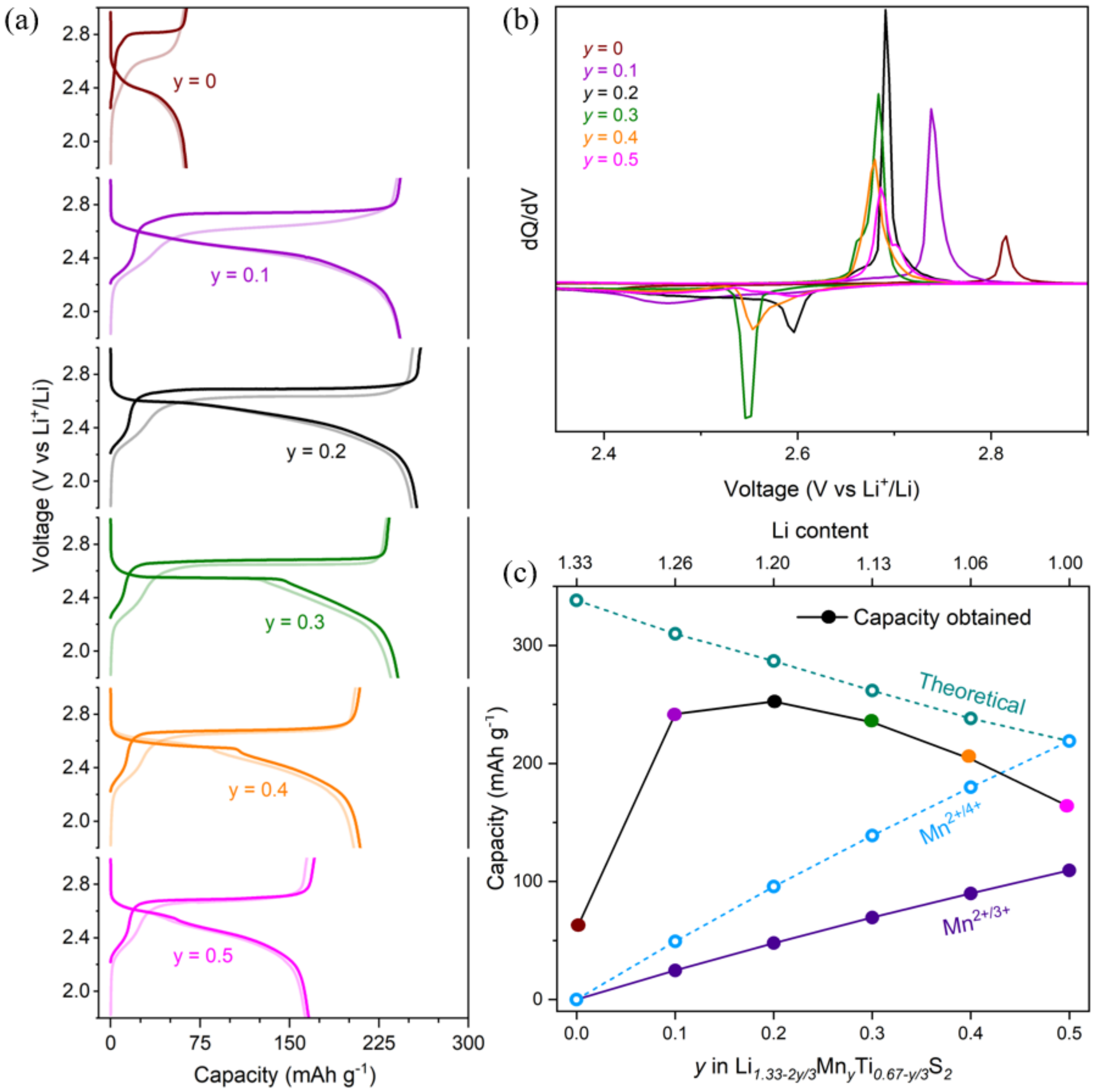

Figure A5.2: Electrochemical behavior of the $Li_{1.33-2y/3}Mn_yTi_{0.67-y/3}S_2$ series. (a) The first two cycles were performed at 10 mA g^{-1} within a voltage range of 1.8 – 3V. The curves in lighter colors correspond to the second cycle. (b) dQ/dV curves for the first cycle of various compositions. (c) Theoretical capacity and the actual first discharge capacity obtained for the compounds over the first cycle for different compositions. The capacity expected from cationic $Mn^{2+/3+}$ and hypothetical $Mn^{2+/4+}$ is also indicated. The capacity decrease beyond $y > 0.3$ primarily arises from the reduced amount of available Li in the $Li_{1.33-2y/3}Mn_yTi_{0.67-y/3}S_2$ samples as the Mn content (y) increases.

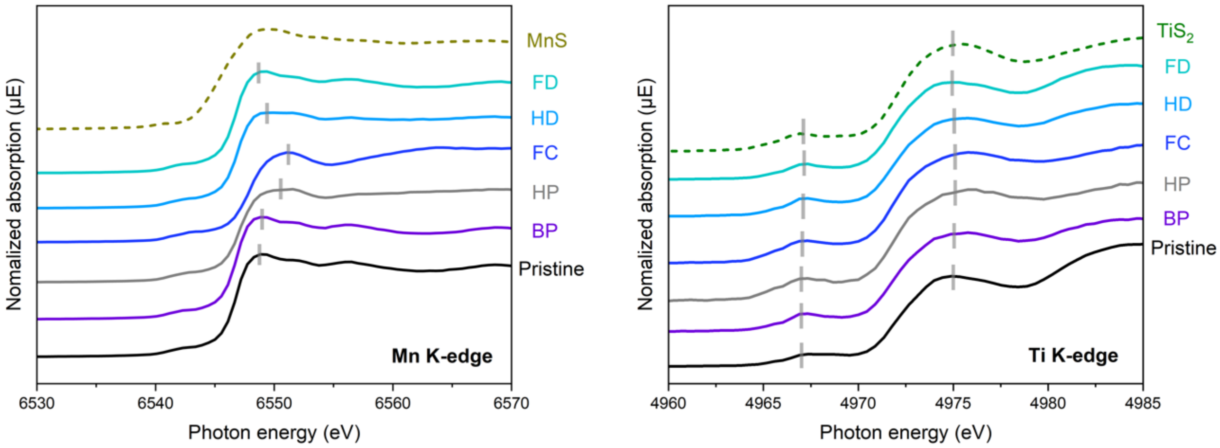

Figure A5.3: Mn and Ti K-edge XANES spectra for $Li_{1.2}Mn_{0.2}Ti_{0.6}S_2$ at different states of charge during the first cycle. The energy position of both edges, defined as the absorption edge energy (E_0), which is the maximum of the first derivative of μ(E), is extracted and plotted in Figure 5.4. The Ti K-edge XANES spectra for $Li_{1.2}Ti_{0.8}S_2$ are shown in Figure 3.6

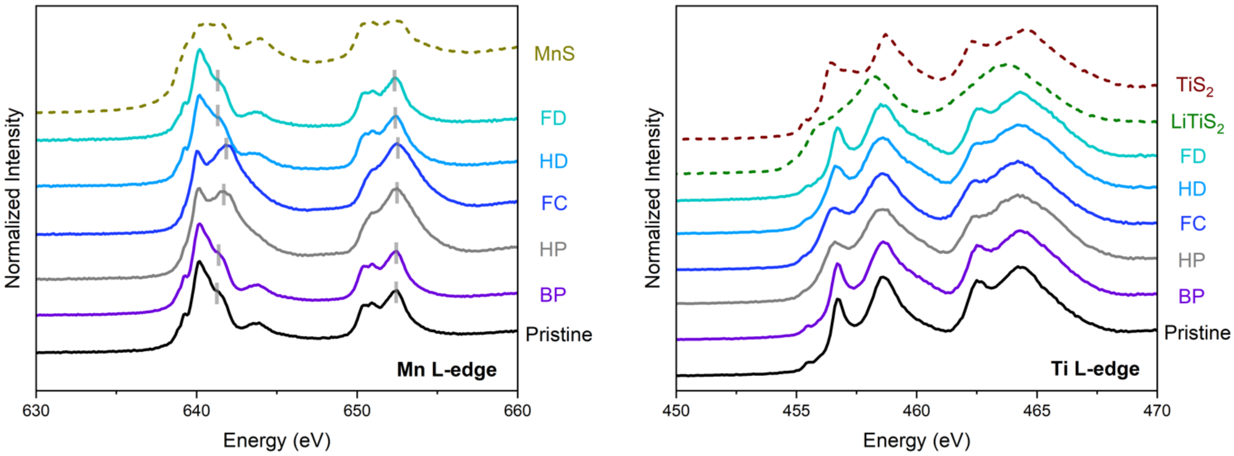

Figure A5.4: Mn and Ti L-edge XAS spectra for $Li_{1.2}Mn_{0.2}Ti_{0.6}S_2$ at different states of charge during the first cycle. The spectra were collected in fluorescence PFY mode, providing bulk sensitivity to a depth of ~ 100 nm. The spectra reveal continuous Mn oxidation and reduction, while Ti remains predominantly in the inactive Ti^{4+} state, consistent with the Mn and Ti K-edge XANES results.

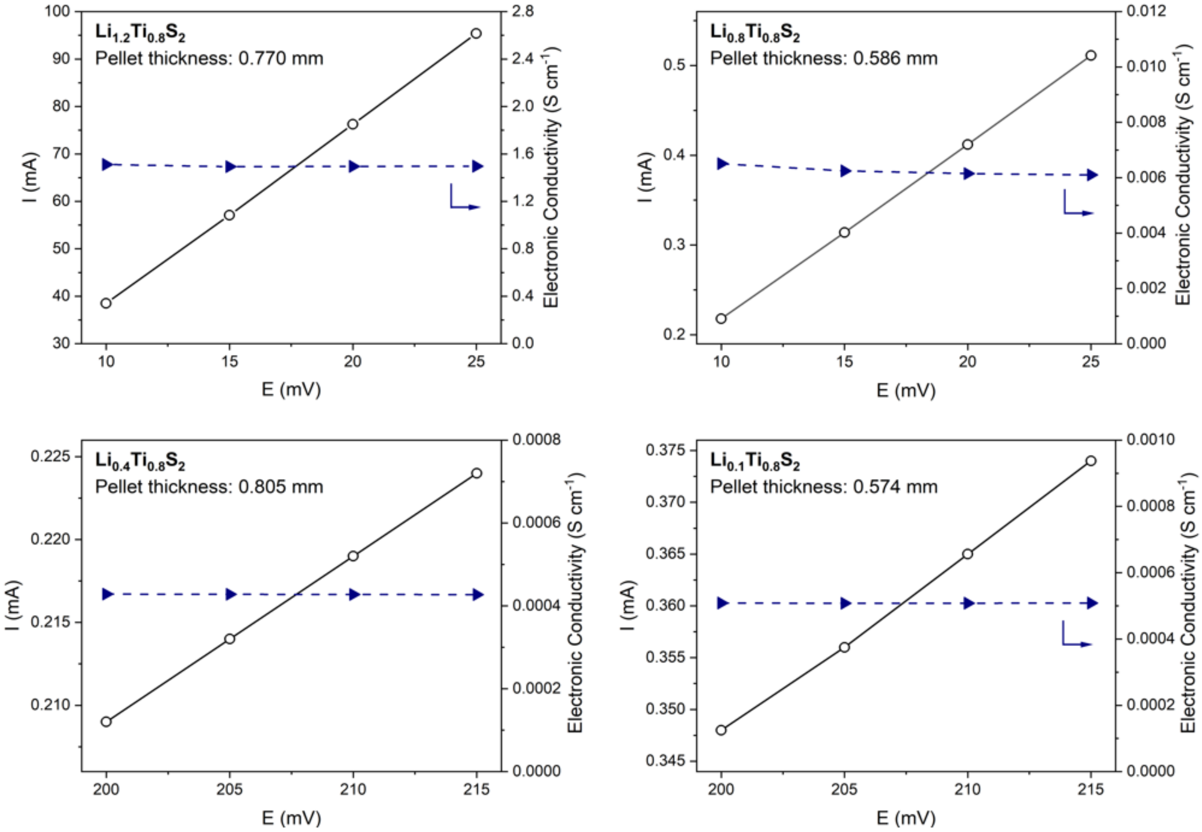

Figure A5.5: DC polarization plots of $Li_xTi_{0.8}S_2$ (x = 1.2, 0.8, 0.4, 0.1). Steady-state current (circles) and DC conductivity determination (triangles) measured on a pelletized sample at different states of delithiation.

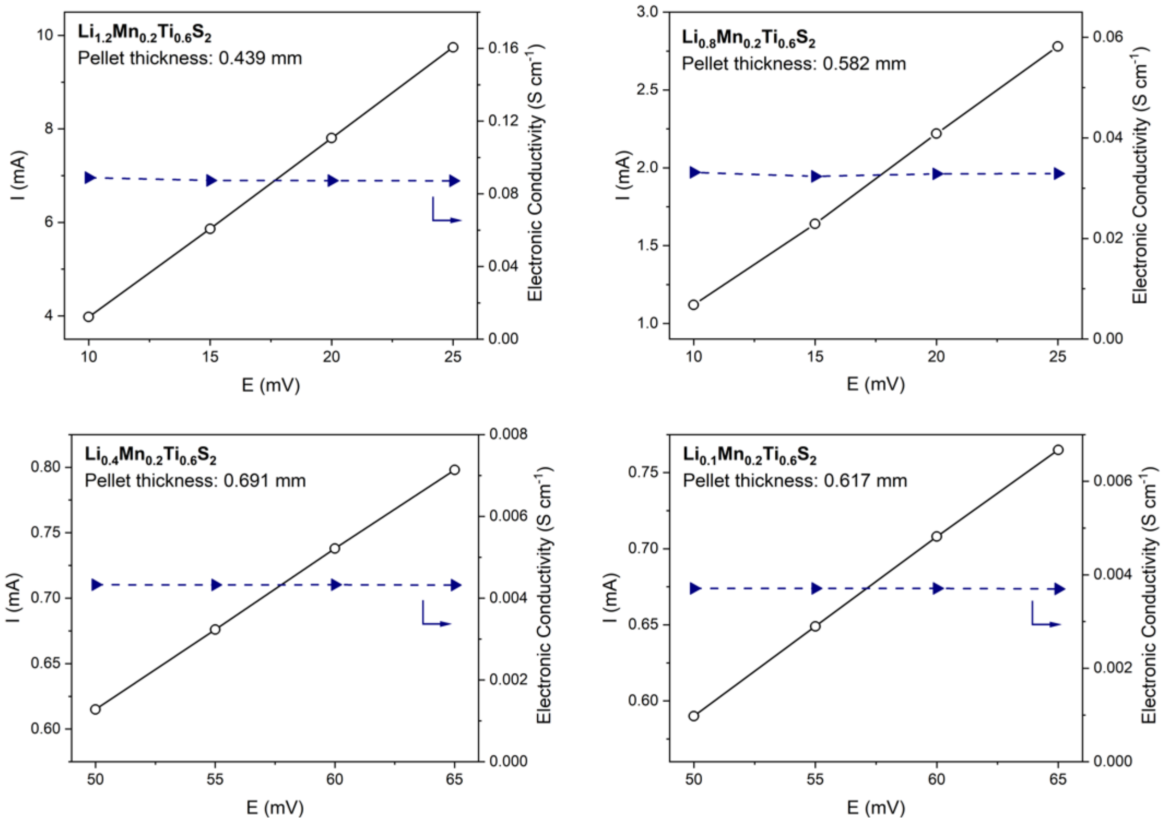

Figure A5.6: DC polarization plots of $Li_xMn_{0.2}Ti_{0.8}S_2$ (x = 1.2, 0.8, 0.4, 0.1). Steady-state current (circles) and DC conductivity determination (triangles) measured on a pelletized sample at different states of delithiation.

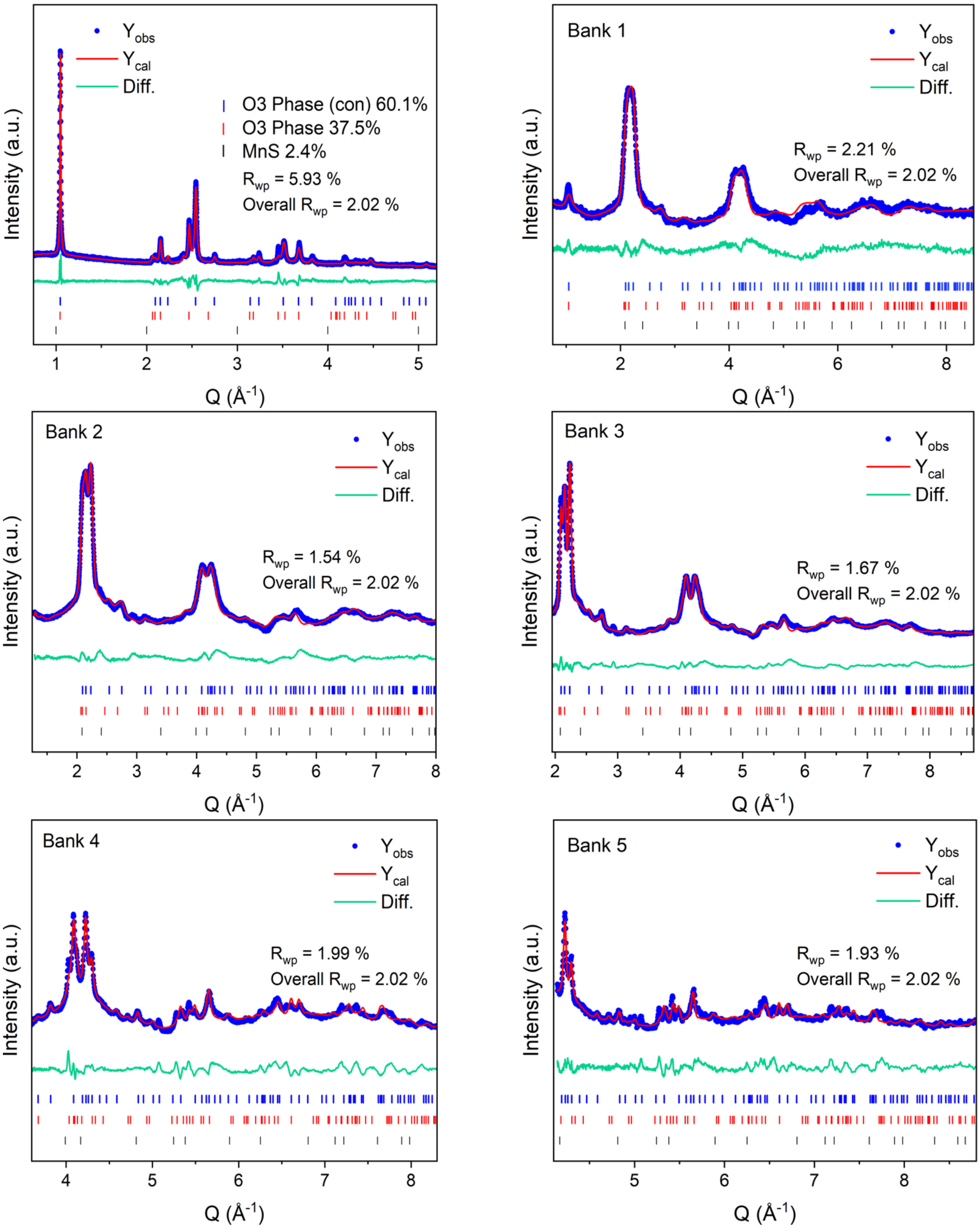

Figure A5.7: Rietveld refinements of the FC sample ($Li_{1.2}Mn_{0.2}Ti_{0.8}S_2$ charged to 3V). Joint Rietveld refinements of the PXRD (top left) and neutron diffraction data from five detector banks. The FC sample exhibits a biphasic mixture of two different O3 phases: a dominant, more contracted O3 phase (denoted O3 phase (con)) and a minor phase with lattice parameters similar to the pristine state. This observation is consistent with the *operando* XRD results shown in Figure 5.7.

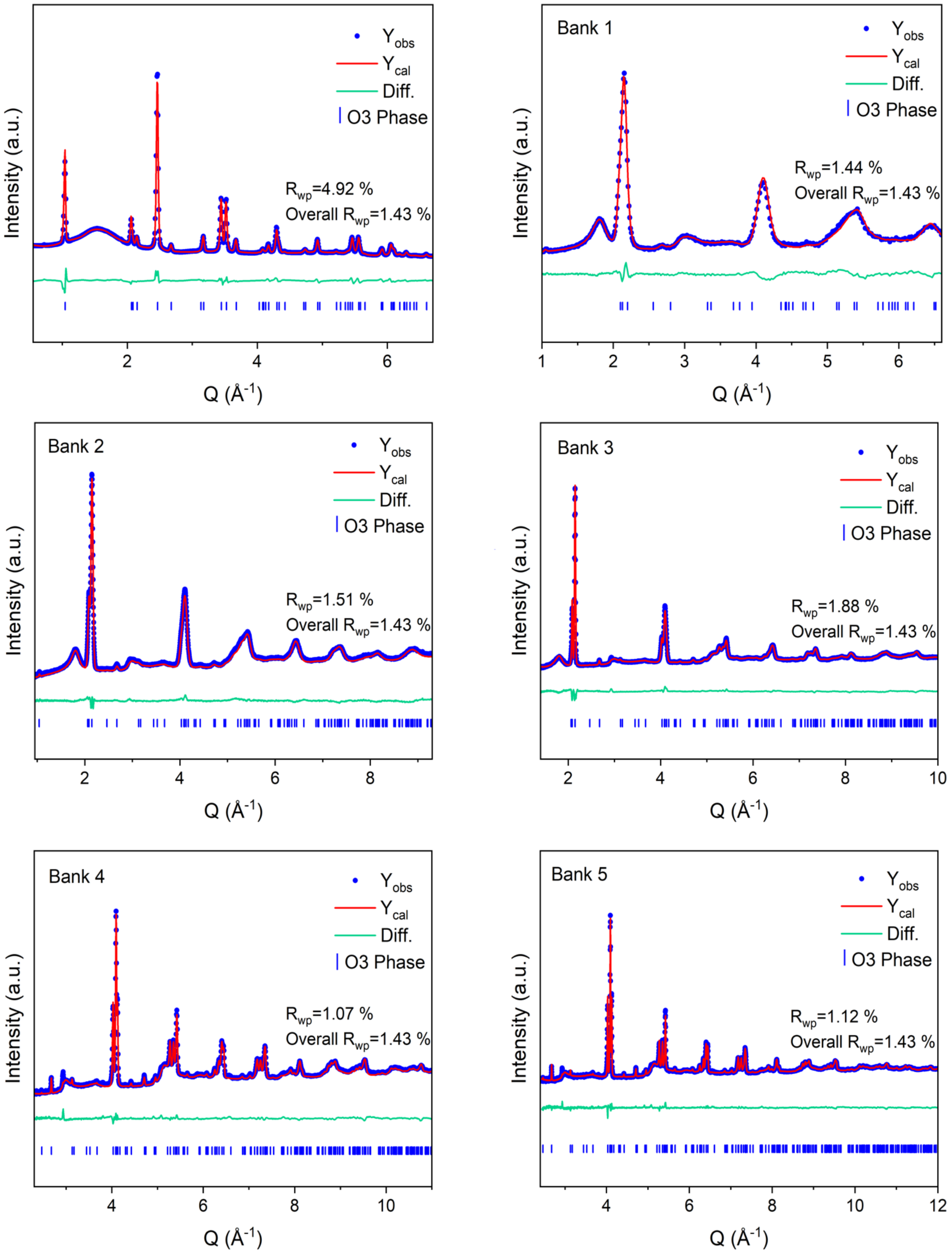

Figure A5.8: Rietveld refinements of the FD sample ($Li_{1.2}Mn_{0.2}Ti_{0.6}S_2$ discharged to 1.8V). Joint Rietveld refinements of the PXRD (top left) and neutron diffraction data from five detector banks. Following a full cycle, the FD sample remains the O3-type structure with lattice parameters closely matching the pristine state, suggesting a highly reversible long-range structural evolution.

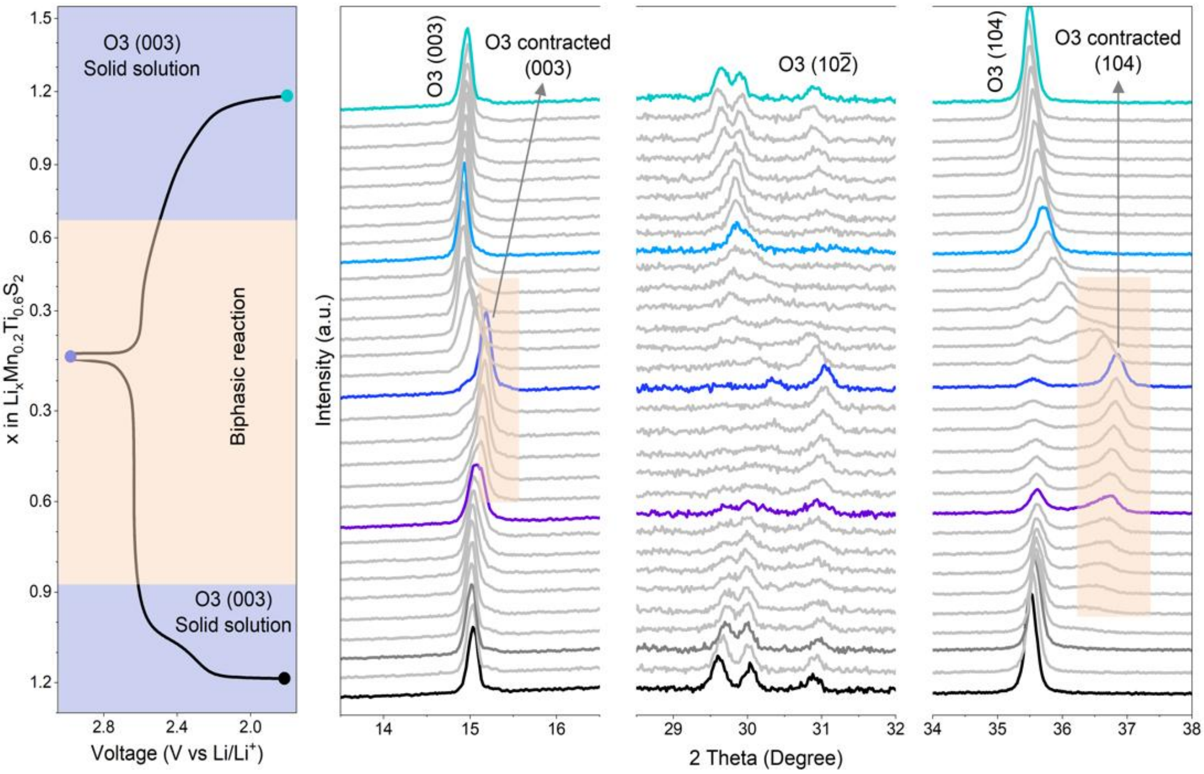

Figure A5.9: Structural evolution of $Li_{1.2}Mn_{0.2}Ti_{0.6}S_2$ during the second cycle. $Li_{1.2}Mn_{0.2}Ti_{0.6}S_2$ undergoes the phase evolution observed in the initial cycle. The left panel shows the corresponding cycling profile for the second cycle between 1.8V and 3V at 10 mA g^{-1}.

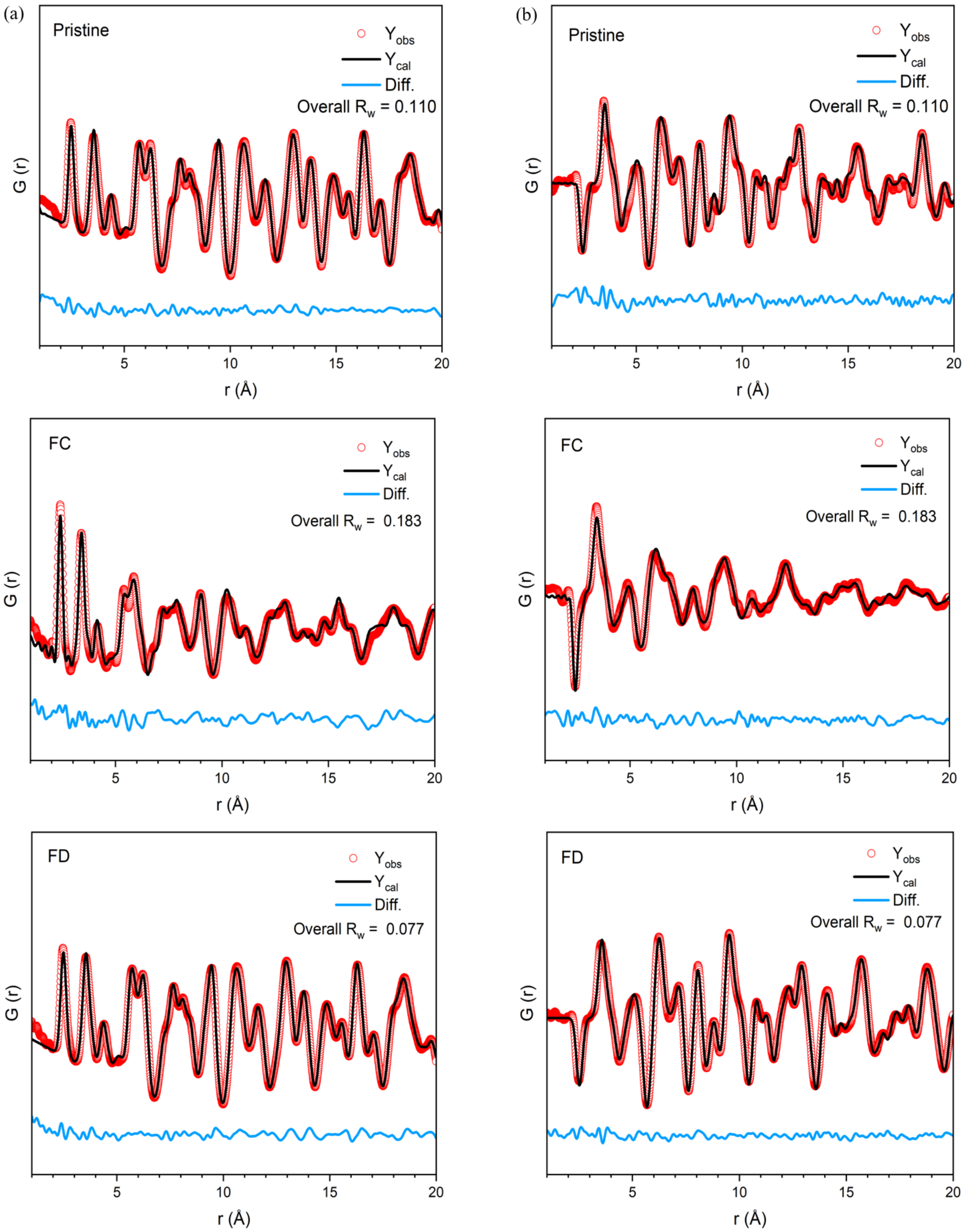

Figure A5.10: Fitting results of X-ray (a) and neutron PDFs (b) of $Li_{1.2}Mn_{0.2}Ti_{0.6}S_2$ at various states of charge, with Q_{max} = 22 Å. At each state of charge, the X-ray and Neutron PDFs were jointly refined between 1 – 20 Å using PDFgui. The PDF of the FC sample was fitted using a biphasic O3/more-contracted O3 structural model, whereas the other states were refined using a single-phase O3-type structure, consistent with diffraction results.

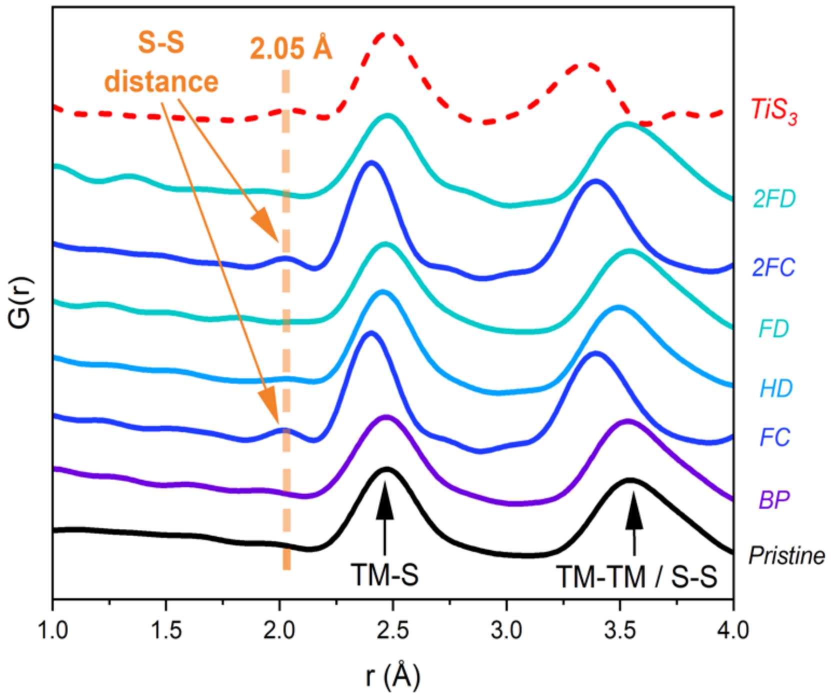

Figure A5.11: X-ray PDFs of $Li_{1.2}Mn_{0.2}Ti_{0.6}S_2$ in the 1 – 4 Å region at various states of charge, generated from total scattering data measured at room temperature, Q_{max} = 22 Å. The reversible formation and disappearance of a peak at 2.05 Å (highlighted in orange) was also observed in the second cycle, suggesting the reversible S-redox process.

Appendices Tables

Table A5.1: Refined structural parameters for the pristine $Li_{1.2}Mn_{0.2}Ti_{0.6}S_2$ sample obtained from joint Rietveld refinement of PXRD and neutron diffraction data.

Atom	Wyckoff	x	y	z	Occupancy	Uiso
Li1	3b	0	0	0.5	1	0.0171(6)
Li2	3a	0	0	0	0.2	0.0171(6)
Ti	3a	0	0	0	0.6	0.0084(5)
Mn	3a	0	0	0	0.2	0.0084(5)
S	6c	0	0	0.2569(2)	1	0.0105(8)
Space group $R\bar{3}m$, a = 3.573(3) Å, c = 18.0295(9) Å, Overall R_{wp} = 4.65%						

Table A5.2: Refined structural parameters for (a) contracted O3 phase and (b) O3 phase in the fully charged sample, ~ $Li_{0.1}Mn_{0.2}Ti_{0.6}S_2$, obtained from joint co-refinement of PXRD and neutron diffraction.

(a)

Atom	Wyckoff	x	y	z	Occupancy	Uiso
Li1	3b	0	0	0.5	0.05	0.05
Li2	3a	0	0	0	0.05	0.05
Ti	3a	0	0	0	0.6	0.0048(4)
Mn	3a	0	0	0	0.2	0.0048(4)
S	6c	0	0	0.2532(2)	1.0	0.0294(2)
Space group $R\bar{3}m$, a = 3.4187(7) Å, c = 17.9910(8) Å, Overall R_{wp} = 2.02%						

(b)

Atom	Wyckoff	x	y	z	Occupancy	Uiso
Li1	3b	0	0	0.5	0.05	0.05
Li2	3a	0	0	0	0.05	0.05
Ti	3a	0	0	0	0.6	0.0488(9)
Mn	3a	0	0	0	0.2	0.0488(9)
S	6c	0	0	0.2645(3)	1	0.0538(8)
Space group $R\bar{3}m$, a = 3.5629(2) Å, c = 18.0309(8) Å, Overall R_{wp} = 2.02%						

Table A5.3: Refined structural parameters for the FD sample, $Li_{1.2}Mn_{0.2}Ti_{0.6}S_2$, obtained from joint Rietveld refinement of PXRD and neutron diffraction data.

Atom	Wyckoff	x	y	z	Occupancy	Uiso
Li1	3b	0	0	0.5	1	0.0125(0)
Li2	3a	0	0	0	0.2	0.0125 (0)
Ti	3a	0	0	0	0.6	0.0083(4)
Mn	3a	0	0	0	0.2	0.0083(4)
S	6c	0	0	0.2554(7)	1	0.0102(6)
Space group $R\bar{3}m$, a = 3.5651(3) Å, c = 18.0507(1) Å, Overall R_{wp} = 1.43%						

Table A5.4: Refined structural parameters for the pristine $Li_{1.2}Mn_{0.2}Ti_{0.6}S_2$ sample obtained from joint Rietveld refinement of X-ray and neutron PDFs.

Atom	Wyckoff	x	y	z	Occupancy	Uiso
Li1	3b	0	0	0.5	1	0.0102(5)
Li2	3a	0	0	0	0.2	0.0102(5)
Ti	3a	0	0	0	0.6	0.0100(8)
Mn	3a	0	0	0	0.2	0.0100(8)
S	6c	0	0	0.2581(0)	1	0.0119(7)

Space group $R\bar{3}m$, a = 3.572 Å, c = 18.0144 Å
r = 1-20 Å, Q_{max} = 22 Å, Overall R_w = 0.110

Table A5.5: Refined structural parameters for (a) contracted O3 phase and (b) O3 phase in the fully charged sample (~ $Li_{0.1}Mn_{0.2}Ti_{0.6}S_2$) obtained from joint Rietveld refinement of X-ray and neutron PDFs

(a)

Atom	Wyckoff	x	y	z	Occupancy	Uiso
Li1	3b	0	0	0.5	0.05	0.05
Li2	3a	0	0	0	0.05	0.05
Ti	3a	0	0	0	0.6	0.0365(1)
Mn	3a	0	0	0	0.2	0.0365(1)
S	6c	0	0	0.2554(5)	1	0.0193(2)

Space group $R\bar{3}m$, a = 3.397 Å, c = 17.631 Å
r = 1-20 Å, Q_{max} = 22 Å, Overall R_w = 0.183

(b)

Atom	Wyckoff	x	y	z	Occupancy	Uiso
Li1	3b	0	0	0.5	0.05	0.05
Li2	3a	0	0	0	0.05	0.05
Ti	3a	0	0	0	0.6	0.1528(4)
Mn	3a	0	0	0	0.2	0.1528(4)
S	6c	0	0	0.2601(5)	1	0.0654(5)

Space group $R\bar{3}m$, a = 3.576 Å, c = 18.134 Å
r = 1-20 Å, Q_{max} = 22 Å, Overall R_w = 0.183

Table A5.6: Refined structural parameters for the FD sample ($Li_{1.2}Mn_{0.2}Ti_{0.6}S_2$) obtained from joint Rietveld refinement of X-ray and neutron PDFs.

Atom	Wyckoff	x	y	z	Occupancy	Uiso
Li1	3b	0	0	0.5	1	0.0225(0)
Li2	3a	0	0	0	0.2	0.0225(0)
Ti	3a	0	0	0	0.6	0.0159(3)
Mn	3a	0	0	0	0.2	0.0159(3)
S	6c	0	0	0.2562(9)	1	0.0147(5)
Space group $R\bar{3}m$, a = 3.565 Å, c = 18.027 Å r = 1-20 Å, Q_{max} = 22 Å, Overall R_w = 0.077						

Table A5.7: Refined structural parameters for the disordered rocksalt $Li_{1.2}Ti_{0.8}S_2$ sample, obtained from Rietveld refinement of PXRD.

Atom	Wyckoff	x	y	z	Occupancy	Uiso
Li1	4a	0	0	0	0.6	0.0050(6)
Ti1	4a	0	0	0	0.4	0.0202(8)
S1	4b	0.5	0.5	0.5	1	0.0040(5)
Space group $R\bar{3}m$, a = 5.0365(5) Å, Overall R_{wp} = 3.79%						